Clay Minerals (2023), **58**, 143–194
doi:10.1180/clm.2023.20

CAMBRIDGE UNIVERSITY PRESS

Review Article

Generalized relationships between the ionic radii of octahedral cations and the *b* crystallographic parameter of clays and related minerals

Sabine Petit, Alain Decarreau, Brian Grégoire and Eric Ferrage
Institut de Chimie des Milieux et Matériaux de Poitiers (IC2MP), CNRS, Université de Poitiers, Poitiers, France

Abstract

Over several decades, a wealth of literature has been devoted to correlations between the chemistries of phyllosilicates and their crystallographic unit-cell parameter values. The *c* parameter is currently used because of its relation to the layer-to-layer distance, characteristic of the various families of phyllosilicates. The *b* parameter is also of interest because it allows measurement of the layer lateral dimensions and inherent structural adjustments. This unit-cell distance can be extracted from X-ray diffraction traces from the (06ℓ;33ℓ) diffraction region and by attributing the main diffraction peak observed to a 060 reflection, leading to the relationship $b = 6.d(060)$. The aim of this paper is to revisit the relationships between the *b* value (or equivalent) of the phyllosilicate (i.e. TO, TOT and TOTO) or hydroxide (i.e. hydroxide, oxyhydroxide and layered double hydroxide) families and the layer chemistry based on a mean ionic radius *R* of octahedral cations, calculated as $R = \sum_{i=1}^{n} (r_i.x_i)$, where r_i is the ionic radius of the octahedral cation *i* and x_i is its molar fraction over *n* types of octahedral cations ($\sum_{i=1}^{n} (x_i) = 1$). The data were collected from the literature and involved both natural and synthetic samples with both dioctahedral and trioctahedral structures of the octahedral sheet. The results showed that *b* values can be linked strongly to *R*, leading to suitable linear regressions for all of the studied structures. All correlations were found to be applicable irrespective of the di- or trioctahedral nature of the octahedral sheet, and these are discussed in light of (1) the lateral dimension of the octahedral sheet and (2) the dimensional misfit between the tetrahedral and octahedral sheets. For hydroxide families, all data can be gathered on a single *b vs R* correlation line, and the dimensional properties of the octahedral sheet can be interpreted simply based on an oxygen–cation–oxygen mean distance. For TO structures, two general *b vs R* correlation trends were reported, and these were assigned to two adjustment mechanisms corresponding to distinct types of tetrahedral and octahedral distortions. For the mica TOT family, two main trends were also reported, whereas the use of the synthetic mica series allowed us to demonstrate that the obtained scattering of data was mainly driven by the presence of multiple limited solid solutions. Such chemical complexity was also noted for smectites, especially regarding the tetrahedral composition and associated variability in layer charge. This variability made it difficult to propose a general regression correlating *b* to *R* values for smectites, although the regression obtained for neutral TOT layers can apply as a first-order relation. Finally, a single general *b vs R* correlation was obtained for chlorites, and the observed slope of the regression was interpreted according to the role played by the isolated hydroxide sheet on the evolution of the lateral dimension of the structures.

Keywords: *b* parameter; chlorite; hydroxide; ionic radius; mica; phyllosilicate; serpentine; smectite

(Received 8 September 2022; revised 5 July 2023; Accepted Manuscript online: 18 August 2023; Editor: George Christidis)

Phyllosilicates are layer silicates whose layer unit is composed of an octahedral sheet (O; closed packed array of anions) linked to one or two tetrahedral sheets (T; near-hexagonal rings of tetrahedra). Three basic structures of layers are generally found: the so-called TO (1:1), TOT (2:1) and TOTO (2:1 + interlayer octahedral sheet) layers (Fig. 1a). Adjacent layers are linked by hydrogen bonds (e.g. TO minerals), by van de Waals forces (e.g. talc and pyrophyllite) or by various interlayer materials (hydrated cations, e.g. smectite; cations, e.g. mica; metal-hydroxyl octahedral sheets, e.g. chlorite). The assemblage of a layer plus interlayer is a unit structure and must be electrostatically neutral overall (e.g. Bailey, 1981; Brigatti *et al.*, 2011). In the T sheet, the most common cations are Si, Al and Fe^{3+}, whereas in the O sheet, the most common cations are Al, Mg, Fe^{3+} and Fe^{2+}. Numerous other substitutions occur in natural and synthetic phyllosilicates (e.g. Kloprogge, 2017). When the octahedral cations are divalent, all octahedral sites are occupied and the structure is trioctahedral, whereas if octahedral cations are trivalent, only two-thirds of octahedral sites are occupied and the structure is dioctahedral (Fig. 1b). The position of (OH) in the dioctahedral sheet determines *trans* and *cis* octahedra (Fig. 1c). The plane layer cell is classically described by an (*a*,*b*) ortho-hexagonal cell in which the *b* parameter value (simply noted '*b*' in the following) is equal to three times the distance between two adjacent octahedral cations. The structures of the O sheets are similar to those of hydroxide structures.

Corresponding author: Sabine Petit; Email: sabine.petit@univ-poitiers.fr
Cite this article: Petit S, Decarreau A, Grégoire B, Ferrage E (2023). Generalized relationships between the ionic radii of octahedral cations and the *b* crystallographic parameter of clays and related minerals. *Clay Minerals* **58**, 143–194. https://doi.org/10.1180/clm.2023.20

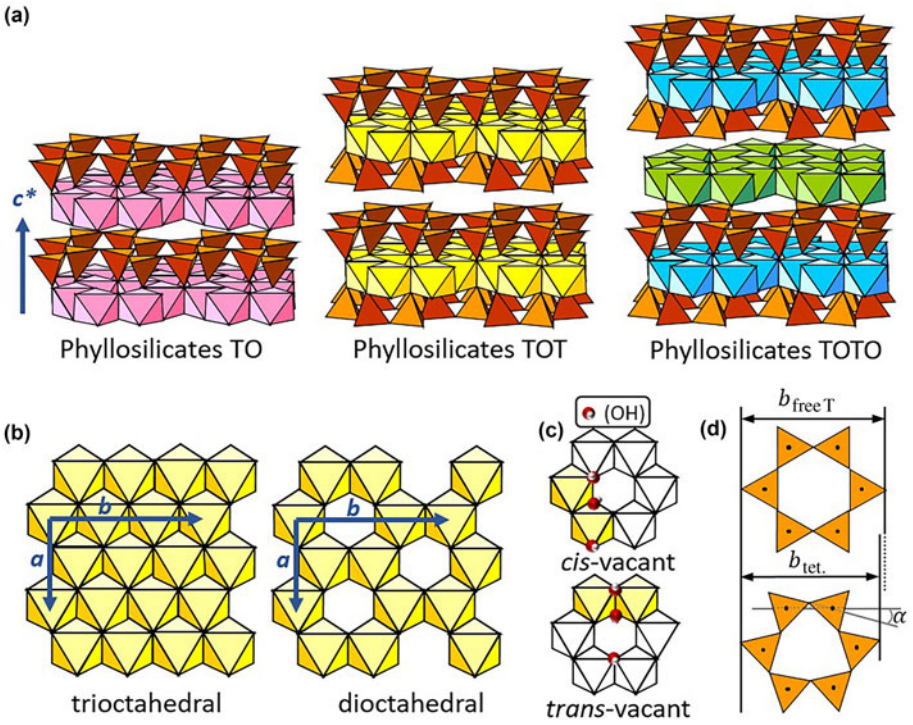

Figure 1. Schematic representation of (a) basic structures of TO, TOT and TOTO phyllosilicates. (b) Projection of *a* and *b* cell parameters (orthorhombic representation) on the surface of a trioctahedral and a dioctahedral sheet. (c) Distinction between *cis*- and *trans*-vacant di-octahedral sheets. (d) Tetrahedral rotation angle α.

To form a layer, similar lateral dimensions are required between the O and T sheets. In general, the lateral dimensions of the T sheet are larger than those of the O sheet, and a dimensional misfit occurs between these sheets. The T and O sheets can better form layers by contraction of T sheets *via* rotation of adjacent tetrahedra as measured by the α angle (Fig. 1d; e.g. Radoslovich & Norrish, 1962; Bailey, 1991b). An expansion of the lateral dimensions of the O sheet by flattening can better accommodate the linkage to the T sheet (e.g. Brigatti *et al.*, 2013). Other structural adjustments depending on the amount of strain at the sheet junction and the flexibility of the component O and T sheets can occur (e.g. Guggenheim & Eggleton, 1986). The degree of stress on the plane of the junction between O and T sheets greatly influences the resultant crystal size, morphology and structure of phyllosilicates (Bailey, 1981).

Numerous authors have studied the correlations between the compositions of phyllosilicates and unit-cell parameters. The *c* parameter is particularly useful for phyllosilicates because in monoclinic unit cells the $c\sin(\beta) = c^* = d(001)$ corresponds to the 'basal spacing', or the layer-to-layer distance (Fig. 1a). The periodicity along c^* can vary depending on the polytypic arrangement because of the different number of layers involved in the stacking sequence (e.g. Brigatti *et al.*, 2011). The *b* parameter is also of interest because it describes the O sheet lateral dimensions (Fig. 1b). Its value is obtained from X-ray diffraction (XRD) traces of the (06ℓ;33ℓ) reflections, with (060) giving $b = 6.d(060)$. The $d(060)$ value is commonly used to distinguish dioctahedral from trioctahedral phyllosilicates, the former ranging from 1.49 to 1.52 Å and the latter ranging from 1.52 to 1.53 Å (e.g. Środoń, 2013). Nontronite, a Fe^{3+}-rich smectite, is an exception, with *b* superposed over the trioctahedral range (e.g. Petit *et al.*, 2017). *b* is sensitive to the octahedral site composition of phyllosilicates, and many correlations are available in the literature. For example, $d(060)$ has been used to identify octahedral substitutions in kaolinite (e.g. Petit *et al.*, 1990). Brigatti (1983) correlated the octahedral site content of Fe and *b* of smectites (discussed below).

Most such results were presented as linear relationships (e.g. Russell & Clark, 1978; Brigatti, 1983; Petit *et al.*, 2017) between the *b* and octahedral site (and sometimes tetrahedral site) content. Many authors (e.g. Radoslovich, 1962; Rieder *et al.*, 1971; Wiewiora & Wilamowski, 1996) used multiple regression equations such as in Equation 1:

$$b = b_0 + \sum_{i=1}^{n} (a_i.c_i) \quad (1)$$

where b_0 is the *b* cell parameter of the end member mineral with a_i is the required regression coefficient for substituting cation *i*, and c_i is the atomic content of cation *i* in the structural formulas (SFs) containing *n* types of substituting cations. These relations are restricted to a given family of phyllosilicates and do not allow generalized relationships. Hazen & Wones (1972) established a clear correlation between the *b* of trioctahedral micas and the ionic radius of M^{2+} octahedral-site cations. Similarly, Brindley & Kao (1984) correlated the *a* and *c* unit-cell parameters of $M(OH)_2$ hydroxides and *M*–O distances. Gerth (1990) observed that the unit-cell *b* dimension varied with the ratio of metal-substituted goethite and was related to the ionic radii of incorporated metals. Bentabol & Ruiz Cruz (2013) examined the unit-cell values of lizardites with the ionic radius of the dominant *M* cations. However, for several *M* cations, the unit-cell values depend on the contribution of all octahedral cations (relative proportions and distribution). The current paper explores, in the light of the dimensional misfit between T and O sheets, the connection between the *b* of clay minerals and some related minerals with the mean ionic radius *R* of octahedral cations calculated as in Equation 2:

$$R = \sum_{i=1}^{n} (r_i.x_i) \quad (2)$$

https://doi.org/10.1180/clm.2023.20 Published online by Cambridge University Press

where r_i is the ionic radius of octahedral cation i and x_i is its molar fraction over n types of octahedral cations ($\sum_{i=1}^{n}(x_i) = 1$). Each family of minerals is discussed in this paper within a dedicated section that can be read separately.

Methods

Data for natural and synthetic samples were obtained from the literature. Most of the available b values were calculated from d(060) values measured from XRD unorientated powder traces according to the relation $b = 6.d(060)$. The diffraction band at (060) is observed at 1.49–1.54 Å for clay minerals and represents several overlapping (06ℓ;33ℓ) reflections with small differences in d-spacing. Accordingly, differences between actual *vs* extracted b values are to be expected and must be considered for comparing data between measurement methods.

The d(hkl) values (in Å) derived from XRD experiments are generally given to ±0.005 Å, whereas the spot sizes in the figures represent the estimated uncertainties in the unit-cell parameters of samples. The mean ionic radius R of octahedral cations is calculated following Equation 2. Ionic radii are from Shannon (1976; Table 1) and are given with ±0.01 Å uncertainty. SFs are from the literature or were calculated from chemical compositions. The uncertainty of R values cannot be generalized or estimated with accuracy. The data were selected carefully. For example, samples with SFs appearing to be obviously erroneous were disregarded.

The b dimension of a theoretical 'free' T sheet (i.e. with hexagonal symmetry and no tetrahedral rotations) is $b_{tet.} = (4\sqrt{2}) \times$ (Si–O) ≈ 9.15 Å, with an average bond length for Si–O = 1.618 ± 0.01 Å (Fig. 1d; Bailey, 1981, 1984b), and substitutions of larger cations for Si increase this value following Equation 3:

$$b_{tet.} = ax + 9.15 \quad (3)$$

where x is the number of tetrahedral atoms substituted for Si ($Si^{IV}_{1-x}T_x$). Accordingly, parameter a takes the value of 0.74, 1.26 or 1.15 for Al, Fe^{3+} or Ga, respectively. Be is treated as equivalent to Si in calculating $b_{tet.}$, as the Be–O bond length is close to that of Si–O (1.62 *vs* 1.618 Å, respectively). Equation 4 can be used to calculate α, the tetrahedral rotation angle, also termed ditrigonal rotation:

$$\alpha = \arccos(b/b_{tet.}) \quad (4)$$

This unique relationship assumes that contraction occurs by tetrahedral rotation alone (e.g. Radoslovich & Norrish, 1962), and it is not very accurate compared to structure refinement XRD single crystal data (Brigatti & Guggenheim, 2002). Clearly, for $b/b_{tet.}$ values >1, tetrahedral rotations do not apply because: (1) there are existing uncertainties in the bond lengths (e.g. the Si–O and ^{IV}Al–O bond lengths used are from Bailey (1984b) and are greater than those of Shannon (1976)); (2) various other mechanisms are involved to adjust T and O sheet lateral dimensions; and (3) tetrahedral angles may vary. Accordingly, $b/b_{tet.}$, which also provides a measure of misfit (McCauley & Newnham, 1971), was used here over the α value to compare samples. Moreover, Peterson *et al.* (1979) estimated from semi-empirical molecular-orbital cluster calculations that a six-fold ring of a 'free' ideal T sheet has a minimum energy at α = 16° and not at α = 0°, suggesting that the ring has an intrinsic ditrigonal character irrespective of octahedral articulation.

Finally, the M–O bond lengths were calculated using R (Equation 2) as the average of the ionic radii in six-fold coordination (Table 1). For octahedral oxygen ions, coordination is (1) in four-fold for trioctahedral configuration (i.e. each oxygen ion is bonded to three M^{2+} cations and one H^+ ion) or (2) in three-fold for dioctahedral configuration (i.e. each oxygen ion is bonded to two M^{3+} cations and one H^+ ion). The b dimension of a theoretical 'free' O sheet (i.e. with regular octahedra) is $b_{oct.} = 3\sqrt{2}M$–O (e.g. Guggenheim & Eggleton, 1987), and thus (Equation 5):

$$b_{oct.} = 3\sqrt{2}(R + 1.38) \quad (5)$$

The percentage of octahedral enlargement (% O enlargement) corresponding to the difference between the calculated $b_{oct.}$ and observed b is according to Equation 6:

$$\%\,\text{O enlargement} = ((b/b_{oct.}) - 1).100) \quad (6)$$

The % O enlargement reflects variations in O sheet lateral dimensions and is related to octahedral flattening and to O sheet thickness as described for micas by Toraya (1981). An increase in the % O enlargement is related to an increase in octahedral flattening and a decrease in O sheet thickness. The % O enlargement *vs* R plot is another graphic representation of the R *vs* b plot that can be useful to discuss the variations in O sheet dimensions (Guggenheim & Eggleton, 1987) and O sheet thicknesses.

Table 1. Ionic radii (Å) of cations and O2– and their coordination from Shannon (1976).

Ion	Radius
$^{VI}Al^{3+}$	0.535
$^{IV}Al^{3+}$	0.390
$^{IV}Be^{2+}$	0.270
$^{VI}Ca^{2+}$	1.000
$^{VI}Cd^{2+}$	0.950
$^{VI}Co^{2+}$	0.745
$^{VI}Co^{3+}$	0.545
$^{VI}Cr^{3+}$	0.615
$^{VI}Cu^{2+}$	0.730
$^{VI}Fe^{2+}$	0.780
$^{VI}Fe^{3+}$	0.645
$^{IV}Fe^{3+}$	0.490
$^{VI}Ga^{3+}$	0.620
$^{IV}Ga^{3+}$	0.470
$^{IV}Ge^{4+}$	0.390
$^{VI}Li^{+}$	0.760
$^{VI}Mg^{2+}$	0.720
$^{IV}Mn^{2+}$	0.660
$^{VI}Mn^{2+}$	0.830
$^{VI}Mn^{3+}$	0.645
$^{VI}Ni^{2+}$	0.690
$^{II}O^{2-}$	1.350
$^{III}O^{2-}$	1.360
$^{IV}O^{2-}$	1.380
$^{IV}Si^{4+}$	0.260
$^{VI}Ti^{4+}$	0.605
$^{VI}V^{3+}$	0.640
$^{VI}Zn^{2+}$	0.740

Results

Hydroxides, oxyhydroxides and layered double hydroxides

Hydroxides, oxyhydroxides and layered double hydroxides (LDHs; Fig. 2) require cell parameters to be transformed for comparison to phyllosilicates. Thus, to be equivalent to the b

https://doi.org/10.1180/clm.2023.20 Published online by Cambridge University Press

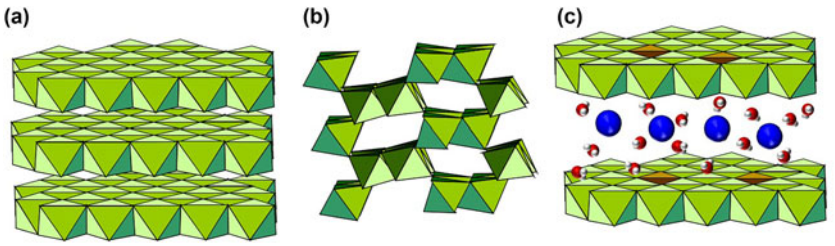

Figure 2. Basic structure of (a) hydroxide (brucite), (b) oxyhydroxide (goethite) and (c) LDH.

parameter of phyllosilicates, the hexagonal a of $M(OH)_2$ hydroxides, the orthorhombic c of diaspore, the orthorhombic b cell parameters of other oxyhydroxides and the a of LDHs were each tripled. Table 2 provides the data used, which are plotted in Fig. 3 as a function of R.

The plots for synthetic $M^{2+}(OH)_2$ brucite-like hydroxide structures (Fig. 2) with M = Mg, Ni, Co, Fe, Mn, Cd and Ca are in excellent agreement with the b *vs* R correlation (Fig. 3a). The relation, $b = 4.4878R + 6.2462$, is consistent with Brindley & Kao (1984). Moreover, the $M^{2+}(OH)_2$ minerals plus gibbsite fall on the same correlation line with a very high R^2 (0.996). In gibbsite, each octahedron is distorted, and the vacant site has the greatest size (Saalfeld & Wedde, 1974). As b conforms to the mean ionic radius of either di- or trivalent actual octahedral cations, the contribution of the vacant site is integrated within R.

For MO(OH) oxyhydroxides (Figs 2 & 3b), a unique regression was derived for the group except for $M = Mn^{3+}$ (see below), yielding the relation $b = 4.6673R + 6.0546$. Diaspore (Al), goethite (Fe^{3+}), synthetic GaO(OH) end members and synthetic goethite substituted by heterovalent (divalent, tetravalent) cations are in good agreement with the regression. Except for Ga^{3+}, cation substitution is very limited in goethite (Table 2). For example, Stiers & Schwertmann (1985) failed to synthesize the complete Fe^{3+}–Mn^{3+} goethite solid solution and achieved ≤15% Mn^{3+} (Table 2). Groutite (α-MnOOH), which is isostructural with goethite, has an orthorhombic b of ~2.87 Å, but this is ~3.02 Å for goethite (Table 2), although $r(Mn^{3+})$ is identical to $r(Fe^{3+})$ (Table 1). Because of Jahn Teller effects (Shannon *et al.*, 1975), octahedra are distorted strongly in groutite, with four short Mn–O distances (two of 1.895 Å and two of 1.965 Å) and two long Mn–O distances (2.174 and 2.338 Å), with a mean Mn–O distance of 2.039 Å (Kohler & Armbruster, 1997). Assuming this mean Mn–O distance and $r(O^{2-}) = 1.36$ Å, the mean $r(Mn^{3+})$ would be 0.679 Å, which cannot account for the large difference in the equivalent b between groutite and goethite. When using the regression obtained for MO(OH) structures (Fig. 3b), the b for groutite corresponds to an 'effective' $r(Mn^{3+}) = 0.548$ Å. Using this 'effective' $r(Mn^{3+})$, the synthetic Mn-goethites (Stiers & Schwertmann, 1985) follow the regression well (Fig. 3b), and the R^2 of the regression was slightly greater when the Mn^{3+} data were included (0.9845 *vs* 0.9818). This suggests that in the groutite structure b is mainly dependent on the shortest Mn–O distances.

The LDH structure is based on brucite $Mg(OH)_2$ with octahedral coordination around the metal ions (Fig. 2). Substitutions of divalent M^{2+} cations by trivalent M^{3+} cations produce many isostructural materials with the general formula $M^{2+}_{1-x}M^{3+}_{x}(OH)_2A^{n-}_{x/n}yH_2O$ (Table 2). These layered materials are readily synthesized (e.g. Forano *et al.*, 2013) and have numerous applications (e.g. Choi *et al.*, 2008; Costantino et *al.*, 2009). Studying natural as well as synthetic hydroxy-carbonates, Brindley & Kikkawa (1979) observed a very good correlation between the a parameter and the extent of Al/M^{2+} substitution, but they considered the Mg–Al and Ni–Al systems separately. Using the mean ionic radius R of octahedral cations, the cell parameters can be compared, regardless of the elemental composition of the LDHs, and this leads to the relation $b = 4.2043R + 6.3758$ (Fig. 3c). The lower value of the regression coefficient for the LDH minerals compared to the other hydroxides may be related to uncertainties in their more complex chemical composition. Indeed, because LDHs are synthesized under pH conditions in which cations can precipitate, bulk chemical analyses would give elemental compositions consistent with the elemental composition of the starting solution. However, the coprecipitation of amorphous or nanocrystalline phases cannot be excluded and may be barely detectable using conventional analytical methods, so that the true elemental composition of LDH phases may be different from the expected composition. Chemical analyses obtained using transmission electron microscopy coupled to an energy-dispersive X-ray detector would thus give more reliable results, as the elemental composition and its dispersion through the sample are good indicators of the purity of the studied samples. As an example, for the shigaite natural sample, which was found relatively far from the range (Fig. 3c), the calculated value for the M^{2+}:M^{3+} ratio using the correlation equation would be 2.57 instead of 2.00 (i.e. 2.16 for the number of Mn^{2+} atoms instead of 2).

The regressions between the O sheet dimensions and R for the three types of hydroxide families have similar slopes (Fig. 3d), despite their different crystallographic structures, implying that the O sheet dimension depends essentially on the shape and size of neighbouring octahedra. The effect of the octahedral composition on the distance between two octahedral cations located in two adjacent octahedra is similar for $M^{n+}(OH)_n$, MO(OH) and LDHs, regardless of the di- or trioctahedral character of the minerals. For the same R, the octahedral dimension of $M^{n+}(OH)_n$ hydroxide minerals is slightly greater (0.08 ± 0.005 Å) than those of the two other structures that are more constrained due to their greater complexity (Fig. 3d). The impact of structure is similar for oxyhydroxides and LDHs in the existing compositional range.

Brindley & Kao (1984) showed that the octahedral sheets in trioctahedral brucite-like structures are all flattened to the same extent with a mean flattening angle τ = O–M–O, with O in the same plane varying slightly from 97.1° to 98.1° (average 97.4°). The unique linear regression observed here between gibbsite and trioctahedral hydroxides suggests that τ is similar for gibbsite and for all $M^{n+}(OH)_n$ hydroxides. Accordingly, from refined structures, the values of the flattening angle τ were found to be 98.5° and 98.3° for gibbsite (Saalfeld & Wedde, 1974) and brucite (Parise *et al.*, 1994), respectively.

The structure of $M^{n+}(OH)_n$ hydroxides approximates a hexagonally close-packed arrangement of anions with M^{n+} ions in

https://doi.org/10.1180/clm.2023.20 Published online by Cambridge University Press

Table 2. Data used for hydroxide, oxy-hydroxide and LDH structures.

SF/composition	Sample[a]	*R*	Parameter	*b*	References	Comments
Hydroxides						
$Al(OH)_3$	Gibbsite	0.535		8.684	Saalfeld & Wedde (1974)	
$M^{2+}(OH)_2$	Synthetic series		*a*	*b* = 3*a*	Brindley & Kao (1984)	For *b* = 3*a*, see text
Ni		0.690	3.117	9.351		
Mg		0.720	3.147	9.441		
Zn		0.740	3.194	9.582		
Co		0.745	3.173	9.519		
Fe		0.780	3.262	9.786		
Mn		0.830	3.316	9.948		
Cd		0.950	3.499	10.497		
Ca		1.000	3.592	10.776		
Oxihydroxide			*c*	*b* = 3*c*		For *b* = 3*c*, see text
αAlO(OH)	Diaspore	0.535	2.844	8.532	Hill (1979)	
FeO(OH)	Goethite	0.645	3.022	9.065	Schulze (1984)	
	Synthetic series					
Al-goethite	Mole% Al				Schulze (1984)	
$Fe^{3+}_{(1-x)}Al^{3+}_xO(OH)$ (*x*)						
0.005	0.5	0.644	3.021	9.063		
0.017	1.7	0.643	3.02	9.060		
0.027	2.7	0.642	3.019	9.057		
0.042	4.2	0.640	3.016	9.048		
0.067	6.7	0.638	3.013	9.039		
0.097	9.7	0.634	3.008	9.024		
0.113	11.3	0.633	3.005	9.015		
0.047	4.7	0.640	3.015	9.045		
0.09	9	0.635	3.009	9.027		
0.124	12.4	0.631	3.004	9.012		
0.157	15.7	0.628	3.000	9.000		
0.016	1.6	0.643	3.021	9.063		
0.026	2.6	0.642	3.020	9.060		
0.035	3.5	0.641	3.018	9.054		
0.314	31.4	0.610	2.964	8.892		
0.249	24.9	0.618	2.978	8.934		
0.186	18.6	0.625	2.991	8.973		
0.203	20.3	0.623	2.998	8.994		
Co-goethite	Mole% Co				Gerth (1990)	
$Fe^{3+}_{(1-x)}Co^{3+}_xO(OH)$ (*x*)						
0.0049	0.49	0.645	3.024	9.071		
0.0249	2.49	0.643	3.021	9.063		
0.451	4.51	0.640	3.018	9.055		
0.0455	4.55	0.640	3.021	9.063		
0.0487	4.87	0.640	3.016	9.048		
0.0825	8.25	0.637	3.013	9.038		
0.0971	9.71	0.635	3.010	9.030		
Ni-goethite	Mole% Ni				Gerth (1990)	
$Fe^{3+}_{(1-x)}Ni^{2+}_xO(OH)$ (*x*)						
0.0051	0.51	0.645	3.025	9.074		
0.0122	1.22	0.646	3.022	9.067		
0.0208	2.08	0.646	3.023	9.069		
0.0253	2.53	0.646	3.024	9.073		
0.0393	3.93	0.647	3.025	9.074		
0.0396	3.96	0.647	3.024	9.073		
0.0542	5.42	0.647	3.026	9.077		
Cu-goethite	Mole% Cu				Gerth (1990)	
$Fe^{3+}_{(1-x)}Cu^{2+}_xO(OH)$ (*x*)						
0.0051	0.51	0.645	3.024	9.071		
0.0287	2.87	0.647	3.024	9.072		
0.0464	4.64	0.649	3.026	9.079		
0.0482	4.82	0.649	3.026	9.077		
0.0488	4.88	0.649	3.025	9.075		
Zn-goethite	Mole% Zn				Gerth (1990)	
$Fe^{3+}_{(1-x)}Zn^{2+}_xO(OH)$ (*x*)						
0.0056	0.56	0.646	3.024	9.071		
0.0282	2.82	0.648	3.026	9.077		
0.0436	4.36	0.650	3.028	9.084		
0.0458	4.58	0.650	3.028	9.083		
0.0477	4.77	0.650	3.029	9.086		
0.0573	5.73	0.651	3.032	9.097		
0.0686	6.86	0.652	3.033	9.099		
	Mole% Cd				Gerth (1990)	

(*Continued*)

https://doi.org/10.1180/clm.2023.20 Published online by Cambridge University Press

Table 2. (*Continued.*)

SF/composition	Sample[a]	*R*	Parameter	*b*	References	Comments
Cd-goethite						
$Fe^{3+}_{(1-x)}Cd^{2+}_{x}O(OH)$ (*x*)						
0.0048	0.48	0.646	3.025	9.075		
0.0066	0.66	0.647	3.025	9.074		
0.0221	2.21	0.652	3.030	9.089		
0.0256	2.56	0.653	3.032	9.097		
0.0274	2.74	0.653	3.033	9.100		
0.0379	3.79	0.657	3.036	9.107		
0.0401	4.01	0.657	3.037	9.112		
0.0409	4.09	0.657	3.038	9.114		
0.0414	4.14	0.658	3.040	9.119		
0.044	4.4	0.658	3.040	9.120		
0.0442	4.42	0.658	3.039	9.117		
0.0454	4.54	0.659	3.040	9.120		
0.0506	5.06	0.660	3.042	9.125		
0.0743	7.43	0.668	3.050	9.149		
Pb-goethite	Mole% Pb					
$Fe^{3+}_{(1-x)}Pb^{4+}_{x}O(OH)$ (*x*)						
0.0039	0.38	0.645	3.023	9.070		
0.008	0.8	0.646	3.022	9.066		
0.0154	1.54	0.647	3.021	9.064		
0.0163	1.63	0.647	3.024	9.071		
0.017	1.7	0.647	3.023	9.068		
0.0216	2.16	0.648	3.022	9.066		
0.0229	2.29	0.648	3.021	9.064		
Ga-goethite	Ga/Ga + Fe (%)				Martin *et al.* (1997)	
$Fe^{3+}_{(1-x)}Ga^{3+}_{x}O(OH)$ (*x*)						
0	0	0.645	3.022	9.065		
0.1	10	0.643	3.021	9.063		
0.25	25	0.639	3.015	9.045		
0.4	40	0.635	3.008	9.024		
1	100	0.620	2.973	8.920		
Cr-goethite	Cr/Cr + Fe (%)				Schwertmann *et al.* (1989)	
$Fe^{3+}_{(1-x)}Cr^{3+}_{x}O(OH)$ (*x*)						
0	0	0.645	3.025	9.074		
0.02	2	0.644	3.023	9.070		
0.05	5	0.643	3.022	9.066		
0.1	10	0.642	3.019	9.058		
Mn^{3+}-goethite	Mn/Mn + Fe (%)				Stiers & Schwertmann (1985)	
$Fe^{3+}_{(1-x)}Mn^{3+}_{x}O(OH)$ (*x*)						
0	0	0.645	3.024	9.073		
0.05	5	0.640	3.022[b]	9.065		
0.1	10	0.635	3.016[b]	9.047		
0.15	15	0.630	3.008[b]	9.023		
1	groutite	0.548	2.870	8.613		Natural sample
LDHs			*a*	$b = 3a$		For $b = 3a$, see text
$M^{2+}_{a}M^{3+}_{b}(OH)_{2(a+b)}[Z^{c-}]_{b/c}$						
	Natural samples					
$Mg_6Al_2(OH)_{16}[CO_3]4H_2O$	Hydrotalcite	0.670	3.066[c]	9.199	Brindley & Kikawa (1979)	
$Ni_6Al_2(OH)_{16}[CO_3]4H_2O$	Takovite	0.646	3.025[c]	9.075		
$Mg_6Cr_2(OH)_{16}[CO_3]4H_2O$	Stichite	0.695	3.096	9.287[d]	Mills *et al.* (2011)	
$Mg_3Fe^{3+}(OH)_8[Cl]$	Iowaite	0.701	3.118	9.355[d]	Braithwaite *et al.* (1994)	
$Mg_3Fe^{3+}(OH)_8[CO_3]$	Pyroaurite	0.701	3.109	9.328[d]	Allman (1968)	
$Mn_2Al(OH)_6[SO_4]$	Shigaite	0.733		9.512[d]	Cooper & Hawthorne (1996)	
$Fe^{2+}_2Al(OH)_6[SO_4]$	Nikisherite	0.700		9.347[d]	Huminicki & Hawthorne (2003)	
$Zn_2Al\ (OH)_6[CO_3]$	Zaccagnaite	0.672	3.073	9.218[d]	Merlino & Orlandi (2001)	
$Mg_5Fe^{3+}(OH)_{12}[CO_3]$	Coalingite	0.708	3.120	9.360[d]	Pastor-Rodriguez & Taylor (1971)	
$Mg_7Al_{1.14}Fe^{3+}_{0.86}(OH)_{18}[SO_4]$	Wermlandite	0.690		9.303[d]	Rius & Allmann (1984)	
	Synthetic series					
$Mg_{1-x}Al_x[CO_3]$ (*x*)	Mg^{2+}/Al^{3+}					
0.167	5	0.689	3.081	9.242	Bellotto *et al.* (1996)	
0.33	2	0.659	3.046	9.138		
0.20	4	0.683	3.068	9.204	Grégoire *et al.* (2012)	
0.25	3	0.674	3.057	9.171		
0.33	2	0.658	3.042	9.126		
0.33	2	0.659	3.045	9.136	Costantino *et al.* (1998)	
0.33	2	0.658	3.042	9.127	Radha *et al.* (2007)	
$Ni_{1-x}Al_x[CO_3]$ (*x*)					Brindley & Kikawa (1979)	
0.35	S1	0.655	3.045[c]	9.136		
0.30	S2	0.664	3.050[c]	9.150		

(*Continued*)

https://doi.org/10.1180/clm.2023.20 Published online by Cambridge University Press

Table 2. (*Continued.*)

SF/composition	Sample[a]	*R*	Parameter	*b*	References	Comments
0.27	S3	0.670	3.063[c]	9.189		
0.23	S4	0.677	3.074[c]	9.223		
0.35	Gast1	0.655	3.040[c]	9.121		
0.20	Gast2	0.683	3.079[c]	9.237		
$Ni_{1-x}Al_x[CO_3]$ (x)	Sample name				Brindley & Kikawa (1979)	
0.28	S11	0.646	3.023[c]	9.069		
0.27	S12	0.648	3.027[c]	9.081		
0.22	S13	0.657	3.044[c]	9.133		
0.19	S14	0.660	3.051[c]	9.153		
0.17	S15	0.663	3.052[c]	9.157		
	Ni^{2+}/Al^{3+}					
0.09	10	0.676	3.074	9.222	Grégoire *et al.* (2012)	
0.14	6	0.668	3.063	9.189		
0.20	4	0.659	3.052	9.156		
0.25	3	0.651	3.043	9.129		
0.33	2	0.638	3.026	9.078		
0.33	2	0.639	3.027	9.081	d'Espinose de la Caillerie (1995)	
0.28	2.5	0.647	3.035	9.105		
0.25	3	0.651	3.041	9.123		
0.25	3	0.651	3.034	9.101	Radha *et al.* (2007)	
$Ni_{1-x}Fe^{3+}{}_x[CO_3]$ (x)	Ni^{2+}/Fe^{3+}				Grégoire *et al.* (2012)	
0.09	10	0.686	3.09	9.27		
0.14	6	0.684	3.09	9.27		
0.2	4	0.681	3.087	9.261		
0.25	3	0.679	3.086	9.258		
0.333	2	0.675	3.084	9.252		
$Mg_{1-x}Fe^{3+}{}_x[CO_3]$ (x)	Mg^{2+}/Fe^{3+}				Grégoire *et al.* (2012)	
0.20	4	0.705	3.113	9.339		
0.25	3	0.701	3.109	9.327		
0.33	2	0.695	3.107	9.321		
0.22	3.5	0.703	3.108	9.323	Manohara *et al.* (2011)	
0.29	2.4	0.698	3.100	9.300		
0.31	2.2	0.697	3.100	9.300		
$Co^{2+}_{1-x}Al_x[CO_3]$ (x)	Co^{2+}/Al^{3+}					
0.25	3	0.693	3.08	9.24	Grégoire *et al.* (2012)	
0.33	2	0.675	3.07	9.21		
0.33	2	0.675	3.07	9.20	Radha *et al.* (2007)	
$Co^{2+}_{1-x}Fe^{3+}{}_x[CO_3]$ (x)	Co^{2+}/Fe^{3+}					
0.25	3	0.720	3.13	9.39	Grégoire *et al.* (2012)	
0.33	2	0.712	3.13	9.39		
$M^{2+}_{1-x}Ga^{3+}{}_x[CO_3]$ (M, x)	M^{2+}/Ga^{3+}					
Ni, 0.33	2	0.667	3.071	9.214	Manohara & Vishnu Kamath (2010)	
Co, 0.33	2	0.704	3.110	9.331		
Mg, 0.25	3	0.695	3.087	9.260		
Mg, 0.167	5	0.703	3.106	9.318	Bellotto *et al.* (1996)	
Mg, 0.33	2	0.687	3.087	9.261		
$Zn^{2+}_{1-x}Al^{3+}{}_x[Z]$ (x, Z)	Zn^{2+}/Al^{3+}					
0.35, CO_3^{2-}	1.86	0.668	3.076	9.227	Lombardo *et al.* (2005)	
0.35, Cl^-	1.86	0.668	3.075	9.225		
0.33, Cl^-	2	0.672	3.091	9.273	Ennadi *et al.* (2000)	
0.32, SO_3^{2-}	2.1	0.674	3.080	9.240	Radha *et al.* (2011)	
0.34, IO_3^-	1.92	0.670	3.072	9.216		
$M^{2+}_{1-x}Cr^{3+}{}_x[Cl]$ (M, x)	M^{2+}/Cr^{3+}					
0.34, Zn	1.97	0.698	3.106	9.317	Roussel *et al.* (2000)	
0.31, Cu	2.25	0.695	3.111	9.333		
$Co^{2+}{}_xCu^{2+}{}_yAl^{3+}{}_z[CO_3]$ (x, y, z)	M^{2+}/M^{3+}					
0.66, 0.09, 0.25	2.91	0.691	3.076	9.228	Sankaranarayanan *et al.* (2015)	
0.50, 0.25, 0.25	3.01	0.689	3.076	9.228		
0.34, 0.42, 0.24	3.21	0.688	3.080	9.240		
0.23, 0.53, 0.24	3.14	0.687	3.082	9.246		
0.07, 0.70, 0.23	3.39	0.686	3.082	9.246		
0.77, 0, 0.23	3.45	0.697	3.085	9.255		
$Mg^{2+}{}_wCo^{2+}{}_xAl^{3+}{}_yFe^{3+}{}_z[CO_3]$ (w, x, y, z)					Nestroinaya *et al.* (2017)	
0.59, 0.1, 10.26, 0.04	2.36	0.672	3.06	9.18		
0.50, 0.23, 0.21, 0.07	2.60	0.682	3.07	9.21		

a, *b* and *c* are crystallographic parameters (Å).
R = mean ionic radius of octahedral cations (Å; see text for details).
[a]Sample reference in the paper.
[b]Using $r(Mn^{3+}) = 0.548$ Å (see text).
[c]Extracted from Fig. 5.
[d]Single-crystal XRD measurement.

https://doi.org/10.1180/clm.2023.20 Published online by Cambridge University Press

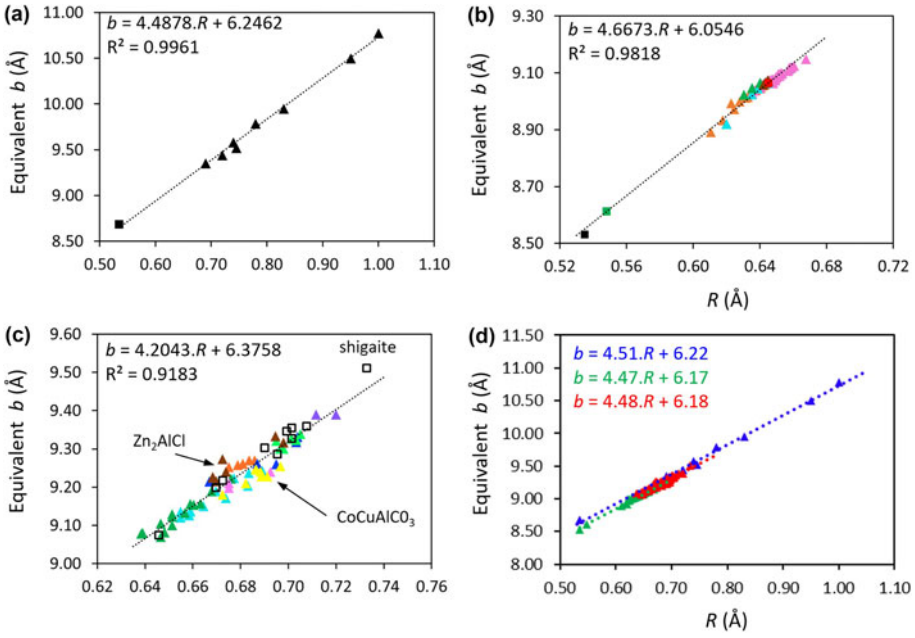

Figure 3. Evolution of the equivalent *b* parameter (in Å) with the mean ionic radius of octahedral cations *R* (in Å) for hydroxide families (Table 2). (a) $M^{n+}(OH)_n$ hydroxides: square = natural gibbsite; triangles = M^{2+}-hydroxide synthetic series. (b) *M*O(OH) oxyhydroxides, with squares and triangles corresponding to natural and synthetic samples, respectively: black = diaspore; red = goethite; green = groutite; dark blue = GaO(OH); light blue = Ga-goethite series; orange = Co^{3+}-, Ni^{2+}-, Cu^{2+}-, Zn^{2+}-, Cd^{2+}- and Pb^{4+}-goethite series; pink = Al-goethite series; green = Mn^{3+}-goethite series; brown = Cr^{3+}-goethite series. (c) LDHs, with squares and triangles corresponding to natural and synthetic samples, respectively: light blue = $MgAlCO_3$; green = $NiAlCO_3$; light green = $MgFeCO_3$; orange = $NiFeCO_3$; pink = $CoAlCO_3$; violet = $CoFeCO_3$; dark blue = $GaM^{2+}CO_3$; yellow = $CoCuAlCO_3$; brown = others. (d) Comparative regressions calculated from the model between the octahedral sheet dimension and *R* (see text for details): blue dotted line = $M^{n+}(OH)_n$; green dotted line = *M*O(OH); red dotted line = LDHs.

octahedrally coordinated positions between alternating pairs of anion planes. The *b* used here is given by $b = 6(M\text{–O})\sin(\tau/2)$, with the (*M*–O) distance being the sum of the effective ionic radii for cations (*M*) in six-fold coordination and oxygen ions (O) in four-fold coordination ($r(^{IV}O^{2-}) = 1.38$ Å; Table 1; Brindley & Kao, 1984). Using the mean ionic radius of octahedral cations *R*, this relation can be easily rewritten as $b = 6(R + 1.38)\sin(\tau/2)$.

Following a structurally based interpretation, a relation $b = AR + C$ can be obtained for each family of hydroxides studied here using a simple model with $A = 6\sin(\tau/2)$ and $C = A1.38$ (in Å). The *A* (and thus τ and *C*) were determined by fitting with the experimental regressions (Fig. 3d).

For $M^{n+}(OH)_n$ hydroxides, *A* and *C* are 4.51 and 6.22, respectively (Fig. 3d), close to the experimental values derived from the correlation line shown in Fig. 3a (4.49 and 6.25, respectively). The corresponding $\tau = 97.3°$ agrees well with the literature (see above). The corresponding % O enlargement (or octahedral flattening) is ~6.3%.

The proposed model for $M^{n+}(OH)_n$ hydroxides is also suitable for *M*O(OH) and LDHs, as seen in Fig. 3d, where the *A* values are very close for *M*O(OH) and LDHs, at 4.47 and 4.48, respectively. The octahedra are slightly less flattened in *M*O(OH) and LDHs compared to $M^{n+}(OH)_n$ hydroxides, with $\tau = 96.3°$ (~5.4% octahedral enlargement) for *M*O(OH) and $\tau = 96.6°$ (5.6% octahedral enlargement) for LDHs.

The structurally based model of the hexagonally close-packed arrangement of anions with M^{n+} ions in octahedrally coordinated positions shows very good efficiency in reconciling structural and chemical data for all families of studied hydroxides as well as for both di- and trioctahedral minerals (Fig. 3d), and the relation between the equivalent *b* and the mean ionic radius of octahedral cations *R* for each mineral allows us to measure the flattening of octahedra, which is similar for all of the families and does not vary significantly within each family.

TO phyllosilicates

TO phyllosilicates are composed of the superimposition of a T sheet of a pseudo-hexagonal ring of $(SiO_4)^{4-}$ units on an O sheet of edge-sharing octahedra leading to an electrostatically neutral layer (Fig. 1a). The general SF is $(Si_aR^{3+}{}_b)_2(R^{3+}{}_cR^{2+}{}_d\square_e)_3O_5(OH)_4$, with R^{3+} being mainly Al and Fe^{3+}, R^{2+} being mainly Mg (but this could other divalent cations, such as Ni and Fe^{2+}) and □ being a vacant site. Anions other than OH^-, such as F^- or Cl^-, are rarely reported as occurring and will not be discussed here. Kaolins and serpentines constitute the dioctahedral and trioctahedral families, respectively. Kaolin group minerals include kaolinite, dickite, nacrite and halloysite and have a general composition of $Al_2Si_2O_5(OH)_4$ (+ nH_2O for halloysite), with similar *b* values (Giese, 1991) and very few substitutions. Consequently, only kaolinite was considered in the following as a representative of the whole kaolin group.

Contrary to kaolins representing Al end members with no tetrahedral substitutions and a very simple chemical composition, serpentines display a wide range of chemical compositions, leading to many end members depending on the extent of the tetrahedral substitutions and the nature of the dominant octahedral cations. For instance, lizardite (Mg) and nepouite (Ni; $a \approx 2$ and $d \approx 3$), berthierine ($b \approx 0.5$, $c \approx 0.5$ and $d \approx 2.5$), brindleyite ($b \approx 0.5$, $c \approx 1$, $d \approx 1.75$ and $e \approx 0.25$) and amesite (Al–Mg) and cronstedtite (Fe^{3+}, Fe^{2+}; $b \approx 1$, $c \approx 1$ and $d \approx 2$) represent different minerals of these serpentine families (Wiewiora, 1990). Three structural groups of serpentines based on particle shape are also distinguished: flat layers as for lizardite (Fig. 4a), cylindrical layers as for chrysotile (Fig. 4b) and corrugated layers as for antigorite (Fig. 4c; e.g. Wicks & Whittaker, 1975), and many morphologies have been reported (e.g. Andreani *et al.*, 2008).

Kaolinite and lizardite

Kaolinite and lizardite are the Al-dioctahedral and Mg-trioctahedral end members, respectively, for TO phyllosilicates having the general SF of $Si_2(R^{3+}{}_cR^{2+}{}_d)O_5(OH)_4$. For the kaolinite dioctahedral end member, *c* and *d* are 2 and 0, respectively, and R^{3+} is Al, while for the lizardite trioctahedral end member, *c* and *d* are 0 and 3, respectively, and R^{2+} is Mg. No or limited octahedral substitutions (mainly Fe^{3+} for Al^{3+}) occur in natural kaolinite. Using the synthesis method, the Fe^{3+} substitution

https://doi.org/10.1180/clm.2023.20 Published online by Cambridge University Press

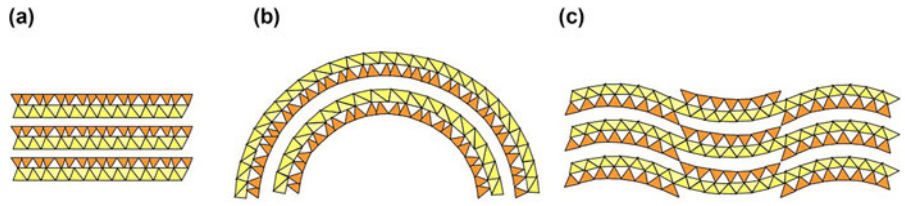

Figure 4. Schematic representation of various structures of TO serpentines based on crystal morphology: (a) flat morphology, (b) curved morphology and (c) wavy corrugated morphology.

amount can be increased slightly and other octahedral cations can be introduced into the structure (Table 3). Among the large set of published data available for pure natural Al end member kaolinite, the Keokuk kaolinite studied using Rietveld refinement (Bish &Von Dreele, 1989) was selected as representative for this study. According to the general SF above, lizardite *sensu stricto* does not have tetrahedral substitutions. Consequently, in this study, lizardite with >0.1 ^{IV}Al was considered in the Al-serpentine series rather than in the lizardite series.

As shown in Fig. 5a, the *b vs R* plots for all TO samples display a relatively scattered pattern. Two different regressions (i.e. the kaolinite–lizardite (*K–L*) and greenalite–caryopilite (*G–C*) lines) can be distinguished, however, with a wide cloud of dots at their intersection (Fig. 5a).

Natural kaolinite, the synthetic Al–Fe^{3+} kaolinite series and the synthetic Ni–Mg lizardite series appear quasi-aligned ((*K–L*) line in Fig. 5a,b). The (*K–L*) line was first calculated with the synthetic series of Fe^{3+}-kaolinites (Petit *et al.*, 1990; Iriarte *et al.*, 2005) and Ni–Mg lizardites (Baron *et al.*, 2016b; Fig. 5a,b). Including natural kaolinite in these two synthetic series increases the correlation coefficient slightly (0.9987 instead of 0.9985) without modifying the regression significantly ($b = 1.5092R + 8.1371$ instead of $b = 1.5097R + 8.1368$). The *K–L* regression including the natural kaolinite was kept in the following analyses. Because aluminium is the octahedral cation with the smallest ionic radius (0.535 Å; Table 1), the *b* of the pure Al end member exhibits the smallest value observed for TO phyllosilicates when forming a TO clay structure. Accordingly, the natural Keokuk pure kaolinite is located at the origin of the regression line with an *R* value of 0.535 Å and a *b* value of 8.945 Å according to Bish & Von Dreele (1989). Few *b* values for synthetic Fe^{3+}- and Ga^{3+}-substituted kaolinites of Bentabol *et al.* (2009) are lower than 8.945 Å (Fig. 5b & Table 3), suggesting an underestimation of these *b* values. The data for the kaolinite synthesized with the greatest Cr^{3+} content also deviate slightly from the correlation lines (Fig. 5b). Except for the samples described in Bentabol *et al.* (2009), the dataset for other synthetic diversely substituted kaolinites is located on or close to the regression line (Fig. 5b).

Up to ~0.1 octahedral Fe^{3+} per formula unit (pfu) is observed in natural kaolinites, whereas up to 0.6 substituted Fe^{3+} pfu can be measured in synthetic kaolinites (Table 3). For the theoretical Fe^{3+}-kaolinite end member ($Si_2Fe^{3+}_2O_5(OH)_4$), *b* extrapolated using the experimental data from Iriarte *et al.* (2005) is located close to the *K–L* regression line, supporting the suitability of the dataset for a wide range of compositions (Fig. 5b). Moreover, as concluded previously by some authors (Petit *et al.*, 1988; Petit & Decarreau, 1990; Iriarte *et al.*, 2005), the Al–Fe^{3+} kaolinite synthetic series behaves like a solid solution within the compositional range explored, and no evidence exists to date to suggest that the maximum value obtained experimentally (0.6 pfu) corresponds to a steric limit of Fe^{3+} substitution in kaolinite.

In contrast to kaolinite, various end members of lizardite are encountered, and Mg cations are commonly replaced at least partially by other divalent cations (Table 3). As shown in Fig. 5b, the synthetic Mg–Ni lizardites are well aligned on the (*K–L*) line, The Co-lizardite does not fit the regression well. The two different *b* values were measured in the same sample, as Bayliss (1981) calculated a significantly greater *b* than that measured by Dalmon & Martin (1968; Fig. 5b). The deviation from the (*K–L*) regression line and the *b* fluctuations probably suggest there being a problem with these data. In a review of serpentine group minerals, Bayliss *et al.* (1980) observed some significant fluctuations in reported *b* values with apparently the same chemistry, suggesting different methods had been employed to measure this parameter or inaccuracies had occurred during these measurements. Fluctuations are noticed for synthetic Mg end members, with *b* ranging from 9.204 to 9.241 Å (Table 3). Fluctuations are also observed for natural lizardites whose single-crystal XRD refinement of two different crystals from a same sample with an assumed homogeneous chemical composition resulted in two different *b* values, as illustrated by the Gew-graze lizardite-1*T* (Mellini *et al.*, 2010) and the Monte Fico lizardite-1*T* (Mellini & Viti, 1994; Table 3). More consistent with the results observed here, Mellini & Zanazzi (1987) measured a slight variation in *b* coupled with a slight variation in the chemical composition between two polytypes of the Coli lizardite sampled within the same vein (Table 3). These examples illustrate how the established correlation lines can help us to identify whether deviation originated from structural features or difficulties in accurately measuring *b*.

Lizardite, chrysotile and antigorite are three polymorphs with flat, curved and corrugated wavy layer structures, respectively. Antigorite corresponds to a polysomatic series, with regularly inversed T sheets in polysomes (Fig. 4). A more correct general formula for antigorite would then be $(Mg)_{3m-3}Si_{2m}O_{5m}(OH)_{4m-6}$, where *m* represents the number of tetrahedra within a full wavelength, and $m = 17$ has been proposed as the most common value (Capitani & Mellini, 2004). The dataset does not allow for the identification of possible differences between the polymorphs. As far as synthetic Mg- and Ni-lizardites (Baron *et al.*, 2016b) and chrysotiles (Jasmund *et al.*, 1976) are concerned, *b* values measured for chrysotiles appear slightly lower than those measured for lizardites (Table 3). Because the two sets of samples were measured using various techniques, we cannot conclude with certainty that *b* values for chrysotiles are lower than for lizardites.

Al- and Fe^{3+}-serpentines

Al- and Fe^{3+}-serpentines whose general SFs are $(Si_{2-x}Al_x)(Mg_{3-x}Al_x)O_5(OH)_4$ and $(Si_{2-x}Fe^{3+}{}_x)(Fe^{3+}{}_xFe^{2+}_{3-x})O_5(OH)_4$, respectively, most often exhibit great tetrahedral substitution contents (up to 1 Al or Fe^{3+} per $O_5(OH)_4$) to neutralize the positive octahedral layer charge generated by the heterovalent octahedral substitutions of divalent cations (mainly Mg and Fe^{2+}) by trivalent cations (mainly Fe^{3+} and Al). The dataset for Al- and Fe^{3+}-serpentines are scattered significantly (Fig. 5a), and this scattering is more pronounced for natural samples than for

https://doi.org/10.1180/clm.2023.20 Published online by Cambridge University Press

Table 3. Data used for TO phyllosilicates.

TO structure	Sample[a]	*R*	*b*	References	Comments
Natural kaolinite					
$Si_2Al_2O_5(OH)_4$	Keokuk (IA, USA)	0.535	8.945	Bish & Von Dreele (1989)	
Synthetic kaolinites					
Fe^{3+}-kaolinite series $Si_2(Al_{2-x}Fe^{3+}{}_x)O_5(OH)_4$ (octahedral composition)				Petit (1990)	
$Al_{1.93}Fe^{3+}_{0.07}$	$a = 0.1$	0.539	8.952		
$Al_{1.88}Fe^{3+}_{0.12}$	$a = 0.2$	0.542	8.959		
$Al_{1.85}Fe^{3+}_{0.15}$	$a = 0.3$	0.543	8.966		
$Al_{1.68}Fe^{3+}_{0.32}$	KAF28	0.553	8.960	Iriarte *et al.* (2005)	
$Al_{1.59}Fe^{3+}_{0.41}$	KAF42	0.558	8.976		
$Al_{1.49}Fe^{3+}_{0.51}$	KAF54	0.563	8.984		
Fe^{3+}_2	Theoretical end member	0.645	9.094		
R^{3+}-kaolinite series $Si_2(Al_{2-x}R^{3+}{}_x)O_5(OH)_4$ (octahedral composition)				Bentabol *et al.* (2009)	
$Al_{1.96}Fe_{0.04}$	Fe K100	0.537	8.928		
$Al_{1.95}Ga_{0.05}$	Ga K100	0.537	8.934		
$Al_{1.89}Fe_{0.01}Cr_{0.11}$	Cr K100 (1)	0.539	8.946		
$Al_{1.47}Fe_{0.01}Cr_{0.52}$	Cr K100 (2)	0.556	9.030		
Ga^{3+}-kaolinite					
$Si_2(Al_{1.76}Ga^{3+}_{0.24})O_5(OH)_4$		0.545	8.97	Martin *et al.* (1998)	
Lizardite (anhydrous composition)					
$(Si_{1.94}Al_{0.06})(Mg_{2.83}Fe^{2+}_{0.07}Al_{0.09})$	Coli *1T*	0.716	9.223	Mellini & Zanazzi (1987)	
$(Si_{1.93}Al_{0.07})(Mg_{2.83}Fe^{2+}_{0.05}Al_{0.1})$	Coli *2H1*	0.715	9.211		
$(Si_{1.93}Al_{0.07})(Mg_{2.74}Fe^{2+}_{0.16}Al_{0.09})$	Monte Fico *1T*			Mellini & Viti (1994)	
	MFN3-1	0.718	9.232		
	MFN3-6		9.246		
$(Si_{1.996}Al_{0.004})(Mg_{2.987}Fe^{2+}_{0.004}Mn_{0.005}Al_{0.004})$	Gew-graze *1T*			Mellini *et al.* (2010)	
	KG-2	0.720	9.163		
	KG-3		9.199		
$Si_2(Mg_{2.87}Ni_{0.05}Fe^{3+}_{0.03}Al_{0.02})$	Valojoro, Madagascar	0.717	9.180	Brindley & Wan (1975)	
Synthetic lizardite series $Si_2(Mg_{3-x}\ Ni_x)O_5(OH)_4$ (octahedral composition)				Baron *et al.* (2016a)	
Mg_3	$x = 0$	0.720	9.226		
$Mg_{2.5}Ni_{0.5}$	$x = 0.5$	0.715	9.218		
Mg_2Ni_1	$x = 1$	0.710	9.209		
$Mg_{1.5}Ni_{1.5}$	$x = 1.5$	0.705	9.199		
Mg_1Ni_2	$x = 2$	0.700	9.191		
$Mg_{0.5}Ni_{2.5}$	$x = 2.5$	0.695	9.185		
Ni_3	$x = 3$	0.690	9.181		
Synthetic co-lizardite					
$Si_2Co_3O_5(OH)_4$	Co-antigorite	0.745	9.220	Dalmon & Martin (1968)	Same sample
	$Co_3Si_2O_5(OH)_4$		9.350	Bayliss (1981)	*b* recalculated from the same XRD pattern
Synthetic chrysotile series $Si_2(R^{2+})_3O_5(OH)_4$ (octahedral composition)				Jasmund *et al.* (1976)	
Mg_3	Mg-chrysotile	0.720	9.216		
Ni_3	Ni-chrysotile	0.690	9.162		
Co_3	Co-chrysotile	0.745	9.240		
Mg_3	Mg-chrysotile	0.720	9.241	Falini *et al.* (2004)	
Antigorite (anhydrous composition)					
$(Si_{1.99}Al_{0.01})(Mg_{2.67}Fe^{2+}_{0.1}Al_{0.04})$	Val Malenco, Italy	0.719	9.251	Capitani & Mellini (2004)	
$(Si_{1.87}Al_{0.13})(Mg_{2.57}Fe^{2+}_{0.195}\ Fe^{3+}_{0.156}Al_{0.01})$	Natural n°9	0.719	9.350	Tomisaka & Kato (1963)	
$Si_{2.008}(Mg_{2.58}Fe^{2+}_{0.208}\ Fe^{3+}_{0.06}Al_{0.138})$	Natural n°14	0.714	9.350		
$(Si_{1.99}Al_{0.01})(Mg_{2.57}Fe^{2+}_{0.24}\ Fe^{3+}_{0.11}Al_{0.09})$	Natural n°17	0.717	9.350		
$Si_{2.00}(Mg_{2.55}Fe^{2+}_{0.25}\ Fe^{3+}_{0.12}Al_{0.03})$	Natural n°18	0.720	9.350		
$(Si_{1.94}Al_{0.06})(Mg_{2.58}Fe^{2+}_{0.07}\ Fe^{3+}_{0.35}Al_{0.01})$	Natural n°7	0.712	9.220		
$(Si_{1.95}Al_{0.01}Fe^{3+}_{0.04})(Mg_{2.87}Fe^{2+}_{0.01}Fe^{3+}_{0.06})$	Antigorite n°1	0.719	9.219	Brindley & Von Knorring (1953)	
$Si_2(Mg_{2.72}Al_{0.01}Fe^{3+}_{0.13})$	Antigorite n°2	0.716	9.219		
Al-serpentine (anhydrous composition)					
Berthierine					
$(Si_{1.32}Al_{0.68})(Mg_{0.23}Fe^{2+}_{1.82}Fe^{3+}_{0.01}Al_{0.83})$	Chamosite	0.705	9.360	Brindley & Youell (1953)	Named chamosite at this time
$(Si_{1.29}Al_{0.71})(Mg_{0.17}Fe^{2+}_{1.81}Fe^{3+}_{0.02}Al_{0.90})$[b]	N°874	0.700	9.312[c]		
$(Si_{1.22}Al_{0.78})(Mg_{0.17}Fe^{2+}_{1.79}Fe^{3+}_{0.01}Al_{0.93})$[b]	Wabana	0.697	9.348[c]		
$(Si_{1.46}Al_{0.54})(Mg_{0.4}Fe^{2+}_{1.72}Fe^{3+}_{0.32}Al_{0.45})$[d]	Frodingham	0.720	9.342[c]		
$(Si_{1.53}Al_{0.47})(Mg_{0.38}Fe^{2+}_{1.64}Fe^{3+}_{0.29}Al_{0.52})$[d]	Schmiedefeld	0.714	9.336[c]		
$(Si_{1.29}Al_{0.71})(Mg_{0.46}Fe^{2+}_{1.13}Ti_{0.77}Al_{0.12})$	Ti-berthierine	0.703	9.252	Arima *et al.* (1985)	

(*Continued*)

https://doi.org/10.1180/clm.2023.20 Published online by Cambridge University Press

Table 3. (*Continued.*)

TO structure	Sample[a]	*R*	*b*	References	Comments
Amesite					
$(Si_{1.052}Al_{0.948})(Mg_{1.15}Fe^{2+}_{0.96}Al_{0.99}Mn_{0.02})$	Amesite Lake Asbestos	0.679	9.294	Taner & Laurent (1984)	
$(Si_{1.01}Al_{0.99})(Mg_{1.63}Fe^{2+}_{0.33}Al_{0.999})$	Amesite Chester	0.664	9.186		
$(Si_{1.027}Al_{0.973})(Mg_{1.94}Fe^{2+}_{0.03}Cr_{0.07}Al_{0.94})$	Amesite	0.660	9.195	Anderson & Bailey (1981)	
$(Si_{1.075}Al_{0.925})(Mg_{1.9}Fe^{2+}_{0.025}Ni_{0.01}Al_{0.875}Cr_{0.145})$	Amesite	0.660	9.212[e]	Wiewiora *et al.* (1991)	
Others					
$(Si_{1.83}Al_{0.17})(Mg_{2.79}Fe^{2+}_{0.04}Fe^{3+}_{0.1}Al_{0.07})$	Lizardite Val Sissone	0.714	9.235[e]	Mellini (1982)	
$(Si_{1.81}Al_{0.19})(Mg_{2.64}Fe^{2+}_{0.05}Fe^{3+}_{0.13}Al_{0.03})$	Thompson Lake	0.719	9.239	Olsen (1961)	
$(Si_{1.48}Al_{0.52})(Mg_{2.07}Fe^{2+}_{0.07}Al_{0.72})$	Al-serpentine	0.675	9.171	Jahanbagloo & Zoltai (1968)	
$(Si_{1.67}Al_{0.33})(Mg_{0.27}Fe^{2+}_{0.16}Ni_{1.36}Al_{0.92})$	Brindleyite	0.623	9.133	Maksimovic & Bish (1978)	
$(Si_{179}Al_{0.21})(Mg_{0.77}Fe^{2+}_{0.28}Fe^{3+}_{0.78}Al_{0.56}\ Mn_{0.15})$	Odinite	0.660	9.334 9.326	Bailey (1988)	Purest sample – mixture of 1*T* and 1*M* polytypes
$(Si_{0.98}Al_{1.02})(Mg_{0.245}Mn_{1.825}Fe^{3+}_{0.09}Al_{0.84})$	Kellyite	0.733	9.420	Peacor *et al.* (1974)	
Fe^{3+}-serpentine (anhydrous composition)					
Pecoraite					
$(Si_{1.88}Fe^{3+}_{0.15})(Mg_{0.08}Ni_{2.93})$	Sterling Mine, USA	0.691	9.180	Robinson & Chamberlain (1984)	
Cronstedtite					
$(Si_{1.51}Fe^{3+}_{0.49})(Fe^{2+}_{1.64}Fe^{3+}_{0.49}Mg_{0.71}Mn_{0.16})$	Pribram, Czech Republic	0.747	9.467[e]	Geiger *et al.* (1983)	
$(Si_{1.22}Fe^{3+}_{0.78})(Fe^{2+}_{2.2}Fe^{3+}_{0.8}Al_{0.02})$	Herja, Romania	0.743	9.547[e]	Hybler *et al.* (2000)	Triangular tabular crystal
$(Si_{1.34}Fe^{3+}_{0.66})(Fe^{2+}_{2.32}Fe^{3+}_{0.68}Al_{0.02})$	Lostwithiel, UK	0.749	9.532[e]		Conical crystal
	Pohled, Czech Republic			Hybiler *et al.* (2016)	
$(Si_{1.249}Fe^{3+}_{0.751})(Fe^{2+}_{2.245}Fe^{3+}_{0.755})$	$2H_1$ (+$2H_2$)	0.746[f]	9.516[e,f]		
$(Si_{1.271}Fe^{3+}_{0.729})(Fe^{2+}_{2.271}Fe^{3+}_{0.729})$	$6T_2$	0.747[f]	9.516[e,f]		
$(Si_{1.228}Fe^{3+}_{0.772})(Fe^{2+}_{2.228}Fe^{3+}_{0.772})$	$3T + 1M$	0.745	9.514[e]		
	Pohled, Czech Republic			Hybler (2016)	
$(Si_{1.575}Fe^{3+}_{0.485})(Fe^{2+}_{2.515}Fe^{3+}_{0.485})$	$6T_2$	0.758	9.522[e]		
	Nižná Slaná, Slovakia			Hybler *et al.* (2017)	
$(Si_{1.182}Fe^{3+}_{0.818})(Fe^{2+}_{2.182}Fe^{3+}_{0.818})$	$3T$	0.743[f]	9.521[e,f]		
$(Si_{1.197}Fe^{3+}_{0.803})(Fe^{2+}_{2.197}Fe^{3+}_{0.803})$	$3T + 1M$	0.744[f]	9.527[e,f]		
$(Si_{1.206}Fe^{3+}_{0.794})(Fe^{2+}_{2.206}Fe^{3+}_{0.794})$	$2H_1$	0.744[f]	9.532[e,f]		
	Chyňava, Czech Republic			Hybler & Sejkora (2017)	
$(Si_{1.206}Fe^{3+}_{0.794})(Fe^{2+}_{2.047}Fe^{3+}_{0.794}Mg_{0.159})$	$2H_1$	0.741[f]	9.527[e,f]		
$(Si_{1.185}Fe^{3+}_{0.815})(Fe^{2+}_{2.030}Fe^{3+}_{0.815}Mg_{0.155})$	$2H_1$ (+$2H_2$)	0.740[f]	9.522[e,f]		
$(Si_{1.236}Fe^{3+}_{0.764})(Fe^{2+}_{2.034}Fe^{3+}_{0.764}Mg_{0.202})$	$3T$	0.742[f]	9.518[e,f]		
$(Si_{1.371}Fe^{3+}_{0.629})(Fe^{2+}_{2.148}Fe^{3+}_{0.629}Mg_{0.223})$	$1T + 3T$	0.747[f]	9.513[e,f]		
$(Si_{1.387}Fe^{3+}_{0.613})(Fe^{2+}_{2.151}Fe^{3+}_{0.613}Mg_{0.236})$	$1T$	0.748[f]	9.521[e,f]		
	Nagybörzsöny, Hungary			Hybler *et al.* (2020)	
$(Si_{1.19}Fe^{3+}_{0.81})(Fe^{2+}_{2.19}Fe^{3+}_{0.80}Mg_{0.002})$		0.746[f]	9.547[e,f]		
	Litošice, Czech Republic			Hybler *et al.* (2021)	
$(Si_{1.22}Fe^{3+}_{0.78})(Fe^{2+}_{1.80}Fe^{3+}_{0.78}Mg_{0.02}Mn_{0.41})$	$1T$	0.751[f]	9.572[e,f]		
$(Si_{1.24}Fe^{3+}_{0.76})(Fe^{2+}_{1.86}Fe^{3+}_{0.76}Mg_{0.31}Mn_{0.066})$	$2H_1 + 2H_2$	0.741	9.540[e]		
Guidottite	Republic of South Africa			Wahle *et al.* (2010)	
$(Mn_{1.86}Fe^{3+}{}_{0.61}Mg_{0.54})(Si_{1.36}Fe^{3+}_{0.64})$		0.773	9.608		
$(Mn_{1.70}Fe^{3+}{}_{0.96}Mg_{0.24})(Si_{1.26}Fe^{3+}_{0.74})$		0.760	9.608		
Synthetic serpentine series $(Si_{2-x}\ Al_x)(Mg_{3-x}Al_x)O_5(OH)_4$					
$(Si_2)(Mg_3)$	241M	0.720	9.204	Chernosky (1975)	
$(Si_{1.95}Al_{0.05})(Mg_{2.95}Al_{0.05})$	75G	0.717	9.222		
$(Si_{1.925}Al_{0.075})(Mg_{2.925}Al_{0.075})$	73G	0.715	9.204		
$(Si_{1.9}Al_{0.1})(Mg_{2.9}Al_{0.1})$	72G 87G	0.714	9.219		
$(Si_{1.875}Al_{0.125})(Mg_{2.875}Al_{0.125})$	70G	0.712	9.207		
$(Si_{1.625}Al_{0.375})(Mg_{2.625}Al_{0.375})$	349M	0.697	9.210		
$(Si_{1.625}Al_{0.375})(Mg_{2.625}Al_{0.375})$	368M	0.697	9.204		
$(Si_{1.5}Al_{0.5})(Mg_{2.5}Al_{0.5})$	366M	0.689	9.210		
$(Si_{1.5}Al_{0.5})(Mg_{2.5}Al_{0.5})$	391M	0.689	9.200		
$(Si_{1.25}Al_{0.75})(Mg_{2.25}Al_{0.75})$	390M	0.674	9.175		
$(Si_1Al_1)(Mg_2Al_1)$	367M	0.658	9.148		
$(Si_{1.625}Al\ _{0.375})(Mg_{2.625}Al_{0.375})$	One-layer ortho-serpentine	0.697	9.245	Gillery (1959)	
$(Si_{1.25}Al_{0.75})(Mg_{2.25}Al_{0.75})$	Six-layer ortho-serpentine	0.674	9.193		
$(Si_{1.75}Al_{0.25})(Mg_{2.75}Al_{0.25})$	Lizardite	0.705	9.229	Caruso & Chernosky (1979)	
$(Si_{2-x}Al_x)(R^{2+}{}_yAl_z)O_5(OH)_4$					
$(Si_{1.78}Al\ _{0.22})(Ni_{1.62}Fe^{3+}_{0.05}Al_{0.96})$	Al–Ni lizardite	0.633	9.162	Bentabol & Ruiz Cruz (2013)	
$(Si_{1.81}Al\ _{0.19})(Co_{1.73}Fe^{3+}_{0.05}Al_{0.88})$	Al–Co lizardite	0.673	9.234		
$Si_{2.02}(Co_{1.58}Fe^{3+}_{0.04}\ Al_{0.89})$	Al–Co lizardite	0.669	9.155		
Synthetic serpentine (anhydrous composition)					

(*Continued*)

https://doi.org/10.1180/clm.2023.20 Published online by Cambridge University Press

Table 3. (*Continued.*)

TO structure	Sample[a]	*R*	*b*	References	Comments
$(Si_{1.74}Al_{0.26})(Mg_{2.00}\ Fe^{3+}_{0.02}Al_{0.73})$	Al–Mg lizardite	0.670	9.203	Bentabol *et al.* (2010)	
Fe–Mn serpentines (anhydrous composition)					Corrugated structures
$Si_2(Fe^{2+})_3$	Synthetic greenalite	0.780	9.624	Jasmund *et al.* (1976)	
$Si_2(Fe^{2+}_{2.25}Fe^{3+}_{0.5})$	Greenalite	0.755	9.612	Steadman & Youell (1958)	
$(Si_{1.51}Fe^{3+}_{0.49})(Fe^{2+}_{1.64}Fe^{3+}_{0.49}Mg_{0.71}Mn_{0.16})$	Greenalite	0.747	9.467	Geiger *et al.* (1983)	
$(Si_{1.95}Al_{0.05})(Mg_{0.18}Fe^{2+}_{1.71}Mn_{0.49}Al_{0.27}Fe^{3+}_{0.18})$	Greenalite	0.753	9.63	Bayliss (1981)	
$(Si_{1.77}Al_{0.23})(Mg_{1.47}Fe^{2+}_{0.44}Mn_{0.6}Al_{0.2}Fe^{3+}_{0.03}Zn_{0.27})$	Baumite	0.739	9.6	SF from Frondel & Ito (1975), *b* from Guggenheim & Bailey (1989)	
$Si_2(Mg_{0.35}Fe^{2+}_{0.05}Mn_{2.47}Al_{0.13})$	Mn-serpentine[g]	0.804	9.804	Yoshimura *et al.* (1963)	
$Si_2(Mg_{0.29}Fe^{2+}_{0.16}Mn_{1.83}Zn_{0.11})$	Mn-serpentine[g]	0.809	9.834	Kato (1963)	
$Si_2(Mg_{0.4}Fe^{3+}_{0.06}Mn_{2.17})$	Mn-serpentine[g]	0.797	9.804	Kato (1963)	
$Si_2(Mg_{0.6}Fe^{2+}_{0.27}Mn_{1.76})$	Mn-serpentine[g]	0.800	9.708	Kato (1963)	
$Si_2(Mg_{0.34}Fe^{2+}_{0.18}Mn_{1.76}Al_{0.07})$	Mn-serpentine[g]	0.802	9.852	Kato (1963)	

b is a crystallographic parameter (Å).
R = mean ionic radius of octahedral cations (Å; see text for details).
[a]Sample reference in the paper.
[b]Brindley (1982).
[c]Brindley *et al.* (1951).
[d]Calculated from chemical analyses in Brindley *et al.* (1951).
[e]Crystal structure refinement.
[f]Average value.
[g]Caryopilite.

synthetic Al-serpentines, which lie close to the (*K*–*L*) regression line (Fig. 5b). The natural Al- and Fe^{3+}-serpentines exhibit a wide range of tetrahedral substitutions and several polytypes, but no specific trend can be observed between these two characteristics and *b* (Fig. 5c).

Greenalite and caryopilite

Greenalite and caryopilite are, respectively, Fe^{2+}- and Mn-rich TO phyllosilicates with corrugated structures and with the following general SF: $Si_2(M)_{(2.5-3)}O_5(OH)_4$, with *M* = Fe, Mn, Mg and Al as the main octahedral cations. Partial oxidation of octahedral Fe and Mn often occurs, and some octahedral sites may be vacant. The regression parameters for the (*G*–*C*) line (Fig. 5a) and the structural interpretation are discussed in detail below. The slope of the (*G*–*C*) regression line is ~4.5 times greater than that of the (*K*–*L*) line. Jasmund *et al.* (1976) reported that the greenalite synthesized with the Fe^{2+} end member was structurally non-equivalent to the Ni-, Mg- and Co-lizardites. The observed scattering of samples around the (*G*–*C*) line (Fig. 5a) can be tentatively assigned to uncertainties in the data and/or to the various modulated local substructures. Greenalite and caryopilite exhibit domed island-like structures due to tilting of the tetrahedra with periodic inversions of three- and four-fold rings (Guggenheim & Eggleton, 1998). This structural adjustment is a way to enlarge the T sheet dimensions to allow congruence with the large O sheet dimensions due to the occurrence of significant amounts of octahedral cations with large ionic radii, such as Mn^{2+} and Fe^{2+} (Table 1).

Influence of tetrahedral composition

Whereas no relation can be observed between tetrahedral content and *b* as shown above (Fig. 5c), it is clear, however, from a simple comparison between, for example, Mn-rich serpentines (i.e. kellyite; ^{IV}Al-serpentine, guidottite ($^{IV}Fe^{3+}$-serpentine) and caryopilite (negligible tetrahedral substitution and corrugated structure), that the tetrahedral composition plays a role in the

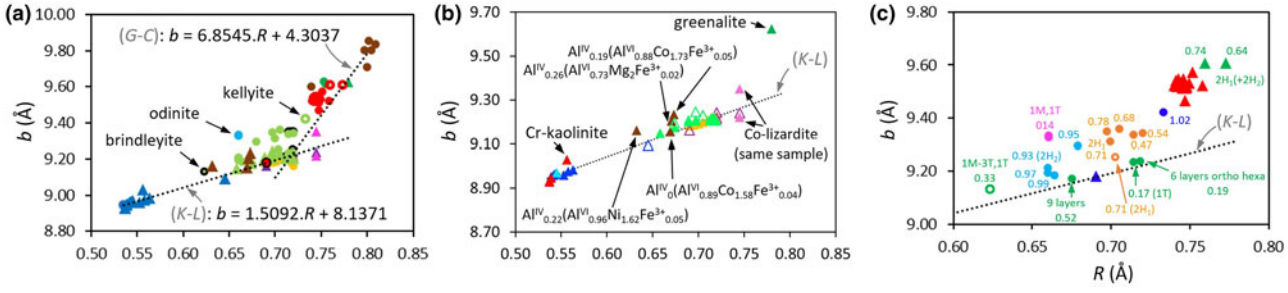

Figure 5. *b vs* mean ionic radius of octahedral cations *R* for TO phyllosilicates (Table 3). (a) Circles represent natural samples and triangles represent synthetic samples: dark blue = kaolinite; yellow = lizardite; black = antigorite; light green = Al-serpentine, with black border = brindleyite, open circle = kellyite; red = Fe^{3+}-serpentine, full circles = cronstedtite, with black border = pecoraite, open circles = guidottite; dark green = greenalite; brown = caryopilite; violet = R^{2+}-chrysotile series; pink = Co-lizardite. (*K*–*L*) and (*G*–*C*) correspond to kaolinite–lizardite and greenalite–caryopilite regression lines, respectively. (b) Focus on the synthetic kaolinite–lizardite series: dark blue triangles = Fe^{3+}-kaolinite series, open triangle = theoretical end member; light blue triangle = Ga^{3+}-substituted kaolinite; red triangles = R^{3+}-kaolinite series; yellow triangles = Ni–Mg lizardite series; pink triangles = Co-lizardite; open violet triangles = R^{2+}-chrysotile; light green triangles = Mg–Al serpentine series (Chernosky, 1975), open light green triangles = other Mg–Al serpentines; brown triangles = R^{2+}–Al serpentine series; green triangle = greenalite. (c) Focus on natural Al-serpentines (circles) and Fe^{3+}-serpentines (triangles). Polytype (partly) and tetrahedral Al or Fe^{3+} pfu are indicated: light blue circles = amesite; orange circles = berthierine, orange open circle = Ti-berthierine; green open circle = brindleyite; pink circles = odinite; dark blue circle = kellyite; green circles = other; red triangles = cronstedtite ($2H_1$, $2H_2$, 3*T*, 1*T*, $6T_2$ and 3*T* + 1*M* polytypes); blue triangle = pecoraite; green triangles = guidottite.

https://doi.org/10.1180/clm.2023.20 Published online by Cambridge University Press

dimensional misfit between T and O sheets. All of these Mn-rich serpentines have great R (from ~0.73 to ~0.80 Å) and b values (from ~9.4 to ~9.8 Å) due to their great Mn content. The tetrahedral substitutions in kellyite and guidottite allow the lateral dimension of the T sheet to increase, making the fit between T and O sheets possible without corrugation of the layer.

The $b/b_{tet.}$ values were calculated for all TO phyllosilicates and plotted as a function of R (Fig. 6a). Three general trends are observed. The (*K–L*)' correlation line (Fig. 6a) corresponds to the (*K–L*) line (Fig. 5a), and the regression was calculated using the same data. These samples have no tetrahedral substitutions and thus the correction with the $b_{tet.}$ value does not influence the data alignment (Fig. 6a). Note that the synthetic R^{2+}–Al serpentine samples (Bentabol & Ruiz Cruz, 2013) that were above the (*K–L*) line (Fig. 5a,b) are now closer to the (*K–L*)' line (Fig. 6a). The odinite data deviate systematically from the trend (Figs 5a & 6a), and possible impurities and redox variation make their SF unsure. Compared to the b *vs* R plot (Fig. 5a), the cloud of dots associated with the Al-serpentine disappeared in Fig. 6a. Less predictable is that the corrugated Fe^{2+}–Mn serpentines approximately follow the same high-slope (*G–C*)' line as most of the Al-serpentines (Fig. 6a). For this (*G–C*)' line, the regression was calculated using antigorites, greenalites, caryopilites and Al-serpentines that are on (or close to) the (*G–C*)' line. Furthermore, the Fe^{3+}-serpentines, except the pecoraite sample, which lies on the (*G–C*)' line, follow fairly well the different linear trend of (*Fe^{3+}–Serp*)' with the same slope as the (*G–C*)' line (Fig. 6a).

For Al- and Fe^{3+}-serpentines, a general relationship of b *vs* R, introducing the tetrahedral composition, can be formulated from each (*K–L*)', (*G–C*)' and (*Fe^{3+}–Serp*)' regression line (Fig. 6a) according to Equation 7:

$$b = R(aT + c) + dT + e \quad (7)$$

with T being the number of ^{IV}Al or $^{IV}Fe^{3+}$ pfu.

For Al-serpentines following the (*K–L*)' line (Fig. 6a):

$$b = R(0.061T + 1.509) + 0.327T + 8.137$$

For Al-serpentines (and Fe^{3+}-serpentine; i.e. pecoraite) following the (*G–C*)' line (Fig. 6a):

$$b = R(0.275T + 6.854) + 0.173T + 4.302$$

For Fe^{3+}-serpentines following the (*Fe^{3+}–Serp*)' line (Fig. 6a):

$$b = R(0.470T + 6.854) + 0.27T + 3.932$$

The intersect coordinates for the two (*K–L*)' and (*G–C*)' lines are $R = 0.717$ and $b = 9.220$ Å, approximately corresponding to the Mg-lizardite end member. The corresponding $b/b_{tet.}$ value is 1.007, thus indicating a tetrahedral rotation angle α close to 0°. Accordingly, theoretical modelling using the distance least-squares method indicates that the O and T sheets fit together without any major distortions in the Mg-lizardite structure

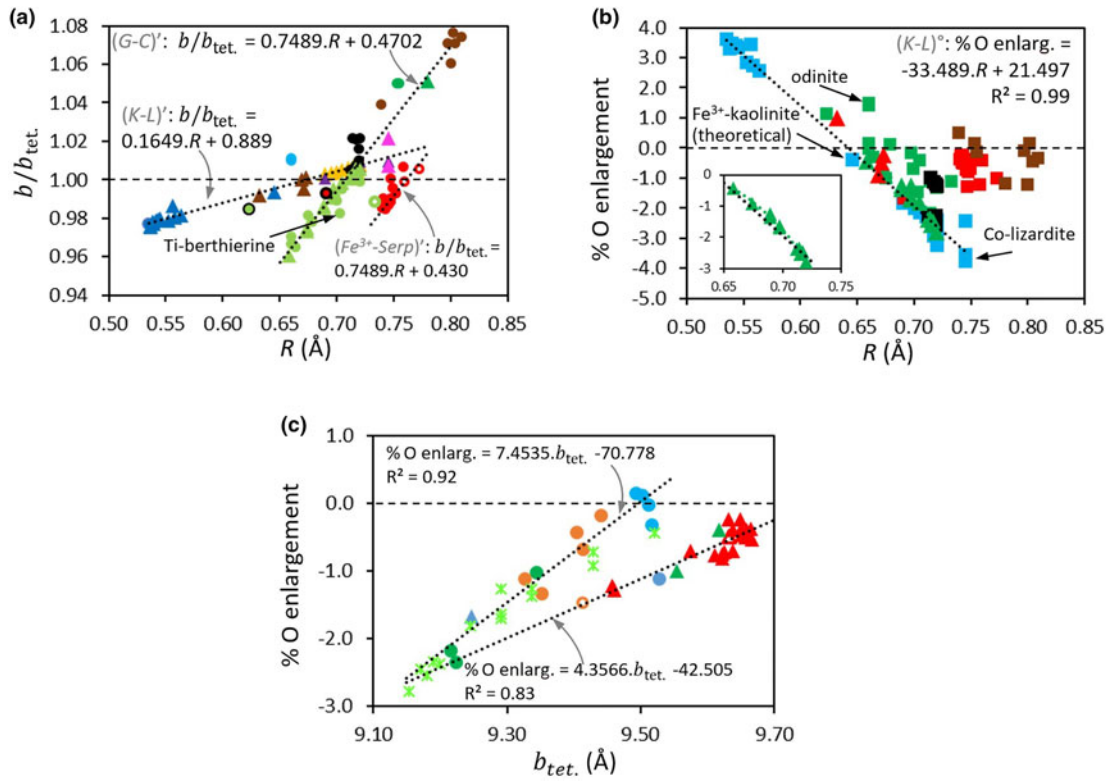

Figure 6. (a) $b/b_{tet.}$ ratio *vs* mean ionic radius of octahedral cations R for TO phyllosilicates (Table 3), with the same symbols and colours as in Fig. 5a. (*K–L*)' and (*G–C*)' correspond to kaolinite–lizardite and greenalite– caryopilite regression lines, respectively. (b) Evolution of the percentage of octahedral enlargement compared to hydroxides (Equation 6; see text for details) *vs* R: blue squares = kaolinites and lizardites; green squares = natural Al-serpentines; green triangles = synthetic Al-serpentines (focus on the Chernosky's (1975) series); red squares = Fe^{3+}-serpentines; black squares = antigorite; brown squares = caryopilites and greenalites; blue dotted line = regression for the kaolinite–lizardite series. (c) Evolution of the percentage of octahedral enlargement *vs* $b_{tet.}$ for Al- and Fe^{3+}-serpentines, with the same symbols and colours as in Fig. 5c for natural samples, except light green crosses = synthetic Al-serpentines.

https://doi.org/10.1180/clm.2023.20 Published online by Cambridge University Press

(Bish, 1981; Wicks & Hawthorne, 1986; Wicks & O'Hanley, 1991), and α measured using structure refinement is close to 0° (approximately –1.5(1)°) for the natural Mg end member lizardite (Guggenheim & Zhan, 1998; Mellini *et al.*, 2010).

Based on all of the results above, three main distinct mechanisms of adjustment between O and T sheet lateral dimensions to compensate for the misfit of kaolinite–lizardite, Al- and Fe^{3+}-serpentines and phyllosilicates with corrugated structure are proposed in the following subsections.

Focus on the structural adjustment mechanism for the kaolinite–lizardite family

Samples on the (*K*–*L*)' line (Fig. 6a) are those for which *b* is driven by *R* according to the good regression observed for the (*K*–*L*) line (Fig. 5a). For pure kaolinite (Al end member that exhibits the lowest *R*), T sheets are relatively large compared to O sheets and have to reduce their lateral dimensions to adjust to the O sheets. Moving to lizardite, and thus increasing *R*, makes the dimensional misfit decrease. The (*K*–*L*)' trend (Fig. 6a) gives evidence of a progressive decrease of the angle of tetrahedral rotation α with increasing *R*. Accordingly, the rotation of tetrahedra to ditrigonal symmetry (Fig. 1d) is the principal process for overcoming the misfit when $b_{oct.} < b_{tet.}$ in TO phyllosilicates by reducing the lateral dimension of the T sheet (e.g. Radoslovich, 1963; Bailey, 1966; Wicks & Whittaker, 1975; Guggenheim & Eggleton, 1987). However, this process is not the only one to achieve congruency between the T and O sheet dimensions. Indeed, the O sheet enlargement (Equation 6) increases progressively with a decrease of *R* (Fig. 6b). The O sheet enlargement corresponds to a lateral expansion of the sheet by thinning (Bailey, 1984b). The $b_{oct.}$ value corresponding to an unconstrained O sheet was taken for hydroxides as determined above ($b_{oct.} = 4.51R + 6.22$; Fig. 3d). Consequently, positive % O enlargement corresponds to an O sheet flattening (or thinning) compared to hydroxides, whereas negative % O enlargement corresponds to a thickening of the O sheet compared to hydroxides, with a null value being obtained for $R = 0.642$. With the ionic radius of Fe^{3+} being 0.645 Å (Table 1), the theoretical Fe^{3+}-kaolinite end member would have similar dimension to the corresponding hydroxide. The $Fe(OH)_3$ mineral bernalite exists but it has a pseudo-cubic structure of perovskite type (Birch *et al.*, 1993) that cannot be compared. Kaolinite exhibits the greatest enlargement: 3.6% as compared to hydroxides (10.1% as compared to undistorted O sheets), which agrees well with the value measured using structure refinement (10.1%; Bish & Von Dreele, 1989). Co-lizardite with the lowest octahedral enlargement (–3.7% and 2.3% compared to hydroxides and undistorted O sheets, respectively) and has the thickest O sheet of the family. The linear regression observed between kaolinite and lizardite (Fig. 6b & (*K*–*L*) line Fig. 5a) suggests an increase of the size of the vacant site with an increase of *R* for dioctahedral samples.

The few Al- and Fe^{3+}-serpentines with a rather low rate of tetrahedral substitution that lie on (or close to) the (*K*–*L*)' line (i.e. brindleyite, pecoraite and synthetic R^{2+}–Al serpentines; Fig. 6a) behave similarly to the kaolinite and lizardite family. These Al-serpentines exhibit a great number of octahedral vacant sites, possibly increasing the plasticity of the octahedral sheet compared to the other serpentines.

Focus on the Al- and Fe^{3+}-serpentines family

The samples that are scattered between the (*K*–*L*) and (*G*–*C*) lines exhibit a high degree of misfit due to their relatively small O sheet lateral dimensions (small *R*) compared to their large T sheet lateral dimensions due to tetrahedral substitutions. The T sheet dimensions have to decrease significantly to adjust to the O sheet. As for kaolinite and lizardite, this reduction of T sheet dimensions with decreasing *R* is due to a progressive increase in the tetrahedral rotation angle α, as evidenced by the (*G*–*C*)' and (*Fe^{3+}*–*Serp*)' regressions (Fig. 6a). However, contrary to the kaolinite–lizardite series, the O sheet enlargement does not vary linearly with *R* and is relatively more pronounced than for kaolinite–lizardite (Fig. 6b). This explains the greater *b* relative to *R* observed for Al- and Fe^{3+}-serpentines compared to the kaolinite–lizardite series (Fig. 5a). In Al- and Fe^{3+}-serpentines, the O sheet enlargement is linked directly to the tetrahedral substitutions, as shown by the plot of the O sheet enlargement *vs* $b_{tet.}$ (Fig. 6c). Each of the two observed regressions (calculated using natural samples only) concerns mainly Al-serpentines or Fe^{3+}- serpentines and corresponds to the (*G*–*C*)' or (*Fe^{3+}*–*serp*)' lines, respectively (Fig. 6a). The two regressions intersect for $b_{tet.} \approx 9.13$ Å and % O enlargement ≈ –2.7 (~3.4% compared to a free O sheet). This $b_{tet.}$ value is close to the theoretical 9.15 Å value calculated for a free T sheet (e.g. Equation 3; Bailey, 1981). The % O enlargement is negative or close to 0 for amesite, meaning that O sheets are always thicker/never thinner in Al- and Fe^{3+}-serpentines than in their corresponding hydroxides (i.e. hydroxide with the same *R*). For amesite, the ~0% O enlargement compared to hydroxides means than the flattening of the O sheet is the same as for hydroxides: ~6.3% compared to the free O sheet, agreeing well with the structural refinement of amesite (Wiewiora et *al.*, 1991; Zheng & Bailey, 1997a).

In serpentine, when Tschermak substitutions (coupled tetrahedral R^{3+}/Si^{4+} to octahedral R^{3+}/R^{2+} substitutions) occur, there is a cumulative antagonistic effect of R^{3+}. Note, however, that in the case where Tschermak substitutions occur with coupled tetrahedral Al^{3+}/Si^{4+} to $^{VI}M^{3+}/Mg^{2+}$ substitutions, with $r(^{VI}M^{3+}) > r(^{VI}Al^{3+})$ such as for $^{VI}M^{3+} = {}^{VI}Fe^{3+}$, the antagonistic effect can be neutralized. The antagonistic effect of Al is well illustrated with the synthetic series $((Si_{2-x}Al_x)(Mg_{3-x}Al_x)O_5(OH)_4$, with $0 \leq x \leq 1$) of Chernosky (1975; Table 3). For this series, $b_{tet.}$ and $b_{oct.}$ are anticorrelated, making the misfit increase dramatically when *R* decreases (Fig. 6a). The lateral dimensions of the O and T sheets are identical for $b_{tet.} = b_{oct.} = 9.33$ Å, corresponding to $R = 0.690$, $x = 0.49$ and $b \approx 9.2$ Å. This *x* value has been discussed widely in the past, and an Al content corresponding to $x \approx 0.3$ (corresponding to $R \approx 0.702$) has been proposed (Bates, 1959; Radoslovich, 1963; Chernosky, 1975; Caruso & Chernosky, 1979). The difference between these two *x* values comes mainly from the values taken for *M*–O bond length calculations of $b_{tet.}$ and $b_{oct.}$.

Due to the antagonistic effect of Al, tetrahedral substitutions are not expected to release the misfit between T and O sheets in aluminous serpentines but to promote it further. Consequently, strong constraints are expected to occur for the Al-richest samples as a result of T and O sheet lateral dimension accommodation. Furthermore, for the Al-richest serpentine with an end member amesite-like composition, T sheets contract significantly ($b/b_{tet.} = 0.961$; Fig. 6a), all the more so as O sheet enlargement is relatively limited (Fig. 6b). This contraction corresponds to an angle of tetrahedral rotation $\alpha \approx 16°$, a value that agrees well with $\alpha \approx 14$–$15°$ measured using structure refinement of natural amesite (Bailey, 1991c; Wiewiora *et al.*, 1991; Zheng & Bailey, 1997a). With increasing heterovalent substitutions, an increasing linkage by H bonding from layer to layer occurs, and

https://doi.org/10.1180/clm.2023.20 Published online by Cambridge University Press

the interlayer thickness decreases when the ditrigonalization of the T sheet increases (Mellini & Viti, 1994). Structural refinement of natural amesites also indicates various cation ordering patterns. This cation ordering and the electrostatic attraction between layers due to substantial tetrahedral substitutions are believed to have positive effects on the regularity of the stacking of layers in amesite (Bailey, 1991c). This may explain its platy morphology even though a curled morphology might be expected due to misfit constraints. This may also explain the existence of multilayer polytypes in serpentine with significant amounts of trivalent cations. Accordingly, Chernosky (1975) observed a one-layer ortho-cell structure for $0.05 \leq x \leq 0.375$ and a six-1ayer ortho-cell structure for $x > 0.375$.

Focus on the phyllosilicates with corrugated structure

These samples follow the (*G*–*C*) and (*G*–*C*)' lines (Figs 5a & 6a), and the high degree of misfit is due to O sheet lateral dimensions being greater than T sheet lateral dimensions. In greenalite and caryopilite, high $b_{oct.}$ values are due to large octahedral cations such as Fe^{2+} and Mn^{2+}, whereas $b_{tet.}$ values are relatively low compared to Al- and Fe^{3+}-serpentines due to negligible tetrahedral substitutions. The stretching of the T sheet attains its limits, constraining the O sheet to curl and the T sheet to be discontinuous, forming modulated layers. It is worth noting that for these TO phyllosilicates the % O enlargement is similar to those of equivalent hydroxides (Fig. 6b). Detailed descriptions of the various *n*-ring arrangements to accommodate misfit in modulated 1:1 layer silicates can be found in the literature (Guggenheim & Eggleton, 1987, 1988, 1998) and will not be discussed here.

Impact of misfit on layer curling and morphology

Layer curling arises because of the complex interplay between chemical compositions and the structural adjustments required to achieve articulation between the O and T sheets. From the above results, it is hypothesized that samples close to the $b/b_{tet.} = 1$ line correspond mostly to samples with a flat morphology. The misfit between the O and T sheets dimensions is accommodated mainly by tetrahedra rotation to reduce T sheet dimensions. The existence of vacant sites also probably increases the plasticity of O sheets, facilitating their lateral dimension increase. Exceptions must be made for chrysotiles (Fig. 6a), which exhibit a non-flat morphology (cylindrical morphology; Fig. 4b). Only three data points were available, and these samples are synthetic and may not be representative. However, the curling observed in chrysotile is not due to misfit between T and O sheet dimensions, but rather to reaction kinetics, with chrysotile occurring as a metastable form of a serpentine (Evans, 1976, 2004; Andréani *et al.*, 2008). Accordingly, Jasmund & Sylla (1971) observed that tubes of synthetic Mg- and Ni-chrysotiles transformed into platy Mg- and Ni-antigorites with increasing reaction time. An analogy, previously highlighted by Bates (1959), can be made with halloysite (which is not represented in this study, its *b* and *R* values being similar to those of kaolinite). Halloysite probably curls for the same reason as chrysotile. The morphology of halloysite, which can be tubular, spheroidal, onion-like, crumpled lamellar and so on, but also platy, is related to crystallization conditions and geological occurrences (Joussein *et al.*, 2005). Notably, synthetic kaolinites can also exhibit spherical metastable particles precipitating from solution with a high degree of supersaturation (e.g. Fiore *et al.*, 1995).

For samples with $b/b_{tet.} < 1$ (Fig. 6a), the T sheet is compressed, constraining the O sheet to increase its lateral dimensions by flattening the octahedra, as described above. If layers curl, the O sheets are always on the convex side of the layer. However, in Al- and Fe^{3+}-serpentines, increasing heterovalent substitutions induce increased electrostatic attraction between layers and an ordering of cation distributions favouring a flat morphology.

It is tempting to further discuss the morphology of serpentines as a function of misfit, as has been examined previously by many authors (e.g. Pauling, 1930; Bates, 1959; Radoslovich, 1963; Bailey, 1966). However, the simple approach developed here cannot replace detailed structural studies for determining the actual structure and morphology of TO layer silicates. For example, some serpentines, such as polygonal serpentines, may appear as fibres, but are composed of 1:1 flat layers (Baronnet *et al.*, 1994; Mellini, 2013), and conversely, structural modulation can account for apparently plate-like particles (Guggenheim & Eggleton, 1987). Moreover, mixtures of several morphologies are often reported in synthetic series (Chernosky, 1975; Bentabol & Ruiz Cruz, 2013) as well as in natural samples (Capitani *et al.*, 2021).

TOT phyllosilicates

Pyrophyllite–talc

Pyrophyllite and talc are TOT layer silicates composed of electroneutral stacked 2:1 layers formed by two T sheets sandwiching one O sheet (Fig. 7a). These two minerals correspond to the Al-dioctahedral and Mg-trioctahedral end members, respectively, having the general SF of $Si_4(R^{3+}, R^{2+}, \square)_3O_{10}(OH,F)_2$, with R^{3+} being mainly Al, R^{2+} being mainly Mg but also potentially being very different and $\square$ being a vacant site. In the present study, kerolites were also included in this group because these clay minerals are considered hydrated (but disordered) talc-like minerals (Brindley *et al.*, 1977). The available data found in the literature for this group of minerals cover only a small range of chemical variability (Table 4). For dioctahedral minerals, only pyrophyllite, with limited Fe^{3+} substitutions, and ferripyrophyllite are reported to occur, with ferripyrophyllite exhibiting the highest *R* and *b* values. For trioctahedral phyllosilicates, Ni-talc exhibits the lowest *R* and *b* values. Natural talcs with significant amounts

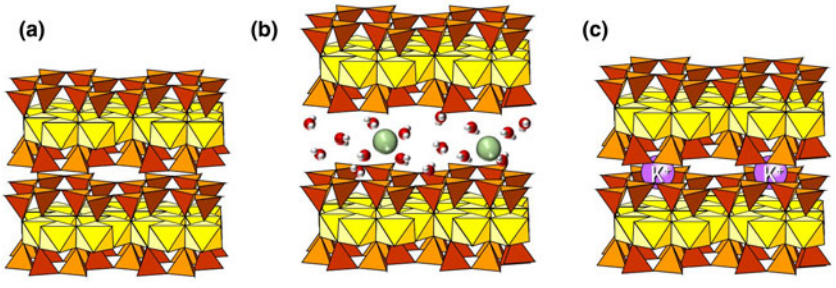

Figure 7. Schematic representation of the structures of various TOT phyllosilicates: (a) neutral TOT (e.g. pyrophyllite and talc), (b) low-charge hydrated TOT (e.g. smectite) and (c) high-charge TOT (e.g. mica).

https://doi.org/10.1180/clm.2023.20 Published online by Cambridge University Press

Table 4. Data used for TOT phyllosilicates with a neutral structure.

TOT neutral structure (anhydrous composition)	Sample[a]	*R*	*b*	References	Comments
Pyrophyllite					
Si_4Al_2	Pyrophyllite	0.535	8.966[b]	Drits *et al.* (2012)	
$(Si_{3.94}Fe^{3+}_{0.06})(Mg_{0.1}Fe^{3+}_{1.9})$	Ferripyrophyllite	0.649	9.080	Badaut *et al.* (1992)	
$(Si_{3.80}Al_{0.13}Fe^{3+}_{0.07})(Fe^{3+}_{1.96}Mg_{0.11})Ca_{0.05}$	Ferripyrophyllite	0.649	9.100	Chukhrov *et al.* (1979a)	
$(Si_{3.80}Al_{0.04}Fe^{3+}_{0.16})(Al_{0.09}Fe^{3+}_{1.96}Mg_{0.11})Ca_{0.05}$	Same sample	0.644		Coey *et al.* (1984)	
Talc					
Si_4Mg_3	Talc	0.720	9.173[b]	Drits *et al.* (2012)	
$Si_4(Al_{0.02}Fe^{3+}_{0.26}Fe^{2+}_{0,78}Mg_{1.90})$	Antwerp	0.728	9.180	Robinson & Chamberlain (1984)	
$(Si_{3.93}Al_{0.07})(Fe^{3+}_{0.1}Ni_{2.12}Mg_{0.81})$	Willemseite	0.697	9.149	De Waal (1970)	
$Si_4(Al_{0.02}Fe^{3+}_{0.26}Fe^{2+}_{0,78}Mg_{1.90})$					
Minnesotaite					
$Si_4(Fe^{2+}_{2.28}Mg_{0.72})$	Mesabi range, MN, USA	0.766	9.410	Grüner (1944)	SF calculated from chemical data
$(Si_{3.88}Al_{0.17})(Fe^{2+}_{2.50}Mg_{0.39}Mn_{0.06})$	Sample 1	0.773	9.419[b]	Guggenheim & Eggleton (1986)	
Synthetic Fe^{2+}-talc series (magnetite–iron and magnetite–wüstite buffers)				Forbes (1969)	
$Si_4(Mg_{3-x}Fe^{2+}_x)$					
Mg_3	Fe/Fe + Mg = 0	0.720	9.156		
$Mg_{2.97}Fe^{2+}_{0.03}$	0.01	0.721	9.157		
$Mg_{2.955}Fe^{2+}_{0.045}$	0.015	0.721	9.159		
$Mg_{2.925}Fe^{2+}_{0.075}$	0.025	0.722	9.160		
$Mg_{2.895}Fe^{2+}_{0.105}$	0.035	0.722	9.161		
$Mg_{2.775}Fe^{2+}_{0.225}$	0.075	0.725	9.165		
$Mg_{2.4}Fe^{2+}_{0.6}$	0.2	0.732	9.181		
Kerolite					
$Si_4(Al_{0.07}Fe^{3+}_{0.02}Mg_{2.8})$	Sample 1	0.715	9.134	Martin de Vidales *et al.* (1991)	
$(Si_{3.96}Al_{0.04})(Al_{0.07}Fe^{3+}_{0.03}Mg_{2.72}Li_{0.09})$	P-7	0.718	9.078	Eberl *et al.* (1982)	
$(Si_{3.95}Al_{0.05})(Al_{0.015}Fe^{3+}_{0.015}Mg_{2.945}Ti_{0.005})$	SAN I-1	0.718	9.133	Pozo & Casas (1999)	
Kerolite–pimelite series				Brindley *et al.* (1979)	
$(Si_{3.94}Al_{0.01}Fe^{3+}_{0.01})(Mg_{3.09}Ni_{0.01})$	1	0.720	9.132		
$(Si_{3.94}Al_{0.02}Fe^{3+}_{0.03})(Mg_{2.16}Ni_{0.87})$	6	0.711	9.150		
$(Si_{3.97}Al_{0.03})(Mg_{2.04}Ni_{0.91}Fe^{3+}_{0.01})$	8	0.711	9.168		
$(Si_{3.99}Al_{0.01})(Mg_{1.22}Ni_{1.74}Fe^{3+}_{0.02})$	17	0.702	9.156		
Synthetic Ni–Mg kerolite series				Baron *et al.* (2016a)	Description of samples only, SF and *b* values are unpublished
$Si_4(Mg_{3-x}Ni_x)$					
Mg_3	$x = 0$	0.720	9.160		
$Mg_{2.36}Ni_{0.64}$	$x = 0.5$	0.714	9.154		
$Mg_{1.8}Ni_{1.2}$	$x = 1$	0.708	9.144		
$Mg_{1.28}Ni_{1.72}$	$x = 1.5$	0.703	9.138		
$Mg_{0.82}Ni_{2.18}$	$x = 2$	0.698	9.136		
$Mg_{0.42}Ni_{2.58}$	$x = 2.5$	0.694	9.134		
Ni_3	$x = 3$	0.690	9.130		

b is a crystallographic parameter (Å).
R = mean ionic radius of octahedral cations (Å; see text for details).
[a]Sample reference in the paper.
[b]Refined unit cell.

of Fe and Ni are not rare. The Mg–Ni solid solution is complete in talc (talc–willemseite sequence) and kerolite (kerolite–pimelite sequence), whereas the Fe^{2+}–Mg solid solution is limited to (Fe^{2+}/(Fe^{2+} + Mg)) values near 0.4 for natural as well as synthetic minerals (Corona *et al.*, 2015). Minnesotaite, a chemically Fe^{2+} talc-like end member, is reported here, but it displays a modulated structure (Guggenheim & Bailey, 1982; Guggenheim & Eggleton, 1986, 1987). Synthetic talcs with other divalent octahedral cations, such as Co (complete solid solution), Zn and Cu (limited solid solution), can be synthesized (e.g. Wilkins & Ito, 1967). Unfortunately, detailed XRD data are not available for these minerals.

Except for minnesotaites and some natural kerolites, data for natural and synthetic samples appear quasi-aligned on a line joining dioctahedral (i.e. pyrophyllite) and trioctahedral (i.e. talc) end members on the *b vs R* plot (Fig. 8a). This agrees with the work of MacEwan (1961), who deduced a coefficient proportional to the ionic radius of Mg and Al from the pyrophyllite–talc pair, which can be used to calculate *b* by multiple regression. The *b vs R* regression for the pyrophyllite–talc (*P*–*T*) line, calculated using pyrophyllite and the three natural talc samples (Mg, Antwerp Fe^{2+}-substituted talc and Ni^{2+}-substituted talc (i.e. willemseite); Table 4) is excellent, and leads to the relation $b = 1.1162R + 8.3691$ (Fig. 8a).

Another regression was calculated using the synthetic Fe^{2+}–Mg talc (Forbes, 1969) and Ni–Mg kerolite series (Baron *et al.*, 2016b) only, and the equation is similar to the former one (Fig. 8a), with the slight difference being possibly due to the lower crystallinity of these samples.

Ferripyrophyllites follow the general trend (Fig. 8a), but the data selected here appear prone to bias given that the three

https://doi.org/10.1180/clm.2023.20 Published online by Cambridge University Press

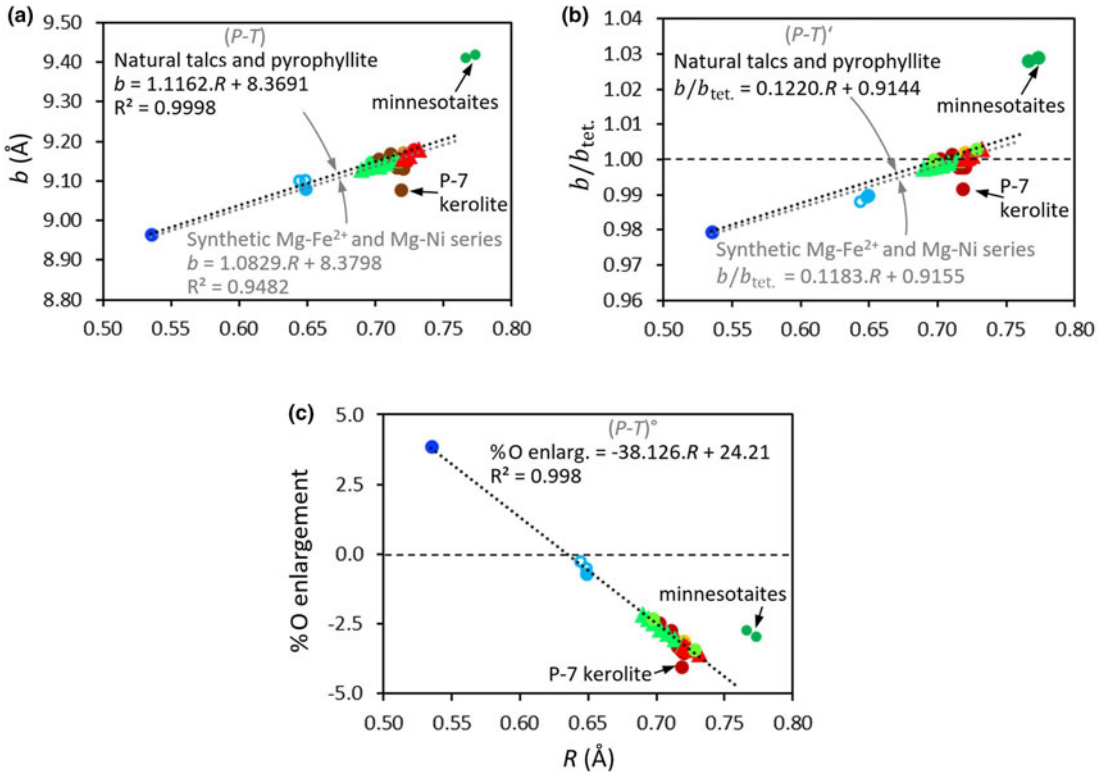

Figure 8. (a) *b vs* mean ionic radius of octahedral cations *R* for electro-neutral TOT phyllosilicates (Table 4), with circles representing natural samples and triangles representing synthetic samples: dark blue circles = pyrophyllite; light blue circles = ferripyrophyllites; open circles = same sample; yellow circle = Mg-talc; red circle = Fe^{2+}-talc; light green circles = willemseite; dark green circles = minnesotaites; brown circles = natural kerolites; light green triangles = synthetic Mg–Ni kerolite series; red triangles = Mg–Fe^{2+} synthetic talc series. (*P–T*) corresponds to the natural pyrophyllite–talc regression line. Grey dotted line = regression calculated with Mg–Fe^{2+} and Mg–Ni synthetic series. (b) $b/b_{tet.}$ ratio *vs* the mean ionic radius of octahedral cations *R* for the same samples (and colour code) as (a). (c) Evolution of the percentage of octahedral enlargement (Equation 6; see text for details) *vs R* for the same samples (and colour code) as (a); dotted line = regression calculated excluding ferripyrophyllite, natural kerolite and minnesotaite samples.

available SFs exhibit a deficit of layer charge, probably due to impurities (Table 4). Accordingly, Chukhrov *et al.* (1979a) identified ~5% smectite in their ferripyrophyllite sample, justifying the Ca presence in the SF to balance the layer charge. Coey *et al.* (1984) studied the same sample using Mössbauer spectroscopy and revisited its SF, attributing more Fe^{3+} to the T sheet (Table 4). However, in light of recent studies: (1) the partition coefficient of Al^{3+} and Fe^{3+} between tetrahedral sites in dioctahedral smectites indicated a strong preference of Al^{3+} to substitute for Si in the T sheet (Decarreau & Petit, 2014); and (2) Mössbauer spectroscopy was shown to be inadequate for quantifying tetrahedral Fe^{3+} in smectite if its content was unknown (Baron *et al.*, 2017). Consequently, it appears that the SF given by Chukhrov *et al.* (1979a) is probably more suitable than the SF revisited by Coey *et al.* (1984).

Some natural kerolites deviate from the general trend (Fig. 8a). As mentioned above, kerolites differs from talcs by their water content, possibly due to a small charge occurrence from octahedral vacant sites, resulting in some swelling properties. Some natural kerolite samples were also characterized as talc–stevensite mixed-layer minerals (Maksimovic, 1966; Brindley *et al.*, 1977; Eberl *et al.*, 1982; Pozo & Casas, 1999). Their deviation from the pyrophyllite–talc regression line could reflect the degree of their 'smectitic' character. Accordingly, the P-7 kerolite (Eberl *et al.*, 1982; Table 4), possessing the greatest charge of the kerolite group in this study and in which Eberl *et al.* identified 30% expandable layers, is the farthest above the (*P–T*) line. These results suggest that the occurrence of a negative octahedral charge in trioctahedral TOT clay minerals tends to induce a decrease in *b*.

Minnesotaites are dramatically out of trend and exhibit greater *b* values than expected from *R* (Fig. 8a). This can be seen as reminiscent of the roles played by structure and morphology on crystal parameters, similarly to TO phyllosilicates with corrugated structures (see below).

Calculated with the same data than for the (*P–T*) line, the regression for the (*P–T*)' line is $b/b_{tet.} = 0.122R + 0.9144$ (Fig. 8b). The similarity between Fig. 8a and Fig. 8b is related to the negligible amounts of tetrahedral substitutions for the pyrophyllite–talc family. The lower $b/b_{tet.}$ is 0.984 for pyrophyllite. The calculated tetrahedral rotation angle $\alpha \approx 11.6°$, which is in agreement with that determined using structure refinement ($\alpha \approx 10°$; Evans & Guggenheim, 1991), allows the lateral dimensions of T sheets to be reduced to adjust to the smaller O sheets. When *R* increases, $b/b_{tet.}$ increases linearly to a value slightly greater than 1, thus indicating that the mismatch between the T and O sheet lateral dimensions decreases progressively, as discussed above for TO phyllosilicates. Accordingly, the angle of tetrahedral rotation α is low, being ~3.6° in talc (Perdikatsis & Burzlaff, 1981). The synthetic Fe^{2+}-richest talc (with octahedral composition: $Mg_{2.4}Fe^{2+}_{0.6}$) exhibits the greatest $b/b_{tet.}$ (1.008). Note that the natural Antwerp talc contains a similar Fe^{2+} amount, but the presence of octahedral Al and Fe^{3+} tends to lower *R* (Table 4). The continuous increase in $b/b_{tet.}$ with *R* implies a progressive decrease in tetrahedral rotation angle

https://doi.org/10.1180/clm.2023.20 Published online by Cambridge University Press

approaching 0° with T sheets stretched maximally for the greatest R (i.e. Fe^{2+}-rich talc). Although a miscibility gap between Fe^{2+}-rich talc and minnesotaite, if one exists, has not been determined between the limit R values of ~0.74 (Fe^{2+}-rich talc) and ~0.76 (minnesotaite), the misfit between the T and O sheets is too high (high $b/b_{tet.}$; Fig. 8b) and the constraints are released by structural modulations, inducing the development of a superlattice for minnesotaite (Guggenheim & Eggleton, 1986). Minnesotaite has a continuous O sheet with adjacent Si tetrahedra on each side. Tetrahedral strip widths are narrow, being three and four tetrahedra wide compared to the seven tetrahedra found across the island in greenalite (Guggenheim & Eggleton, 1986). This is consistent with the smaller $b/b_{tet.}$ measured for minnesotaite (~1.03) compared to greenalite TO phyllosilicate (~1.05).

Thexcelent linear relation, according to the (P–T) line, observed between O sheet enlargement (Equation 6) with R for all samples except minnesotaites and the out-of-trend kerolite P-7 (Fig. 8c), indicates that O sheet thinning (and thickening compared to hydroxides) acts together with the tetrahedral rotation angle to attain congruency between T and O sheet dimensions, as observed for the kaolinite–lizardite family (Fig. 6b). The O sheet enlargement increases progressively with decreasing of R from –3.6% to 3.8% compared to hydroxides (2.5% and 10.3% compared to an ideal unconstrained O sheet, respectively; Fig. 8c), with a null value being obtained for $R = 0.635$, corresponding well to ferripyrophyllite. According to the results above, the crystal structure refinement of a Mg-talc indicates that the O sheet was thinner than the ideal dimensions and that O sheet flattening occurs before the T sheet is stretched maximally ($\alpha \approx 3.6°$; Perdikatsis & Burzlaff, 1981).

Two compositional gaps are observed between the pyrophyllite and talc end members for R from ~0.54 to ~0.65 and from ~0.65 to ~0.69 (Fig. 8a–c). For the former range, all values of R could be obtained by varying the Al^{3+}:Fe^{3+} ratio, suggesting that the pyrophyllite–ferripyrophyllite solid solution is limited due to the respective contrasting geological occurrences of the two end members: mainly low-grade, Al-rich metamorphic rocks for pyrophyllite (Deer *et al.*, 2009) and precipitation from low-temperature, Fe-rich hydrothermal fluids for ferripyrophyllite (Chukhrov *et al.*, 1979b; Badaut *et al.*, 1992).

The second range of R values corresponds to the 'di-trioctahedral region', with the greatest value for the dioctahedral end member being $R = 0.645$ (for $r(^{VI}Fe^{3+})$) and the lowest value for trioctahedral end members being 0.69 ($r(Ni^{2+})$; Table 1). Neutral di-trioctahedral structures would then require Tschermak substitutions and/or extra octahedral vacant sites to neutralize the charge due to heterovalent substitutions. Tschermak substitution would create stress within the structure due to the antagonistic effect of the trivalent cations on the misfit, as discussed above for TO phyllosilicates. However, in contrast to TO structures, excessive out-of-plane tilting of tetrahedra in TOT phyllosilicates cannot occur because the identical sheets on opposite sides of a neighbouring O sheet hold it flat under tension (Guggenheim & Eggleton, 1986). To our knowledge, no neutral di-trioctahedral TOT layer silicates have been reported to occur to date.

Smectites

Smectites are TOT clay minerals with a negative layer charge generally ranging between 0.2 and 0.6 pfu due to isomorphous octahedral and/or tetrahedral heterovalent substitutions. This charge is balanced by the presence of cations located in the interlayer space, whereas hydration of the cations leads to the intercalation of between 0 and several water sheets (Fig. 7b; e.g. Ferrage, 2016). The general SF takes the form of $(Si_{4-x}R^{3+}_x)(R^{3+}_aR^{2+}_bR^{+}_c\square_d)O_{10}(OH)_2M_y$, where $a + b + c + d = 3$ and $y = x - 3a - 2b - c + 6$ if the interlayer cation M is monovalent. Smectites present great variability in their chemical composition, density and location of layer charge, giving rise to numerous end members with a dedicated terminology (e.g. Brigatti *et al.*, 2013).

The dataset used is representative of the large compositional range encountered for both natural and synthetic smectites (Table 5). Vermiculite, although generally composed of macroscopic particles (e.g. de la Calle & Suquet, 1991), was added to this category because it has the same SF as smectite at $y > 0.6$ and cannot be distinguished from high-charge saponite in its swelling properties (Suquet *et al.*, 1977).

Especially for smectites, which are typically finely divided clay minerals, b and R are probably less reliable in terms of assessing value than for the other phyllosilicates. No single-crystal structural refinements have been carried out on smectites, and b has most often been measured using direct measurement of the (06ℓ;33ℓ) band. Using a Rietveld simulation of XRD traces of smectites synthesized by Andrieux *et al.* (2010), Heuser *et al.* (2013) found b to be significantly greater than values obtained from the (06ℓ;33ℓ) band (Table 5; Petit *et al.*, 2015). The nature of the interlayer cation and the hydration state were also shown to induce variation in b up to 0.03 Å (Suquet *et al.*, 1981). The SF must also be viewed with caution due to:

(1) The difficulty in obtaining pure smectite, with admixtures affecting its chemical composition.
(2) The chemical heterogeneity within a given sample. Several populations of smectites may occur in the same sample, and the resulting R and b values measured thus represent mean values. For example, Ferrage *et al.* (2007) identified two populations of beidellites in a dioctahedral smectite, while the Ölberg iron-rich smectite first studied by Köster *et al.* (1999) was shown to be heterogeneous, being constituted by Fe^{3+}-montmorillonite and smectite with some tetrahedral charge and with less Mg and more Al than Fe^{3+}-montmorillonite (Petit *et al.*, 2002).
(3) The chemical heterogeneity between samples from a given site. As an illustration, the SF of the Manito nontronite revealed $0.21\,^{VI}Al$ and $0.1\,^{VI}Fe^{2+}$ in Köster *et al.* (1999), while no $^{VI}Fe^{2+}$ and only $0.03\,^{VI}Al$ were proposed by Radoslovich (1962), both leading to different but coherent values (0.642 and 0.644 for R and 9.125 and 9.155 for b, respectively; Table 5). Similar observations can be made for some other smectites (Otay montmorillonite, Black Jack mine beidellite, Garfield nontronite, Unterrupsroth beidellite (Nadeau *et al.*, 1985)).
(4) The difficulty in evaluating the actual rate of tetrahedral substitutions.
(5) The redox state.

Despite these limitations, the b *vs* R plot reveals that the samples generally follow the pyrophyllite–talc (P–T) trend (Fig. 9a). The scattering of data may be related mostly to the layer charge occurrence in smectite. For example, for the synthetic Fe^{3+}-nontronite series $(Si_{4-x}Fe^{3+}_x)Fe^{3+}_2O_{10}(OH)_2Na_x$ (with $0.43 \leq x \leq 1.54$), where tetrahedral iron was the only variable parameter, R is constant, while b increases with tetrahedral iron content (Fig. 10a), leading to vertical dot alignment on the b *vs* R plot (green triangles in Fig. 9a). A similar observation is

https://doi.org/10.1180/clm.2023.20 Published online by Cambridge University Press

Table 5. Data used for smectites.

Smectites (octahedral and tetrahedral anhydrous compositions)	Sample[a]	*R*	*b*	References	Comments
Natural smectites					
Dioctahedral smectites				Russell & Clark (1978)	
$(Si_{3.845}Al_{0.155})(Al_{1.565}Fe^{3+}_{0.2}Mg_{0.25})$	Wyoming montmorillonite	0.569	8.988		
$(Si_{3.665}Al_{0.335})(Al_{1.755}Mg_{0.255})$	Unterrupsroth montmorillonite	0.558	8.976		
$(Si_{3.995}Al_{0.005})(Al_{1.36}Fe^{3+}_{0.06}Mg_{0.60})$	Otay montmorillonite	0.593	8.994		
$(Si_{3.82}Al_{0.18})(Al_{1.27}Fe^{3+}_{0.42}Mg_{0.37})$	Woburn montmorillonite	0.591	9.024		
$(Si_{3.105}Al_{0.07}Fe^{3+}_{0.82})(Fe^{3+}_{2.02}Mg_{0.1})$	California nontronite	0.649	9.210		
$(Si_{3.65}Al_{0.35})(Al_{0.53}Fe^{3+}_{1.37}Mg_{0.13})$	Washington nontronite	0.621	9.072		
$(Si_{3.67}Al_{0.05}Fe^{3+}_{0.28})(Fe^{3+}_{1.95}Mg_{0.05})$	El Pao nontronite	0.647	9.162		
$(Si_{3.41}Al_{0.47}Fe^{3+}_{0.12})(Fe^{3+}_{2}Mg_{0.02})$	Pfaffenreuth nontronite	0.646	9.144		
$(Si_{3.42}Al_{0.525}Fe^{3+}_{0.055})(Fe^{3+}_{1.98}Mg_{0.02})$	Garfield nontronite	0.646	9.138		
Dioctahedral smectites				Brigatti (1983)	
$(Si_{3.98}Al_{0.02})(Al_{0.15}Fe^{3+}_{1.45}Mg_{0.39})$	1	0.651	9.085		
$Si_{4.0}(Al_{0.4}Fe^{3+}_{1.31}Mg_{0.25})$	2	0.632	9.070		
$(Si_{3.98}Al_{0.02})(Al_{0.6}Fe^{3+}_{1.06}Mg_{0.39})$	3	0.627	9.030		
$(Si_{3.65}Al_{0.35})(Al_{0.68}Fe^{3+}_{0.87}Mg_{0.48})$	4	0.626	9.005		
$(Si_{3.77}Al_{0.23})(Al_{0.99}Fe^{3+}_{0.78}Mg_{0.24})$	5	0.600	8.993		
$(Si_{3.56}Al_{0.44})(Al_{0.9}Fe^{3+}_{0.72}Mg_{0.55})$	6	0.618	8.978		
$(Si_{3.36}Al_{0.64}))(Al_{0.75}Fe^{3+}_{0.71}Mg_{0.81})$	7	0.635	9.015		
$(Si_{3.25}Al_{0.75}))(Al_{0.95}Fe^{3+}_{0.7}Mg_{0.59})$	8	0.618	9.020		
$(Si_{3.84}Al_{0.16})(Al_{1.12}Fe^{3+}_{0.57}Mg_{0.35})$	9	0.597	8.965		
$(Si_{3.55}A_{0.45})(Al_{0.87}Fe^{3+}_{0.53}Mg_{0.82})$	10	0.630	8.952		
$(Si_{3.41}Al_{0.59})(Al_{1.4}Fe^{3+}_{0.46}Mg_{0.39})$	11	0.590	8.942		
$(Si_{3.75}Al_{0.25})(Al_{1.44}Fe^{3+}_{0.35}Mg_{0.31})$	12	0.581	8.944		
$(S_{i3.82}A_{l0.18})(Al_{1.35}Fe^{3+}_{0.31}Mg_{0.45})$	13	0.591	8.940		
$(Si_{3.87}Al_{0.13})(Al_{1.38}Fe^{3+}_{0.25}Mg_{0.4})$	14	0.585	8.942		
$(Si_{3.89}Al_{0.11})(Al_{1.52}Fe^{3+}_{0.17}Mg_{0.32})$	15	0.574	8.945		
Dioctahedral smectites				Tsipursky & Drits (1984)	
$(Si_{3.95}Al_{0.05})(Al_{1.38}Fe^{3+}_{0.18}Mg_{0.44})$	1 cv	0.586	8.97		cv, tv = *cis*, *trans* octahedral vacant site (Drits *et al.*, 2006)
$(Si_{3.96}Al_{0.04})(Al_{1.54}Fe^{3+}_{0.18}Mg_{0.26})$	2 tv-cv	0.569	8.98		
$(Si_{3.98}Al_{0.02})(Al_{1.38}Fe^{3+}_{0.14}Mg_{0.48})$	3 tv-cv	0.587	8.97		
$(Si_{3.91}Al_{0.09})(Al_{1.36}Fe^{3+}_{0.41}Mg_{0.24})$	4 tv	0.580	8.98		
$Si_4(Al_{1.51}Fe^{3+}_{0.10}Mg_{0.39})$	5 cv	0.577	8.98		
$Si_4(Al_{1.40}Fe^{3+}_{0.26}Mg_{0.34})$	6 tv	0.581	9.00		
$(Si_{3.98}Al_{0.02})(Al_{1.32}Fe^{3+}_{0.26}Mg_{0.41})$	7 tv	0.587	9.00		
$Si_4(Al_{1.39}Fe^{3+}_{0.31}Mg_{0.30})$	8 tv	0.580	8.97		
$(Si_{3.83}Al_{0.17})(Al_{1.47}Fe^{3+}_{0.19}Mg_{0.34})$	9 cv	0.577	8.98		
$(Si_{3.89}Al_{0.11})(Al_{0.89}Fe^{3+}_{0.62}Fe^{2+}_{0.03}Mg_{0.46})$	10 tv-cv	0.615	8.98		
$Si_4(Al_{0.2}Fe^{3+}_{1.51}Mg_{0.29})$	11 tv	0.645	9.06		
$(Si_{3.71}Al_{0.29})(Al_{1.64}Fe^{3+}_{0.05}Fe^{2+}_{0.01}Mg_{0.31})$	12 tv tv-cv	0.567	8.98		
$(Si_{3.73}Al_{0.27})(Al_{1.05}Fe^{3+}_{0.37}Mg_{0.57})$	13 tv-cv	0.608	8.97		
$(Si_{3.86}Al_{0.14})(Al_{1.68}Mg_{0.32})$	14 cv	0.565	8.98		
$(Si_{3.41}Al_{0.59})(Al_{1.57}Fe^{3+}_{0.37}Fe^{2+}_{0.01}Mg_{0.05})$	15 tv-cv	0.561	8.98		
$(Si_{3.53}Al_{0.47})(Al_{0.96}Fe^{3+}_{0.88}Fe^{2+}_{0.02}Mg_{0.26})$	16 tv	0.606	9.01		
$(Si_{3.45}Al_{0.55})(Al_{0.33}Fe^{3+}_{1.59}Mg_{0.08})$	17 tv	0.630	9.12		
$(Si_{3.49}Al_{0.51})(Fe^{3+}_{1.87}Fe^{2+}_{0.17})$	18 tv	0.656	9.17		
$(Si_{3.65}Al_{0.35})(Fe^{3+}_{1.92}Mg_{0.08})$	19 tv	0.648	9.12		
$(Si_{3.46}Al_{0.54})(Al_{0.16}Fe^{3+}_{1.85}Mg_{0.04})$	20 tv	0.638	9.14		
Dioctahedral smectites				Heuser *et al.* (2013)	
$(Si_{3.78}Al_{0.22})(Al_{1.55}Fe^{3+}_{0.25}Mg_{0.2})$	BeC	0.567	9.010		*b* measured using Rietveld refinement
$(Si_{3.89}Al_{0.11})(Al_{1.43}Fe^{3+}_{0.28}Mg_{0.29})$	BeD	0.577	9.026		
$(Si_{3.88}Al_{0.12})(Al_{1.40}Fe^{3+}_{0.27}Mg_{0.23})$	BeE	0.573	9.037		
$(Si_{3.60}Al_{0.40})(Al_{1.15}Fe^{3+}_{0.74}Mg_{0.11})$	BeH	0.586	9.064		
$(Si_{3.92}Al_{0.08})(Al_{1.55}Fe^{3+}_{0.19}Mg_{0.26})$	BeW	0.570	9.030		
$(Si_{3.69}Al_{0.31})(Al_{1.61}Fe^{3+}_{0.09}Mg_{0.30})$	FR 10-0382	0.568	9.013		
$(Si_{3.79}Al_{0.21})(Al_{1.68}Fe^{3+}_{0.11}Mg_{0.21})$	FR10-0532	0.560	9.017		
$(Si_{3.85}Al_{0.15})(Al_{1.24}Fe^{3+}_{0.48}Mg_{0.28})$	FR11-0229	0.587	9.053		
$(Si_{3.69}Al_{0.31})(Al_{1.47}Fe^{3+}_{0.35}Mg_{0.18})$	Cameron	0.571	9.041		
$(Si_{3.56}Al_{0.44})(Al_{0.74}Fe^{3+}_{1.25}Mg_{0.01})$	Cheney	0.605	9.145		
Iron-rich smectites				Köster *et al.* (1999)	
$(Si_{3.68}Al_{0.32})(Al_{1.24}Fe^{3+}_{0.6}Fe^{2+}_{0.05}Mg_{0.19})$	Oberpullendorf	0.590	8.997		
$(Si_{3.86}Al_{0.14})(Al_{1.4}Fe^{3+}_{0.35}Fe^{2+}_{0.02}Mg_{0.26})$	Sauteloup	0.580	8.968		
$(Si_{3.67}Al_{0.26}Fe^{3+}_{0.07})(Fe^{3+}_{1.91}Fe^{2+}_{0.08}Mg_{0.03})$	Hoher Hagen nontronite	0.651	9.151		
$(Si_{3.49}Al_{0.51})(Al_{0.21}Fe^{3+}_{1.69}Fe^{2+}_{0.1}Mg_{0.05})$	Manito nontronite	0.642	9.125		
$(Si_{3.92}Al_{0.08})(Al_{0.37}Fe^{3+}_{0.98}Fe^{2+}_{0.06}Cr_{0.03}Ni_{0.02}Mg_{0.71})$	Ölberg	0.655	9.040		

(*Continued*)

https://doi.org/10.1180/clm.2023.20 Published online by Cambridge University Press

Table 5. (*Continued.*)

Smectites (octahedral and tetrahedral anhydrous compositions)	Sample[a]	*R*	*b*	References	Comments
Other nontronites					
$(Si_{3.73}Al_{0.27})(Al_{0.15}Fe^{3+}_{1.68}Mg_{0.14})$	Tyrrhenian Sea	0.642	9.110	Dekov *et al.* (2007)	
$(Si_{3.59}Al_{0.41})(Al_{0.39}Fe^{3+}_{1.53}Mg_{0.08}Cu_{0.02})$	Serra Dos Carajas, Brazil	0.628	9.108	Petit *et al.* (1992)	
Beidellites				Post *et al.* (1997)	
$(Si_{3.6}Al_{0.4})(Al_{1.96}Fe^{3+}_{0.05}Mg_{0.02})$	Idawa Mine	0.540	8.964		
$(Si_{3.7}Al_{0.3})(Al_{1.84}Fe^{3+}_{0.08}Mg_{0.11})$	DeLamar Mine	0.549	8.946		
$(Si_{3.64}Al_{0.36})(Al_{1.9}Fe^{3+}_{0.09}Mg_{0.04})$	Blain tunnel	0.544	8.958		
$(Si_{3.46}Al_{0.54})(Al_{1.96}Fe^{3+}_{0.04}Mg_{0.02})$	Black Jack Mine	0.539	8.988		
Other natural smectites				Radoslovich (1962)	
Al-rich dioctahedral smectites					
Si_4 $(Al_{1.46}Fe^{3+}_{0.06}Mg_{0.49})$	Santa Rita	0.583	8.993		
$(Si_{3.80}Al_{0.20})(Al_{1.55}Fe^{3+}_{0.21}Mg_{0.23})$	Belle Fourche	0.568	8.993		
$(Si_{3.78}Al_{0.22})(Al_{1.51}Fe^{3+}_{0.27}Mg_{0.23})$	Merritt	0.571	9.000		
$(Si_{3.86}Al_{0.12}Fe^{3+}_{0.02})(Al_{1.58}Fe^{3+}_{0.18}Mg_{0.25})$	Clay Spur	0.568	9.001		
Si_4 $(Al_{1.47}$ $Fe^{3+}_{0.06}Mg_{0.49})$	Polkville	0.583	9.002		
$(Si_{3.91}Al_{0.09})(Al_{1.46}Fe^{3+}_{0.18}Mg_{0.31})$	Amory	0.575	9.004		
$(Si_{3.88}Al_{0.08}Fe^{3+}_{0.04})(Al_{1.42}Fe^{3+}_{0.19}Mg_{0.41})$	Plymouth	0.583	9.011		
$Si_4(Al_{1.28}Fe^{3+}_{0.06}Mg_{0.71})$	Otay	0.602	9.014		
$(Si_{3.80}Al_{0.20})(Al_{1.51}Fe^{3+}_{0.31}Mg_{0.20})$	Little Rock	0.570	8.996		
$(Si_{3.85}Al_{0.15})(Al_{1.37}Fe^{3+}_{0.19}Mg_{0.47})$	Chambers	0.588	9.004		
$(Si_{3.90}Al_{0.10})(Al_{1.55}Fe^{3+}_{0.20}Mg_{0.25})$	Upton	0.569	8.997		
$(Si_{3.91}Al_{0.09})(Al_{1.57}Fe^{3+}_{0.18}Fe^{2+}_{0.02}Mg_{0.23})$	Belle Fourche	0.569	8.988		
$(Si_{3.89}Al_{0.11})(Al_{1.45}Fe^{3+}_{0.16}Fe^{2+}_{0.01}Mg_{0.44})$	Lemon	0.584	9.019		
$(Si_{3.97}Al_{0.03})(Al_{1.55}Fe^{3+}_{0.06}Mg_{0.39})$	Rideout	0.574	8.994		
$(Si_{3.99}Al_{0.01})(Al_{1.57}Fe^{3+}_{0.12}Mg_{0.30})$	San Antonio	0.570	8.997		
$Si_4(Al_{1.45}Mg_{0.58}Li_{0.16})$	Honeycomb	0.600	8.979		
$(Si_{3.74}Al_{0.26})(Al_{1.77}Fe^{3+}_{0.03}Mg_{0.20})$	Unter-Rupsroth	0.555	9.000		
$(Si_{3.46}Al_{0.54})(Al_{1.96}Fe^{3+}_{0.04})$	Black Jack	0.537	8.940		
$(Si_{3.48}Al_{0.52})(Al_{1.98}Fe^{3+}_{0.02}Mg_{0.01})$	Black Jack	0.537	8.978		
Nontronites					
$(Si_{3.5}Al_{0.5})(Al_{0.03}Fe^{3+}_{2.02}Mg_{0.01})$	Manito	0.644	9.155		
$(Si_{3.5}Al_{0.5})(Al_{0.05}Fe^{3+}_{1.93}Mg_{0.12})$	Garfield	0.647	9.175		
$(Si_{3.5}Al_{0.5})(Al_{0.08}Fe^{3+}_{1.84}Mg_{0.08})$	Nontron	0.644	9.12		
$(Si_{3.57}Al_{0.43})(Al_{0.08}Fe^{3+}_{1.79}Fe^{2+}_{0.04}Mg_{0.08})$	Behenjy	0.646	9.13		
Trioctahedral smectites					
$(Si_{3.19}Al_{0.75}Fe^{3+}_{0.06})(Fe^{3+}_{0.45}Fe^{2+}_{0.26}Mg_{2.29})$	Saponite	0.714	9.258		
$(Si_{3.70}Al_{0.30})(Al_{0.04}Fe^{3+}_{0.01}Mg_{2.85})$	Saponite	0.717	9.165		
$(Si_{3.38}Al_{0.62})(Al_{0.03}Fe^{3+}_{0.02}Mg_{2.95})$	Saponite	0.718	9.218		
$(Si_{3.63}Al_{0.37})(Fe^{3+}_{0.01}Mg_{2.99})$	Saponite	0.720	9.198		
$(Si_{3.50}Al_{0.50})(Al_{0.15}Fe^{3+}_{0.04}Mg_{2.92}Mn_{0.01})$	Saponite	0.717	9.178		
$(Si_{3.38}Al_{0.52}Fe^{3+}_{0.1})(Al_{0.05}Fe^{2+}_{0.05}Mg_{2.91})$	Saponite	0.718	9.197		
$(Si_{3.19}Al_{0.81})(Al_{0.04}Fe^{3+}_{0.44}Fe^{2+}_{0.52}Mg_{1.88})$	Griffithite	0.717	9.246		
$(Si_{3.30}Al_{0.70})(Al_{0.79}Fe^{3+}_{0.02}Zn_{1.85}Mg_{0.14})$	Sauconite	0.680	9.228		
$(Si_{3.39}Al_{0.61})(Al_{0.78}Fe^{3+}_{0.23}Zn_{1.54}Mg_{0.15})$	Sauconite	0.672	9.220		
$(Si_{3.27}Al_{0.73})(Al_{0.12}Fe^{3+}_{0.13}Zn_{2.64}Mg_{0.11})$	Sauconite	0.727	9.251		
$(Si_{3.35}Al_{0.65})(Al_{0.04}Fe^{3+}_{0.02}Zn_{2.89}Mg_{0.10}Mn_{0.01})$	Sauconite	0.736	9.247		
$(Si_{3.39}Al_{0.61})(Al_{0.17}Fe^{3+}_{0.58}Zn_{1.95}Mg_{0.12})$	Sauconite	0.707	9.259		
$(Si_{3.47}Al_{0.53})(Al_{0.22}Fe^{3+}_{0.17}Zn_{2.40}Mg_{0.18})$	Sauconite	0.718	9.252		
$Si_4(Al_{0.01}Mg_{2.71}Li_{0.34})$	Hectorite	0.724	9.119		
$(Si_{3.95}$ $Al_{0.05})(Mg_{2.73}Li_{0.33})$	Hectorite	0.724	9.180		
$Si_4(Fe^{3+}_{0.02}Mg_{2.88}Mn_{0.02})$	Stevensite	0.720	9.156		
$(Si_{3.82}Al_{0.18})(Al_{0.4}Cr^{3+}_{0.35}Fe^{3+}_{0.58}Mg_{0.82})$	Volkonskoite	0.648	9.119		
Other volkonskoite					
$(Si_{3.7}Al_{0.3})(Cr^{3+}_{1.1}Mg_{1.26})$	Jordan	0.671	9.162	Khoury *et al.* (1984)	
$(Si_{3.59}Al_{0.41})(Cr^{3+}_{1.07}Fe^{3+}_{0.35}Mg_{0.75})$	R4820	0.656	9.08	Foord *et al.* (1987)	
Other saponite					
$(Si_{3.30}Al_{0.68}Fe^{3+}_{0.02})(Mg_{2.50}Fe^{2+}_{0.26}Fe^{3+}_{0.24})$	Kosakov	0.719	9.233	Suquet *et al.* (1975)	
Other trioctahedral smectites					
$Si_4Mg_{2.85}$	Stevensite n°1	0.720	9.120	Faust (1959)	
$Si_4(Mg_{2.66}Li_{0.3})$	Hectorite	0.724	9.120		
$Si_4(Mg_{2.87}Li_{0.1}Fe^{2+}_{0.06}Al_{0.03})$	Ghassoulite	0.721	9.100		
Smectitic series (Murrin Murrin, Australia)				Gaudin *et al.* (2004)	
$(Si_{3.8}Al_{0.2})(Al_{0.36}Fe^{3+}_{1.19}Mg_{0.29}Cr_{0.09}Ni_{0.13})$	2-22	0.638	9.078		
$(Si_{3.79}Al_{0.21})(Al_{0.67}Fe^{3+}_{0.91}Mg_{0.19}Cr_{0.13}Ni_{0.13})$	2-21	0.617	9.054		
$(Si_{3.78}Al_{0.22})(Al_{0.47}Fe^{3+}_{1.01}Mg_{0.2}Cr_{0.17}Ni_{0.19})$	2-19	0.629	9.072		
$(Si_{3.78}Al_{0.22})(Al_{0.59}Fe^{3+}_{0.91}Mg_{0.23}Cr_{0.19}Ni_{0.12})$	2-17	0.621	9.060		
$(Si_{3.79}Al_{0.21})(Al_{0.08}Fe^{3+}_{1.3}Mg_{0.55}Cr_{0.05}Ni_{0.12})$	5-19v	0.660	9.072		
$(Si_{3.69}Al_{0.31})(Al_{0.54}Fe^{3+}_{0.99}Mg_{0.19}Cr_{0.21}Ni_{0.1})$	5-46	0.622	9.060		
$(Si_{3.8}Al_{0.2})(Al_{0.31}Fe^{3+}_{1.29}Mg_{0.2}Cr_{0.1}Ni_{0.11})$	5-43v3	0.636	9.078		

(*Continued*)

https://doi.org/10.1180/clm.2023.20 Published online by Cambridge University Press

Table 5. (*Continued.*)

Smectites (octahedral and tetrahedral anhydrous compositions)	Sample[a]	*R*	*b*	References	Comments
$(Si_{3.79}Al_{0.21})(Al_{0.11}Fe^{3+}_{1.41}Mg_{0.37}Cr_{0.08}Ni_{0.12})$	5-36	0.654	9.084		
$(Si_{3.79}Al_{0.21})(Al_{0.15}Fe^{3+}_{1.33}Mg_{0.5}Cr_{0.03}Ni_{0.13})$	5-25	0.657	9.090		
$(Si_{3.65}Al_{0.35})(Fe^{3+}_{1.67}Mg_{0.46}Cr_{0.05}Ni_{0.12})$	5-23	0.662	9.090		
Other intermediary smectites					
$(Si_{3.49}Al_{0.51})(Al_{0.17}Fe^{3+}_{0.85}Mg_{1.39})$	Mont Megantic, Quebec	0.680	9.150	Kodama *et al.* (1988)	
Vermiculite					
$(Si_{2.86}Al_{1.14})(Al_{0.15}Fe^{3+}_{0.01}Mg_{2.83})$	Llano	0.684	9.255	Shirozu & Bailey (1966)	
$(Si_{2.72}Al_{1.28})(Al_{0.16}Fe^{3+}_{0.48}Mg_{2.36})$	Kenya	0.668	9.18	Mathieson & Walker (1954)	
$(Si_{2.65}Al_{1.35})(Al_{0.35}Fe^{3+}_{0.29}Fe^{2+}_{0.04}Mg_{2.68})$	Ajmer, India	0.709	9.168	http://www.handbookofmineralogy.org/	
Synthetic smectites					
Dioctahedral Al–Fe^{3+} smectitic series $(SiAl)_4(Fe^{3+}_{(2-x)}Al_x)$				Petit *et al.* (2015)	
$(Si_{3.52}Al_{0.35}Fe^{3+}_{0.13})(Fe^{3+}_2)$	1	0.645	9.186		
$(Si_{3.64}Al_{0.36})(Fe^{3+}_{1.89}Al_{0.11})$	14	0.639	9.168		
$(Si_{3.61}Al_{0.39})(Fe^{3+}_{1.74}Al_{0.26})$	19	0.631	9.132		
	Beidellite 19		9.189	Heuser *et al.* (2013)	Italicized = same sample, *b* measured using Rietveld refinement
$(SiAl)_4(Fe^{3+}_{0.38}Al_{1.62})$	23	0.556	8.982		
	Beidellite 23		*9.059*	Heuser *et al.* (2013)	
$(SiAl)_4(Fe^{3+}_{0.34}Al_{1.66})$	31	0.554	8.970		
	Beidellite 31		*9.019*	Heuser *et al.* (2013)	
$(Si_{3.47}Al_{0.45}Fe^{3+}_{0.07})(Fe^{3+}_{1.97}Al_{0.03})$	39	0.643	9.156		
$(Si_{3.51}Al_{0.36}Fe^{3+}_{0.13})(Fe^{3+}_{1.80}Al_{0.20})$	41	0.634	9.126		
$(Si_{3.5}Al_{0.5})(Fe^{3+}_{1.64}Al_{0.36})$	43	0.625	9.138		
$(SiAl)_4(Fe^{3+}_{1.26}Al_{0.74})$	52	0.604	9.096		
$(Si_{3.6}Al_{0.4})(Fe^{3+}_{0.8}Al_{1.2})$	53	0.579	9.048		
$(Si_{3.7}Al_{0.3})(Fe^{3+}_{0.57}\ Al_{1.43})$	54	0.566	9.000		
Dioctahedral Ga–Fe^{3+} smectitic series $(SiGa)_4(Fe^{3+}_{(2-x)}Ga_x)$				Petit *et al.* (2016)	
$(Si_{3,24}Ga_{0.76})Ga_2)$	0.00	0.620	9.100		
$(Si_{3.25}Ga_{\ 0.75})Fe^{3+}_{0.5}Ga_{1.5})$	0.25	0.626	9.114		
$(Si_{3.42}Ga_{\ 0.58})Fe^{3+}_{0.86}Ga_{1.14})$	0.50	0.631	9.117		
$(Si_{3.48}Ga_{\ 0.52})Fe^{3+}_{1.11}Ga_{0.89})$	0.75	0.634	9.123		
$(Si_{3.48}Ga_{\ 0.52})Fe^{3+}_{1.24}Ga_{0.76})$	1.00	0.636	9.127		
Dioctahedral Fe^{3+}-nontronite series $(Si_{4-x}Fe^{3+}{}_x)(Fe^{3+}_2)$ (tetrahedral composition)				Baron *et al.* (2016b)	
$Si_{3.57}Fe^{3+}_{0.43}$		0.645	9.174		
$Si_{3.54}Fe^{3+}_{0.46}$		0.645	9.168		
$Si_{3.51}Fe^{3+}_{0.49}$		0.645	9.180		
$Si_{3.50}\ Fe^{3+}_{0.50}$		0.645	9.186		
$Si_{3.49}Fe^{3+}_{0.51}$		0.645	9.180		
$Si_{3.47}\ Fe^{3+}_{0.53}$		0.645	9.186		
$Si_{3.43}Fe^{3+}_{0.57}$		0.645	9.198		
$Si_{3.32}Fe^{3+}_{0.68}$		0.645	9.198		
$Si_{3.15}\ Fe^{3+}_{0.85}$		0.645	9.216		
$Si_{3.13}\ Fe^{3+}_{0.87}$		0.645	9.222		
$Si_{3.01}Fe^{3+}_{0.99}$		0.645	9.240		
Di-trioctahedral Fe^{3+}–Mg smectitic series $(Si,Fe^{3+})_4(Fe^{3+}Mg)_y$				Grauby *et al.* (1994)	
$(Si_{3.88}Fe^{3+}_{0.12})(Fe^{3+}_{1.73}Mg_{0.24})$	2	0.654	9.095		
$(Si_{3.9}Fe^{3+}_{0.1})(Fe^{3+}_{1.58}Mg_{0.47})$	3	0.662	9.092		
$(Si_{3.87}Fe^{3+}_{0.13})(Fe^{3+}_{1.40}Mg_{0.76})$	4	0.671	9.104		
$(Si_{3.97}Fe^{3+}_{0.03})(Fe^{3+}_{1.17}Mg_{1.02})$	5	0.680	9.129		
$(Si_{3.96}Fe^{3+}_{0.04})(Fe^{3+}_{1.08}Mg_{1.22})$	6	0.685	9.122		
$(Si_{3.97}Fe^{3+}_{0.03})(Fe^{3+}_{0.84}Mg_{1.58})$	7	0.694	9.126		
$(Si_{3.96}Fe^{3+}_{0.04})(Fe^{3+}_{0.56}Mg_{2.03})$	8	0.704	9.143		
$Si_4(Fe^{3+}_{0.30}Mg_{2.43})$	9	0.712	9.152		
Fe^{2+}-rich saponite series				Chemtob *et al.* (2015)	
$(Si_{3.54}Al_{0.46})(Fe^{2+}_{2.66}Al_{0.27})$	A	0.757	9.384		
$(Si_{3.54}Al_{0.46})(Fe^{2+}_{2.36}Al_{0.28}\ Mg_{0.27})$	B	0.751	9.300		
$(Si_{3.42}Al_{0.58})(Fe^{2+}_{1.43}Al_{0.17}Fe^{3+}_{0.27}Mg_{0.99})$	C	0.732	9.228		
$(Si_{3.52}Al_{0.48})(Fe^{2+}_{0.82}Al_{0.17}Fe^{3+}_{0.04}Mg_{1.75})$	D	0.725	9.192		
$(Si_{3.6}Al_{0.4})(Fe^{2+}_{1.5}Al_{0.86}Fe^{3+}_{0.17})$	E	0.688	9.258		
$(Si_{3.58}Al_{0.42})(Fe^{2+}_{0.83}Al_{0.8}Fe^{3+}_{0.06}Mg_{0.78})$	F	0.678	9.174		
$(Si_{3.63}Al_{0.37})(Fe^{2+}_{2.57}Mg_{0.56})$	G	0.769	9.222		
$(Si_{3.63}Al_{0.37})(Fe^{2+}_{0.98}Fe^{3+}_{0.05}Mg_{2.15})$	H	0.737	9.198		
Saponite series $Na(Si_{4-x}Al_x)(Mg_{(3-y)}Al_y)$				Suquet *et al.* (1981)	

(*Continued*)

https://doi.org/10.1180/clm.2023.20 Published online by Cambridge University Press

Table 5. (*Continued.*)

Smectites (octahedral and tetrahedral anhydrous compositions)	Sample[a]	*R*	*b*	References	Comments
$(Si_{3.67}Al_{033})(Mg_{3.0})$	1	0.720	9.184		
$(Si_{3.5}Al_{0.5})(Mg_{3.0})$	2	0.720	9.199		
$(Si_{3.3}Al_{0.7})(Mg_{2.8}Al_{0.2})$	3	0.708	9.201		
$(Si_{3.2}Al_{0.8})(Mg_{2.8}Al_{0.2})$	4	0.708	9.214		
$(Si_{3.1}Al_{0.9})(Mg_{2.8}Al_{0.2})$	5	0.708	9.217		
$(Si_{3.2}Al_{0.8})(Mg_{3.0})$	6	0.720	9.219		
$(Si_{3.0}Al_{1.0})(Mg_{2.8}Al_{0.2})$	7	0.708	9.221		
$(Si_{3.0}Al_{1.0})(Mg_{3.0})$	8	0.720	9.237		
Trioctahedral smectites					
$(Si_{3.6}Al_{0.4})Zn_3$	Sauconite	0.740	9.192	Higashi *et al.* (2002)	
$Si_4(Zn_{2.6}Li_{0.4})$	Zn-hectorite	0.743	9.150		
$Si_4(Mg_{2.6}Li_{0.4})$	Hectorite	0.725	9.120		
Hectorite					
$Si_4(Mg_{2.67}Li_{0.33})$	Hectorite	0.724	9.096	Decarreau (1980)	
Zn-stenvensite series (Si_4Zn_x)				Petit *et al.* (2008)	
$Si_4Zn_{2.77}$	Zn80	0.740	9.198		
$Si_4Zn_{2.97}$	Zn100	0.740	9.198		
$Si_4Zn_{2.99}$	Zn120	0.740	9.210		
$Si_4Zn_{2.90}$	Zn150	0.740	9.180		
$Si_4Zn_{2.97}$	Zn200	0.740	9.150		
Stenvensite series ($Si_4R^{2+}_{3-\mathcal{E}}$)				Decarreau (1983)	
$Si_4Ni_{3-\mathcal{E}}$	Ni	0.690	9.087		
$Si_4Mg_{3-\mathcal{E}}$	Mg	0.720	9.144		
$Si_4Zn_{3-\mathcal{E}}$	Zn	0.740	9.219		
$Si_4Fe^{2+}_{3-\mathcal{E}}$	Fe	0.780	9.270		
$Si_4(Mg_{0.82}Zn_{0.18})_{3-\mathcal{E}}$	Zn 0.18	0.724	9.150		
$Si_4(Mg_{0.43}Zn_{0.47})_{3-\mathcal{E}}$	Zn 0.47	0.729	9.190		

b is a crystallographic parameter (Å).
R = mean ionic radius of octahedral cations (Å; see text for details).
[a]Sample reference in the paper.

made for natural and synthetic saponites (light green squares and triangles in Fig. 9a, respectively). For the synthetic saponite series with the general SF $(Si_{4-x}Al_x)(Mg_{(3-y)}Al_y)Na_{x-y}$ (with $0.33 \leq x \leq 1$ and $y = 0$ and 0.2, giving *R* of 0.720 and 0.708, respectively), Suquet *et al.* (1981) established the following relationship: $b = 9.174 + 0.079^{IV}Al - 0.07^{VI}Al$. Tetrahedral Al increases *b*, while octahedral Al decreases *b*. For $y = 0$, *x* corresponds to the layer charge and to the ^{IV}Al content, and *b* increases linearly with it (Fig. 10b). For $y = 0.2$, the variation appears to be non-rigorously linear (Fig. 10b). Unfortunately, without having strong confidence in the accurate ^{IV}Al and ^{VI}Al contents (Suquet *et al.*, 1977), we cannot discuss this matter further.

The vertical dot alignments are also observed on the $b/b_{tet.}$ *vs* *R* plot (Fig. 9b). Most of the samples lie below the (*P*–*T*)' line. Those that are the most above the line are synthetic samples that display $b/b_{tet.} > 1$ and are suspected to be erroneous. A small underestimation of the tetrahedral charge may induce a deviation from the (*P*–*T*)' line. For example, modifying the ^{IV}Al content from 0.46 to ~0.62 for sample A of Chemtob *et al.* (2015), which exhibits the greatest deviation, would place it on the (*P*–*T*)' line.

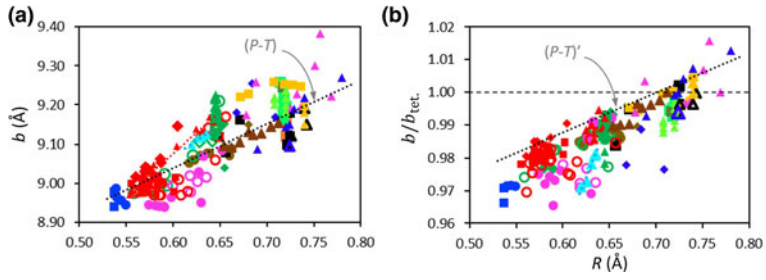

Figure 9. (A) *b* *vs* mean ionic radius of octahedral cations *R* for smectites (Table 5). (*P*–*T*) corresponds to the pyrophyllite–talc regression line (Fig. 8a). Triangles = synthetic smectites: red = $(SiAl)_4(Fe^{3+}_{(2-x)}Al_x)$; light blue = $(SiGa)_4(Fe^{3+}_{(2-x)}Ga_x)$; green = $(Si_{4-x}Fe^{3+}_x)Fe^{3+}_2$; brown = $(SiFe^{3+})_4(Fe^{3+}Mg)_y$; pink = Fe^{2+}-saponite series; light green = $(Si_{4-x}Al_x)(Mg_{(3-y)}Al_y)$; yellow = Zn-stevensite; dark blue = stevensite series; dark blue open symbol = hectorite; black open symbol = hectorite and Zn-hectorite. Other symbols = natural samples. Squares = samples from Radoslovich (1962): blue = beidellites; red = montmorillonites; green = nontronites; light green = saponites; yellow = sauconites; dark green = griffithite; black = hectorites; orange = stevensites; black = volkonskoites. Pink circles = samples from Brigatti (1983): open circles = nontronites; full circles = Al- and Fe^{3+} -montmorillonites. Green circles = dioctahedral smectites (Russell & Clark, 1978); red open circles = dioctahedral smectites (Tsipursky & Drits, 1984); blue circles = beidellites (Post *et al.*, 1997); brown circles = intermediary smectites (Gaudin *et al.*, 2004). Red diamonds = dioctahedral smectites (Heuser *et al.*, 2013); green diamonds = dioctahedral smectites (Köster *et al.*, 1999); open green diamonds = other nontronites; brown diamonds = other intermediary smectites; blue diamonds = vermiculites. (b) $b/b_{tet.}$ ratio *vs* the mean ionic radius of octahedral cations *R* for the same samples (and colour code) as (a). (*P*–*T*)' corresponds to the pyrophyllite–talc regression line derived from Fig. 8b.

https://doi.org/10.1180/clm.2023.20 Published online by Cambridge University Press

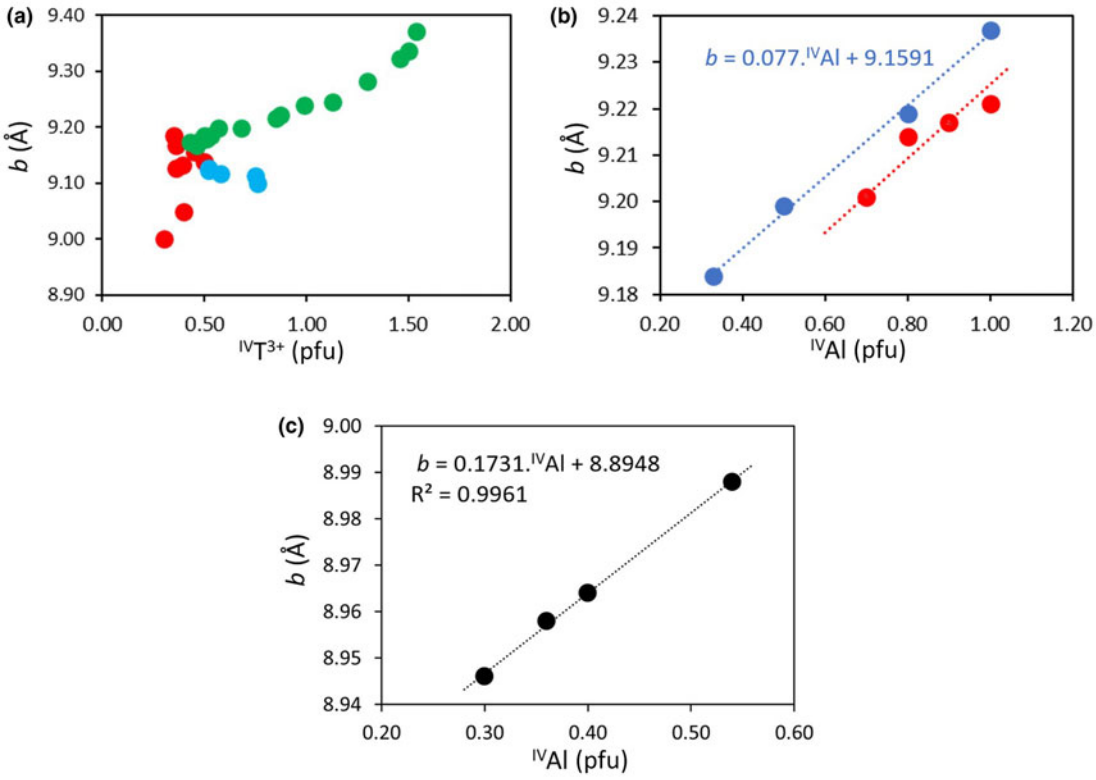

Figure 10. *b vs* tetrahedral substitution rate for selected smectites (Table 5). (a) Data for synthetic dioctahedral smectites series: red = $(SiAl)_4(Fe^{3+}_{(2-x)}Al_x$; Petit *et al.*, 2015); light blue = $(SiGa)_4(Fe^{3+}_{(2-x)}Ga_x$; Petit *et al.*, 2016); green = $(Si_{4-x}Fe^{3+}_x)Fe^{3+}_2$ (Baron *et al.*, 2016b). (b) Data for synthetic saponites (Suquet *et al.*, 1977), with blue circles representing the $y = 0$ series and red circles representing the $y = 0.2$ series (see text for details). (c) Data for natural beidellites (Post *et al.*, 1997).

The specific influence of the tetrahedral composition when *R* varies, even in a simple system, is difficult to measure. For the synthetic Al–Fe^{3+} smectitic series $(SiAl)_4(Fe^{3+}_{(2-x)}Al_x)$, with 0–1.66 Al and 0.34–2 Fe^{3+} (Table 5; Petit *et al.*, 2017), *b* increases with *R* (i.e. with increasing octahedral Fe^{3+}), with a greater slope compared to the (*P*–*T*) line (Fig. 9a). For this series, Petit *et al.* (2017) observed that tetrahedral substitutions were dominated by Al except when total Fe exceeded 1.8 pfu, and tetrahedral and octahedral Fe^{3+} had similar (and inseparable) effects on *b*. The specific role of tetrahedral Al could not be measured quantitatively (see the review of Petit *et al.*, 2017). A similar observation can be made for the Ga–Fe^{3+} smectitic series (Table 5), whose dots are also aligned on a slope greater than that of the regression (*P*–*T*) line (Fig. 9a) and whose *b* values were correlated with total Fe^{3+} (Petit *et al.* 2016). For these Ga–Fe^{3+} smectites, the great $b/b_{tet.}$ slope (Fig. 9b) is due to the combined effect of the increase in $b_{oct.}$ due to the relative increase in octahedral Fe^{3+} and the decrease in $b_{tet.}$ due to the decrease in tetrahedral Ga^{3+}. Various relations linking *b* with iron content are available in the literature for iron-rich natural smectites (e.g. Heuser *et al.*, 2013) and generally work well, at least when Fe^{3+} is the dominant cation. Brigatti (1983) observed a linear correlation between total iron and *b* but for $Fe^{3+} > 0.5$ pfu only.

For the natural beidellite sample series from Post *et al.* (1997), *b* does not follow the general (*P*–*T*) trend. Indeed, *b* decreases as *R* increases (dark blue circles in Fig. 9a), related to the fact that the *R* and Al contents of beidellites vary inversely. *b* increases linearly with increasing tetrahedral Al (Fig. 10c), resulting in $b/b_{tet.}$ values that are exactly the same for the four samples (0.9716 ± 0.0001; Fig. 9b). Such a $b/b_{tet.}$ value corresponds to an angle of tetrahedra rotation $\alpha \approx 13.7°$, which is within the range of that measured in aluminous dioctahedral TOT phyllosilicates (pyrophyllite and micas).

By analogy with the aforementioned other phyllosilicate structures, it is hypothesized that T sheets adjust their lateral dimensions *via* tetrahedral rotation to match those of the O sheet, and all the more so as they are further below the (*P*–*T*)' line (Fig. 9b).

The % O enlargement *vs R* plot reveals an excellent alignment of samples along the line determined for neutral TOT structures (Fig. 11), indicating that smectite samples follow closely the same trend as for P–T. However, it can be observed that samples that

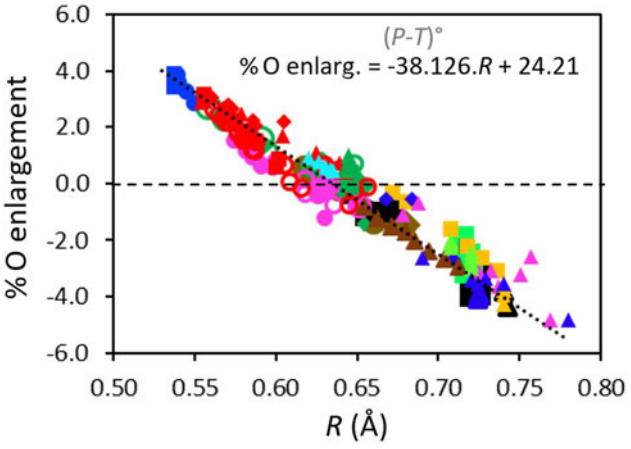

Figure 11. Evolution of the percentage of octahedral enlargement (Equation 6; see text for details) *vs R* for the same smectite samples (and colour code) as Fig. 9. (*P*–*T*)° corresponds to the pyrophyllite–talc regression (Fig. 8c).

https://doi.org/10.1180/clm.2023.20 Published online by Cambridge University Press

are above the line mainly have dominant tetrahedral charge (e.g. beidellites, nontronites, saponites, sauconites, vermiculites; Table 5). These samples are those located above the (*P*–*T*) line (Fig. 9a; i.e. with *b* values greater than they should be with regard to *R*). The thinning of O sheets *via* octahedral flattening is greater than in neutral phyllosilicates to facilitate dimensional congruency between the T and O sheets, with $b_{tet.}$ having greater values due to tetrahedral substitutions.

In a less pronounced manner, smectites with dominant octahedral layer charge (e.g. montmorillonites, stevensites, hectorites) are either below or on the (*P*–*T*) line (Fig. 11), similarly to the intermediary Fe^{3+}–Mg natural smectitic series (Gaudin *et al.*, 2004) and the Fe^{3+}–Mg synthetic series (Grauby *et al.*, 1994) that possess an almost constant layer charge from an octahedral origin. For samples located below the (*P*–*T*) line (Fig. 9a), *b* values are lower than they should be with regard to *R*, and it can be hypothesized that the flattening of octahedra is reduced compared to neutral TOT phyllosilicates.

When considering the whole series of samples, *R* covers the entire compositional range from dioctahedral to trioctahedral smectites, and, contrary to neutral TOT phyllosilicates, no compositional gaps could be observed (Figs 9 & 11). The possibility of having various tetrahedral compositions and balancing the negative layer charge with interlayer cations allows for a very wide range of compositions, including di-trioctahedral smectites. The variability in the chemistry and type of layer charge compensation, associated with the difficulty of accounting for the wide range of tetrahedral charges through $b/b_{tet.}$, make it inappropriate to propose a general regression correlating *b* to *R* for smectites. One may thus assume that the (*P*–*T*) correlation line can apply as a first-order relation, but with a greater degree of uncertainty compared to other mineral families. To go a step further, one could derive specific sub-correlations, as has been done for beidellites or saponites (Fig. 10b,c).

Micas

Micas are 2:1 phyllosilicates having a general SF similar to that of smectites but with a negative layer charge of ∼1 pfu (true micas) or ∼2 pfu (brittle micas), balanced by anhydrous monovalent interlayer cations (mostly K^+) in true micas and divalent interlayer cations (such as Ca^{2+} and Ba^{2+}) in brittle micas (Fig. 7). Illite, phengite, glauconite and, to a lesser extent, celadonite are non-expanding interlayer-deficient mica-like minerals. Isomorphic substitutions in O and T sheets and interlayer spaces vary and are used to define the complex nomenclature of micas and mica-like minerals (Bailey, 1984a; Brigatti *et al.*, 2013). Note that the substitution of OH^- by F^- is also common and complicates the system even more. Many names and varieties have been used previously, as can be seen for the sample series of Radoslovich & Norrish (1962; Table 6), sometimes erroneously (Bailey, 1984b; Rieder *et al.*, 1998). Several synthetic and natural sample series, which cover a very wide range of compositions, were considered in the present study (Table 6). The Al end member muscovite used here was issued from an average of 12 end-member synthetic muscovites (Guidotti *et al.*, 1992).

A global trend correlating *b* with increasing *R* was observed, with a strong scattering of data. The two main sub-correlations were plotted for more clarity (Fig. 12a): The muscovite–phlogopite (*M*–*Ph*) line $(K(Si_3Al_1)(Al_{2-x}Mg_{3x/2})O_{10}(OH)_2)$, with the relation $b = 1.1478R + 8.3794$, calculated using the synthetic muscovite and phlogopite end member data ($x = 0$ and 2, respectively); and the phlogopite–annite (*Ph*–*A*) line $(K(Si_3Al_1)(Mg_{3-x}Fe^{2+}{}_x)O_{10}(OH)_2)$, with the relation $b = 2.3942R + 7.4821$, calculated using the synthetic phlogopite and annite end member data ($x = 0$ and 3, respectively; Table 7). Accordingly, the true micas with tetrahedral Al and K contents with the 0.8–1.2 pfu compositional window are located on or not far from these lines. The synthetic Mn-mica end member exhibits the greatest *R* and *b* values and is relatively close to the (*M*–*Ph*) line. By contrast, interlayer-deficient micas (^{IV}Al-poorest micaceous samples), Na-micas, brittle micas and synthetic ferri-annites and Ge-micas are generally located far from the (*M*–*Ph*) and (*Ph*–*A*) lines (Fig. 12a).

Data points for Li-bearing micas are scattered strongly (Fig. 12a). However, a deeper analysis of the data shows that *b* values decrease globally with increasing Li content (Fig. 13a), but increase with increasing ^{IV}Al content (Fig. 13b), with Li and tetrahedral Al being negatively correlated (Fig. 13c). These correlations illustrate the impact of Li content on *b* and that the chosen value for $r(^{VI}Li^+)$ used in the calculation of *R* is critical for these samples. The choice of a $r(^{VI}Li^+)$ value close to that of other octahedral cations (e.g. Mg or Fe^{2+}) can reduce the range of obtained *R*, whereas an increased contrast between $r(^{VI}Li^+)$ and that of other cations can lead to a spreading of the calculated *R* values. In the present case (Fig. 13d), the *b vs R* dataset appears more scattered for $r(^{VI}Li^+)$ at 0.76 Å than for lower $r(^{VI}Li^+)$ values (Fig. 13e), probably demonstrating an overestimation of the chosen $r(^{VI}Li^+)$ at 0.76 Å (Table 1; Shannon, 1976). The ionic sizes for Li cations in other coordination numbers, such as $r(^{IV}Li^+)$ and $r(^{V}Li^+)$, are 0.59 Å (Shannon, 1976) and 0.69 Å, respectively (Brown & Shannon, 1973). This could help us to enlarge the *R* window, but structural refinement of the studied micas excludes their occurrence (Brigatti *et al.*, 2000, 2001, 2007). As discussed above for Mn in groutite, Li octahedra are probably considerably distorted in Li-rich micas. However, the maximum distortion for octahedra in *M*–O bonds is limited to $\sim 10^{-3}$ Å (Brown & Shannon, 1973) and alone cannot account for the potential decrease in the $r(^{VI}Li^+)$ size. For Li-micas, the substitution of OH^- by F^- is common, and the value of $r(^{VI}Li^+) = 0.685$ Å, as in LiF, was tested and found to improve the correlation between *b* and *R* (Fig. 13e). Lowering the values of $r(^{VI}Li^+)$ gradually to $r(^{VI}Li^+) = 0.535$ Å further increases the regression coefficient (Fig. 13d–f). Radoslovich (1962) observed that for Li-micas, Li behaves similarly to Al with regard to the variation in *b* with composition, and he used $r(^{VI}Li^+) = 0.60$ Å. A low $r(^{VI}Li^+)$ is found in the Li_3AlF_6 perovskite-like structure, where ^{VI}Li–F bond lengths of 1.95 Å were measured (Jain *et al.*, 2013), leading to $r(^{VI}Li^+) = 0.62$ Å (with $r(F^-) = 1.33$ Å). By contrast, Weiss *et al.* (1985) found good agreement between the mean fictive ionic radii calculated from 66 refined crystal structures of micas, including Li-bearing ones, and the crystal radii of Shannon (1976). However, Bailey (1984b) observed that the relative ratio of large octahedra (especially Li^+ with the crystal radii of Shannon, 1976) over small octahedra measured using structural refinement is not always in agreement with the ratio of large to small octahedral cations present. In such a case, the ordering pattern with Li occurring both in small and large sites has been described in lepidolites, agreeing well with the suitability of a lower $r(^{VI}Li^+)$ value than that proposed by Shannon (1976). Regarding the correlative approach used in the present study, an estimated $r(^{VI}Li^+)$ of ∼0.6 Å is suggested to be adequate. Accordingly, the whole *b vs R* dataset shown in Fig. 12a can be replotted considering $r(^{VI}Li^+) = 0.6$ Å (Fig. 12b), and the data points for Li-micas are logically less scattered and

https://doi.org/10.1180/clm.2023.20 Published online by Cambridge University Press

Table 6. Data used for micas.

Mica (anhydrous composition)	Sample[a]	*R*	*b*	References	Comments
Synthetic mica					
$(Si_3Al_1)(Al_2)K$	2*M* muscovite	0.535	8.995	Yoder & Eugster (1955)	
$(Si_3Al_1)(Al_2)K$	Muscovite	0.535	8.992	Guidotti *et al.* (1992)	Average of 12 muscovites
				Radoslovich & Norrish (1962)	As named in the paper
$(Si_3Al_1)(Al_2)Na$	32	0.535	8.900		Paragonite
$(Si_3Al_1)(Mg_3)K$	27	0.720	9.204		Phlogopite
$(Si_3Al_1)(Mg_3)KF$	28	0.720	9.195		Fluorophlogopite
				Frondel & Ito (1966)	
$(Si_3Al_1)(Mn_3)K$	Mn-mica	0.830	9.37		
$(Si_3Al_1)(Zn_3)K$	Zn-mica	0.740	9.32		
Synthetic series $(Si_3Al_1)(Mg_{3-x}R^{2+}_x)K$				Hazen & Wones (1972)	
Mg_3	M#1	0.720	9.204		
Co_3	M#114	0.745	9.240		
Cu_3	M#29	0.730	9.238		
Ni_3	M#115	0.690	9.175		
$Mg_{2.5}Fe^{2+}_{0.5}$	0.169	0.730	9.230		
$Mg_{2.25}Fe^{2+}_{0.75}$	0.250	0.735	9.242		
$Mg_{1.94}Fe^{2+}_{1.06}$	0.352	0.741	9.260		
$Mg_{1,65}Fe^{2+}_{1.35}$	0.450	0.747	9.276		
$Mg_{1,35}Fe^{2+}_{1.65}$	0.550	0.753	9.285		
$Mg_{0.7}Fe^{2+}_{2.3}$	0.765	0.766	9.312		
$Mg_{0.36}Fe^{2+}_{2.64}$	0.880	0.773	9.335		
Fe^{2+}_3	Fe^{2+}_3	0.780	9.347		
Synthetic series $(Si_{3-z}Al_{1+z})(Mg_xFe^{2+}{}_yAl_z)K$				Hewitt & Wones (1975)	
$(Si_3Al)(Mg_3)$	222-69	0.720	9.206		
$(Si_3Al_1)(Mg_{2.25}Fe^{2+}_{0.75})$	45-73	0.735	9.243		
$(Si_3Al_1)(Mg_{2.01}Fe^{2+}_{0.99})$	40-73	0.740	9.253		
$(Si_3Al_1)(Mg_{1.50}Fe^{2+}_{1.50})$	53-73	0.750	9.280		
$(Si_3Al_1)(Mg_{0.75}Fe^{2+}_{2.25})$	68-73	0.765	9.312		
$(Si_3Al_1)(Fe^{2+}_3)$	142-70	0.780	9.352		
$(Si_{2.87}Al_{1.13})(Fe^{2+}_{2.87}Al_{0.13})$	67-73	0.770	9.339		
$(Si_{2.83}Al_{1.17})(Mg_{2.83}Al_{0.17})$	55-73	0.710	9.193		
$(Si_{2.75}Al_{1.25})(Mg_{2.75}Al_{0.25})$	189-70	0.705	9.191		
$(Si_{2.75}Al_{1.25})(Mg_{2.06}Fe^{2+}_{0.69}Al_{0.25})$	28-73	0.718	9.230		
$(Si_{2.75}Al_{1.25})(Mg_{1.375}Fe^{2+}_{1.375}Al_{0.25})$	29-73	0.732	9.267		
$(Si_{2.75}Al_{1.25})(Mg_{0.69}Fe^{2+}_{2.06}Al_{0.25})$	11-72	0.746	9.301		
$(Si_{2.75}Al_{1.25})(Fe^{2+}_{2.75}Al_{0.25})$	143-70	0.760	9.336		
$(Si_{2.62}Al_{1.38})(Fe^{2+}_{2.62}Al_{0.38})$	4-72	0.749	9.325		
$(Si_{2.50}Al_{1.50})(Mg_{2.50}Al_{0.50})$	224-69	0.689	9.170		
$(Si_{2.50}Al_{1.50})(Mg_{1.95}Fe^{2+}_{0.55}Al_{0.50})$	153-70	0.700	9.201		
$(Si_{2.50}Al_{1.50})(Mg_{1.88}Fe^{2+}_{0.62}Al_{0.50})$	26634	0.702	9.207		
$(Si_{2.50}Al_{1.50})(Mg_{1.25}Fe^{2+}_{1.25}Al_{0.50})$	13-72	0.714	9.240		
$(Si_{2.50}Al_{1.50})(Mg_{1.10}Fe^{2+}_{1.40}Al_{0.50})$	193-70	0.717	9.251		
$(Si_{2.50}Al_{1.50})(Mg_{0.70}Fe^{2+}_{1.80}Al_{0.50})$	152-70	0.725	9.271		
$(Si_{2.50}Al_{1.50})(Mg_{0.625}Fe^{2+}_{1.875}Al_{0.50})$	14-72	0.727	9.279		
$(Si_{2.50}Al_{1.50})(Fe^{2+}_{2.50}Al_{0.50})$	38-73	0.739	9.312		
$(Si_{2.37}Al_{1.63})(Fe^{2+}_{2.37}Al_{0.63})$	6-72	0.729	9.295		
$(Si_{2.37}Al_{1.63})(Mg_{2.37}Al_{0.63})$	179-70	0.681	9.164		
$(Si_{2.25}Al_{1.75})(Mg_{1.69}Fe^{2+}_{0.56}Al_{0.75})$	15-72	0.685	9.190		
$(Si_{2.25}Al_{1.75})(Mg_{1.125}Fe^{2+}_{1.125}Al_{0.75})$	16-72	0.696	9.225		
$(Si_{2.25}Al_{1.75})(Mg_{0.56}Fe^{2+}_{1.69}Al_{0.75})$	17-72	0.708	9.261		
$(Si_{2.25}Al_{1.75})(Fe^{2+}_{2.25}Al_{0.75})$	7-72	0.719	9.287		
Synthetic series $(SiAl)_4(Fe^{2+}Fe^{3}Mg)_3K$	*P* (bar); *T* (°C)			Wones & Eugster (1965)	
$Mg_{2.1}Fe^{2+}_{0.48}Fe^{3+}_{0.42}$	1035; 850	0.719	9.238		
$Mg_{1.95}Fe^{2+}_{0.60}Fe^{3+}_{0.45}$	1035; 750	0.721	9.238		
$Mg_{2.19}Fe^{2+}_{0.42}Fe^{3+}_{0.39}$	2070; 900	0.719	9.233		
$Mg_{1.95}Fe^{2+}_{0.60}Fe^{3+}_{0.45}$	2070; 800	0.721	9.238		
$Mg_{1.59}Fe^{2+}_{1.26}Fe^{3+}_{0.15}$	1035; 800	0.741	9.262		
$Mg_{0.93}Fe^{2+}_{1.86}Fe^{3+}_{0.21}$	1035; 700	0.752	9.296		
$Mg_{1.32}Fe^{2+}_{1.50}Fe^{3+}_{0.18}$	2070; 800	0.746	9.281		
Synthetic series $(Si_{4-x}Al_x)(Mg_yAl_z)K$				Robert (1976)	
$(Si_3Al)Mg_3$	1	0.720	9.209		
$(Si_{2.875}Al_{1.125})(Mg_{2.875}Al_{0.125})$	2	0.712	9.206		
$(Si_{2.825}Al_{1.175})(Mg_{2.825}Al_{0.175})$	3	0.709	9.201		

(*Continued*)

https://doi.org/10.1180/clm.2023.20 Published online by Cambridge University Press

Table 6. (*Continued.*)

Mica (anhydrous composition)	Sample[a]	*R*	*b*	References	Comments
$(Si_{2.775}Al_{1.225})(Mg_{2.775}Al_{0.225})$	4	0.706	9.199		
$(Si_{2.750}Al_{1.250})(Mg_{2.750}Al_{0.250})$	5	0.705	9.198		
$(Si_{2.625}Al_{1.375})(Mg_{2.625}Al_{0.375})$	6	0.697	9.191		
$(Si_{2.500}Al_{1.500})(Mg_{2.500}Al_{0.500})$	7	0.689	9.185		
$(Si_{2.812}Al_{1.188})(Mg_{2.738}Al_{0.238})$	8	0.705	9.195		
$(Si_{2.925}Al_{1.075})(Mg_{2.715}Al_{0.215})$	9	0.706	9.191		
$(Si_{2.575}Al_{1.425})(Mg_{2.500}Al_{0.475})$	10	0.690	9.173		
$(Si_{2.650}Al_{1.350})(Mg_{2.500}Al_{0.450})$	11	0.692	9.182		
$(Si_{2.725}Al_{1.275})(Mg_{2.500}Al_{0.425})$	12	0.693	9.186		
$(Si_{2.800}Al_{1.200})(Mg_{2.500}Al_{0.400})$	13	0.694	9.187		
$(Si_{2.775}Al_{1.225})(Mg_{2.325}Al_{0.525})$	14	0.686	9.171		
$(Si_{2.862}Al_{1.138})(Mg_{2.338}Al_{0.488})$	15	0.688	9.172		
$(Si_{2.687}Al_{1.313})(Mg_{2.313}Al_{0.563})$	16	0.684	9.168		
$(Si_{2.600}Al_{1.400})(Mg_{2.300}Al_{0.600})$	17	0.682	9.165		
$(Si_{2.512}Al_{1.488})(Mg_{2.288}Al_{0.638})$	18	0.680	9.162		
$(Si_{2.425}Al_{1.575})(Mg_{2.275}Al_{0.675})$	19	0.678	9.159		
$(Si_{2.400}Al_{1.600})(Mg_{2.100}Al_{0.800})$	20	0.671	9.160		
$(Si_{2.500}Al_{1.500})(Mg_{2.125}Al_{0.750})$[b]	21	0.672	9.162		
$(Si_{2.600}Al_{1.400})(Mg_{2.150}Al_{0.700})$	22	0.675	9.163		
$(Si_{2.700}Al_{1.300})(Mg_{2.175}Al_{0.650})$	23	0.677	9.168		
$(Si_{2.537}Al_{1.463})(Mg_{2.013}Al_{0.813})$	24	0.667	9.155		
$(Si_{2.650}Al_{1.350})(Mg_{2.050}Al_{0.750})$	25	0.670	9.150		
$(Si_{2.762}Al_{1.238})(Mg_{2.088}Al_{0.688})$	26	0.674	9.155		
$(Si_{2.625}Al_{1.375})(Mg_{1.950}Al_{0.825})$	27	0.665	9.150		
$(Si_{2.750}Al_{1.250})(Mg_{2.000}Al_{0.750})$	28	0.670	9.155		
$(Si_4)(Mg_{2.5})$	29	0.720	9.108		
Synthetic K-micas				Redhammer & Roth (2002)	
$(Si_{2.92}Al_{1.08})(Ni_3Al_{0.04})$	NiPhl	0.688	9.180		
$(Si_{2.92}Al_{1.08})(Mg_{2.98}Al_{0.03})$	Phl	0.718	9.204		
$(Si_3Ga)(Mg_3)$	GaPhl	0.720	9.214		
$(Si_{2.91}Al_{1.09})(Co_{2.94}Al_{0.06})$	CoAn	0.741	9.247		
$(Si_{2.91}Al_{1.09})(Mg_{2.68}Fe^{2+}_{0.33}Al_{0.03})$	A20#2	0.725	9.225		
$(Si_{2.91}Al_{1.09})(Mg_{2.68}Fe^{2+}_{0.33}Al_{0.03})$	A20#4	0.725	9.225		
$(Si_{2.96}Al_{1.04})(Mg_{2.45}Fe^{2+}_{0.53}Al_{0.03})$	A40	0.729	9.231		
$(Si_{2.91}Al_{1.09})(Mg_{2.35}Fe^{2+}_{0.68}Al_{0.01})$	A60	0.733	9.247		
$(Si_{2.97}Al_{1.03})(Mg_{2.19}Fe^{2+}_{0.82}Al_{0.01})$	Mga1.2	0.736	9.254		
$(Si_{2.94}Al_{1.06})(Mg_{2.51}Fe^{2+}_{0.50}Al_{0.01})$	Mga1.6	0.729	9.224		
$(Si_{2.91}Al_{1.09})(Co_{1.67}Ni_{1.32}Al_{0.04})$	CoNi1.8	0.718	9.220		
$(Si_{2.28}Al_{1.72})(Al_{0.79}Fe^{2+}_{2.18})$	Sd87	0.715	9.289		
Synthetic K-(Si_3Al_1)-micas (octahedral composition)				Mercier *et al.* (2005)	Structure refined
	JLRMgCo				
$(Co_{0.3}Mg_{2.7})$	0.3	0.723	9.206		
$(Co_{0.6}Mg_{2.4})$	0.60	0.725	9.205		
$(Co_{0.6}Mg_{2.4})$	0.60	0.725	9.211		
$(Co_{0.9}Mg_{2.1})$	0.90	0.728	9.212		
$(Co_{1.2}Mg_{1.8})$	1.2	0.730	9.216		
$(Co_{1.5}Mg_{1.5})$	1.5	0.733	9.218		
$(Co_{1.8}Mg_{1.2})$	1.8	0.735	9.227		
$(Co_{2.1}Mg_{0.9})$	2.1	0.738	9.237		
$(Co_{2.4}Mg_{0.6})$	2.4	0.740	9.234		
$(Co_{2.4}Mg_{0.6})$	2.4	0.740	9.238		
$(Co_{2.7}Mg_{0.3})$	2.7	0.743	9.244		
(Co_3)	3	0.745	9.247		
	JLRMgFe				
(Mg_3)	0	0.720	9.204		
$(Fe_{0.6}Mg_{2.4})$	0.6	0.732	9.223		
$(Fe_{1.2}Mg_{1.8})$	1.2	0.744	9.254		
$(Fe_{1.2}Mg_{1.8})$	1.2	0.744	9.262		
$(Fe_{1.8}Mg_{1.2})$	1.8	0.756	9.295		
$(Fe_{2.4}Mg_{0.6})$	2.4	0.768	9.310		
(Fe_3)	3	0.780	9.350		
	FeNiGR				
(Ni_3)	3	0.690	9.177		
$(Fe_{0.2}Ni_{2.8})$	2.8	0.696	9.191		
$(Fe_{0.6}Ni_{2.4})$	2.4	0.708	9.213		
(Fe_1Ni_2)	2	0.720	9.242		
$(Fe_{1.4}Ni_{1.6})$	1.6	0.732	9.261		
$(Fe_{1.8}Ni_{1.2})$	1.2	0.744	9.285		
$(Fe_{2.2}Ni_{0.8})$	0.8	0.756	9.308		

(*Continued*)

https://doi.org/10.1180/clm.2023.20 Published online by Cambridge University Press

Table 6. (*Continued.*)

Mica (anhydrous composition)	Sample[a]	*R*	*b*	References	Comments
$(Fe_{2.6}Ni_{0.4})$	0.4	0.768	9.329		
Synthetic 2M$_1$ K-mica series				Zviagina & Drits (2019)	Selected data from Schmidt *et al.* (2001)
$(Si_{3.987}Al_{0.013})(Al_{1.021}Mg_{0.974})$	P13-1	0.625	9.016		
$(Si_{3.947}Al_{0.053})(Al_{1.053}Mg_{0.957})$	P17	0.623	9.019		
$(Si_{3.823}Al_{0.177})(Al_{1.135}Mg_{0.838})$	P11-2	0.614	9.021		
$(Si_{3.817}Al_{0.183})(Al_{1.187}Mg_{0.809})$	P18-2	0.610	9.028		
$(Si_{3.662}Al_{0.338})(Al_{1.341}Mg_{0.662})$	P12-1	0.596	9.032		
$(Si_{3.642}Al_{0.358})(Al_{1.352}Mg_{0.654})$	P15	0.595	9.031		
$(Si_{3.478}Al_{0.522})(Al_{1.574}Mg_{0.416})$	P28	0.574	9.024		
$(Si_{3.401}Al_{0.599})(Al_{1.578}Mg_{0.442})$	P25	0.575	9.026		
$(Si_{3.288}Al_{0.712})(Al_{1.708}Mg_{0.308})$	P33	0.563	9.022		
$(Si_{3.219}Al_{0.781})(Al_{1.770}Mg_{0.249})$	P30	0.558	9.015		
$(Si_{3.176}Al_{0.824})(Al_{1.773}Mg_{0.292})$	P26	0.561	9.025		
$(Si_{3.124}Al_{0.876})(Al_{1.918}Mg_{0.108})$	P31	0.545	8.998		
$(Si_{3.113}Al_{0.887})(Al_{1.908}Mg_{0.097})$	P29	0.544	8.997		
$(Si_{3.81}Al_{0.19})(Al_{1.21}Mg_{0.75}Fe^{2+}_{0.04})$	2M_1 Al-celadonite	0.609	9.037		
Various synthetic micas (collected data) – K as the main interlayer cation if not specified				Brigatti & Guggenheim (2002)	Structure refined
$(Si_{3.45}Al_{0.55})(Al_{1.88})Na_{0.91}$	2	0.535	8.890		Paragonite
$(Si_{2.84}Al_{1.16})(Li_{0.77}Mg_{2.23})Ba_{0.97}F_{2.08}$	15	0.730	9.157		Lithian kinoshitaite
$(Si_{3.07}Al_{0.03}Fe^{3+}_{0.90})(Fe^{2+}_{2.97}Fe^{3+}_{0.03})Cs_{0.89}$	60	0.779	9.506		Caesium tetra-ferri-annite
$(Si_{3.0}Fe^{3+}_{1.0})(Fe^{2+}_{3.0})$	61	0.780	9.404		Tetra-ferri-annite
$(Si_{2.98}Al_{1.02})(Mg_{2.97})F_{2.08}$	72	0.720	9.183		Fluoro-phlogopite
$(Si_{4.0})(Li_{2.0}\ Al_{1.0})F_{2.0}$	96	0.685	8.968		Polylithionite
$(Si_{3.25}\ Al_{0.75})(Mg_{2.80}Li_{0.20})F_{2.0}$	97	0.723	9.210		Li-containing phlogopite
$(Si_{2.98}\ Al_{1.02})(Mg_{2.97})F_{1.94}$	98	0.720	9.195		Fluoro-phlogopite
$(Ge_{3.0}\ Al_{1.0})(Mg_{1.04}Mn_{1.946})F_{2.0}$	102	0.775	9.509		Tetra-Ge–Mn–F phlogopite
$(Ge_{3.0}\ Al_{1.0})(Mg_{2.36}Mn_{0.64}\ Al_{1.0})F_{2.0}$	103	0.743	9.413		Tetra-Ge–Mn–F phlogopite
$(Si_{4.0})(Mg_{2.50})F_{2.0}$	104	0.720	9.086		Tetrasilicic–F phlogopite
$(Si_{4.0})(Mg_{2.0}Li_{1.0})F_{2.0}$	105	0.733	9.065		Tainiolite
$(Ge_{4.0})(Mg_{2.5})F_{2.0}$	106	0.720	9.353		Tetra-Ge–F phlogopite
$(Ge_{4.0})(Mg_{2.0}\ Li_{1.0})F_{2.0}$	107	0.733	9.341		Tetra-Ge tainiolite
$(Si_{3.50}\ Al_{0.50})(Mg_{2.75})F_{2.0}$	108	0.720	9.164		Fluoro-phlogopite
$(Ge_{3.0}\ Al_{1.0})(Mg_{3.0})F_{2.0}$	109	0.720	9.345		Tetra-Ge–F phlogopite
$(Si_{2.82}\ Mn_{0.18})(Mg_{2.44}Mn_{0.24})F_{2.0}$	110	0.728	9.157		Fluoro-phlogopite
Natural micas (anhydrous composition – K as the main interlayer cation if not specified)					
Muscovites and phengites				Zviagina & Drits (2019)	
$(Si_{3.12}Al_{0.88})(Al_{1.88}Fe^{2+}_{0.14}Mg_{0.01})$	1 – muscovite 2M_1	0.553	9.016		
$(Si_{3.06}Al_{0.94})(Al_{1.72}Fe^{3+}_{0.15}Mg_{0.10}Ti_{0.02}Mn^{3+}_{0.02})$	2 – muscovite 2M_1	0.548	9.018		
$(Si_{3.16}Al_{0.84})(Al_{1.84}Fe^{3+}_{0.06}Fe^{2+}_{0.01}Mg_{0.10})$	3 – muscovite 2M_1	0.548	9.000		
$(Si_{3.102}Al_{0.98})(Al_{1.90}Fe^{3+}_{0.02}Fe^{2+}_{0.05}Mg_{0.06}Ti_{0.01})$	4 – muscovite 2M_1	0.548	9.008		
$(Si_{3.10}Al_{0.90})(Al_{1.83}Fe^{2+}_{0.16}Mg_{0.01})$	5 – muscovite 2M_1	0.556	9.021		
$(Si_{3.11}Al_{0.89})(Al_{1.86}Fe^{2+}_{0.04}Mg_{0.08}Cr_{0.06})$	6 – muscovite 2M_1	0.549	9.011		
$(Si_{3.09}Al_{0.91})(Al_{1.83}Fe^{2+}_{0.07}Mg_{0.06})$	7 – muscovite 2M_1	0.552	9.004		
$(Si_{3.07}Al_{0.93})(Al_{1.88}Fe^{2+}_{0.07}Mg_{0.06}Ti_{0.03})$	8 – muscovite 2M_1	0.550	8.996		
$(Si_{3.03}Al_{0.97})(Al_{1.86}Fe^{3+}_{0.01}Fe^{2+}_{0.06}Mg_{0.07}Ti_{0.02})$	9 – muscovite 2M_1	0.550	9.013		
$(Si_{3.09}Al_{0.91})(Al_{1.71}Fe^{3+}_{0.16}Fe^{2+}_{0.13}Mn^{2+}_{0.01})$	10 – muscovite 2M_1	0.561	9.035		
$(Si_{3.2.92}Al_{1.08})(Al_{1.88}Fe^{3+}_{0.09}Mg_{0.05}Ti_{0.02})$	11 – muscovite 2M_1	0.545	8.991		
$(Si_{3.18}Al_{0.82})(Al_{1.64}Fe^{3+}_{0.08}Fe^{2+}_{0.08}Mg_{0.16}Ti_{0.02})$	12 – muscovite 2M_1	0.565	9.022		
$(Si_{3.018}Al_{0.82})(Al_{1.78}Fe^{2+}_{0.12}Mg_{0.06}Ti_{0.04})$	13 – muscovite 2M_1	0.557	8.982		
$(Si_{3.30}Al_{0.70})(Al_{1.65}Fe^{2+}_{0.29}Ti_{0.01}Mn^{2+}_{0.07})$	14 – Fe-rich muscovite 2M_1	0.581	9.074		
$(Si_{3.26}Al_{0.74})(Al_{1.67}Fe^{2+}_{0.34}Mg_{0.04})$	15 – Fe-rich muscovite 2M_1	0.579	9.052		
$(Si_{3.25}Al_{0.75})(Al_{1.51}Fe^{2+}_{0.15}Mg_{0.27}Ti_{0.01}Cr_{0.09})$	16 – Mg-rich muscovite 2M_1	0.582	9.043		
$(Si_{3.38}Al_{0.62})(Al_{1.55}Fe^{2+}_{0.21}Mg_{0.24}Ti_{0.02})$	17 – phengite 2M_1	0.583	9.051		
$(Si_{3.45}Al_{0.55})(Al_{1.42}Fe^{2+}_{0.24}Mg_{0.33}Ti_{0.04})$	18 – phengite 2M_1	0.595	9.057		
Dioctahedral true micas (collected data)				Brigatti & Guggenheim (2002)	Single crystal refinement structure
	1*M* space group *C2*				
$(Si_{3.51}Al_{0.49})(Al_{1.83}Fe^{3+}_{0.03}Fe^{2+}_{0.04}Mg_{0.10}Mn_{0.04})$	1	0.556	8.952		Muscovite
	1*M* space group *C2/c*				Muscovite
$(Si_{3.11}Al_{0.89})(Al_{1.83}Fe^{3+}_{0.12}Fe^{2+}_{0.36}Mg_{0.06})$	4	0.547	8.996		Muscovite
$(Si_{3.30}Al_{0.70})(Al_{1.65}Fe^{2+}_{0.29}Mn_{0.07}Ti_{0.01})F_{0.22}$	5	0.581	9.074		Muscovite
$(Si_{3.18}Al_{0.82})(Al_{1.78}Fe^{2+}_{0.12}Mg_{0.06}Ti_{0.04})$	6	0.557	8.982		Muscovite

(*Continued*)

https://doi.org/10.1180/clm.2023.20 Published online by Cambridge University Press

Table 6. (*Continued.*)

Mica (anhydrous composition)	Sample[a]	*R*	*b*	References	Comments
$(Si_{2.92}Al_{1.08})(Al_{1.88}Fe^{3+}_{0.09}Mg_{0.03}Ti_{0.02})F_{0.11}$	7	0.545	8.991		Muscovite
$(Si_{3.03}Al_{0.97})(Al_{1.86}Fe^{3+}_{0.01}Fe^{2+}_{0.06}Mg_{0.07}Ti_{0.02})$	8	0.550	9.013		Muscovite
$(Si_{3.09}Al_{0.91})(Al_{1.71}Fe^{3+}_{0.16}Fe^{2+}_{0.13}Mn_{0.01})F_{0.22}$	9	0.561	9.035		Muscovite
$(Si_{3.18}Al_{0.82})(Al_{1.83}Fe^{2+}_{0.07}Mg_{0.07}Ti_{0.06})$	10	0.552	9.005		Muscovite
$(Si_{3.07}Al_{0.93})(Al_{1.88}Fe^{2+}_{0.07}Mg_{0.06}Ti_{0.03})F_{0.19}$	11	0.550	8.996		Muscovite
$(Si_{3.09}Al_{0.91})(Al_{1.83}Fe^{2+}_{0.07}Mg_{0.07}Ti_{0.06})F_{0.23}$	12	0.552	9.004		Muscovite
$(Si_{3.17}Al_{0.83})(Al_{1.78}Fe^{2+}_{0.13}Mg_{0.15}Ti_{0.04})F_{0.19}$	13	0.565	9.003		Muscovite
$(Si_{2.87}Al_{1.13})(Al_{1.80}Fe^{2+}_{0.07}Mg_{0.15}Ti_{0.05})F_{0.41}$	14	0.558	8.997		Muscovite
$(Si_{3.18}Al_{0.82})(Al_{1.64}Fe^{3+}_{0.08}Fe^{2+}_{0.08}Mg_{0.16}Ti_{0.04})$	15	0.565	9.022		Muscovite
$(Si_{3.11}Al_{0.89})(Al_{1.86}Cr_{0.06}Fe^{2+}_{0.04}Mg_{0.08}Ti_{0.04})$	16	0.550	9.011		Cr-containing muscovite
$(Si_{3.07}Al_{0.93})(Al_{1.84}Cr_{0.10}Fe^{2+}_{0.02}Mg_{0.02}Ti_{0.02})$	17	0.544	8.979		Cr-containing muscovite
$(Si_{3.14}Al_{0.86})(Al_{1.83}Cr_{0.11}Fe^{2+}_{0.10}Mg_{0.11}Ti_{0.03})$	18	0.561	9.040		Cr-containing muscovite
$(Si_{3.02}Al_{0.98})(Al_{0.27}Cr_{1.42}Fe^{2+}_{0.01}Mg_{0.18}V_{0.13})F_{0.30}$	30	0.616	9.103		Chromphyllite
$(Si_{3.09}Al_{0.91})(Al_{1.93}Fe^{2+}_{0.01}Mg_{0.01}Mn_{0.01})\ F_{0.12}$	33	0.539	8.950		Muscovite
$(Si_{3.02}Al_{0.98})(Al_{1.90}Fe^{3+}_{0.02}Fe^{2+}_{0.05}Mg_{0.06}Ti_{0.02})$	36	0.548	9.008		Muscovite
$(Si_{3.39}Al_{0.61})(Al_{1.45}Fe^{3+}_{0.05}Fe^{2+}_{0.09}Mg_{0.50}Ti_{0.01})$	37	0.593	9.038		Magnesian muscovite
$(Si_{2.94}Al_{1.06})(Al_{1.99}Fe_{0.03}Mg_{0.01}Ti_{0.003})(K_{0.04}Na_{0.92}Ca_{0.02})$	39	0.538	8.898		Paragonite
$(Si_{3.01}Al_{0.68}Fe^{3+}_{0.14})(Al_{1.87}Mn^{3+}_{0.03}Mg_{0.06}Ti_{0.01})F_{0.14}$	45	0.542	9.027		Muscovite
$(Si_{3.09}Al_{0.91})(Al_{1.81}Fe^{2+}_{0.14}Mg_{0.12})F_{0.19}$	46	0.562	9.015		Muscovite
$(Si_{2.98}Al_{1.02})(Al_{1.93}Fe^{2+}_{0.02}Mg_{0.10})(K_{0.10}Na_{0.60}Ca_{0.03})$	48	0.546	8.894		Paragonite
	$2M_2$ space group *C2/c*				
$(Si_{3.16}Al_{0.84})(Al_{1.64}Fe^{2+}_{0.17}Mg_{0.22}Li_{0.15})(K_{0.06}Cs_{0.88}Rb_{0.01})F_{0.21}$	49	0.588	9.076		Nanpingite
	3*T* space group $P3_112$				
$(Si_{3.34}Al_{0.56})(Al_{1.54}Fe_{0.25}Mg_{0.21}Ti_{0.04})$	51	0.563	9.028		Muscovite
$(Si_{3.54}Al_{0.46})(Al_{1.41}Mg_{0.60}Ti_{0.02})$	52	0.590	9.033		Magnesian muscovite
$(Si_{3.11}Al_{0.89})(Al_{1.c04}Fe^{2+}_{0.04}Mg_{0.09}Ti_{0.01})$	53	0.551	9.000		Muscovite
$(Si_{2.96}Al_{1.04})(Al_{2.02}Fe^{3+}_{0.01}Mg_{0.01})(K_{0.16}Na_{0.71}Ca_{0.03})$	54	0.536	8.889		Paragonite
Dioctahedral brittle micas (collected data)	$2M_1$ space group *Cc*				
$(Si_{2.11}Al_{1.89})(Al_{1.99}Fe^{2+}_{0.01}Mg_{0.03})Ca_{0.81}Na_{0.19}$	19	0.539	8.828		Margarite
$(Si_{1.92}Al_{2.08})(Al_{1.96}Fe_{0.03}Mg_{0.10}Li_{0.12})Ca_{0.73}Na_{0.23}$	21	0.557	8.857		Margarite
Trioctahedral true micas (collected data)					
	1*M* space group *C2/m*				
$(Si_{2.74}Al_{1.26})(Al_{0.24}Fe^{3+}_{0.009}Fe^{2+}_{0.12}Mg_{2.48}Mn_{0.01}Ti_{0.02})$	1	0.705	9.195		Phlogopite
$(Si_{2.65}Al_{1.35})(Al_{0.24}Fe^{3+}_{0.007}Fe^{2+}_{0.11}Mg_{2.55}Mn_{0.01}Ti_{0.02})$	2	0.705	9.180		Phlogopite
$(Si_{2.60}Al_{1.40})(Al_{0.18}Fe^{3+}_{0.15}Fe^{2+}_{0.03}Mg_{2.63}Ti_{0.01})$	3	0.705	9.189		Phlogopite
$(Si_{2.50}Al_{1.50})(Al_{0.47}Fe^{3+}_{0.15}Fe^{2+}_{0.07}Mg_{2.23}Mn_{0.04}Ti_{0.01})$	4	0.692	8.179		Al-phlogopite
$(Si_{2.60}Al_{1.40})(Al_{0.20}Fe^{3+}_{0.11}Fe^{2+}_{0.04}Mg_{2.64}Mn_{0.01})$	5	0.706	9.199		Phlogopite
$(Si_{2.81}Al_{1.39})(Al_{0.05}Fe^{3+}_{0.50}Fe^{2+}_{0.70}Mg_{1.54}Mn_{0.02}Ti_{0.20})$	6	0.712	9.244		Ferroan phlogopite
$(Si_{2.50}Al_{1.37}Fe^{3+}_{0.13})(Fe^{2+}_{1.05}\ Mg_{0.92}Mn_{0.01}Ti_{0.67})$	7	0.715	9.244		Magnesian annite
$(Si_{2.78}Al_{1.19}Fe^{3+}_{0.03})(Fe^{3+}_{0.45}Fe^{2+}_{0.79}Mg_{1.43}Mn_{0.01}Ti_{0.23}Li_{0.01})$	8	0.717	9.258		Ferroan phlogopite
$(Si_{2.80}Al_{1.20})(Al_{0.01}Fe^{3+}_{0.46}Fe^{2+}_{0.71}Mg_{1.50}Mn_{0.03}Ti_{0.15}Li_{0.01})$	9	0.719	9.353		Ferroan phlogopite
$(Si_{2.79}Al_{1.21})(Al_{0.05}Fe^{3+}_{0.39}Fe^{2+}_{0.95}Mg_{1.35}Mn_{0.03}Ti_{0.20}Li_{0.01})$	10	0.695	9.242		Ferroan phlogopite
$(Si_{2.74}Al_{1.26})(Al_{0.02}Fe^{3+}_{0.36}Fe^{2+}_{0.86}Mg_{1.39}Mn_{0.02}Ti_{0.25}Li_{0.01})$	11	0.718	9.258		Ferroan phlogopite
$(Si_{2.85}Al_{1.15})(Al_{0.05}Fe^{3+}_{0.34}Fe^{2+}_{0.91}Mg_{1.35}Mn_{0.03}Ti_{0.23}Li_{0.02})$	12	0.718	9.251		Ferroan phlogopite
$(Si_{2.94}Al_{1.06})(Al_{0.01}Fe^{3+}_{0.18}Fe^{2+}_{0.06}Mg_{2.33}Mn_{0.01}Ti_{0.41})F_{0.79}$	13	0.700	9.207		Titanian phlogopite
$(Si_{2.68}Al_{1.32})(Al_{0.93}Fe^{3+}_{0.41}Fe^{2+}_{0.39}Mg_{1.10}Mn_{0.03}Ti_{0.14})$	14	0.656	9.219		Al-phlogopite
$(Si_{2.68}Al_{1.32})(Al_{0.14}Fe^{3+}_{0.38}Fe^{2+}_{0.31}Mg_{2.00}Mn_{0.01}Ti_{0.17})$	15	0.702	9.222		Ferrian phlogopite
$(Si_{3.25}Al_{0.75})(Fe^{2+}_{0.74}Mg_{1.70}Mn_{0.01}Ti_{0.49})F_{0.31}$	16	0.716	9.245		Ferroan phlogopite
$(Si_{2.75}Al_{1.25})(Al_{0.02}Fe^{3+}_{0.39}Fe^{2+}_{0.60}Mg_{1.61}Mn_{0.01}Ti_{0.37})F_{0.23}$	17	0.707	9.230		Ferroan phlogopite
$(Si_{2.65}Al_{1.35})(Al_{0.12}Fe^{3+}_{0.47}Fe^{2+}_{0.42}Mg_{1.85}Mn_{0.01}Ti_{0.14})$	18	0.704	9.219		Ferrian phlogopite
$(Si_{2.62}Al_{1.38})(Al_{0.13}Fe^{3+}_{0.72}Fe^{2+}_{0.30}Mg_{1.67}Mn_{0.01}Ti_{0.18})$	19	0.701	9.224		Ferrian phlogopite
$(Si_{2.59}Al_{1.41})(Al_{0.24}Fe^{3+}_{0.23}Fe^{2+}_{0.76}Mg_{1.58}Ti_{0.17})$	20	0.708	9.241		Ferroan phlogopite
$(Si_{2.86}Al_{1.14})(Al_{0.22}Cr_{0.05}Fe^{2+}_{0.39}Mg_{2.17}Mn_{0.02}Ti_{0.14})F_{0.20}$	21	0.708	9.207		Ferroan phlogopite
$(Si_{2.91}Al_{1.09})(Cr_{0.03}Fe^{2+}_{0.28}Mg_{2.42}Mn_{0.01}Ti_{0.1})F_{0.72}$	22	0.718	9.190		Phlogopite
$(Si_{2.93}Al_{1.07})(Al_{0.09}Cr_{0.05}Fe^{2+}_{0.59}Mg_{1.60}Mn_{0.03}Ti_{0.52})F_{0.57}$	23	0.706	9.228		Ferroan phlogopite
$(Si_{2.87}Al_{1.13})(Al_{0.15}Cr_{0.07}Fe^{2+}_{0.50}Mg_{1.90}Mn_{0.03}Ti_{0.33})F_{0.30}$	24	0.707	9.204		Ferroan phlogopite
$(Si_{2.90}Al_{1.10})(Al_{0.04}Cr_{0.05}Fe^{2+}_{0.50}Mg_{2.09}Mn_{0.02}Ti_{0.27})F_{0.44}$	25	0.717	9.190		Ferroan phlogopite
$(Si_{2.73}Al_{1.27})(Al_{0.01}Cr_{0.01}Fe^{2+}_{0.94}Mg_{1.48}Mn_{0.02}Ti_{0.39})$	26	0.724	9.235		Ferroan phlogopite
$(Si_{2.81}Al_{1.19})(Al_{0.08}Cr_{0.01}Fe^{2+}_{1.24}Mg_{1.40}Mn_{0.02}Ti_{0.23})F_{0.31}$	27	0.731	9.256		Ferroan phlogopite
$(Si_{2.76}Al_{1.24})(Al_{0.19}Cr_{0.01}Fe^{2+}_{1.30}Mg_{1.24}Mn_{0.01}Ti_{0.20})$	28	0.727	9.215		Magnesian annite
$(Si_{2.84}Al_{1.04}Fe^{3+}_{0.12})(Fe^{3+}_{0.16}Fe^{2+}_{0.09}Mg_{2.65}Ti_{0.08})$	29	0.715	9.211		Phlogopite
$(Si_{2.82}Al_{1.13}Fe^{3+}_{0.05})(Fe^{3+}_{0.22}Fe^{2+}_{0.09}Mg_{2.60}Ti_{0.09})$	30	0.713	9.230		Phlogopite
$(Si_{2.81}Al_{1.14}Fe^{3+}_{0.05})(Fe^{3+}_{0.23}Fe^{2+}_{0.09}Mg_{2.57}Ti_{0.10})$	31	0.712	9.219		Phlogopite
$(Si_{2.71}Al_{1.20}Fe^{3+}_{0.24})(Fe^{3+}_{0.24}Fe^{2+}_{0.62}Mg_{1.90}Mn_{0.02}Ti_{0.18})$	32	0.720	9.244		Ferroan phlogopite
$(Si_{3.11}Fe^{3+}_{0.89})(Fe^{3+}_{0.05}Fe^{2+}_{0.17}Mg_{2.70}Ti_{0.01})F_{0.14}$	33	0.722	9.270		Tetra-ferriphlogopite
$(Si_{3.07}Fe^{3+}_{0.93})(Fe^{3+}_{0.06}Fe^{2+}_{0.17}Mg_{2.75}Mn_{0.01}Ti_{0.01})$	34	0.723	9.277		Tetra-ferriphlogopite
$(Si_{2.82}Al_{1.11}Fe^{3+}_{0.07})(Fe^{3+}_{0.15}Fe^{2+}_{0.08}Mg_{2.68}Mn_{0.01}Ti_{0.08})F_{0.11}$	35	0.715	9.239		Phlogopite
$(Si_{2.85}Al_{1.07}Fe^{3+}_{0.08})(Fe^{3+}_{0.19}Fe^{2+}_{0.07}Mg_{2.68}Ti_{0.05})$	36	0.715	9.214		Phlogopite
$(Si_{2.85}Al_{1.10}Fe^{3+}_{0.05})(Fe^{3+}_{0.21}Fe^{2+}_{0.07}Mg_{2.64}Mn_{0.01}Ti_{0.06})$	37	0.714	9.235		Phlogopite

(*Continued*)

https://doi.org/10.1180/clm.2023.20 Published online by Cambridge University Press

Table 6. (*Continued.*)

Mica (anhydrous composition)	Sample[a]	*R*	*b*	References	Comments
$(Si_{2.76}Al_{1.19}Fe^{3+}_{0.05})(Fe^{3+}_{0.30}Fe^{2+}_{0.38}Mg_{2.17}Mn_{0.01}Ti_{0.13})$	38	0.715	9.238		Ferroan phlogopite
$(Si_{2.74}Al_{1.15}Fe^{3+}_{0.11})(Fe^{3+}_{0.25}Fe^{2+}_{0.34}Mg_{2.19}Mn_{0.01}Ti_{0.13})$	39	0.716	9.228		Ferroan phlogopite
$(Si_{2.91}Al_{0.71}Fe^{3+}_{0.38})(Fe^{3+}_{0.10}Fe^{2+}_{0.22}Mg_{2.64}Mn_{0.01}Ti_{0.03})$	40	0.721	9.247		Tetra-ferriphlogopite
$(Si_{3.15}Al_{0.04}Fe^{3+}_{0.81})(Fe^{3+}_{0.23}Fe^{2+}_{0.20}Mg_{2.54}Ti_{0.02})$	41	0.717	9.284		Tetra-ferriphlogopite
$(Si_{3.05}Fe^{3+}_{0.95})(Fe^{3+}_{0.08}Fe^{2+}_{0.17}Mg_{2.73}Ti_{0.01})$	42	0.721	9.288		Tetra-ferriphlogopite
$(Si_{3.05}Fe^{3+}_{0.95})(Fe^{3+}_{0.11}Fe^{2+}_{0.20}Mg_{2.68}Mn_{0.01})$	43	0.722	9.292		Tetra-ferriphlogopite
$(Si_{2.77}Al_{1.23})(Al_{0.18}Fe^{3+}_{0.18}Fe^{2+}_{1.01}Mg_{1.26}Mn_{0.02}Ti_{0.28})$	44	0.714	9.252		Ferroan phlogopite
$(Si_{2.85}Al_{1.5})(Al_{0.21}Fe^{2+}_{1.37}Mg_{1.15}Mn_{0.03}Ti_{0.25})F_{0.16}$	45	0.726	9.263		Magnesian annite
$(Si_{2.82}Al_{1.18})(Al_{0.18}Fe^{3+}_{0.13}Fe^{2+}_{1.20}Mg_{1.19}Mn_{0.02}Ti_{0.29})F_{0.14}$	46	0.719	9.258		Magnesian annite
$(Si_{2.77}Al_{1.23})(Al_{0.31}Fe^{3+}_{0.16}Fe^{2+}_{1.10}Mg_{1.23}Mn_{0.01}Ti_{0.19})F_{0.12}$	47	0.712	9.260		Ferroan phlogopite
$(Si_{2.76}Al_{1.17}Fe^{3+}_{0.07})(Fe^{3+}_{0.23}Fe^{2+}_{0.38}Mg_{2.25}Mn_{0.01}Ti_{0.13})$	48	0.717	9.230		Ferroan phlogopite
$(Si_{2.90}Al_{1.06}Fe^{3+}_{0.04})(Fe^{3+}_{0.20}Fe^{2+}_{0.11}Mg_{2.59}Mn_{0.01}Ti_{0.05})$	49	0.716	9.219		Phlogopite
$(Si_{3.01}Al_{0.13}Fe^{3+}_{0.86})(Fe^{3+}_{0.30}Fe^{2+}_{0.54}Mg_{1.99}Mn_{0.02}Ti_{0.01})$	50	0.724	9.306		Ferroan tetra-ferriphlogopite
$(Si_{2.71}Al_{1.29})(Al_{0.35}Fe^{3+}_{0.01}Fe^{2+}_{1.45}Mg_{0.77}Mn_{0.04}Ti_{0.21})$	51	0.721	9.268		Magnesian annite
$(Si_{2.62}Al_{1.38})(Al_{0.54}Fe^{3+}_{0.01}Fe^{2+}_{1.41}Mg_{0.83}Mn_{0.03}Ti_{0.17})$	52	0.709	9.239		Magnesian annite
$(Si_{2.63}Al_{1.37})(Al_{0.48}Fe^{2+}_{1.48}Mg_{0.70}Mn_{0.06}Ti_{0.20})$	53	0.714	9.257		Magnesian annite
$(Si_{2.68}Al_{1.32})(Al_{0.64}Fe^{2+}_{1.33}Mg_{0.73}Mn_{0.04}Ti_{0.17})$	54	0.702	9.222		Magnesian annite
$(Si_{2.69}Al_{1.31})(Al_{0.60}Fe^{2+}_{1.36}Mg_{0.73}Mn_{0.02}Ti_{0.14})F_{0.12}$	55	0.705	9.232		Magnesian annite
$(Si_{2.72}Al_{1.28})(Al_{0.50}Fe^{2+}_{1.46}Mg_{0.70}Mn_{0.03}Ti_{0.16})F_{0.15}$	56	0.713	9.256		Magnesian annite
$(Si_{3.49}Al_{0.51})(Li_{1.48}Fe^{2+}_{0.02}Fe^{3+}_{0.008}Mg_{0.05}Mn_{0.03}Al_{1.30})$	62	0.659	9.011		Trilithionte
$(Si_{2.75}Al_{1.15}Fe^{3+}_{0.07}Ti_{0.03})(Fe^{3+}_{0.06}Fe^{2+}_{0.20}Mg_{1.74}Mn^{2+}_{0.95}Mn^{3+}_{0.18})$	63	0.756	9.295		Manganoan phlogopite
$(Si_{2.91}Al_{1.09})(Al_{0.38}Fe^{2+}_{1.00}Mg_{1.90}Li_{0.34}Mn_{0.04}Ti_{0.05})(K_{0.46}Cs_{0.23}Rb_{0.28})F_{0.45}$	65	0.721	9.247		Rb,Cs phlogopite
$(Si_{2.81}Al_{1.19})(Al_{0.09}Fe^{3+}_{0.19}Mg_{0.12}Mn_{0.05}Ti_{0.22})$	66	0.749	9.324		Annite
$(Si_{2.95}Fe^{3+}_{1.05})(Mg_{3.0})F_{1.30}$	67	0.720	9.199		Phlogopite
$(Si_{2.91}Al_{1.09})(Al_{0.07}Fe^{2+}_{0.16}Mg_{2.70}Ti_{0.03})F_{1.13}$	70	0.718	9.202		Phlogopite
$(Si_{2.86}Al_{1.07}Fe^{3+}_{0.02}Ti_{0.03})(Fe^{3+}_{0.03}Mg_{2.27}Mn^{2+}_{0.49})$	71	0.739	9.241		Manganoan phlogopite
$(Si_{2.82}Al_{1.04}Fe^{3+}_{0.14})(Fe^{3+}_{0.08}Fe^{2+}_{0.13}Mg_{2.73}Ti_{0.06})F_{0.11}$	73	0.718	9.239		Phlogopite
$(Si_{3.03}Al_{0.07}Fe^{3+}_{0.90})(Fe^{3+}_{0.01}Fe^{2+}_{0.60}Mg_{2.36}Mn_{0.01}Ti_{0.01})$	74	0.732	9.293		Octa-ferroan tetra-ferriphlo.
$(Si_{3.02}Al_{0.06}Fe^{3+}_{0.92})(Fe^{2+}_{0.60}Mg_{2.38}Mn_{0.01}Ti_{0.01})$	75	0.732	9.290		Octa-ferroan tetra-ferriphlo.
$(Si_{2.94}Al_{0.78}Fe^{3+}_{0.28})(Fe^{3+}_{0.04}Fe^{2+}_{0.43}Mg_{2.39}Mn_{0.01}Ti_{0.08})$	76	0.725	9.267		Ferroan phlogopite
$(Si_{2.82}Al_{1.10}Fe^{3+}_{0.08})(Fe^{3+}_{0.10}Fe^{2+}_{0.44}Mg_{2.36}Mn_{0.01}Ti_{0.09})$	77	0.723	9.246		Ferroan phlogopite
$(Si_{2.84}Al_{1.14}Fe^{3+}_{0.02})(Fe^{3+}_{0.06}Fe^{2+}_{0.60}Mg_{2.23}Mn_{0.01}Ti_{0.10})$	78	0.727	9.244		Ferroan phlogopite
$(Si_{3.00}Al_{0.90}Fe^{3+}_{0.10})(Fe^{2+}_{1.14}Mg_{1.73}Mn_{0.04}Ti_{0.09})$	79	0.741	9.259		Ferroan phlogopite
$(Si_{3.01}Al_{0.92}Fe^{3+}_{0.07})(Fe^{2+}_{0.44}Mg_{2.51}Ti_{0.05})F_{0.18}$	80	0.727	9.227		Ferroan phlogopite
$(Si_{2.94}Al_{1.06})(Fe^{3+}_{0.03}Fe^{2+}_{0.35}Mg_{2.07}Ti_{0.33})F_{0.93}$	81	0.713	9.208		Phlogopite
$(Si_{2.12}Al_{1.88})(Al_{0.93}Fe_{0.17}Mg_{1.20}Cr_{0.01})(K_{0.02}Na_{0.83})$	83	0.666	9.050		Preiswerkite
$(Si_{2.84}Al_{1.16})(Al_{0.16}Fe^{3+}_{0.86}Fe^{2+}_{0.01}Mg_{1.67}Mn_{0.01}Ti_{0.34})F_{0.17}$	85	0.677	9.210		Ferrian phlogopite
$(Si_{2.88}Al_{1.12})(Fe^{2+}_{0.10}Mg_{2.77}Ti_{0.11})F_{0.51}$	86	0.718	9.206		Phlogopite
$(Si_{2.97}Al_{1.06})(Fe^{2+}_{1.07}Mg_{1.57}Mn_{0.06}Ti_{0.10})F_{0.94}$	91	0.738	9.241		Ferroan phlogopite
$(Si_{3.36}Al_{0.64})(Al_{1.13}Li_{1.3})F_{1.53}$	93	0.656	9.010		Trilithionite
$(Si_{2.98}Al_{0.08}Fe^{3+}_{0.85}Ti_{0.03})(Fe^{2+}_{0.16}Mg_{2.89}Mn_{0.01})$	94	0.723	9.297		Tetra-ferri-phlogopite
$(Si_{3.00}Fe^{3+}_{1.00})(Mg_{3.00})$	95	0.720	9.292		Tetra-ferri-phlogopite
$(Si_{2.86}Al_{1.14})(Al_{0.19}Fe^{2+}_{0.71}Fe^{3+}_{0.19}Mg_{1.68}Mn_{0.01}Ti_{0.34})F_{0.17}$	99	0.706	9.231		Ferroan phlogopite
$(Si_{2.71}Al_{1.29})(Al_{0.18}Fe^{3+}_{0.01}Fe^{2+}_{2.31}Mg_{0.28}Li_{0.04}Mn_{0.02}Ti_{0.10})F_{0.14}$	101	0.758	9.311		Annite
$(Si_{4.00})(Li_{1.00}Mn^{3+}_{2.00})$	111	0.683	8.914		Norrishite
$(Si_{2.98}Al_{1.02})(Al_{0.47}Fe^{2+}_{2.02}Mg_{0.03}Li_{0.33}Mn_{0.07})F_{0.99}$	112	0.739	9.293		Al-fluoro-annite
	1*M* space group *C2*				
$(Si_{3.48}Al_{0.53})(Al_{1.10}Fe^{3+}_{0.03}Fe^{2+}_{0.15}Mg_{0.16}Li_{1.51}Mn_{0.16})F_{1.67}$	113	0.679	9.005		Polylithionite
$(Si_{3.87}Al_{0.13})(Al_{1.13}Fe^{2+}_{0.07}Mg_{0.16}Li_{1.41}Mn_{0.05})F_{x}$	128	0.666	9.055		Polylithionite
$(Si_{3.09}Al_{0.91})(Al_{1.05}Fe^{2+}_{0.77}Fe^{3+}_{0.16}Mg_{0.01}Li_{0.67}Mn_{0.050}Ti_{0.01})F_{1.21}$	129	0.673	9.14		Polylithionite–siderophylite
$(Si_{3.33}Al_{0.67})(Al_{0.98}Fe^{2+}_{0.09}Fe^{3+}_{0.03}Mg_{0.01}Li_{1.27}Mn_{0.50}Ti_{0.005})F_{1.58}$	130	0.695	9.102		Masutomilite
	$2M_1$ space group *C2/c*				
$(Si_{2.78}Al_{1.22})(Fe^{2+}_{0.70}Fe^{3+}_{0.52}Mg_{1.53}Mn_{0.02}Ti_{0.22})$	131	0.713	9.249		Ferroan phlogopite
$(Si_{2.84}Al_{1.16})(Al_{0.40}Fe^{3+}_{0.17}Fe^{2+}_{1.36}Mg_{0.80}Mn_{0.01}Ti_{0.26})$	132	0.709	9.242		Magnesian annite
$(Si_{2.79}Al_{1.21})(Al_{0.23}Fe^{2+}_{0.81}Mg_{1.63}Mn_{0.02}Ti_{0.33})F_{0.31}$	133	0.709	9.220		Ferroan phlogopite
$(Si_{2.87}Al_{1.13})(Al_{0.34}Fe^{2+}_{0.79}Mg_{1.57}Mn_{0.002}Ti_{0.30})F_{0.26}$	134	0.703	9.222		Ferroan phlogopite
$(Si_{2.79}Al_{1.21})(Al_{0.12}Fe^{2+}_{1.39}Mg_{1.16}Mn_{0.007}Ti_{0.32})Cl_{0.14}$	135	0.728	9.245		Magnesian annite
$(Si_{2.71}Al_{1.29})(Al_{0.60}Fe^{2+}_{1.36}Mg_{0.71}Mn_{0.04}Ti_{0.16})$	136	0.705	9.242		Magnesian annite
$(Si_{2.84}Al_{1.16})(Al_{0.16}Fe^{3+}_{0.01}Fe^{2+}_{1.36}Mg_{1.67}Mn_{0.01}Ti_{0.34})$	137	0.685	9.212		Ferrian phlogopite
$(Si_{3.62}Al_{0.38})(Al_{1.26}Fe^{2+}_{0.002}Mg_{0.002}Li_{1.65}Mn_{0.04}Ti_{0.001})F_{1.52}$	138	0.666	9.026		Polylithionite
$(Si_{2.86}Al_{1.14})(Al_{0.19}Fe^{3+}_{0.19}Fe^{2+}_{0.71}Mg_{1.68}Mn_{0.01}Ti_{0.34})F_{0.17}$	139	0.706	9.234		Hydrogenated ferroan phlogopite
	$2M_1$ space group *Cc*				
$(Si_{3.00}Al_{1.00})(Al_{0.97}Fe^{3+}_{0.14}Mg_{0.02}Li_{0.50}Mn_{0.03})F_{0.91}$	140	0.682	9.187		Lithian siderophyllite
	$2M_1$ space group *C1*				
	141	0.604	8.872		Ephesite

(*Continued*)

https://doi.org/10.1180/clm.2023.20 Published online by Cambridge University Press

Table 6. (*Continued.*)

Mica (anhydrous composition)	Sample[a]	*R*	*b*	References	Comments
$(Si_{2.01}Al_{1.99})(Al_{2.01}Fe^{3+}_{0.01}Li_{0.85}Mg_{0.03}Mn_{0.005}Cr_{0.01})(K_{0.001}Na_{0.94}Ca_{0.03})$					
	2M_2 space group *C2/c*				
$(Si_{3.49}Al_{0.51})(Al_{1.30}Fe^{3+}_{0.008}Fe^{2+}_{0.002}Mg_{0.05}Li_{1.48}Mn_{0.03})F_x$	142	0.656	9.023		Trilithionite
$(Si_{3.36}Al_{0.64})(Al_{1.26}Fe^{3+}_{0.003}Mg_{0.007}Li_{1.76}Mn_{0.03})F_{1.53}$	143	0.666	9.040		Polylithionite
$(Si_{3.39}Al_{0.61})(Al_{1.40}Fe^{2+}_{0.07}Mg_{0.03}Li_{1.03}Mn_{0.03})F_{1.20}$	144	0.637	9.032		Trilithionite
	3*T* space group $P3_112$				
$(Si_{3.48}Al_{0.52})(Al_{1.25}Fe_{0.015}Mg_{0.01}Li_{1.62}Mn_{0.09})F_{1.54}$	145	0.668	9.007		Polylithionite
$(Si_{2.97}Al_{1.03})(Al_{0.68}Al_{0.19}Fe^{3+}_{0.34}Fe^{2+}_{1.25}Zn_{0.02}Li_{0.37}Mn_{0.04})F_{1.06}$	146	0.699	9.195		Lithian siderophyllite
Trioctahedral brittle micas (collected data)	1*M* space group *C2/m*				
$(Si_{1.20}Al_{2.76})(Al_{0.68}Fe^{3+}_{0.04}Fe^{2+}_{0.11}Mg_{2.21})Ca,F_{0.14}$	1	0.680	9.005		Clintonite
$(Si_{1.19}Al_{2.79})(Al_{0.64}Fe^{2+}_{0.22}Mg_{2.14})Ca,F_{0.11}$	2	0.685	9.006		Clintonite
$(Si_{1.25}Al_{2.75})(Al_{0.76}Fe^{2+}_{0.13}Mg_{2.09})Ca$	3	0.676	8.995		Clintonite
$(Si_{1.24}Al_{2.76})(Al_{0.65}Fe^{2+}_{0.13}Mg_{2.22})Ca,F_{0.17}$	4	0.683	9.026		Clintonite
$(Si_{1.19}Al_{2.78}Fe^{3+}_{0.03})(Al_{0.67}Fe^{2+}_{0.16}Mg_{2.17}Ti_{0.01})Ca,F_{0.19}$	5	0.682	9.003		Clintonite
$(Si_{1.28}Al_{2.70}Fe^{3+}_{0.02})(Al_{0.63}Fe^{2+}_{0.16}Mg_{2.20}Ti_{0.01})Ca,F_{0.18}$	6	0.684	9.005		Clintonite
$(Si_{2.17}Al_{1.83})(Al_{0.17}Fe^{2+}_{0.27}Mg_{2.53}Ti_{0.03})(K_{0.41}Ba_{0.54})F_{0.71}$	7	0.714	9.214		Potassium kinoshitaite
$(Si_{2.03}Al_{1.97})(Al_{0.04}Fe^{2+}_{0.27}Mg_{2.64}Mn_{0.31})Ba,F_{0.37}$	8	0.729	9.230		Kinoshitaite
$(Si_{2.44}Al_{1.56})(Fe^{3+}_{0.15}Fe^{2+}_{1.72}Mg_{0.74}Ti_{0.17})(K_{0.33}Ba_{0.47})F_{0.65}$	9	0.746	9.337		Ferrokinoshitaite
$(Si_{1.20}Al_{2.69}Fe^{3+}_{0.11})(Al_{0.70}Fe^{2+}_{0.05}Mg_{2.29}Ti_{0.006})Ca$	10	0.678	9.013		Clintonite
$(Si_{2.05}Al_{1.95})(Al_{0.22}Fe^{3+}_{0.05}Mg_{2.07}Mn^{2+}_{0.52}Mn^{3+}_{0.21})(K_{0.35}Na_{0.11}Ba_{0.58})$	11	0.724	9.250		Magnesian kinoshitaite
$(Si_{1.10}Al_{2.90})(Al_{0.74}Fe^{2+}_{0.18}Mg_{2.08})Ca$	12	0.678	9.005		Clintonite
$(Si_{1.32}Al_{2.68})(Al_{0.70}Fe^{2+}_{0.11}Mg_{2.18})Ca$	13	0.679	9.005		Clintonite
$(Si_{1.08}Al_{2.92})(Al_{0.82}Fe^{2+}_{0.07}Mg_{2.11})Ca$	14	0.671	9.002		Clintonite
	2M_1 space group *Cc*				
$(Si_{2.02}Al_{1.34}Be_{0.64})(Al_{2.04}Fe^{3+}_{0.007}Li_{0.55})Ca$	16	0.583	8.763		Bityite
	2*Or* space group *Pnmn*				
$(Si_{2.64}Al_{0.08}Fe^{3+}_{0.70}Fe^{2+}_{0.58})(Mg_{0.48}Fe^{2+}_{2.46}Mn_{0.06}Ti_{0.01})Ba_{0.87}S_{0.85}Cl_{0.15}$	17	0.771	9.492		Anandite
$(Si_{2.60}Fe^{3+}_{1.40})(Al_{0.10}Mg_{0.46}Fe^{2+}_{2.46}Mn^{2+}_{0.04}Mn^{3+}_{0.04})Ba_{0.96}S_{0.84}Cl_{0.16}$	18	0.749	9.509		Anandite
*Li- and Fe-rich 1*M *micas*				Brigatti *et al.* (2000)	Pikes Peak batholith, central Colorado, USA
$(Si_{3.536}Al_{0.464})(Al_{1.055}Ti_{0.001}Fe^{3+}_{0.047}Fe^{2+}_{0.403}Mg_{0.002}Mn_{0.038}Zn_{0.002}Li_{1.411})$	114	0.681	9.085		$(OH_{0.143}F_{1.746})$
$(Si_{3.413}Al_{0.587})(Al_{1.115}Ti_{0.008}Fe^{3+}_{0.052}Fe^{2+}_{0.533}Mg_{0.010}Mn_{0.039}Zn_{0.003}Li_{1.111})$	55a	0.675	9.092		$(OH_{0.206}F_{1.627})$
$(Si_{3.412}Al_{0.588})(Al_{1.064}Ti_{0.006}Fe^{3+}_{0.059}Fe^{2+}_{0.546}Mg_{0.006}Mn_{0.046}Zn_{0.008}Li_{1.223})$	55b	0.681	9.085		$(OH_{0.241}F_{1.529})$
$(Si_{3.295}Al_{0.705})(Al_{1.007}Ti_{0.002}Fe^{3+}_{0.092}Fe^{2+}_{0.705}Mg_{0.022}Mn_{0.062}Zn_{0.005}Li_{1.082})$	130-1	0.686	9.128		$(OH_{0.187}F_{1.553})$
$(Si_{3.328}Al_{0.672})(Al_{1.020}Ti_{0.005}Fe^{3+}_{0.059}Fe^{2+}_{0.712}Mg_{0.022}Mn_{0.063}Zn_{0.005}Li_{1.095})$	130-2	0.686	9.105		$(OH_{0.186}F_{1.545})$
$(Si_{3.210}Al_{0.790})(Al_{1.050}Ti_{0.005}Fe^{3+}_{0.072}Fe^{2+}_{0.675}Mg_{0.012}Mn_{0.074}Zn_{0.006}Li_{0.974})$	137	0.681	9.114		$(OH_{0.244}F_{1.739})$
$(Si_{3.303}Al_{0.697})(Al_{1.032}Ti_{0.011}Fe^{3+}_{0.141}Fe^{2+}_{0.639}Mg_{0.013}Mn_{0.011}Zn_{0.006}Li_{0.969})$	104	0.676	9.122		$(OH_{0.244}F_{1.606})$
$(Si_{3.308}Al_{0.692})(Al_{1.035}Ti_{0.006}Fe^{3+}_{0.118}Fe^{2+}_{0.610}Mg_{0.063}Mn_{0.002}Zn_{0.006}Li_{0.941})$	54b	0.677	9.123		$(OH_{0.244}F_{1.654})$
$(Si_{3.229}Al_{0.771})(Al_{0.882}Ti_{0.005}Fe^{3+}_{0.242}Fe^{2+}_{0.648}Mg_{0.009}Mn_{0.065}Zn_{0.012}Li_{0.862})$	177	0.683	9.133		$(OH_{0.149}F_{1.921})$
$(Si_{3.175}Al_{0.825})(Al_{1.019}Ti_{0.026}Fe^{3+}_{0.039}Fe^{2+}_{0.808}Mg_{0.052}Mn_{0.059}Zn_{0.011}Li_{0.855})$	140-1	0.683	9.118		$(OH_{0.248}F_{1.622})$
$(Si_{3.235}Al_{0.765})(Al_{0.981}Ti_{0.025}Fe^{3+}_{0.053}Fe^{2+}_{0.805}Mg_{0.053}Mn_{0.060}Zn_{0.011}Li_{0.852})$	140-2	0.685	9.146		$(OH_{0.248}F_{1.640})$
$(Si_{3.312}Al_{0.688})(Al_{1.109}Ti_{0.006}Fe^{3+}_{0.046}Fe^{2+}_{0.779}Mg_{0.004}Mn_{0.080}Zn_{0.002}Li_{0.765})$	24	0.676	9.139		$(OH_{0.174}F_{1.591})$
$(Si_{3.057}Al_{0.943})(Al_{0.811}Ti_{0.102}Fe^{3+}_{0.094}Fe^{2+}_{1.396}Mg_{0.036}Mn_{0.079}Zn_{0.017}Li_{0.409})$	47	0.700	9.233		$(OH_{0.284}F_{1.080})$
$(Si_{3.225}Al_{0.775})(Al_{0.905}Ti_{0.032}Fe^{3+}_{0.094}Fe^{2+}_{1.192}Mg_{0.023}Mn_{0.053}Zn_{0.013}Li_{0.624})$	103	0.694	9.144		$(OH_{0.154}F_{1.294})$
Li-poor micas					
$(Si_{2.943}Al_{1.057})(Al_{0.835}Ti_{0.024}Fe^{3+}_{0.242}Fe^{2+}_{1.627}Mg_{0.097}Mn_{0.004}Zn_{0.007}Li_{0.169})$	26	0.675	9.092		$(OH_{0.167}F_{0.903})$
$(Si_{3.0.94}Al_{0.906})(Al_{0.349}Ti_{0.108}Fe^{3+}_{0.159}Fe^{2+}_{2.222}Mg_{0.002}Mn_{0.079}Li_{0.082})$	33	0.681	9.085		$(OH_{0.119}F_{1.087})$
*Li-, Fe- and Mn-rich 1*M *micas*				Brigatti *et al.* (2007)	

(*Continued*)

https://doi.org/10.1180/clm.2023.20 Published online by Cambridge University Press

Table 6. (*Continued.*)

Mica (anhydrous composition)	Sample[a]	*R*	*b*	References	Comments
$(Si_{3.43}Al_{0.57})(Al_{1.0}Fe^{2+}_{0.38}Mg_{0.01}Mn_{0.17}Li_{1.44})$	Hirukawa Mine	0.691	9.086		$(OH_{0.12}F_{1.88})$
$(Si_{3.30}Al_{0.70})(Al_{1.0}Fe^{2+}_{0.36}Mg_{0.01}Mn_{0.31}Li_{1.32})$	Mokrusha Mine	0.695	9.133		$(OH_{0.09}F_{1.91})$
$(Si_{3.11}Al_{0.89})(Al_{0.91}\ Ti_{0.02}Fe^{2+}_{0.46}Mg_{0.03}Mn_{0.52}Li_{1.06})$	Boise County	0.706	9.146		$(OH_{0.11}F_{1.89})$
Fe-Li micas[c]				Rieder *et al.* (1970)	
$(Si_{2.975}Al_{1.025})(Fe^{2+}_{1,32}Mg_{0.05}Mn_{0.02}Fe^{3+}_{0.045}Al_{1.00}Ti_{0.02})$	44	0.675	9.253		$(OH_{1.43}F_{0.49})$
$(Si_{2.57}Al_{1.43})(Fe^{2+}_{1.835}Mg_{0.60}Li_{0.025}Mn_{0.01}Fe^{3+}_{0.305}Ti_{0.15})$	12	0.741	9.336		$(OH_{1.63}F_{0.24})$
$(Si_{2.76}Al_{1.24})(Fe^{2+}_{1.61}Mg_{0.21}Li_{0.12}Mn_{0.04}Fe^{3+}_{0.18}Al_{0.575}Ti_{0.02})$	8	0.714	9.255		$(OH_{1.62}F_{0.38})$
$(Si_{2.785}Al_{1.215})(Fe^{2+}_{1.485}Mg_{0.12}Li_{0.21}Mn_{0.035}Fe^{3+}_{0.23}Al_{0.64}Ti_{0.01})$	7	0.707	9.260		$(OH_{1.0}F_{1.01})$
$(Si_{2.74}Al_{1.26})(Fe^{2+}_{1.47}Mg_{0.06}Li_{0.305}Mn_{0.055}Fe^{3+}_{0.32}Al_{0.52}Cr_{0.025}Ti_{0.04})$	18	0.711	9.267		$(OH_{1.01}F_{0.99})$
$(Si_{2.91}Al_{1.09})(Fe^{2+}_{1.345}Mg_{0.025}Li_{0.345}Mn_{0.045}Fe^{3+}_{0.135}Al_{0.815}Ti_{0.01})$	13	0.697	9.229		$(OH_{0.98}F_{1.02})$
$(Si_{2.875}Al_{1.125})(Fe^{2+}_{1.185}Li_{0.30}Mn_{0.02}Fe^{3+}_{0.15}Al_{0.955}Ti_{0.02})$	31	0.680	9.214		$(OH_{1.42}F_{0.58})$
$(Si_{2.87}Al_{1.13})(Fe^{2+}_{1.035}Mg_{0.025}Li_{0.60}Mn_{0.02}Fe^{3+}_{0.155}Al_{0.94}Ti_{0.02})$	29	0.684	9.203		$(OH_{0.77}F_{1.23})$
$(Si_{3.04}Al_{0.96})(Fe^{2+}_{0.955}Mg_{0.01}Li_{0.585}Mn_{0.035}Fe^{3+}_{0.14}Al_{0.965}Ti_{0.01})$	9	0.681	9.186		$(OH_{1.17}F_{0.82})$
$(Si_{3.015}Al_{0.985})(Fe^{2+}_{1.06}Mg_{0.01}Li_{0.725}Mn_{0.05}Fe^{3+}_{0.08}Al_{0.77}Cr_{0.135}Ti_{0.02})$	35	0.696	9.172		$(OH_{0.44}F_{1.56})$
$(Si_{3.135}Al_{0.865})(Fe^{2+}_{0.65}Mg_{0.02}Li_{0.505}Mn_{0.035}Fe^{3+}_{0.155}Al_{1.155}Ti_{0.01})$	38	0.656	9.129		$(OH_{1.10}F_{0.91})$
$(Si_{3.14}Al_{0.86})(Fe^{2+}_{0.725}Li_{0.645}Mn_{0.045}Fe^{3+}_{0.155}Al_{1.035}Ti_{0.02})$	40	0.670	9.146		$(OH_{0.79}F_{1.21})$
$(Si_{3.16}Al_{0.84})(Fe^{2+}_{0.8}Mg_{0.08}Li_{0.715}Fe^{3+}_{0.105}Al_{0.99}Ti_{0.02})$	5	0.677	9.155		$(OH_{0.86}F_{1.14})$
$(Si_{3.07}Al_{0.93})(Fe^{2+}_{0.715}Li_{0.71}Mn_{0.03}Fe^{3+}_{0.16}Al_{1.05}Ti_{0.01})$	37	0.670	9.160		
$(Si_{3.105}Al_{0.895})(Fe^{2+}_{0.66}Mg_{0.025}Li_{0.735}Mn_{0.025}Fe^{3+}_{0.235}Al_{0.985})$	15	0.672	9.150		$(OH_{0.88}F_{1.13})$
$(Si_{2.815}Al_{1.185})(Fe^{2+}_{1.195}Mg_{0.26}Li_{0.375}Mn_{0.035}Fe^{3+}_{0.16}Al_{0.78}Ti_{0.08})$	2	0.692	9.209		$(OH_{1.27}F_{0.38})$
$(Si_{2.825}Al_{1.175})(Fe^{2+}_{1.085}Mg_{0.16}Li_{0.39}Mn_{0.035}Fe^{3+}_{0.305}Al_{0.701}Ti_{0.14})$	23	0.694	9.201		$(OH_{0.99}F_{1.02})$
$(Si_{2.895}Al_{1.105})(Fe^{2+}_{1.14}Mg_{0.23}Li_{0.43}Mn_{0.04}Fe^{3+}_{0.13}Al_{0.80}Ti_{0.05})$	3	0.695	9.209		$(OH_{0.87}F_{1.13})$
$(Si_{2.98}Al_{1.02})(Fe^{2+}_{1.065}Mg_{0.015}Li_{0.495}Mn_{0.035}Fe^{3+}_{0.14}Al_{0.94}Ti_{0.01})$	4	0.683	9.211		$(OH_{1.10}F_{0.91})$
$(Si_{3.02}Al_{0.98})(Fe^{2+}_{1.00}Mg_{0.235}Li_{0.475}Mn_{0.03}Fe^{3+}_{0.09}Al_{0.83}Ti_{0.05})$	6	0.688	9.200		$(OH_{1.14}F_{0.86})$
$(Si_{3.055}Al_{0.945})(Fe^{2+}_{0.765}Mg_{0.01}Li_{0.42}Mn_{0.02}Fe^{3+}_{0.305}Al_{0.99})$	33	0.664	9.194		
$(Si_{2.94}Al_{1.06})(Fe^{2+}_{1.085}Mg_{0.125}Li_{0.60}Mn_{0.025}Fe^{3+}_{0.105}Al_{0.875}Ti_{0.01})$	10	0.692	9.148		$(OH_{0.83}F_{1.17})$
$(Si_{3.20}Al_{0.80})(Fe^{2+}_{0.815}Mg_{0.025}Li_{0.455}Mn_{0.02}Fe^{3+}_{0.085}Al_{1.125}Ti_{0.01})$	14	0.662	9.170		$(OH_{1.17}F_{0.72})$
$(Si_{3.135}Al_{0.865})(Fe^{2+}_{0.685}Mg_{0.015}Li_{0.915}Mn_{0.035}Fe^{3+}_{0.11}Al_{1.00}Ti_{0.02})$	16	0.678	9.099		$(OH_{0.63}F_{1.38})$
$(Si_{3.315}Al_{0.685})(Fe^{2+}_{0.62}Li_{1.10}Mn_{0.07}Fe^{3+}_{0.06}Al_{0.98}Ti_{0.01})$	1	0.685	9.110		$(OH_{0.80}F_{1.21})$
$(Si_{3.27}Al_{0.73})(Fe^{2+}_{0.555}Mg_{0.03}Li_{1.06}Mn_{0.03}Fe^{3+}_{0.08}Al_{1.02}Ti_{0.03})$	22	0.677	9.105		$(OH_{0.30}F_{1.70})$
$(Si_{3.5}Al_{0.5})(Fe^{2+}_{0.26}Li_{1.27}Mn_{0.04}Fe^{3+}_{0.135}Al_{1.05}Ti_{0.01})$	17	0.671	9.058		$(OH_{0.34}F_{1.66})$
$(Si_{3.58}Al_{0.42})(Fe^{2+}_{0.005}Mg_{0.065}Li_{1.61}Mn_{0.05}Fe^{3+}_{0.02}Al_{1.17})$	41	0.669	9.028		$(OH_{0.49}F_{1.52})$
$(Si_{3.48}Al_{0.52})(Mg_{0.055}Li_{1.475}Mn_{0.03}Fe^{3+}_{0.01}Al_{1.28})$	43	0.659	9.026		$(OH_{0.42}F_{1.58})$
$(Si_{3.52}Al_{0.48})(Mg_{0.06}Li_{1.575}Mn_{0.01}Fe^{3+}_{0.005}Al_{1.24})$	42	0.663	9.020		$(OH_{0.47}F_{1.54})$
$Si_4(Mg_{0.035}Li_{1.96}Fe^{3+}_{0.005}Al_{0.955}Ti_{0.05})$	45	0.685	8.970		$(OH_{0.36}F_{1.64})$
Various micas				Radoslovich & Norrish (1962)	As named in the paper
$(Si_{2.80}Al_{1.20})(Fe^{2+}_{1.30}Mg_{1.03}Mn_{0.03}Fe^{3+}_{0.15}Ti_{0.10}Al_{0.33})$	1	0.719	9.265		Biotite
$(Si_{2.82}Al_{1.18})(Fe^{2+}_{1.33}Mg_{0.84}Li_{0.10}Mn_{0.03}Fe^{3+}_{0.20}Ti_{0.10}Al_{0.27})$	3	0.724	9.268		Biotite
$(Si_{2.94}Al_{1.06})(Fe^{2+}_{0.37}Mg_{2.37}Li_{0.04}Fe^{3+}_{0.02}Ti_{0.15}Al_{0.07})$	4	0.717	9.251		Biotite
$(Si_{2.79}Al_{1.21})(Fe^{2+}_{1.13}Mg_{1.11}Li_{0.03}Fe^{3+}_{0.18}Ti_{0.15}Al_{0.25})$	5	0.717	9.261		Biotite
$(Si_{3.00}Al_{1.00})(Fe^{2+}_{1.06}Mg_{1.54}Li_{0.07}Mn_{0.06}Fe^{3+}_{0.11}Ti_{0.13}Al_{0.01})$	6	0.736	9.251		Biotite
$(Si_{2.66}Al_{1.34})(Fe^{2+}_{1.33}Mg_{0.68}Li_{0.02}Mn_{0.02}Fe^{3+}_{0.08}Ti_{0.17}Al_{0.50})$	9	0.707	9.254		Biotite
$(Si_{2.78}Al_{1.22})(Fe^{2+}_{1.34}Mg_{0.94}Li_{0.01}Mn_{0.02}Fe^{3+}_{0.18}Ti_{0.16}Al_{0.26})$	11	0.721	9.262		Biotite
$(Si_{2.54}Al_{1.43})(Fe^{2+}_{1.42}Mg_{0.51}Mn_{0.14}Fe^{3+}_{0.76}Ti_{0.06})$	13	0.733	9.308		Biotite
$(Si_{2.74}Al_{1.26})(Fe^{2+}_{1.27}Mg_{0.88}Li_{0.03}Mn_{0.02}Fe^{3+}_{0.16}Ti_{0.12}Al_{0.38})$	14	0.714	9.246		Biotite
$(Si_{2.73}Al_{1.27})(Fe^{2+}_{1.19}Mg_{1.24}Li_{0.01}Mn_{0.01}Fe^{3+}_{0.09}Ti_{0.14}Al_{0.24})$	16	0.722	9.253		Biotite
$(Si_{2.78}Al_{1.22})(Fe^{2+}_{1.72}Mg_{0.28}Li_{0.04}Mn_{0.03}Fe^{3+}_{0.44}Ti_{0.18}Al_{0.13})$	18	0.731	9.328		Biotite
$(Si_{2.81}Al_{1.19})(Fe^{2+}_{1.05}Mg_{1.05}Fe^{3+}_{0.26}Ti_{0.19}Al_{0.36})$	19	0.705	9.266		Biotite
$(Si_{2.99}Al_{1.01})(Fe^{2+}_{1.82}Mg_{0.69}Fe^{3+}_{0.09}Ti_{0.33}Al_{0.40})$	20	0.717	9.300		Biotite
$(Si_{2.99}Al_{1.01})(Fe^{2+}_{1.80}Mg_{0.51}Fe^{3+}_{0.23}Ti_{0.19}Al_{0.37})$	21	0.720	9.323		Biotite
$(Si_{2.88}Al_{1.12})(Fe^{2+}_{1.00}Mg_{1.18}Fe^{3+}_{0.26}Ti_{0.31})$	22	0.722	9.260		Biotite
$(Si_{2.88}Al_{1.12})(Fe^{2+}_{1.09}Mg_{1.27}Fe^{3+}_{0.19}Ti_{0.17}Al_{0.38})$	23	0.708	9.271		Biotite
$(Si_{3.01}Al_{0.99})(Fe^{2+}_{1.33}Mg_{0.93}Mn_{0.01}Fe^{3+}_{0.23}Ti_{0.21}Al_{0.30})$	24	0.715	9.265		Biotite
$(Si_{2.99}Al_{0.95})(Fe^{2+}_{0.23}Mg_{2.15}Fe^{3+}_{0.12}Ti_{0.48})$	25	0.703	9.241		Phlogopite
$(Si_{3.02}Al_{0.98})(Fe^{2+}_{0.04}Mg_{2.98}Fe^{3+}_{0.02}Al_{0.16})$	26	0.711	9.220		Phlogopite
$(Si_{3.01}Al_{1.01})(Mg_3)$	29	0.720	9.188		Fluorophlogopite
$(Si_{3.11}Al_{0.89})(Al_{1.84}Fe^{3+}_{0.12}Mg_{0.06})$	30	0.547	8.995		Muscovite
$(Si_{3.27}Al_{0.73})(Al_{1.27}Fe^{3+}_{0.42}Fe^{2+}_{0.15}Mg_{0.19})$	31	0.593	9.060		Iron-muscovite
$(Si_{3.58}Al_{0.42})(Fe^{2+}_{0.01}Mg_{0.02}Li_{1.36}Mn_{0.03}Al_{1.32})$	33	0.652	9.006		Lepidolite
$(Si_{3.21}Al_{0.79})(Fe^{2+}_{0.02}Mg_{0.02}Li_{1.35}Fe^{3+}_{0.09}Al_{0.82})$	34	0.675	8.970		Lepidolite

(*Continued*)

https://doi.org/10.1180/clm.2023.20 Published online by Cambridge University Press

Table 6. (*Continued.*)

Mica (anhydrous composition)	Sample[a]	*R*	*b*	References	Comments
$(Si_{3.6}Al_{0.4})(Fe^{3+}_{1.4}Mg_{0.7})$	35	0.670	9.020		Celadonite
$Si_4(Al_{0.07}Fe^{3+}_{0.93}Fe^{2+}_{0.24}Mg_{0.77})$	36	0.686	9.050		Celadonite
$(Si_{3.86}Al_{0.14})(Al_{0.75}Fe^{3+}_{0.36}Fe^{2+}_{0.2}Mg_{0.68})$	37	0.643	9.060		Celadonite
$(Si_{3.74}Al_{0.26})(Al_{0.18}Fe^{3+}_{1}Fe^{2+}_{0.57}Mg_{0.57})$	38	0.688	9.080		Celadonite
$(Si_{3.28}Al_{0.72})(Fe^{2+}_{0.60}Li_{1.05}Mn_{0.02}Fe^{3+}_{0.06}Al_{1.08})$	39	0.651	9.120		Zinwaldite
$(Si_{3.46}Al_{0.54})(Fe^{2+}_{0.33}Mg_{0.02}Li_{1.15}Mn_{0.03}Fe^{3+}_{0.05}Ti_{0.02}Al_{1.16})$	40	0.665	9.060		Zinwaldite
$(Si_{2.95}Al_{1.05})(Fe^{2+}_{1.19}Mg_{0.06}Li_{0.45}Mn_{0.02}Fe^{3+}_{0.03}Ti_{0.02}Al_{0.95})$	41	0.692	9.210		Lithium biotite
$(Si_{3.23}Al_{0.77})(Fe^{2+}_{0.60}Mg_{0.02}Li_{1.01}Mn_{0.08}Fe^{3+}_{0.03}Al_{1.00})$	42	0.683	9.090		Lithium biotite
$(Si_{3.19}Al_{0.77})(Mg_{0.40}Ti_{0.04}Al_{1.48})$	43	0.575	9.040		Gümbelite
$(Si_{2.57}Al_{1.43})(Fe^{2+}_{1.46}Mg_{0.68}Fe^{3+}_{0.35}Ti_{0.23}Al_{0.07})$	44	0.728	9.290		Lepidomelane
$(Si_2Al_2)(Al_2)Ca$	45	0.535	8.920		Margarite
$(Si_{1.95}Al_{2.05})(Fe^{2+}_{0.02}Mg_{0.04}Li_{0.40}Al_{1.90}Fe^{2+}_{0.03})Na$	46	0.572	8.896		Ephesite
$(Si_{1.05}Al_{2.95})(Mg_{2.18}Al_{0.72})Ca$	47	0.674	9.000		Xanthophyllite
$(Si_{1.17}Al_{2.83})(Fe^{2+}_{0.02}Mg_{2.09}Fe^{3+}_{0.15}Al_{0.70})Ca$	48	0.673	9.010		Xanthophyllite
$(Si_{1.22}Al_{2.78})(Fe^{2+}_{0.06}Mg_{2.23}Fe^{3+}_{0.04}Al_{0.72})Ca$	49	0.677	9.000		Xanthophyllite
$(Si_{1.16}Al_{2.84})(Fe^{2+}_{0.04}Mg_{2.14}Fe^{3+}_{0.08}Al_{0.76})Ca$	50	0.672	9.020		Xanthophyllite
$(Si_{2.17}Al_{0.69}Be_{1.14})(Li_{0.63}Al_{2.09})Ca$	51	0.587	8.713		Bityite
$(Si_{2.06}Al_{1.59}Be_{0.35})(Mg_{0.01}Li_{0.71}Al_{1.58})Ca$	52	0.605	8.670		Bityite
Hendricksites (available composition)				Frondel & Ito (1966)	
$Mg_{0.25}Fe^{2+}_{0.03}Mn_{1.22}Zn_{1.50}$	1	0.775	9.338		
$Mg_{0.45}Fe^{2+}_{0.02}Mn_{1.05}Zn_{1.48}$	2	0.769	9.328		
$(Si_{2.664}Al_{1.336})(Al_{0.02}Mg_{0.46}Ti_{0.04}Fe^{3+}_{0.14}Fe^{2+}_{0.02}Zn_{1.43}Mn_{0.88})$	3	0.756	9.324		
$(Si_{2.727}Al_{1.266})(Mg_{0.23}Ti_{0.01}Fe^{3+}_{0.31}Fe^{2+}_{0.05}Zn_{1.36}Mn_{1.01})$	4	0.759	9.324		
$Mg_{0.42}Fe^{3+}_{0.3}Fe^{2+}_{0.08}Mn_{0.81}Zn_{1.39}$	5	0.753	9.332		
$Mg_{0.94}Fe^{2+}_{0.02}Mn_{0.88}Zn_{1.17}$	6	0.760	9.301		
$Mg_{1.66}Fe^{2+}_{0.25}Mn_{0.34}Zn_{0.75}$	7	0.742	9.257		
$Mg_{1.60}Fe^{2+}_{0.34}Mn_{0.36}Zn_{0.70}$	8	0.745	9.222		
$Mg_{2.91}Fe^{2+}_{0.08}Mn_{0.001}Zn_{0.01}$	9	0.722	9.180		
Manganophyllite				Knurr & Bailey (1986)	
$(Si_{2.79}Al_{1.21})(Al_{0.11}Ti_{0.01}\ Fe^{3+}_{0.17}Mg_{2.51}\ Mn_{0.13})$	Manganophyllite	0.713	9.221		
Celadonites				Brigatti & Guggenheim (2002)	
$(Si_{3.94}Al_{0.06})(Al_{0.05}Fe^{3+}_{1.15}Fe^{2+}_{0.36}Mg_{0.41}Ti_{0.01})$	3	0.682	9.050		True mica-1*M* space group *C2/m*
				Wise & Eugster (1964)	
$(Si_{3.88}Al_{0.12})(Al_{0.62}Fe^{3+}_{0.64}Fe^{2+}_{0.13}Mg_{0.61})$	11	0.643	9.000		
$(Si_{3.78}Al_{0.22})(Al_{0.20}Fe^{3+}_{1.01}Fe^{2+}_{0.28}Mg_{0.57})$	13	0.673	9.042		
$(Si_{3.73}Al_{0.27})(Al_{0.30}Fe^{3+}_{1.07}Fe^{2+}_{0.20}Mg_{0.66})$	14	0.665	9.102		
$(Si_{3.90}Al_{0.10})(Al_{0.36}Fe^{3+}_{0.77}Fe^{2+}_{0.21}Mg_{0.68})$	15	0.665	9.054		
$(Si_{3.88}Al_{0.12})(Al_{1.33}Fe^{3+}_{0.01}Fe^{2+}_{0.02}Mg_{0.54})$	16	0.591	9.000		
				Radoslovich & Norrish (1962)	
$(Si_{3.6}Al_{0.4})(Fe^{3+}_{1.4}Mg_{0.7})$	35	0.670	9.020		
$Si_4(Al_{0.07}Fe^{3+}_{0.93}Fe^{2+}_{0.24}Mg_{0.77})$	36	0.686	9.050		
$(Si_{3.86}Al_{0.14})(Al_{0.75}Fe^{3+}_{0.36}Fe^{2+}_{0.2}Mg_{0.68})$	37	0.643	9.060		
$(Si_{3.74}Al_{0.26})(Al_{0.18}Fe^{3+}_{1}Fe^{2+}_{0.57}Mg_{0.57})$	38	0.688	9.080		
				Buckley *et al.* (1978)	
$Si_{4.01}(Al_{0.15}Fe^{3+}_{0.81}Fe^{2+}_{0.39}Mg_{0.75})$	A	0.689	9.053[d]		
$Si_{4.09}(Al_{0.38}Fe^{3+}_{0.49}Fe^{2+}_{0.37}Mg_{0.71})$	B	0.676	9.044[d]		
$(Si_{3.83}Al_{0.17})(Al_{0.28}Fe^{3+}_{0.78}Fe^{2+}_{0.22}Mg_{0.69}Ti_{0.01})$	C	0.670	9.052[d]		
$(Si_{3.96}Al_{0.04})(Al_{0.18}Fe^{3+}_{0.87}Fe^{2+}_{0.24}Mg_{0.71})$	D	0.678	9.050[d]		
$Si_{4.01}(Al_{0.58}Fe^{3+}_{0.56}Fe^{2+}_{0.24}Mg_{0.53})$	E	0.649	9.047[d]		
$Si_{4.01}(Al_{0.13}Fe^{3+}_{0.95}Fe^{2+}_{0.26}Mg_{0.64})$	F	0.680	9.053[d]		
$(Si_{3.95}Al_{0.05})(Al_{0.02}Fe^{3+}_{1.08}Fe^{2+}_{0.19}Mg_{0.71})$	G	0.683	9.061[d]		
$(Si_{3.99}Al_{0.01})(Al_{0.41}Fe^{3+}_{0.75}Fe^{2+}_{0.25}Mg_{0.45})$	H	0.657	9.043[d]		
$(Si_{3.83}Al_{0.17})(Al_{0.1}Fe^{3+}_{0.77}Fe^{2+}_{0.19}Mg_{1.08})$	I	0.690	9.051[d]		
$(Si_{3.91}Al_{0.09})(Al_{0.39}Fe^{3+}_{0.66}Fe^{2+}_{0.2}Mg_{0.72}Ti_{0.01})$	Q	0.664	9.048[d]		
$(Si_{3.95}Al_{0.05})(Al_{0.15}Fe^{3+}_{1.24}Fe^{2+}_{0.13}Mg_{0.37}Ti_{0.01})$	BM32709	0.660	9.069[d]		
Glauconites				Buckley *et al.* (1978)	
$(Si_{3.57}Al_{0.43})(Al_{0.21}Fe^{3+}_{1.02}Fe^{2+}_{0.64}Mg_{0.26})$	1L	0.684	9.091[d]		
$(Si_{3.62}Al_{0.38})(Al_{0.42}Fe^{3+}_{0.96}Fe^{2+}_{0.43}Mg_{0.28})$	5D	0.661	9.088[d]		
$(Si_{3.77}Al_{0.23})(Al_{0.31}Fe^{3+}_{0.95}Fe^{2+}_{0.37}Mg_{0.42})$	9D	0.668	9.069[d]		
$(Si_{3.81}Al_{0.19})(Al_{0.44}Fe^{3+}_{0.82}Fe^{2+}_{0.51}Mg_{0.30})$	11D	0.666	9.081[d]		
$(Si_{3.77}Al_{0.23})(Al_{0.36}Fe^{3+}_{0.98}Fe^{2+}_{0.21}Mg_{0.46})$	12D	0.657	9.073[d]		
$(Si_{3.77}Al_{0.23})(Al_{0.35}Fe^{3+}_{0.99}Fe^{2+}_{0.21}Mg_{0.45})$	13D	0.657	9.072[d]		
$(Si_{3.76}Al_{0.24})(Al_{0.42}Fe^{3+}_{0.92}Fe^{2+}_{0.21}Mg_{0.49})$	14D	0.654	9.072[d]		

(*Continued*)

https://doi.org/10.1180/clm.2023.20 Published online by Cambridge University Press

Table 6. (*Continued.*)

Mica (anhydrous composition)	Sample[a]	*R*	*b*	References	Comments
$(Si_{3.75}Al_{0.25})(Al_{0.36}Fe^{3+}_{0.98}Fe^{2+}_{0.24}Mg_{0.45})$	15D	0.658	9.073[d]		
$(Si_{3.79}Al_{0.21})(Al_{0.33}Fe^{3+}_{0.99}Fe^{2+}_{0.26}Mg_{0.45})$	16D	0.661	9.070[d]		
$(Si_{3.77}Al_{0.23})(Al_{0.32}Fe^{3+}_{0.97}Fe^{2+}_{0.23}Mg_{0.39})$	16L	0.658	9.077[d]		
$(Si_{3.65}Al_{0.35})(Al_{0.45}Fe^{3+}_{0.91}Fe^{2+}_{0.15}Mg_{0.40})$	18B	0.645	9.079[d]		
$(Si_{3.69}Al_{0.31})(Al_{0.40}Fe^{3+}_{1.05}Fe^{2+}_{0.15}Mg_{0.41})$	19	0.648	9.078[d]		
$(Si_{3.57}Al_{0.43})(Al_{0.37}Fe^{3+}_{1.15}Fe^{2+}_{0.17}Mg_{0.33})$	21	0.648	9.089[d]		
$(Si_{3.34}Al_{0.66})(Fe^{+}_{1.42}Fe^{2+}_{0.60}Mg_{0.29})$	23L	0.689	9.108[d]		
$(Si_{3.69}Al_{0.31})(Al_{0.08}Fe^{3+}_{1.26}Fe^{2+}_{0.12}Mg_{0.55})$	27L	0.669	9.100[d]		
$(Si_{3.83}Al_{0.17})(Al_{0.04}Fe^{3+}_{1.17}Fe^{2+}_{0.13}Mg_{0.72})$	29D	0.678	9.093[d]		
$(Si_{3.82}Al_{0.1})(Al_{0.13}Fe^{3+}_{1.16}Fe^{2+}_{0.13}Mg_{0.60})$	34D	0.669	9.088[d]		
$(Si_{3.81}Al_{0.19})(Fe^{3+}_{1.78}Fe^{2+}_{0.09}Mg_{0.43})$	35L	0.664	9.125[d]		
Al-rich illite and phengite				Drits *et al.* (2006)	
$(Si_{3.40}Al_{0.60})(Al_{1.75}Fe^{3+}_{0.08}Fe^{2+}_{0.01}Mg_{0.15})$	3	0.555	9.000		
$(Si_{3.41}Al_{0.59})(Al_{1.66}Fe^{3+}_{0.06}Fe^{2+}_{0.02}Mg_{0.28})$	6	0.566	9.005		
$(Si_{3.63}Al_{0.37})(Al_{1.41}Fe^{3+}_{0.10}Fe^{2+}_{0.07}Mg_{0.42})$	7	0.588	9.018		
$(Si_{3.51}Al_{0.49})(Al_{1.83}Fe^{3+}_{0.03}Fe^{2+}_{0.04}Mg_{0.10})$	8	0.551	8.952		
$(Si_{3.25}Al_{0.75})(Al_{1.84}Fe^{3+}_{0.09}Mg_{0.08})$	9	0.547	8.998		
$(Si_{3.45}Al_{0.55})(Al_{1.57}Fe^{3+}_{0.13}Mg_{0.28})$	10	0.568	9.012		
$(Si_{3.44}Al_{0.56})(Al_{1.27}Fe^{3+}_{0.40}Fe^{2+}_{0.13}Mg_{0.24})$	11	0.594	9.046		
$(Si_{3.54}Al_{0.46})(Al_{1.24}Fe^{3+}_{0.24}Fe^{2+}_{0.12}Mg_{0.44})$	12	0.602	9.042		
$(Si_{3.80}Al_{0.20})(Al_{1.16}Fe^{3+}_{0.09}Fe^{2+}_{0.17}Mg_{0.57})$	13	0.614	9.006		
$(Si_{3.80}Al_{0.20})(Al_{1.18}Fe^{3+}_{0.25}Fe^{2+}_{0.01}Mg_{0.56})$	14	0.602	9.007		
$(Si_{3.40}Al_{0.60})(Al_{1.68}Fe^{3+}_{0.14}Mg_{0.20})$	15	0.561	9.006		
$(Si_{3.27}Al_{0.73})(Al_{1.85}Fe^{3+}_{0.04}Mg_{0.15})$	16a	0.551	9.000		
$(Si_{3.28}Al_{0.72})(Al_{1.87}Fe^{3+}_{0.04}Mg_{0.11})$	17a	0.547	8.994		
$(Si_{3.47}Al_{0.53})(Al_{1.76}Fe^{3+}_{0.04}Mg_{0.26}Ti_{0.01})$	19	0.561	9.006		
$(Si_{3.39}Al_{0.61})(Al_{1.60}Fe^{3+}_{0.20}Mg_{0.24}Ti_{0.01})$	21	0.568	9.005		
$(Si_{3.39}Al_{0.61})(Al_{1.54}Fe^{3+}_{0.14}Mg_{0.335}Ti_{0.02})$	22	0.574	9.005		
$(Si_{3.42}Al_{0.58})(Al_{1.58}Fe^{3+}_{0.11}Mg_{0.29}Ti_{0.01})$	23	0.568	9.005		
$(Si_{3.48}Al_{0.52})(Al_{1.73}Fe^{3+}_{0.06}Mg_{0.20}Ti_{0.01})$	24	0.557	9.005		
$(Si_{3.30}Al_{0.70})(Al_{1.90}Fe^{3+}_{0.02}Mg_{0.08}Ti_{0.04})$	25	0.545	9.005		

b is a crystallographic parameter (Å).
R = mean ionic radius of octahedral cations (Å) calculated with $r(Li^+) = 0.76$ Å (see text for details).
[a]Sample reference in the paper.
[b]Typographical error: original $(Mg_{2.125}Al_{1.250})$.
[c]Original compositions were with Ti in tetrahedra (except sample 45). Ti was reallocated to octahedral sites, and the corresponding amount of octahedral Al was moved to tetrahedral sites. XRD data are available in a table that has been kindly provided to us by the author M. Rieder.
[d]Extracted from Fig. 3.

closer to the global trend. In addition, the compositional gap situated at $0.610 < R < 0.650$ for $r(^{VI}Li^+) = 0.76$ Å (Fig. 12a) now disappears (Fig. 12b). The scattering of Li-mica data points is also reduced significantly comparing the $b/b_{tet.}$ *vs* *R* and the % O enlargement *vs* *R* plots for the two values of $r(^{VI}Li^+)$; not shown for $r(^{VI}Li^+) = 0.76$ Å), arguing for the suitability of a $r(^{VI}Li^+)$ value close to 0.6 Å, agreeing well with Radoslovich (1962).

The dependence of the rate of tetrahedral substitutions on *b* observed for Li-micas (Fig.13b) cannot be generalized for the entire mica group. True micas display similar tetrahedral trisilicic compositions but contrasting *b* values, as illustrated clearly by *b* of muscovite (~8.99 Å) and phlogopite (~9.20 Å; Table 6). However, the various tetrahedral substitution rates are responsible for some data scattering (as for smectites), as revealed through the

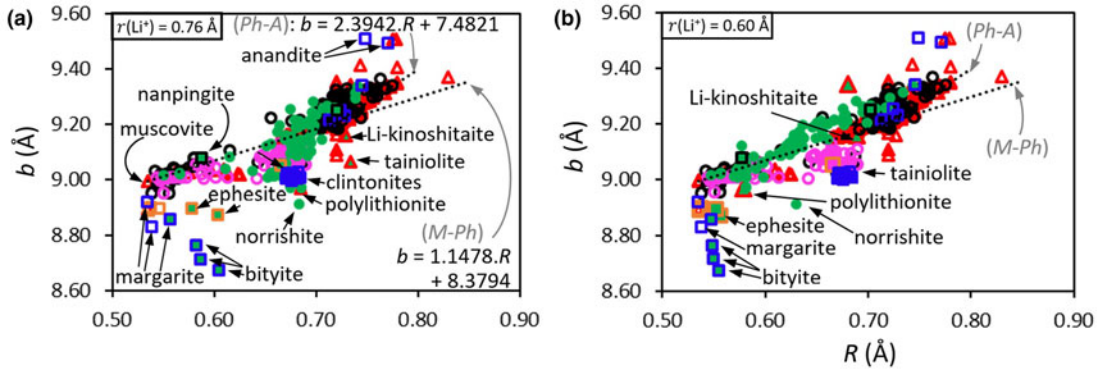

Figure 12. *b* *vs* mean ionic radius of octahedral cations *R* for micas (Table 6). (*M–Ph*) and (*Ph–A*) correspond to muscovite–phlogopite and phlogopite–annite regression lines, respectively. Red triangles = synthetic micas (details in Fig. 15); black open circles = true K-micas; pink open circles = interlayer-deficient K-micaceous samples; green circles and other symbols filled in green = Li-containing micas; orange open squares = Na-micas; black open square = Cs–Rb mica; blue open squares = brittle micas. (a) *R* calculated with $r(Li^+) = 0.76$ Å. (b) *R* calculated with $r(Li^+) = 0.60$ Å (see text for details).

https://doi.org/10.1180/clm.2023.20 Published online by Cambridge University Press

Table 7. Parameters of the regressions calculated for the synthetic micas (Figs 15–19).

Regression type	$b = RA + B$	R^2	Number of points	$b/b_{tet.} = RC + D$	R^2	% O enlargement = $RE + F$	R^2
(*M–Ph*)	$K(Si_3Al)(Mg_{3x/2}Al_{2-x}\square_{1-x/2})O_{10}(OH)_2$						
	$1.1478R + 8.3794$			$0.1229R + 0.8975$		$-37.514R + 24.23$	
(*Ph–A*)	$K(Si_3Al_1)(Mg_xFe^{2+}_{3-x})O_{10}(OH)_2$						
	$2.3942R + 7.4821$			$0.2564R + 0.8014$		$-20.056R + 11.66$	
Dioctahedral							
Schmidt *et al.* (2001)	$K(Si_{3+x}Al_{1-x})(Al_{2-x}Mg_x)O_{10}(OH)_2$						
			16	$0.2553R + 0.827$	0.9805		
Trioctahedral							
Robert (1976)	$K(Si_{3-x+2y}Al_{1+x-2y})(Mg_{3-x-y}Al_x\square_y)O_{10}(OH)_2$						
All except sample 29	$1.1509R + 8.3841$	0.9499	28 ($y \neq 0$)	$0.2515R + 0.8038$	0.7894	$-35.19R + 22.638$	0.9935
$y = 0$	$0.8049R + 8.6308$	0.9895	7	$0.3972R + 0.7005$	0.9995		
$y = 0.025$	$1.5032R + 8.1349$	–	2	$0.4671R + 0.6518$	–		
$y = 0.05$	$1.6159R + 8.064$	–	2	$0.4744R + 0.6485$	–		
$y = 0.075$	$1.7865R + 7.9483$	–	2	$0.4919R + 0.6376$	–		
$y = 0.1$	–	–	3	$0.4511R + 0.6667$	0.9982		
$y = 0.125$	$0.4973R + 8.8279$	–	2	$0.3477R + 0.7382$	–		
$y = 0.15$	$0.7395R + 8.6638$	–	2	$0.3729R + 0.7221$	–		
$y = 0.175$	–	–	3	$0.378R + 0.7198$	0.9922		
$y = 0.225$	$0.5891R + 8.7583$	–	2	$0.3478R + 0.7416$	–		
$y = 0.25 - 0.5x$	$-3.8609R + 11.918$	0.9946	3	$1.418R + 0.0188$	0.9997		
$y = 0.5 - x$	–	–	4 (x, $y \neq 0$)	$1.4313R - 0.0137$	0.9879		
$y = 0.75 - 1.5x$	$1.3164R + 8.2673$	0.9861	6 ($y \neq 0$)	$0.9411R + 0.3323$	0.9994		
$y = 1 - 2x$	$1.1666R + 8.3777$	0.8644	4 ($y \neq 0$)	$1.0084R + 0.2935$	0.9409		
$y = 1.25 - 2.5x$	–	–	3 ($y \neq 0$)	$0.6029R + 0.5694$	0.9853		
$y = 1.5 - 3x$	$1.1509R + 8.33841$	–	2 ($y \neq 0$)	$0.6368R + 0.5494$	–		
Hewitt & Wones (1975)	$K(Si_{3-z}Al_{1+z})(Mg_xFe^{2+}_{3-x-z}Al_z)O_{10}(OH)_2$						
All	$1.8744R + 7.8968$	0.8148	28	$0.3274R + 0.7469$	0.972	$-26.498R + 16.754$	0.8885
$z = 0$	$2.4105R + 7.4706$	0.9991	6	$0.2582R + 0.8001$		$-20.271R + 11.833$	0.9985
$z = 0.25$	$2.6255R + 7.3529$	0.9992	5	$0.2798R + 0.7826$		$-18.512R + 10.86$	0.9988
$z = 0.5$	$2.8435R + 7.2106$	0.9992	8	$0.3016R + 0.7648$		$-16.649R + 9.7787$	0.9975
$z = 0.63$	$2.7579R + 7.2846$	–	2	$0.2582R + 0.8001$		$-17.768R + 10.716$	
$z = 0.75$	$2.9067R + 7.2006$	0.9951	4	$0.2918R + 0.7707$		$-16.334R + 9.9239$	0.9838
	$K(Si_{3-z}Al_{1+z})(Fe^{2+}_{3-z}Al_z)O_{10}(OH)_2$						
	$1.0552R + 8.5304$	0.9662	7	$0.3513R + 0.7277$		$-34.453R + 22.921$	0.997
	$K(Si_{3-z}Al_{1+z})(Mg_{3-z}Al_z)O_{10}(OH)_2$						
	$1.1096R + 8.407$	0.9912	5	$0.4166R + 0.6859$		$-35.267R + 22.629$	0.999

comparison between the b and $b/b_{tet.}$ *vs* R plots (Figs 12b & 14a, respectively). Two main trends between $b/b_{tet.}$ and R are revealed (Fig. 14a). One trend follows the (*Ph–A*)' line, which was calculated simply using the same data as that for (*Ph–A*) and the trisilicic composition for the $b_{tet.}$ value and is mostly concerned with trioctahedral micas in a limited R range ($0.670 < R < 0.780$). The second trend follows a curve that continuously links dioctahedral to trioctahedral K-micas and involves micas with various compositions, including Li-micas, and micaceous samples.

Two main trends are also observed in the % O enlargement *vs* R plot (Fig. 14b). One trend follows the (*M–Ph*)° line, plotted using the muscovite and phlogopite end members, and mostly concerns micas with full interlayers, regardless of their dioctahedral or trioctahedral nature. The second trend, with a greater slope, mostly concerns the interlayer-depleted micas (i.e. glauconites, celadonites, illites and phengites), indicating that the O sheets are thicker for the same R in these micaceous samples. The three b *vs* R (Fig. 12b), $b/b_{tet.}$ *vs* R (Fig. 14a) and % O enlargement *vs* R (Fig. 14b) plots indicate that, for most of the micas, the octahedral flattening is controlled mainly by R, and that it gradually decreases with decreasing misfit between the T and O sheets, as suggested by Toraya (1981).

Some samples do not follow these general trends: mainly Na-micas, most of the brittle micas and synthetic Ge-micas and ferri-annites.

On the Al side ($0.535 \leq R \leq 0.560$), Na-micas (i.e. paragonite and ephesite, a trioctahedral mica with an ideal SF of $(Si_2Al_2)(LiAl_2)(OH)_2Na$)) and brittle Ca-micas (i.e. margarite and bityite, a trioctahedral mica with an ideal SF of $(Si_2AlBe)_4(LiAl_2)(OH)_2Ca$)) exhibit lower b, $b/b_{tet.}$ and % O enlargement values than muscovite. This indicates a significant influence of the nature of the interlayer cation on b and a more limited accommodation of the O sheets to increase their lateral dimensions compared to their K counterparts. Accordingly, small interlayer cations such as Na and Ca allow greater tetrahedral rotations than K^+, which appears to induce a stretching of the O sheets (Bailey, 1984b). Muscovite exhibits a $b/b_{tet.}$ of ~0.96 ($\alpha \approx 15°$), whereas margarite, bityite and ephesite exhibit the lowest $b/b_{tet.}$, corresponding to α as high as 20–23°; these values have been confirmed using structural refinements (Guggenheim, 1984; Brigatti & Guggenheim, 2002).

In brittle micas, the T sheets are much larger than the O sheets due to the high rate of tetrahedral substitution (~2Al pfu; Table 6) and the great tetrahedral rotations reduce the T sheet dimensions. Paragonite also has a relatively large α (~17°) due to the small size of the interlayer Na (Guggenheim, 1984). Note that nanpingite (ideally the muscovite Cs-counterpart) follows the (*M–Ph*) trends well (Figs 12b & 14a,b).

On the trioctahedral side, the Na-micas (preiswerkite) and Ca-micas (clintonite, also previously named xanthophyllite; Table 6) exhibit lower b, $b/b_{tet.}$ and % O enlargement values than their K counterparts, as observed for the Na- and Ca–Al-rich micas. Accordingly, preiswerkite and clintonite exhibit $b/b_{tet.}$ corresponding to large α (~17° and ~21°, respectively),

https://doi.org/10.1180/clm.2023.20 Published online by Cambridge University Press

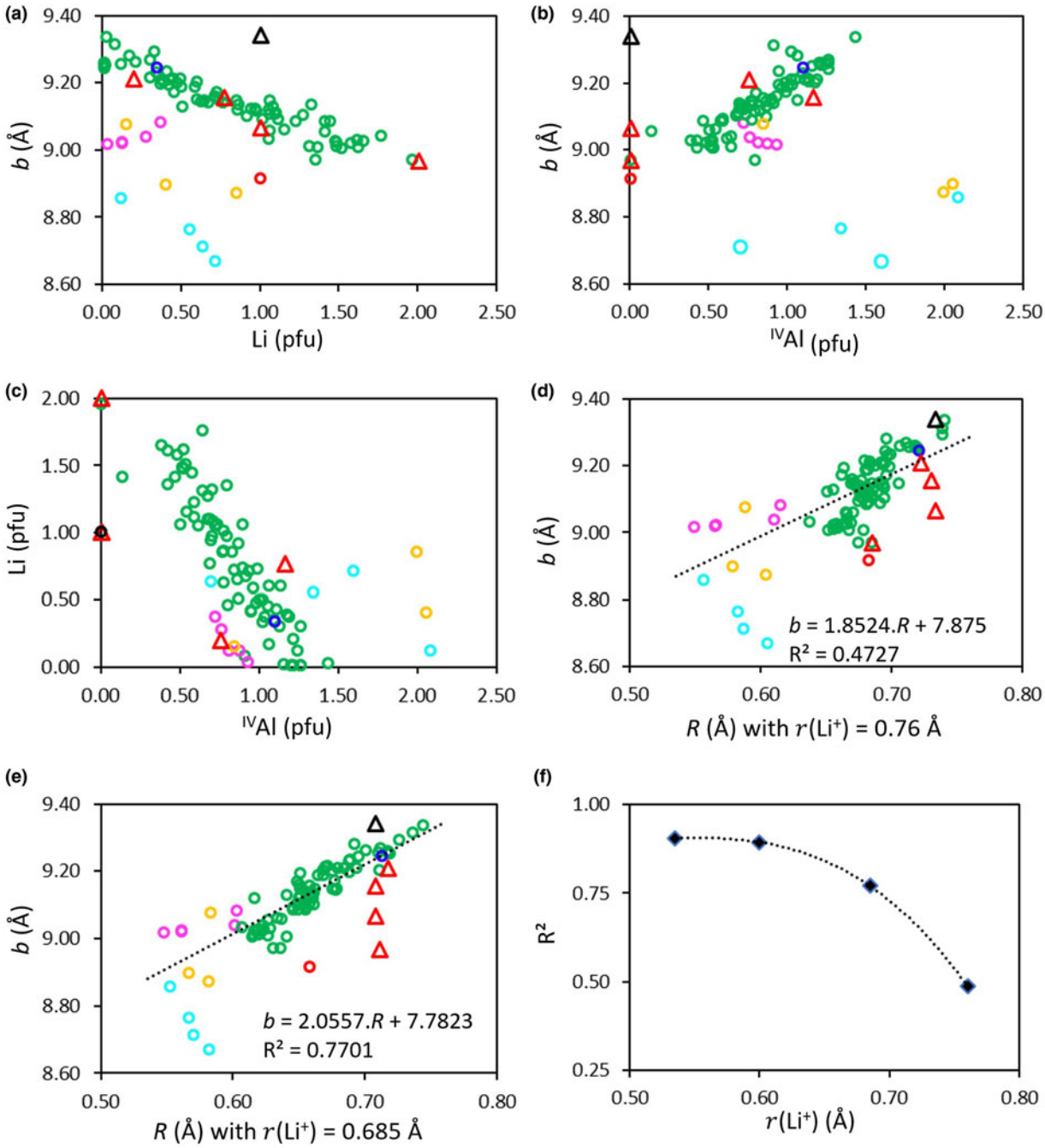

Figure 13. Evolution of structural parameters in Li-micas (Table 6), with circles representing natural samples and triangles representing synthetic samples: green circles = true K- micas; pink circles = Li-muscovites; yellow circles = Na-micas; dark blue circle = Rb–Cs mica; light blue circles = brittle micas; red circle = norrishite ($Si_4(LiMn_2^{3+})K$ mica; red triangles = K–Si micas; black triangle = K–Ge mica. (a) *b vs* octahedral lithium content. (b) *b vs* tetrahedral aluminium content. (c) Octahedral lithium *vs* tetrahedral aluminium. (d) *b vs* the mean ionic radius of octahedral cations *R* with $r(Li^+)$ = 0.760 Å. (e) *b vs R* with $r(Li^+)$ = 0.685 Å. (f) Evolution of the coefficient of the linear regressions for the $r(Li^+)$ considered.

agreeing well with the values determined using structural refinement (~20° and 23–25°, respectively; Brigatti & Guggenheim, 2002).

Brittle Ba-micas (i.e. kinoshitaites and anandites) exhibit various behaviours. Kinoshitaites globally follow the trend of the K-micas with similar *R* due to the similar sizes of the Ba and K interlayer cations (Shannon, 1976). However, anandites exhibit greater *b* (Fig. 12b) and % O enlargement (Fig. 14b) than their K counterparts. This is mainly due to their high content of tetrahedral iron, which induces large T sheet dimension. Consequently, the O sheet has to enlarge comparatively more than the Al micas to reduce the dimensional misfit. The same observation is made for the synthetic tetra-ferri-annites (ideally $Si_{3.0}Fe^{3+}_{1.0})(Fe^{2+}_{3.0})O_{10}OH_2$ K), whose Cs-form has the largest unit-cell volume reported to date for 1*M* micas (Brigatti & Guggenheim, 2002).

For synthetic Ge-micas, due to the ionic radii of Ge^{4+} and Si^{4+} (0.39 and 0.26 Å, respectively; Table 1), the *b* values are greater

https://doi.org/10.1180/clm.2023.20 Published online by Cambridge University Press

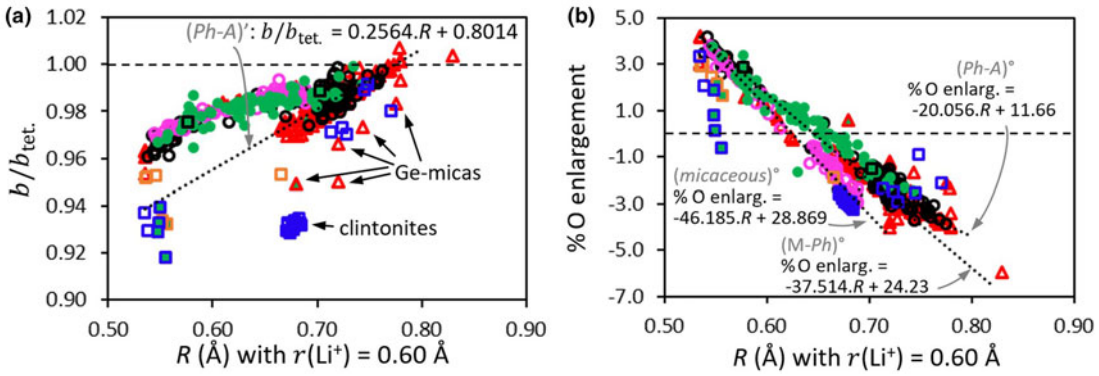

Figure 14. (a) $b/b_{tet.}$ *vs* the mean ionic radius of octahedral cations *R* for the same samples (and colour code) as Fig.12. (*Ph–A*)' corresponds to the phlogopite–annite regression line. (b) Percentage of octahedral enlargement (Equation 6; see text for details) *vs R* for the same samples (and colour code) as Fig. 12. (*M–Ph*)° corresponds to the muscovite–phlogopite regression line and (*micaceous*)° corresponds to the interlayer-depleted micas regression line.

than their silicate counterparts (Figs 12 & 15a), whereas the $b/b_{tet.}$ values are lower (Figs 14a & 15b). Accordingly, Martin *et al.* (1992) observed an increase in the angle α for synthetic Mg-, Ni- and Co-SiGe talc tetrahedral solid solutions when the germanium content increases. As expected when adjusting the O sheet dimensions to the larger T sheets, the % O enlargement is greater for Ge-micas than for Si-micas for a same *R* (Figs 14b & 15c).

To assess the origins of the observed trends, we focus on synthetic micas because their chemical composition is less complex than that of natural systems and because chemical joins are available (Fig. 15a). The dataset of synthetic mica samples reveals generally similar trends to those of natural mica samples (Figs 12 & 14). The $b/b_{tet.}$ *vs R* plot for all of the synthetic samples reveals two main distinct but parallel trends for dioctahedral

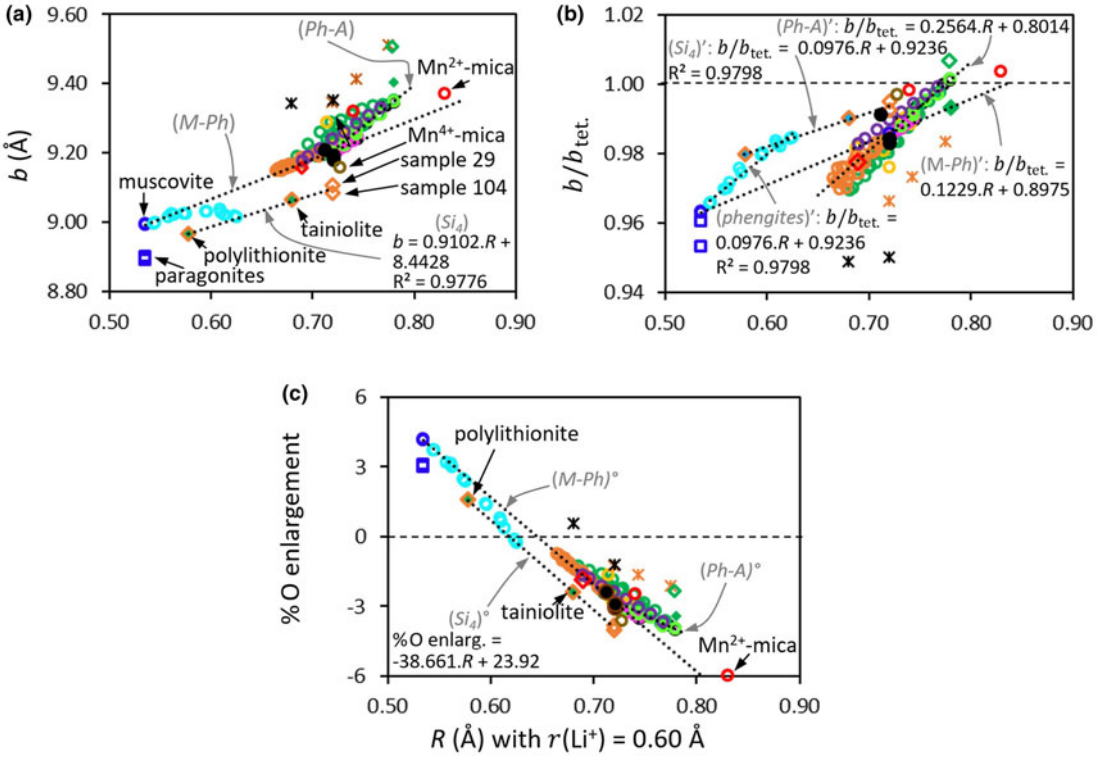

Figure 15. (a) *b vs* mean ionic radius of octahedral cations *R* for synthetic micas (Table 6). (*M–Ph*) and (*Ph–A*) correspond to muscovite–phlogopite and phlogopite–annite regression lines, respectively. (*Si*$_4$) corresponds to the tetrasilicic micas regression line. Dark blue circles = muscovite; light blue circles = $K(Si_{3+x}Al_{1-x})(Al_{2-x}Mg_x)O_{10}(OH)_2$ $2M_1$ mica series (Zviagina & Drits, 2019); orange circles = $K(Si_{3-x+2y}Al_{1+x-2y})(Mg_{3-x-y}Al_x\square_y)O_{10}(OH)_2$ series (Robert, 1976); black full circles = phlogopites; green circles = $K(SiAl)_4(Fe^{2+}\ Fe^{3+}Mg)_3$ series; pink circles = JLRMgCo; light green circles = JLRMgFe; purple circles = FeNiGR; black circles = $K(Si_3Al_1)(Mg_{3-x}R^{2+}{}_x)$ series (Hazen & Wones, 1972); red circles = Zn- and Mn-micas (Frondel & Ito, 1966); brown circle = Mn^{4+}-mica (sample 110; Brigatti & Guggenheim, 2002); orange diamonds = tetrasilicic micas; filled in green symbols = Li-rich; red diamond = Li-kinoshitaite; green diamonds = ferri-annite, full symbol = K, empty symbol = Cs; blue squares = paragonites; crosses = Ge-micas, black = 4Ge, orange = 3GeAl. (b) $b/b_{tet.}$ ratio *vs R* for the same samples (and colour code) as (a). (*M–Ph*)', (*Ph–A*)' and (*Si*$_4$)' correspond to muscovite–phlogopite, phlogopite–annite and tetrasilicic micas regression lines, respectively. (*Phengites*)' corresponds to the $2M_1$ micas in the muscovite–phengite–aluminoceladonite series regression line. (c) Percentage of octahedral enlargement *vs R* for the same samples (and colour code) as (a). (*M–Ph*)°, (*Ph–A*)° and (*Si*$_4$)° correspond to the muscovite–phlogopite, phlogopite–annite and tetrasilicic micas regression lines, respectively.

https://doi.org/10.1180/clm.2023.20 Published online by Cambridge University Press

(muscovite–aluminoceladonite) and trioctahedral micas (phlogopite–annite; Fig. 15b). However, data for synthetic micas are lacking, especially for the compositional range corresponding to $R \approx 0.650$. In natural micas, this compositional gap is filled by Li-micas and by celadonites and glauconites (Fig 12b & 14b).

Except for the Ni-mica, which is on the (*M–Ph*) and (*M–Ph*)' lines, all of the trioctahedral trisilicic micas, including the rather 'exotic' Cu^{2+}- and Co^{2+}-micas (Hazen & Wones, 1972), are on or close to the (*Ph–A*) correlation line (Fig. 15a) and are also located near the (*Ph–A*)' line due to their similar tetrahedral Al contents (Fig. 15b).

The synthetic Mn-mica approximately follows the muscovite–phlogopite trend in the *b*, $b/b_{tet.}$ and % O enlargement *vs R* plots (Fig. 15a–c). The % O enlargement is the smallest of all the dataset (–6% compared to hydroxides) and corresponds to the thickest O sheet very close to the dimensions of an unconstrained O sheet. Regarding the synthetic Fe^{2+} (annite) end member, $b/b_{tet.}$ is >1 (Fig. 15b). Unfortunately, the status of Mn is not sufficiently detailed (Frondel & Ito, 1966) to be confident regarding the greatest *R* and $b_{tet.}$ values. As Mn was assumed to be octahedral and divalent, some octahedral Mn^{3+} would have contributed to *R*, and thus the O sheet lateral dimensions would decrease, while tetrahedral Mn^{2+} would increase $b_{tet.}$ (Table 1).

Three synthetic mica series representing chemical joins will be studied in more detail below.

The first synthetic mica series corresponds to the dioctahedral mica series along the muscovite–aluminoceladonite join ($K(Si_{3+x}\ Al_{1-x})(Al_{2-x}Mg_x)O_{10}(OH)_2$ with $x \leq 1$) of Schmidt *et al.* (2001), which was also later studied and compared to natural samples by Zviagina & Drits (2019; Table 6). With increasing *R*, the dataset for these micas shifted away from the (*M–Ph*) line (Fig. 15a). Accordingly, Schmidt *et al.* (2001) and Zviagina & Drits (2019) reported a 'difficult to understand' reduction of *b* for the greatest Mg content. Schmidt *et al.* (2001) hypothesized that this reduction could be associated with a partial trioctahedral character, with some Mg possibly filling some M_1 octahedral sites (which are theoretically larger than the M_2 octahedra and are empty in ideally dioctahedral structures). Zviagina & Drits (2019) did not confirm this interpretation because their analysis of the M_1 octahedral site occupancies was negligible. Rather, these authors hypothesized that the change in the trend for *b* was associated with a decrease in mutual repulsion of octahedral cations with increasing contents of divalent cations, resulting in a reduced flattening of O sheets for the Mg-richest synthetic micas. This interpretation is confirmed by the % O enlargement *vs R* plot, where the data points deviate progressively from the (*M–Ph*)° line with increasing *R* (Fig. 15c). Moreover, the increase in octahedral charge related to the increase in the Al/Mg substitution rate in this sample series implies a concomitant decrease in tetrahedral charge to keep the layer charge at 1. The coupled increase in Mg and decrease in tetrahedral Al has a direct effect on the dimensional misfit reduction between the T and O sheets. A greater octahedral Mg content (and thus *R*), as hypothesized by Schmidt *et al.* (2001), would not make $b/b_{tet.}$ decreases, as observed in Fig. 15b.

The second synthetic mica series corresponds to Al–Mg micas $K(Si_{3-x+2y}Al_{1+x-2y})(Mg_{3-x-y}Al_x\square_y)O_{10}(OH)_2$ from the sample series of Robert (1976). These samples also lie on (or very close to) the (*M–Ph*) line, except sample 29 with the tetrasilicic composition $Si_4Mg_{2.5}$ (Fig. 15a). This sample series displays a wide range of compositions, with significant variation in the amounts of tetrahedral and octahedral Al as well as in octahedral Mg or vacant sites, whereas the octahedral occupancy ranges from 2.75 to 3, indicating a partial di-trioctahedral character. Robert (1976) observed a linear decrease in *b* with increasing octahedral Al content, but only for nine selected samples with a low number of vacant sites. As shown in Fig. 16a, *b* values for all of the di-trioctahedral Al–Mg micas (except sample 29) plotted as a function of *R* follow a linear regression, despite noticeable compositional changes in the T sheet composition, as ^{IV}Al contents range from 1 to 1.6 (Table 7). However, the regression coefficient is relatively low ($R^2 = 0.95$; Fig. 16a) and even decreases for the $b/b_{tet.}$ correlation ($R^2 = 0.79$; Fig. 16b), whereas it is very high for the % O enlargement ($R^2 = 0.99$; Fig. 16c). Several linear regressions can be observed between *b* and *R* depending on the parameter chosen (Table 7). For instance, if samples with the same *y* value in the SF are compared (i.e. samples having the same octahedral occupancy; Fig. 17a,b), then good correlations can be obtained using *b* or $b/b_{tet.}$ *vs R* graphs. As expected, the decrease in octahedral occupancy (increase in dioctahedral character) globally provokes a gradual decrease in the *b* dimension. For most *y* values, regressions with similar slopes can be drawn for at least the $b/b_{tet.}$ *vs R* graph (Fig. 17b & Table 7). Because this synthetic mica series can be described with *x* and *y* only, as seen in the general SF (i.e. Al, Mg, Si and vacant site amounts are interdependent), precise *b* or $b/b_{tet.}$ *vs R* graphs are also observed for each $y = f(x)$ series (Figs 17c & 17d, respectively, & Table 7). As a consequence, the scattering of data that is greater in the $b/b_{tet.}$ *vs R* plot compared to the *b vs R* plot (Figs 16b & 16a, respectively) results from the superimposition of accurate sub-relationships. The general relationship $b = 1.1509R + 8.3841$ is likely to satisfactorily (± 0.006) predict *b* from *R* for this synthetic mica series (except sample 29) but corresponds to a general trend only. Sample 29 is a tetrasilicic mica and behaves differently from the other samples of the series. For the same *R*, it exhibits lower *b* and % O enlargement and greater $b/b_{tet.}$ (Fig. 16a–c) than the other samples. However, the synthetic tetrasilicic micas (i.e. the synthetic F counterpart of sample 29 (sample 108, tetrasilicic fluorophlogopite), polylithionite and tainiolite (with Li_2Al and Mg_2Li octahedral composition, respectively; Table 6; Brigatti & Guggenheim, 2002) follow trends that include sample 29 (Fig. 15a–c). The data points of the four samples are approximately aligned on a line that is approximately parallel to the muscovite–phlogopite line on all of the plots (Fig. 15a–c). Moreover, when adding the few natural tetrasilicic micas (i.e. some celadonites and a polylithionite (sample 45); Table 6; Rieder *et al.*, 1970), a reasonably good regression is observed (Fig. 18a). Note that the samples of the muscovite–aluminoceladonite synthetic series of Schmidt *et al.* (2001) presented above ($K(Si_{3+x}Al_{1-x})(Al_{2-x}Mg_x)O_{10}(OH)_2$) move to the tetrasilicic mica '(Si_4)' regression line and follow these trends when approaching a tetrasilicic composition (Fig. 15a–c). Even if the (Si_4) regression cannot be considered as robust due to there being only few samples available and that the proposed revised $r(Li^+)$ of 0.6 Å used for calculating *R* for tainiolite and tetraferriphlogopite is only approximate, it argues indirectly for the suitability of $r(Li^+) \approx 0.6$ Å. Using the $r(Li^+)$ of 0.76 Å (Shannon, 1976) would lead to scattered data points (Fig. 18b).

Note that norrishite ($KSi_4(LiMn_2^{3+})$-mica, sample 111; Table 6; Brigatti & Guggenheim, 2002) is systematically outside of all of the trends (Figs 12–14 & 18). Accordingly, Brigatti & Guggenheim (2002) also observed an anomalous behaviour of this norrishite sample compared to the other micas, which they related to octahedral distortions induced by the Jahn–Teller effect.

https://doi.org/10.1180/clm.2023.20 Published online by Cambridge University Press

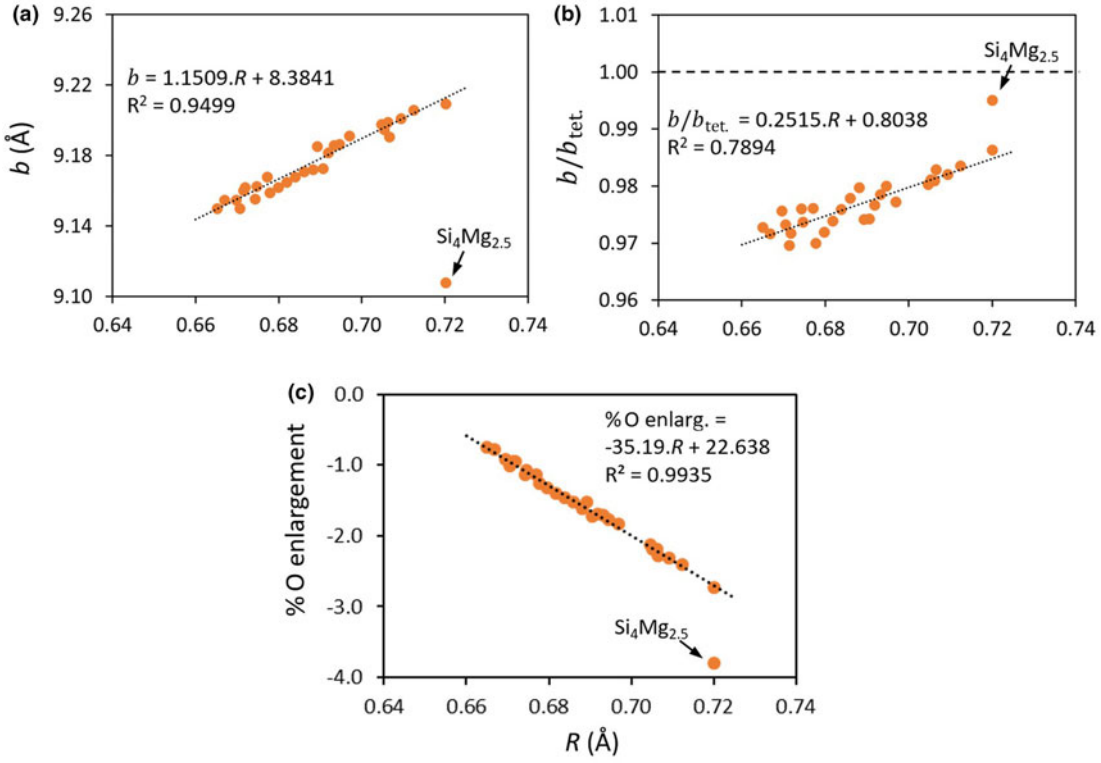

Figure 16. Focus on the $K(Si_{3-x+2y}Al_{1+x-2y})(Mg_{3-x-y}Al_x\square_y)O_{10}(OH)_2$ synthetic series of Robert (1976; Table 6). (a) *b vs* mean ionic radius of octahedral cations *R*. (b) $b/b_{tet.}$ *vs R*. (c) Percentage of octahedral enlargement *vs R*.

In conclusion, the impact of *R* on *b* is similar between tetrasilicic and trisilicic micas, and the lower *b* observed for tetrasilicic micas is related to a reduced flattening of O sheets compared to in trisilicic micas.

The third and last synthetic mica series that will be studied corresponds to the trioctahedral micas $(Si_{3-z}Al_{1+z})(Mg_xFe^{2+}{}_yAl_z)K$ (Hewitt & Wones, 1975; Redhammer & Roth, 2002; Mercier *et al.*, 2005) that appear slightly above the (*Ph–A*) and (*M–Ph*) lines in the *b vs R* and % O enlargement *vs R* plots (Figs 15a & 15c, respectively) and on or below the (*Ph–A*)' line in the $b/b_{tet.}$ *vs R* plot (Fig. 15b). A reduced scattering of data is noticed in the $b/b_{tet.}$ *vs R* plot, as illustrated by the respective regression coefficients (calculated using the Hewitt & Wones, (1975) series only, $R^2 = 0.82$, 0.97 and 0.89; Figs 19a, 19b & 19c, respectively). As for the previous synthetic mica series, several sub-relationships can be noticed that correspond to specific solid solutions. As an illustration, for constant values of *z* (Al content), linear regressions corresponding to the respective Mg–Fe^{2+} solid solutions are observed (Fig. 20a). In such solid solutions, *b* systematically decreases with the Fe^{2+}:Mg ratio, as expected considering the respective ionic radii of Mg and Fe^{2+} (Table 1). The slopes of these regression lines increase slightly from ~2.4 to 2.9 with increasing *z* (Table 7). For $z = 0$, the equation is very similar to that of the (*Ph–A*) line. The small difference is assigned to the fact that both regressions were calculated in different ways, using the end member data for the (*Ph–A*) regression and using the solid solution for $z = 0$. The slopes for each Mg–Fe^{2+} solid solution linear regression are more than twice as high as those for $(Si_{3-z}Al_{1+z})(Mg_{3-z}Al_z)K$ and $(Si_{3-z}Al_{1+z})(Fe^{2+}_{3-z}Al_z)K$, which exhibit similar slopes to each other (Table 7). The regression for the $(Si_{3-z}Al_{1+z})(Mg_{3-z}Al_z)K$ solid solution is close to that of the (*M–Ph*) line, and the small difference is due to the strictly trioctahedral character due to by Tschermak substitutions in the sample series of Hewitt & Wones (1975) compared to the di-trioctahedral muscovite–phlogopite solid solution. The $b/b_{tet.}$ *vs R* plot reveals that regressions also exist for each solid solution (Fig. 20b). The misfit between T and O sheets increases with decreasing *R* (i.e. with decreasing amounts of Fe^{2+} relative to Mg) and more severely with increasing Al content due to Tschermak substitutions and the antagonistic effect of Al, as discussed above for Al-serpentines. For the trisilicic Fe^{2+} end member, $b/b_{tet.}$ slightly exceeds 1 (Fig. 20b), suggesting a T sheet that is fully extended with a symmetry close to hexagonal to fit the large lateral O sheet dimension. Accordingly, the O sheet is the thickest of the series (Fig. 20c).

The increase of tetrahedral Al content induces an increase in lateral T sheet dimensions and the thinning of O sheets *via* octahedral flattening to reduce the misfit (Fig. 20c). For the same Al content, the octahedral flattening also increases with increasing Mg/Fe^{2+} substitution, contributing to the tetrahedral rotation to reduce the misfit. The cumulative effect is demonstrated here by the increase in the slope of the regressions with increasing Al content (i.e. increasing *z*; Fig. 20 & Table 7). As for the sample series of Robert (1976), the scattering of data observed for the series of Hewitt & Wones (1975) is assigned to the superimposition of accurate sub-relationships corresponding to limited solid solutions.

In light of the results obtained for synthetic micas, the observed scattering of data (Figs 12 & 14) for all of the datasets is mainly due to the chemical complexity of the samples, and multiple limited solid solutions probably exist between a multitude of end members.

https://doi.org/10.1180/clm.2023.20 Published online by Cambridge University Press

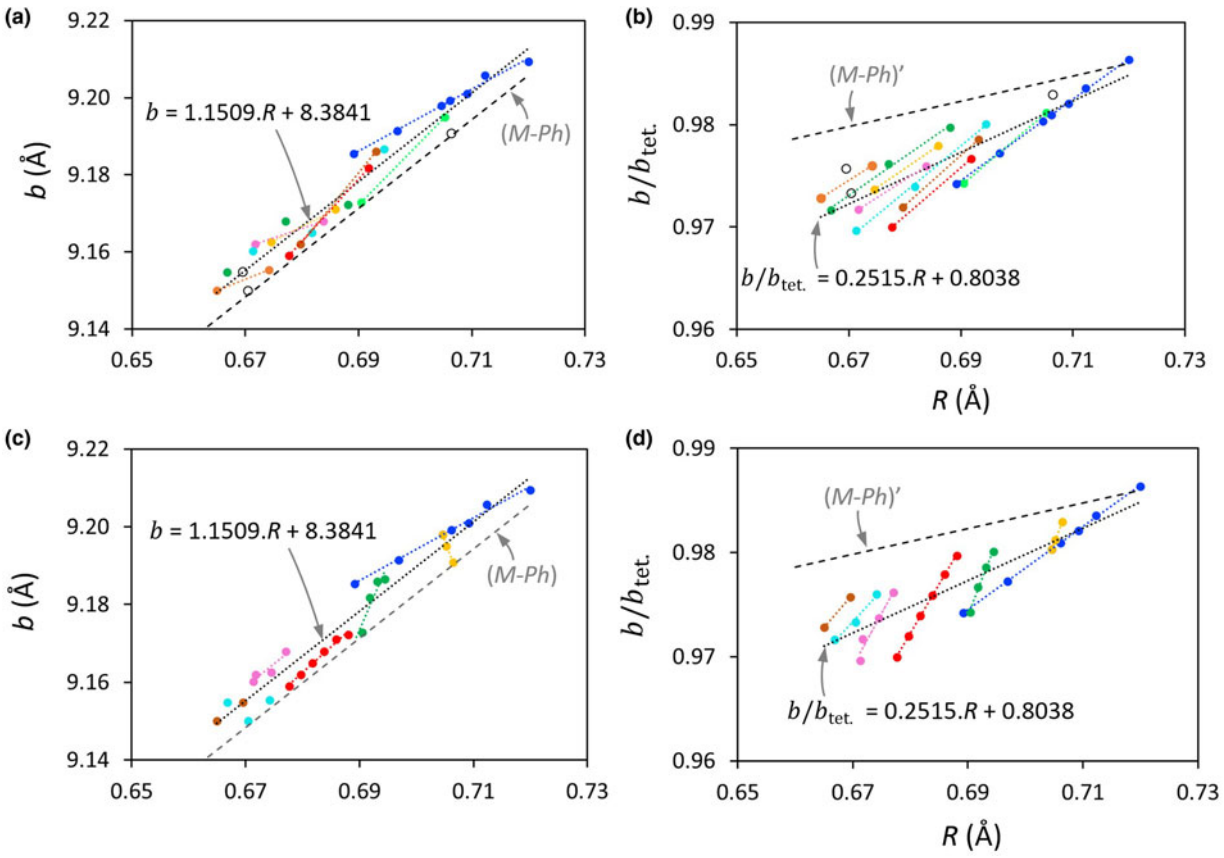

Figure 17. Focus on the $K(Si_{3-x+2y}Al_{1+x-2y})(Mg_{3-x-y}Al_x\square_y)O_{10}(OH)_2$ synthetic series of Robert (1976; Table 6; sample 29 is not represented). (a) *b vs R*. (b) $b/b_{tet.}$ ratio *vs R*: dark blue: $y = 0$; light green: $y = 0.025$; red: $y = 0.05$; brown: $y = 0.075$; light blue: $y = 0.1$; pink: $y = 0.125$; yellow: $y = 0.150$; dark green: $y = 0.175$; orange: $y = 0.225$; open circles: single data point. Evolution of (c) *b* or (d) the $b/b_{tet.}$ ratio with the mean ionic radius of octahedral cations *R*: dark blue: $y = 0$; yellow: $y = -0.5x + 0.25$; green: $y = -x + 0.5$; red: $y = -1.5x + 0,75$; pink: $y = -2x + 1$; light blue: $y = -2.5x + 1.25$; brown: $y = -3x + 1.5$. See Table 7 for the corresponding regressions. (*M–Ph*) and (*M–Ph*)' correspond to the muscovite–phlogopite regression lines.

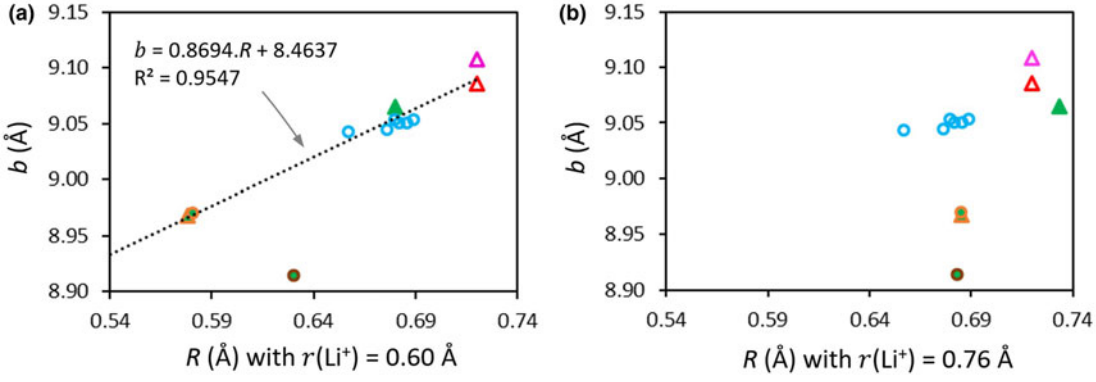

Figure 18. *b vs R* for tetrasilicic K-micas (Table 6). (a) *R* calculated with $r(Li^+) = 0.6$ Å. (b) *R* calculated with $r(Li^+) = 0.76$ Å. Triangles = synthetic samples: pink = $Mg_{2.5}(OH)_2$-mica (sample 29; Robert, 1976); red = $Mg_{2.5}F_2$-mica (sample 104; Brigatti & Guggenheim, 2002); green = Mg_2Li-mica (tainiolite, sample 105; Brigatti & Guggenheim, 2002); orange = $AlLi_2$–mica (polylithionite). Circles = natural samples: orange = polylithionite (sample 45; Rieder, 1970); blue = celadonites; brown = norrishite ($(LiMn_2^{3+})$-mica, sample 111; Brigatti & Guggenheim, 2002). Symbols filled in green = Li-containing micas.

Chlorites

Chlorites are phyllosilicates composed of 2:1 layers whose negative charge, arising mainly from heterovalent tetrahedral substitutions, is most often balanced by the presence of a positively charged O sheet in the interlayer space (Fig. 1a; e.g. Bailey, 1991a). The structure of chlorite is then globally electrostatically neutral, with a general SF of $(Si_{4-x}Al_x)(R^{3+}{}_yR^{2+}{}_z\square_v)O_{10}(OH)_8$, where $\square$ is a vacant site and $y + z + v = 6$. The composition of the layer is $(Si_{4-x}Al_x)(R^{3+}R^{2+}\square)_3O_{10}(OH)_2$ and that of the interlayer octahedral sheet is $(R^{3+}R^{2+}\square)_3(OH)_6$. It is difficult to determine the composition of each of them accurately (e.g. Zazzi *et al.*, 2006), especially because the chemical composition of chlorites is

https://doi.org/10.1180/clm.2023.20 Published online by Cambridge University Press

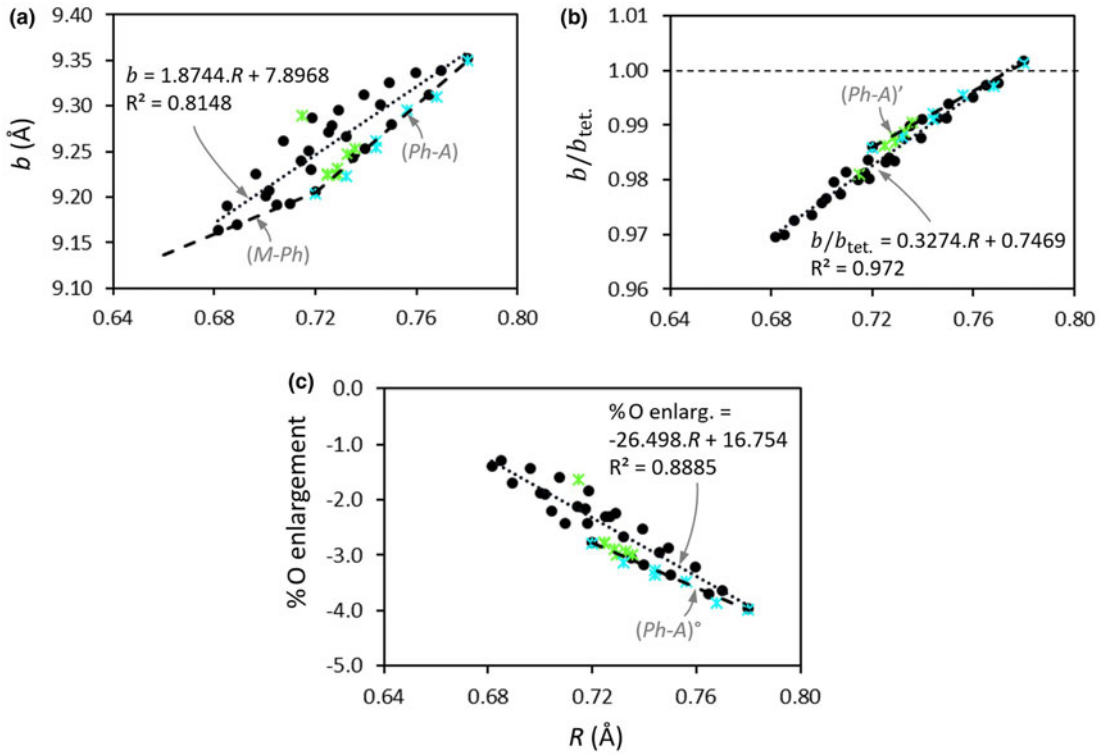

Figure 19. Focus on the $K(Si_{3-z}Al_{1+z})(Mg_xFe^{2+}{}_yAl_z)O_{10}(OH)_2$ synthetic series. Black circles from Hewitt & Wones (1975), green crosses from Redhammer & Roth (2002), blue crosses from Mercier *et al.* (2005; Table 6). (a) *b vs* mean ionic radius of octahedral cations *R*. (b) $b/b_{tet.}$ *vs R*. (c) Percentage of octahedral enlargement *vs R*. The dashed lines correspond to muscovite–phlogopite (*M–Ph*) and phlogopite–annite (*Ph–A*) regression lines. The dotted line is the regression calculated using the Hewitt & Wones (1975) data.

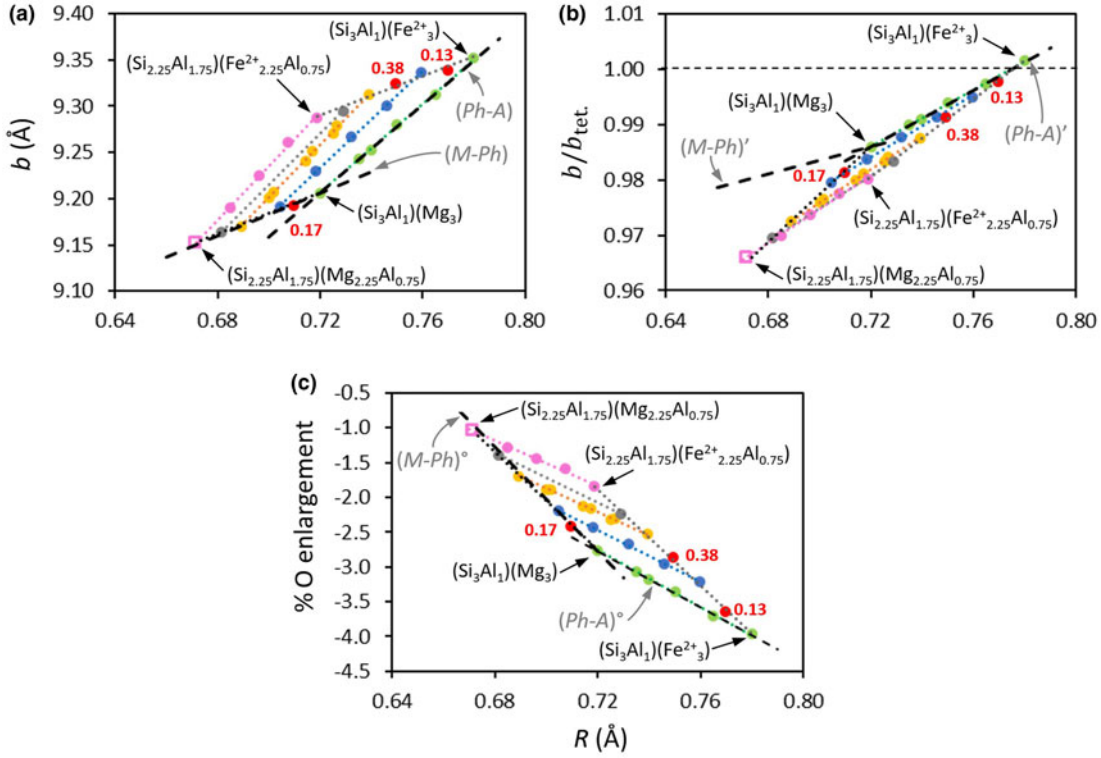

Figure 20. Focus on the $K(Si_{3-z}Al_{1+z})(Mg_xFe^{2+}{}_yAl_z)O_{10}(OH)_2$ synthetic series of Hewitt & Wones (1975; Table 6). Evolutions of (a) *b*, (b) $b/b_{tet.}$ ratio and (c) percentage of octahedral enlargement with the mean ionic radius of octahedral cations *R* for green circles: $z = 0$; blue circles: $z = 0.25$; yellow circles: $z = 0.50$; grey circles: $z = 0.63$; pink circles: $z = 0.75$; pink open square: calculated by extrapolation; red circles: single data point with the indicated *z* value. Dotted lines = linear regression for each *z* series (see Table 7 for the corresponding regressions). The dashed lines correspond to muscovite–phlogopite (*M–Ph*) and phlogopite–annite (*Ph–A*) regression lines.

https://doi.org/10.1180/clm.2023.20 Published online by Cambridge University Press

very variable (e.g. see the review of Wiewiora & Weiss, 1990). Trioctahedral chlorites (trioctahedral in both the layer and the interlayer) are the most common in nature, and several families exist, such as clinochlore, chamosite and penninite, with Mg, Fe^{2+} and Mn^{2+} as the dominant octahedral cations, respectively.

Due to the complex chemical composition of chlorite, numerous studies have been devoted to the relations between b and the amounts of octahedral and tetrahedral cations. Several equations with the form of $b = b_0 + \sum_{i=1}^{n} (a_i x_i)$ can be found in the literature (von Engelhardt, 1942; Radoslovich 1962), especially for trioctahedral chlorites, as exemplified by Lee *et al.* (2007), who observed a robust linear relationship between b and Mg/Mg + Fe for natural chlorite samples from Al-saturated metamorphic assemblages. Wiewiora & Wilamowski (1996) formulated two distinct regression equations for trioctahedral chlorites (Equation 7) and di-tri- and di-dioctahedral chlorites (Equation 8) as follows:

$$b_{\text{tri.}} = 9.225 + 0.027^{\text{IV}}\text{Al} + 0.0386^{\text{VI}}\text{Al} + 0.0376\text{Fe}^{2+} + 0.0376\text{Cr}^{3+} + 0.0665\text{Mn}^{2+} \quad (8)$$

$$b_{\text{di-tri./di-di.}} = 8.860 + 0.112^{\text{IV}}\text{Al} + 0.0524\text{Mg}^{2+} + 0.0752\text{Fe}^{2+} + 0.06\text{Fe}^{3+} - 0.0523\text{Li}^{+} \quad (9)$$

The dataset used in the present study is taken mainly from the review work of Wiewiora & Wilamowski (1996), where several b values were measured using structural refinement. To avoid any potential bias from using a unique data source and to enlarge the range of chemical compositions investigated for chlorite, the compiled data from Radoslovich (1962) were added, as well as a few other samples (i.e. two samples whose single-crystal structure has been refined: one ordered triclinic clinochlore (Smyth *et al.*, 1997) and one cookeite (Zheng & Bailey, 1997b); and four uncommon chlorites, namely V^{3+}-rich chlorites (Whitney & Northrop, 1986) and Fe^{3+}-sudoites (Billault *et al.*, 2002; Table 8).

The evolution of b as a function of R for all samples reveals reasonably good data alignment for all compositions ranging from dioctahedral to trioctahedral chlorites (Fig. 21a). In contrast to Wiewiora & Wilamowski (1996), the b *vs* R regression is suitable for the entire range of chemical compositions. R values for di-tri- and trioctahedral chlorites even overlap in the intermediary range (for $0.64 < R < 0.70$). This is probably because trioctahedral occupancy with cations of various valences, such as $(R^{3+}_{x}R^{2+}_{3-x})$ and $(R^{3+}_{x}R^{+}_{3-x})$, is expected to occur in chlorites, at least in the interlayer O sheets, to counterbalance the negative tetrahedral charge. The clinochlore and cookeite samples with refined single crystals fall on or close to the correlation line. The uncommon vanadium-rich chlorites (Whitney & Northrop, 1986), assuming Fe and V as trivalent cations, as well as Fe^{3+}-sudoites (Billault *et al.*, 2002), do not reveal any specific behaviour (Fig. 21a). Some samples, such as samples 8, 28 and 30 (Table 8), deviate significantly from the regression line (Fig. 21a). For sample 28, R is suspected to be underestimated due to a redox problem, as the Fe^{2+}:Fe^{3+} ratio was reversed in a previous study (Steinfink, 1958). As sample 8 was classified in the trioctahedral group, the Fe^{2+} and Fe^{3+} contents have probably been switched mistakenly (Table 8), and the data point moved close to the regression line after switching back both contents (Fig. 21a). Other typographical errors cannot be excluded, as another one could be identified for sample 82 (Table 8). Unfortunately, data for sample 30 are unpublished and could not be checked.

Some chlorites of the di-tri- and di-di-octahedral series are Li-rich. The Al_2Li configuration is likely to occur in the interlayer hydroxide sheet to create a positive charge balancing the tetrahedral negative charge (Zheng & Bailey, 1997b). The revised $r(Li^+)$ of 0.60 Å (instead of 0.76 Å) determined for Li-rich micas (see above) was used as an alternative (Fig. 21b). The general regression was modified slightly to $b = 2.30R + 7.67$, and the regression coefficient was improved slightly ($R^2 = 0.865$ *vs* 0.884), arguing for the suitability of a lower $r(Li^+)$.

Contrary to Wiewiora & Wilamowski (1996), who included tetrahedral Al in their equations with a greater coefficient for di-tri- and di-dioctahedral chlorites than for trioctahedral chlorites (Equations 7 & 8), the unique linear regression (Fig. 21b) indicates that b is mainly driven by R and that the tetrahedral Al is not a first-order parameter. Accordingly, a unique main trend is also observed for the $b/b_{\text{tet.}}$ *vs* R regression, although its coefficient is lower than for the b *vs* R regression (0.78 (Fig. 22a) and 0.88 (Fig. 21b), respectively). The observed dispersion of data points may be partly due to the scattering of tetrahedral charge ranging from 0.45 to 1.80 (Table 8), but we cannot confident in their accuracy for the entire dataset.

The $b/b_{\text{tet.}}$ values vary from 0.952 (dioctahedral chlorites) to 1.009 (trioctahedral chlorites), which correspond to angles of tetrahedral rotation $\alpha \approx 18°$ and 0°, respectively, matching relatively well with α measured using structural refinement: ~14° for dioctahedral donbassite and ~5–7° for trioctahedral chlorites (Bailey, 1991a). Focusing on some samples whose single-crystal structure was refined (Table 9), an excellent relationship is observed between α_{ref} (the tetrahedral rotation angle measured using structural refinement) and α_{calc} (the tetrahedral rotation angle calculated from $b/b_{\text{tet.}}$; Equation 4; Fig. 22c). Surprisingly, the regression coefficient is greater when using Si–O and Al–O bond lengths of 1.618 and 1.748 Å, respectively, following Bailey (1984a), than when using the T–O mean bond length determined using structural refinement (Fig. 22b). The Si–O and Al–O bond lengths were calculated to match α_{ref}, and very coherent values were obtained (Table 9). This study also shows that by using adequate bond lengths, Equation 4 allows us to calculate the angle of tetrahedral rotation α accurately, at least for most of the common samples.

Going from dioctahedral chlorites to trioctahedral ones (i.e. with R increasing), the tetrahedral rotation angle α progressively decreases, as shown by the $b/b_{\text{tet.}}$ plot (Fig. 22a), while the flattening of O sheets decreases concomitantly (Fig. 22b). For di- and di-tri-octahedral chlorites, O sheets are thinner than the hydroxides with the same R, whereas they are thicker for trioctahedral chlorites.

In chlorite, the element partitioning between both O sheets will not affect R significantly, which is a mean value, but such a partitioning is likely to impact the misfit between the T and O sheets. As for the other phyllosilicate families, the misfit between T and O sheets increases when R decreases, and both shortening of T sheets by tetrahedral rotation and flattening of O sheets are expected to occur. Most trioctahedral chlorites show $b/b_{\text{tet.}}$ values close to 1, demonstrating the easy accommodation of the T and O sheets. Samples with the greatest $b/b_{\text{tet.}}$ and R values are Mn-rich and have a great tetrahedral Al content (cf. samples 1, 2 and 3 of the trioctahedral series of Wiewiora & Wilamowski (1996) and sample 'pennantite' of Radoslovich (1962); Table 8). For these samples, both the T and O sheets have large lateral dimensions, and misfit compensation is likely to be facilitated. It is worth noting that the clinochlore and cookeite samples with refined single crystals fall very close to the b, $b/b_{\text{tet.}}$ and % O enlargement *vs* R

https://doi.org/10.1180/clm.2023.20 Published online by Cambridge University Press

Table 8. Data used for chlorites.

Natural chlorites (anhydrous composition)	Sample[a]	*R*	*b*	References	Comments
Trioctahedral chlorites				Wiewiora & Wilamowski (1996)	
$(Si_{2.57}Al_{1.43})(Al_{1.16}Mg_{0.14}Fe^{3+}_{0.36}Mn^{2+}_{4.3})$	1	0.759	9.500		
$(Si_{2.7}Al_{1.3})(Al_{1.3}Mg_{0.6}Fe^{2+}_{0.2}Mn^{2+}_{2.6}Zn_{1.3})$	2	0.734	9.400		
$(Si_{2.72}Al_{1.28})(Al_{1.36}Mg_{0.26}Fe^{3+}_{0.39}Mn^{2+}_{3.95})$	3	0.746	9.470		
$(Si_{3.4}Al_{0.6})(Al_{0.84}Mg_{4.6}Fe^{2+}_{0.28}Fe^{3+}_{0.11}Cr_{0.02}Ni_{0.07})$	4	0.694	9.216		
$(Si_3Al_1)(Al_{0.2}Mg_5Fe^{2+}_{0.1}Cr_{0.7})$	5	0.703	9.242		
$(Si_{2.8}Al_{1.2})(Al_{1.2}Mg_{2.6}Fe^{2+}_{2.2})$	6	0.705	9.290		
$(Si_{3.3}Al_{0.7})(Al_{0.87}Mg_{3.13}Fe^{2+}_{2})$	7	0.713	9.290		
$(Si_{2.4}Al_{1.6})(Al_{0.85}Mg_{0.7}Fe^{2+}_{3.7}Fe^{3+}_{0.75})^{b}$	8	0.721	9.297		
$(Si_{2.62}Al_{1.38})(Al_{1.17}Mg_{2.82}Fe^{2+}_{1.24}Fe^{3+}_{0.52})$	9	0.689	9.290		
$(Si_{2.8}Al_{1.2})(Al_{1.28}Mg_{4.3}Fe^{2+}_{0.3}Fe^{3+}_{0.06})$	10	0.682	9.220		
$(Si_{2.67}Al_{1.33})(Al_{2.1}Mg_{3.35}Fe^{2+}_{0.03}Fe^{3+}_{0.09})$	11	0.649	9.170		
$(Si_{2.87}Al_{1.13})(Al_{1.45}Mg_{0.79}Fe2^{+}_{2.82}Fe^{3+}_{0.12}Mn^{2+}_{0.59})$	12	0.712	9.350		
$(Si_{2.55}Al_{1.45})(Al_{1.41}Mg_{0.78}Fe^{2+}_{3.88})$	13	0.716	9.336		
$(Si_{2.85}Al_{1.15})(Al_{0.97}Mg_{4.54}Fe^{2+}_{0.28}Fe^{3+}_{0.18}Mn^{2+}_{0.01})$	14	0.691	9.234		
$(Si_{3.16}Al_{0.84})(Al_{0.82}Mg_{4.9}Fe^{2+}_{0.29}Mn^{2+}_{0.005})$	15	0.698	9.232	Structure refinement parameters: Bailey (1991c)	
$(Si_{3.22}Al_{0.78})(Al_{0.65}Mg_{5.04}Fe^{2+}_{0.1}Fe^{3+}_{0.17}Mn^{2+}_{0.01})$	16	0.699	9.216		
$(Si_{3.01}Al_{0.99})(Al_{0.92}Mg_{4.75}Fe^{2+}_{0.13}Fe^{3+}_{0.14})$	17	0.691	9.216		
$(Si_{2.64}Al_{1.36})(Al_{1.17}Mg_{4.02}Fe^{2+}_{0.65}Fe^{3+}_{0.13}Mn^{2+}_{0.02})$	18	0.689	9.240		
$(Si_{2.69}Al_{1.31})(Al_{1.42}Mg_{2.36}Fe^{2+}_{1.72}Fe^{3+}_{0.26}Mn^{2+}_{0.05})$	19	0.690	9.258		
$(Si_{2.6}Al_{1.4})(Al_{1.23}Mg_{2.16}Fe^{2+}_{2.11}Fe^{3+}_{0.3}Mn^{2+}_{0.04})$	20	0.700	9.306		
$(Si_{2.51}Al_{1.49})(Al_{1.04}Mg_{0.37}Fe^{2+}_{3.57}Fe^{3+}_{0.79}Mn^{2+}_{0.01})$	21	0.714	9.354		
$(Si_{2.96}Al_{1.04})(Al_{0.95}Mg_{4.62}Fe^{2+}_{0.14}Fe^{3+}_{0.14}Cr_{0.09}Ni_{0.007})$	22	0.689	9.207		
$(Si_{3.07}Al_{0.93})(Al_{0.63}Mg_{4.95}Fe^{2+}_{0.11}Fe^{3+}_{0.03}Cr_{0.26}Ni_{0.007})$	23	0.697	9.220		
$(Si_{3.19}Al_{0.81})(Al_{0.2}Mg_{5.18}Fe^{2+}_{0.11}Fe^{3+}_{0.04}Cr_{0.51})$	24	0.706	9.231		
$(Si_{3.11}Al_{0.89})(Al_{0.19}Mg_{5.1}Fe^{2+}_{0.16}Cr_{0.60})$	25	0.705	9.215		
$(Si_{2.91}Al_{1.09})(Al_{0.36}Mg_{5.03}Fe^{2+}_{0.23}Fe^{3+}_{0.11}Cr_{0.27}Ni_{0.02})$	26	0.705	9.219		
$(Si_{2.83}Al_{1.17})(Al_{1.26}Mg_{4.06}Fe^{2+}_{0.42}Fe^{3+}_{0.15})$	27	0.683	9.192		
$(Si_{2.88}Al_{1.12})(Al_{1.0}Mg_{4.56}Fe^{2+}_{0.16}Fe^{3+}_{0.22}Ni_{0.01})$	28	0.688	9.222		
$(Si_{3.55}Al_{0.45})(Al_{0.97}Mg_{4.2}Fe^{2+}_{0.06}Fe^{3+}_{0.2}Ni_{0.22})$	29	0.685	9.192		
$(Si3_{.0}Al_{1.0})(Al_{0.2}Mg_{5.0}Fe^{2+}_{0.1}Cr_{0.7})$	30	0.703	9.240		
$(Si_{3.21}Al_{0.79})(Al_{0.56}Mg_{4.72}Fe^{2+}_{0.10}Cr_{0.47}Mn^{2+}_{0,001}Ni_{0.03})$	31	0.695	9.170		
$(Si_{3.0}Al_{1.0})(Al_{1.0}Mg_{5.0})$	32	0.689	9.187		
$(Si_{3.17}Al_{0.83})(Al_{0.83}Mg_{4.28}Fe^{2+}_{0.20}Fe^{3+}_{0.28}Cr_{0.023}Ni_{0.25})$	33	0.691	9.246		
$(Si_{2.72}Al_{1.28})(Al_{1.35}Mg_{0.41}Fe^{2+}_{3.42}Fe^{3+}_{0.46}Mn^{2+}_{0.015})$	34	0.706	9.306		
$(Si_{2.54}Al_{1.46})(Al_{0.84}Mg_{0.7}Fe^{2+}_{2.51}Fe^{3+}_{1.15}Mn^{2+}_{0.53})$	35	0.714	9.350		
$(Si_{3.28}Al_{0.98})(Al_{0.72}Mg_{4.95}Fe^{2+}_{0.04}Fe^{3+}_{0.04,}Cr_{0.23}Ni_{0.02})$	36	0.694	9.227	Structure refinement parameters: Bailey (1991c)	
$(Si_{2.99}Al_{1.01})(Al_{0.71}Mg_{4.92}Fe^{2+}_{0.06}Fe^{3+}_{0.06}\ Cr_{0.25})$	37	0.694	9.228	Structure refinement parameters: Bailey (1991c)	
$(Si_{3.17}Al_{0.83})(Al_{0.77}Mg_{4.82}Fe^{2+}_{0.17}Fe^{3+}_{0.18})$	38	0.695	9.230		
$(Si_{2.64}Al_{1.36})(Al_{0.85}Mg_{3.1}Fe^{2+}_{1.82}Fe^{3+}_{0.32})$	39	0.708	9.286		
$(Si_{2.69}Al_{1.31})(Al_{1.55}Mg_{3.47}Fe^{2+}_{0.86})$	40	0.680	9.241		
$(Si_{2.87}Al_{1.13})(Al_{0.79}Mg_{4.6}Fe^{2+}_{0.48}Fe^{3+}_{0.21})$	41	0.698	9.236		
$(Si_{2.62}Al_{1.38})(Al_{1.32}Mg_{2.85}Fe^{2+}_{1.53}Fe^{3+}_{0.22}Cr_{0.002})$	42	0.692	9.267	Structure refinement: Rule & Bailey (1987)	
$(Si_{3.55}Al_{0.45})(Al_{1.17}Mg_{0.76}Fe^{2+}_{1.2}Mn^{2+}_{0.01})$	43	0.703	9.257		
$(Si_{2.84}Al_{1.16})(Al_{0.95}Mg_{0.79}Fe^{2+}_{3.05}Fe^{3+}_{0.65}Mn^{2+}_{0.33})$	44	0.719	9.344		
$(Si_{2.73}Al_{1.27})(Al_{1.16}Mg_{4.74}Fe^{3+}_{0.07}Mn^{2+}_{0.054})$	45	0.685	9.210		
$(Si_{3.1}Al_{0.9})(Al_{0.79}Mg_{4.54}Fe^{2+}_{0.55}Fe^{3+}_{0.11}Mn^{2+}_{0.01})$	46	0.700	9.240		
$(Si_{2.69}Al_{1.31})(Al_{1.13}Mg_{2.86}Fe^{2+}_{1.85}Fe^{3+}_{0.14}Mn^{2+}_{0.04})$	47	0.703	9.290		
$(Si_{2.56}Al_{1.44})(Al_{1.25}Mg_{1.02}Fe^{2+}_{3.49}Fe^{3+}_{0.19}Mn^{2+}_{0.05})$	48	0.715	9.350		
$(Si_{2.43}Al_{1.57})(Al_{1.54}Mg_{0.2}Fe^{2+}_{4.17}Fe^{3+}_{0.03}Mn^{2+}_{0.06})$	49	0.715	9.365		
$(Si_{2.54}Al_{1.46})(Al_{1.20}Mg_{1.01}Fe^{2+}_{3.24}Fe^{3+}_{0.41}Mn^{2+}_{0.053})$	50	0.711	9.348		
$(Si_{2.73}Al_{1.27})(Al_{1.15}Mg_{4.74}Fe^{3+}_{0.074}Mn^{2+}_{0.055})$	51	0.685	9.208		
$(Si_{2.54}Al_{1.46})(Al_{1.20}Mg_{1.01}Fe^{2+}_{3.24}Fe^{3+}_{0.41}Mn^{2+}_{0.053})$	52	0.711	9.354		
$(Si_{2.97}Al_{1.03})(Al_{1.35}Mg_{2.24}Fe^{2+}_{1.44}Fe^{3+}_{0.45}Mn^{2+}_{0.031})$	53	0.685	9.282		
$(Si_{3.17}Al_{0.83})(Al_{0.89}Mg_{3.16}Fe^{2+}_{1.58}Fe^{3+}_{0.20}Mn^{2+}_{0.009})$	54	0.706	9.270		
$(Si_{2.78}Al_{1.22})(Al_{1.24}Mg_{4.27}Fe^{2+}_{0.29}Fe^{3+}_{0.06})$	55	0.683	9.216		
$(Si_{2.3}Al_{1.7})(Al_{2.14}Mg_{3.21}Fe^{2+}_{0.06}Fe^{3+}_{0.2})$	56	0.647	9.198		
$(Si_{2.77}Al_{1.23})(Al_{1.76}Mg_{3.58}Fe^{2+}_{0.29}Fe^{3+}_{0.03}Mn^{2+}_{0.02})$	57	0.666	9.216		
$(Si_{2.7}Al_{1.3})(Al_{1.3}Mg_{1.3}Fe^{2+}_{3.4})$	58	0.714	9.336		
$(Si_{2.91}Al_{1.09})(Al_{1.56}Mg_{1.11}Fe^{2+}_{3.04})$	59	0.701	9.314		
$(Si_{2.64}Al_{1.36})(Al_{1.76}Mg_{0.82}Fe^{2+}_{3.19})$	60	0.697	9.326		
$(Si_{2.59}Al_{1.41})(Al_{1.84}Mg_{0.83}Fe^{2+}_{3.006})$	61	0.692	9.324		
$(Si_{2.67}Al_{1.33})(Al_{1.73}Mg_{0.79}Fe^{2+}_{3.26})$	62	0.698	9.324		
$(Si_{2.62}Al_{1.38})(Al_{1.68}Mg_{0.93}Fe^{2+}_{3.23})$	63	0.700	9.319		
$(Si_{2.61}Al_{1.39})(Al_{1.72}Mg_{1.19}Fe^{2+}_{2.9}Mn^{2+}_{0.02})$	64	0.696	9.311		
$(Si_{2.5}Al_{1.5})(Al_{0.6}Mg_5Fe^{2+}_{0.4})$	65	0.706	9.270		
$(Si_{3.01}Al_{0.99})(Al_{0.99}Mg_{1.67}Fe^{2+}_{0.5}Fe^{3+}_{0.14}Mn^{2+}_{0.005}Ni_{2.62})$	66	0.679	9.214		
$(Si_{2.26}Al_{1.74})(Al_{1.33}Mg_{4.42}Fe3^{+}_{0.03}Cr_{0.19})$	67	0.675	9.209		
$(Si_{3.11}Al_{0.89})(Al_{0.69}Mg_{4.44}Fe^{2+}_{0.2}Fe^{3+}_{0.4}Mn^{2+}_{0.01}Ni_{0.01})$	68	0.695	9.245		
$(Si_{2.88}Al_{1.12})(Al_{0.75}Mg_{4.47}Fe^{3+}_{0.57})$	69	0.689	9.256		

(*Continued*)

https://doi.org/10.1180/clm.2023.20 Published online by Cambridge University Press

Table 8. (*Continued.*)

Natural chlorites (anhydrous composition)	Sample[a]	*R*	*b*	References	Comments
$(Si_{2.54}Al_{1.46})(Al_{0.81}Mg_{2.38}Fe^{2+}_{0.9}Fe^{3+}_{1.41}Mn^{2+}_{0.09}Ni_{0.01})$	70	0.686	9.264		
$(Si_{3.01}Al_{0.99})(Al_{1.0}Mg_{4.12}Fe^{2+}_{0.34}Fe^{3+}_{0.3}Mn^{2+}_{0.01})$	71	0.688	9.233		
$(Si_{2.65}Al_{1.35})(Al_{1.18}Mg_{0.63}Fe^{2+}_{3.19}Fe^{3+}_{0.52}Mn^{2+}_{0.09})$	72	0.710	9.362		
$(Si_{2.4}Al_{1.6})(Al_{1.14}Mg_{4.59}Fe3^{+}_{0.08}Cr_{0.25})$	73	0.680	9.206		
$(Si_{2.2}Al_{1.8})(Al_{1.67}Mg_{3.97}Fe3^{+}_{0.17}Cr_{0.12})$	74	0.664	9.192		
$(Si_{3.53}Al_{0.47})(Al_{0.47}Mg_{4.74}Fe^{2+}_{0.28}Fe^{3+}_{0.29}Mn^{2+}_{0,01}Ni_{0.02})$	75	0.704	9.237		
$(Si_{2.81}Al_{1.19})(Al_{1.39}Mg_{0.82}Fe^{2+}_{3.69})$	76	0.714	9.231		
$(Si_3Al_1)(Al_{0.96}Mg_{3.93}Fe^{2+}_{0.95}Fe^{3+}_{0.1}Mn^{2+}_{0.02})$	77	0.699	9.222		
$(Si_{3.13}Al_{0.87})(Al_{0.65}Mg_{4.38}Fe^{3+}_{0.54}Mn^{2+}_{0.01})$	78	0.691	9.224		
$(Si_{2.97}Al_{1.03})(Al_{0.98}Mg_{4.43}Fe^{2+}_{0.17}Fe^{3+}_{0.25}Ni_{0.07})$	79	0.687	9.215		
$(Si_{2.95}Al_{1.05})(Al_{1.05}Mg_{4.51}Fe^{2+}_{0.14}Fe^{3+}_{0.17}Ni_{0.02})$	80	0.686	9.228		
$(Si_{2.64}Al_{1.36})(Al_{1.45}Mg_{1.30}Fe^{2+}_{3.12}Mn^{2+}_{0.084})$	81	0.708	9.336		
$(Si_{3.06}Al_{0.94})(Al_{0.694}Mg_{4.715}{}^{c}Fe^{2+}_{0.109}Fe^{3+}_{0.269}Cr_{0.128}Ni_{0.011})$	82	0.694	9.228		
Di-tri and di-dioctahedral chlorites				Wiewiora & Wilamowski (1996)	
$(Si_{2.86}Al_{1.14})(Al_{2.98}Mg_{1.95}Fe^{2+}_{0.14}Fe^{3+}_{0.08})$	1	0.613	9.058		
$(Si_{3.14}Al_{0.86})(Al_{4.1}Mg_{0.08}Fe^{2+}_{0.01}Fe^{3+}_{0.04}Li_{0.26})$	2	0.553	8.956	Structure refinement parameters: Bailey (1991c)	
$(Si_{3.06}Al_{0.94})(Al_{2.45}Mg_{2.54}Fe^{2+}_{0.01}Fe^{3+}_{0.03})$	3	0.630	9.060		
$(Si_{3.3}Al_{0.7})(Al_{2.7}Mg_{2.3})$	4	0.620	9.014		
$(Si_{3.06}Al_{0.94})(Al_{0.28}Mg_{4.56}Fe^{2+}_{0.06}Fe^{3+}_{0.013}Cr_{0.46}Mn^{2+}_{0,001}Ni_{0.03})$	5	0.702	9.216		
$(Si_{2.48}Al_{1.52})(Al_{1.52}Mg_{0.32}Fe^{2+}_{3.46}Fe^{3+}_{0.04})$	6	0.706	9.314		
$(Si_{2.86}Al_{1.14})(Al_{2.9}Mg_{1.96}Fe^{2+}_{0.22})$	7	0.617	9.054		
$(Si_{3.12}Al_{0.88})(Al_{4.0}Mg_{0.24})$	8	0.545	8.940		
$(Si_{3.08}Al_{0.92})(Al_{3.9}Mg_{0.11}Fe^{3+}_{0.015}Cr_{0.02}Mn^{2+}_{0,005}Li_{0.82})$	9	0.578	8.890		
$(Si_{3.04}Al_{0.96})(Al_{3.8}Mg_{0.14}Fe^{3+}_{0.015}Ni_{0.005}Li_{1.13})$	10	0.590	8.885		
$(Si_{3.3}Al_{0.7})(Al_{2.7}Mg_{2.3})$	11	0.620	9.070		
$(Si_{3.01}Al_{0.99})(Al_{2.84}Mg_{1.91}Fe^{2+}_{0.02}Fe^{3+}_{0.19}Mn^{2+}_{0.02})$	12	0.612	9.080		
$(Si_{2.99}Al_{1.01})(Al_{2.88}Mg_{1.94}Fe^{3+}_{0.17}Mn^{2+}_{0.02})$	13	0.612	9.083		
$(Si_{3.43}Al_{0.57})(Al_{2.7}Mg_{1.97}Fe^{2+}_{0.04}Fe^{3+}_{0.09})$	14	0.615	9.042		
$(Si_{2.95}Al_{1.05})(Al_{3.89}Mg_{0.02}Fe^{2+}_{0.05}Li_{1.11})$	15	0.587	8.930		
$(Si_{3.26}Al_{0.74})(Al_{3.02}Mg_{1.18}Fe^{2+}_{0.033}Fe^{3+}_{0.35}Mn^{2+}_{0.004})$	16	0.593	9.050		
$(Si_{2.88}Al_{1.12})(Al_{2.35}Mg_{2.91}Fe^{3+}_{0.012})$	17	0.637	9.190		
$(Si_{2.79}Al_{1.21})(Al_{1.34}Mg_{2.23}Fe^{2+}_{0.29}Fe^{3+}_{0.69})$	18	0.658	9.180		
$(Si_{3.01}Al_{0.99})(Al_{2.92}Mg_{1.89}Fe^{2+}_{0.12}Fe^{3+}_{0.076}Mn^{2+}_{0.024})$	19	0.613	9.063		
$(Si_{3.0}Al_{1.0})(Al_{2.83}Mg_{2.0}Fe^{3+}_{0.18}Li_{0.015})$	20	0.613	9.067		
$(Si_{3.3}Al_{0.7})(Al_{2.86}Mg_{1.92}Fe^{2+}_{0.13})$	21	0.614	9.090		
$(Si_{3.27}Al_{0.73})(Al_{4.02}Mg_{0.013}Fe^{3+}_{0.003}Li_{0.66})$	22	0.567	8.929		
$(Si_{2.96}Al_{1.04})(Al_{3.97}Li_{1.11})$	23	0.584	8.920		
$(Si_{3.08}Al_{0.92})(Al_{3.96}Mg_{0.017}Fe^{3+}_{0.007}Li_{0.98})$	24	0.580	8.957		
$(Si_{3.2}Al_{0.8})(Al_{3.2}Mg_{1.6})$	25	0.597	9.054		
$(Si_{3.02}Al_{0.98})(Al_{3.05}Mg_{1.79}Fe^{3+}_{0.06}Mn^{2+}_{0.004})$	26	0.604	9.054		
$(Si_{3.28}Al_{0.72})(Al_{3.08}Mg_{1.19}Fe^{2+}_{0.033}Fe^{3+}_{0.35})$	27	0.592	9.054		
$(Si_{2.2}Al_{1.8})(Al_{1.2}Mg_{2.6}Fe^{2+}_{0.3}Fe^{3+}_{1.5})$	28	0.663	9.300	Problematic redox suspected (Steinfink, 1958)	
$(Si_{3.38}Al_{0.62})(Al_{3.96}Fe^{2+}_{0.04}Fe^{3+}_{0.09}Li_{0.7})$	29	0.572	8.900		
$(Si_{2.36}Al_{1.64})(Al_{3.14}Mg_{1.8}Fe^{3+}_{0.1}Cr_{0.12})$	30	0.604	9.207		
$(Si_{2.98}Al_{1.02})(Al_{3.77}Mg_{0.06}Fe^{2+}_{0.12}Fe^{3+}_{0.15}Li_{1.27})$	31	0.599	8.930		
Other chlorites				Radoslovich (1962)	
$(Si_{2.8}Al_{1.2})(Al_{1.3}Mg_{2.8}Fe^{2+}_{1.7})$	Ripidolite	0.696	9.283		
$(Si_{2.6}Al_{1.4})(Al_{1.5}Mg_{0.4}Fe^{2+}_{4.2})$	Bavalite	0.716	9.365		
$(Si_{2.5}Al_{1.5})(Al_{1.2}Mg_{2.2}Fe^{2+}_{0.7}Fe^{3+}_{1.4})$	Thuringite	0.668	9.192		
$(Si_{2.6}Al_{1.4})(Al_{1.22}Mg_{4.2}Fe^{2+}_{0.22})$	Grochanite	0.682	9.227		
$(Si_{2.9}Al_{1.1})(Al_{0.7}Mg_{2.9}Fe^{2+}_{2.2}Fe^{3+}_{10.2})$	Diabantite	0.718	9.305		
$(Si_{3.1}Al_{0.9})(Al_{0.2}Mg_{5.1}Fe^{2+}_{0.2}Cr_{0.6})$	Kammererite	0.706	9.242		
$(Si_{2.5}Al_{1.5})(Al_{1.6}Mg_{4.3}Fe^{2+}_{0.1})$	Sheridanite	0.672	9.226		
$(Si_{2.88}Al_{1.12})(Al_{1.21}Mg_{1.84}Fe^{2+}_{2.82})$	Mg-chamosite	0.711	9.33		
$(Si_{2.62}Al_{1.38})(Al_{1.18}Mg_{0.25}Fe^{3+}_{0.37}Mn_{3.82})$	Pennantite	0.751	9.40		
$(Si_{2.4}Al_{1.6})(Al_{0.85}Mg_{0.7}Fe^{2+}_{3.7}Fe^{3+}_{0.75})$	Thuringite	0.721	9.30		
$(Si_{2.7}Al_{1.3})(Al_{1.4}Fe^{2+}_{3.85}Fe^{3+}_{0.75})$	Thuringite	0.706	9.31		
$(Si_{2.25}Al_{1.75})(Al_{0.8}Mg_{0.35}Fe^{2+}_{4.75}Fe^{3+}_{0.05})$	Bavalite	0.742	9.35		
$(Si_{2.71}Al_{1.29})(Al_{1.35}Mg_{0.92}Fe^{2+}_{3.37}Fe^{3+}_{0.18}Mn_{0.04})$	Daphnite	0.710	9.38		
$(Si_{2.99}Al_{1.01})(Al_{1.12}Mg_{0.75}Fe^{2+}_{3.23}Fe^{3+}_{0.56})$	Chamosite	0.710	9.36		
$(Si_{2.42}Al_{1.58})(Al_{0.83}Mg_{0.72}Fe^{2+}_{3.68}Fe^{3+}_{0.76})$	Thuringite	0.722	9.32		
$(Si_{2.6}Al_{1.4})(Al_{0.75}Mg_{4.9}Fe^{2+}_{0.07}Fe^{3+}_{0.17}Cr_{0.18})$	Corundophillite	0.693	9.27		
$(Si_{3.1}Al_{0.9})(Al_{1.3}Mg_{0.75}Fe^{2+}_{3.35}Fe^{3+}_{0.6})$	Chamosite	0.706	9.36		
$(Si_{2.9}Al_{1.1})(Al_{0.82}Mg_{5.20})$	Leuchtenbergite	0.695	9.19		
$(Si_{2.6}Al_{1.4})(Al_{1.30}Mg_{4.6}Fe^{2+}_{0.02}Fe^{3+}_{0.10})$	Sheridanite	0.679	9.21		
$(Si_{2.6}Al_{1.4})(Al_{1.40}Mg_{3.9}Fe^{2+}_{0.70})$	Chlorite	0.684	9.21		
$(Si_{2.42}Al_{1.58})(Al_{1.01}Mg_{2.7}Fe^{2+}_{2.3})$	Prochlorite	0.712	9.21		
$(Si_{3.03}Al_{0.97})(Al_{0.17}Mg_{5.05}Fe^{2+}_{0.11}Fe^{3+}_{0.04}Cr_{0.71})$	Chrome chlorite	0.703	9.25		
II*b-4* triclinic clinochlore				Smyth *et al.* (1997)	
$(Si_{2.96}Al_{1.04})(Al_{0.841}Mg_{2.924}Fe^{2+}_{0.076}Fe^{3+}_{0.102}Cr_{0.004}Ti_{0.004})$	NMNH #R4513	0.680	9.226		

(*Continued*)

https://doi.org/10.1180/clm.2023.20 Published online by Cambridge University Press

Table 8. (*Continued.*)

Natural chlorites (anhydrous composition)	Sample[a]	*R*	*b*	References	Comments
Cookeite				Zheng & Bailey (1997b)	
$(Si_{3.042}Al_{0.958})(Al_{4.017}Mg_{0.007}Fe_{0.009}Cr_{0.005}Li_{0.852})$	Little Rock	0.575	8.940		Two-layer 'r' structure
Vanadium chlorite				Whitney & Northrop (1986)	
$(Si_{3.54}Al_{0.46})(Al_{2.02}Mg_{1.14}Fe^{3+}_{0.48}V_{0.4}Li_{0.04})$	TM05	0.612	9.120		
$(Si_{3.59}Al_{0.41})(Al_{1.96}Mg_{1.01}Fe^{3+}_{0.5}V_{0.48}Li_{0.05})$	TM6	0.611	9.120		
Fe^{3+}-sudoites				Billault *et al.* (2002)	
$(Si_{3.32}Al_{0.68})(Al_{2.93}Mg_{1.58}Fe^{2+}_{0.13}Fe^{3+}_{0.15})$	MR2	0,606	9.054		
$(Si_{3.42}Al_{0.58})(Al_{2.87}Mg_{1.24}Fe^{2+}_{0.24}Fe^{3+}_{0.33}Mn_{0.01})$	MR11	0,605	9.066		

b is a crystallographic parameter (Å).
R = mean ionic radius of octahedral cations (Å) calculated with $r(Li^+) = 0.76$ Å (see text for details).
[a]Sample reference in the paper.
[b]Typographical error; original value: $Al_{0.85}Mg_{0.7}Fe^{2+}_{0.75}Fe^{3+}_{3.7}$.
[c]Instead of $Mg_{4.175}$ – corrected from the source paper (Zheng & Bailey, 1989).

plot correlation lines (Figs 21 & 22). In this regard, the data scattering shown in Fig. 21 is probably related to the structural complexity of chlorites associated with multiple possibilities of misfit accommodation, variable composition and charge balance between T and O sheets and chemical uncertainties.

Discussion

For the samples studied (i.e. hydroxides, oxyhydroxides, LDHs, TO phyllosilicates (kaolinite–lizardite or modulated series), neutral TOT phyllosilicates (pyrophyllite–talc series), smectites (same as the neutral TOT phyllosilicates), micas (muscovite–phlogopite, phlogopite–annite, tetrasilicic micas series) and chlorites), the first-order relation in Equation 10 can be applied:

$$b = AR + B \quad (10)$$

The *A* and *B* parameters for the various families are reported in Table 10. The ionic radii dataset taken from Shannon (1976) allows us to obtain suitable *R* values, except for Mn^{3+}, as discussed for groutite, and Li^+, as discussed for micas and chlorites, for which a smaller size appears to be more suitable. The equations for the regressions of these minerals were reported (Table 10) with *R* calculated with $r(Li^+) = 0.60$ Å rather than the 0.76 Å value from Shannon (1976).

The *b vs R* correlation lines determined for all of the studied mineral families were reported on the same plot (Fig. 23a). Note that the development of correlation lines does not necessarily imply the existence of a complete isomorphous series between end members, which is obviously dependent on their physico-chemical conditions of formation and thermodynamic stability. Samples that are not represented on this plot because no *b vs R* linear relation could be observed will be discussed later. *b* of a calculated theoretical 'free' T Si–O sheet (= $b_{tet.}$) is ~9.15 Å and increases with tetrahedral substitution (Equation 3; $b_{tet.} \approx 9.34$ Å for $Si^{IV}_{0.75}Al_{0.25}$). The determined *b vs R* regression for $M^{n+}(OH)_n$ hydroxide structures can be considered as representing the 'free' O sheets (i.e. without any constraint from the T sheets). The T sheet and O sheet (hydroxides) lines intercept at $R \approx 0.65$ Å and at $R \approx 0.69$ Å when a quarter of Si is substituted by Al (Fig. 23a).

The slope of the regression line (i.e. the *A* parameter in Equation 10) is found to be significantly higher for hydroxides than for phyllosilicates, except for the TO phyllosilicates with modulated structures (Fig. 23a & Table 10). Such a contrast demonstrates the prominent role played on *b* by the misfit accommodation between the lateral dimensions of the O and T sheets. This finding was used to derive a structurally based interpretation of the evolution of *b* with *R* in terms of processes of misfit accommodation.

Globally, at the lattice scale, the *b vs R* linear relations (Fig. 23a) were interpreted mainly as resulting from the misfit accommodation by coupling more or less pronounced tetrahedral rotation and O sheet flattening whatever the value of *R*. These two processes are often presented as being the main ways by which to

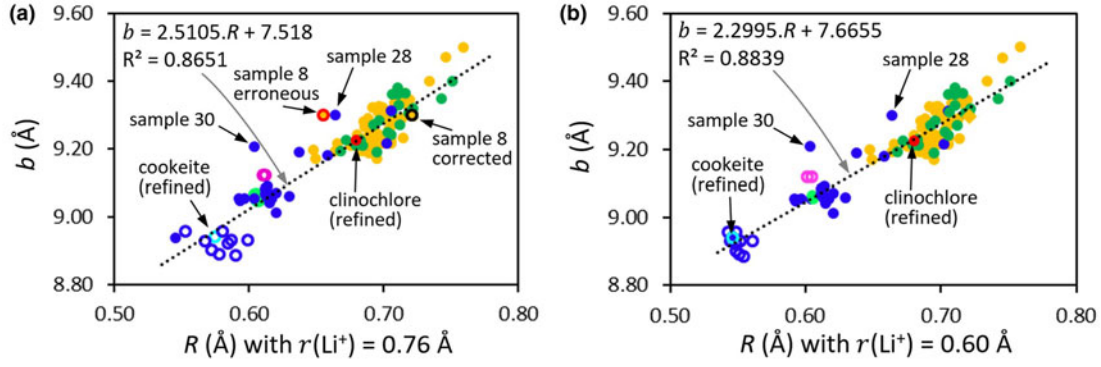

Figure 21. *b vs R* for chlorites (Table 8). Calculation of *R* performed with (a) $r(Li^+) = 0.76$ Å and (b) $r(Li^+) = 0.60$ Å. Dark blue circles = di-tri and di-dioctahedral chlorites; yellow circles = trioctahedral chlorites; dark green circles = various chlorites (Radoslovich, 1962); pink circles = vanadium chlorites; light green circles = Fe^{3+}-sudoites; red circle = clinochlore (Smyth *et al.*, 1997); light blue circle = cookeite (Zheng & Bailey, 1997b); open circles = Li-containing chlorites; dotted line = regression calculated with all samples.

https://doi.org/10.1180/clm.2023.20 Published online by Cambridge University Press

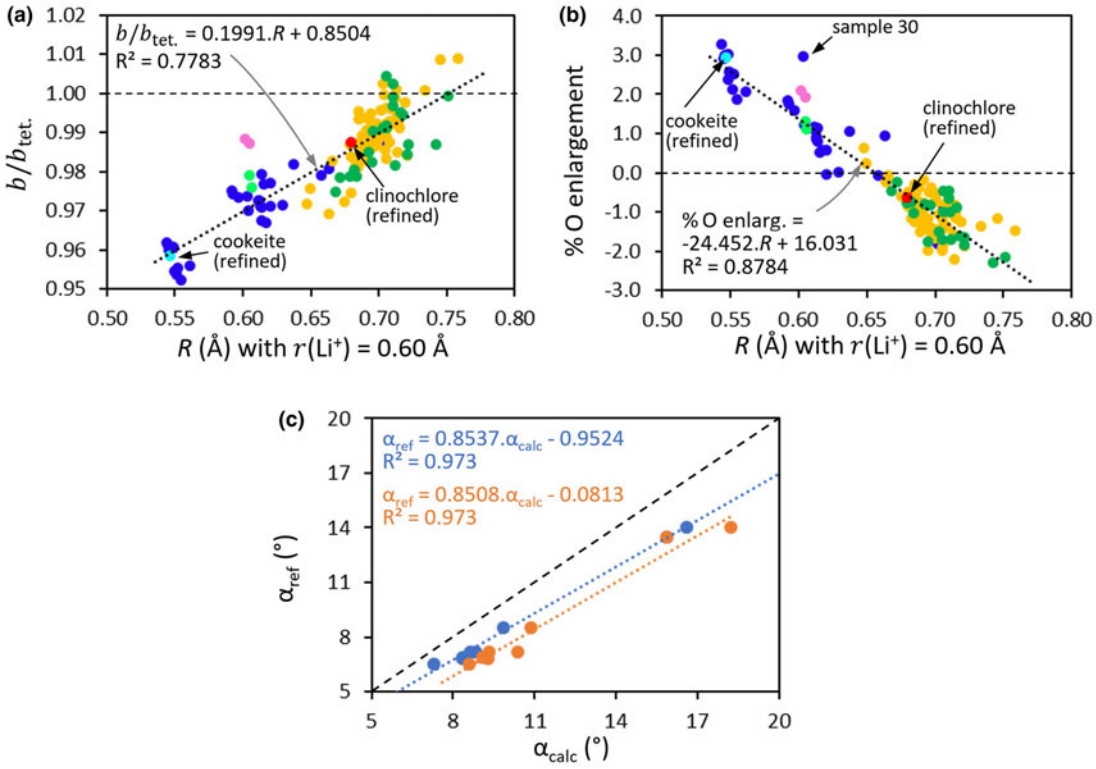

Figure 22. (a) $b/b_{tet.}$ and (b) percentage of octahedral enlargement *vs R* calculated with $r(Li^+)$ = 0.60 Å for chlorites (Table 8). Same samples and colour code as in Fig. 21. (c) Tetrahedral rotation angle measured using structural refinement α_{ref} *vs* calculated tetrahedral rotation angle α_{calc}: blue = using fixed Si–O and Al–O bond lengths (1.618 and 1.748 Å, respectively); orange = using mean T–O bond lengths obtained using structural refinement (see Table 9 and text for details). The dashed line represents the line of isovalues.

accommodate misfit in micas (e.g. Radoslovich, 1962; Donnay *et al.*, 1964; Toraya, 1981). From dioctahedral to trioctahedral phyllosilicates, a decrease of the tetrahedral rotation angle α allows us to decrease the lateral T sheet dimension, whereas a thickening of the O sheet allows us to decrease the lateral O sheet dimension. The $b/b_{tet.}$ and % O enlargement *vs R* plots (Figs 23b & 23c, respectively) are complementary representations of the *b vs R* plot (Fig. 23a), allowing us to distinguish better the respective roles of the T and O sheets.

Table 9. Summary of tetrahedral parameters of chlorite. Sample reference from Table 8. Tetrahedral rotation angle α_{ref}: measured using structural refinement; α_{calc}: calculated ($\alpha = \arccos(b/b_{tet.})$; Equation 4; see text for details).

Sample[a]	^{IV}Al	α_{ref} (°)	α_{calc} (°)	Mean bond length (Å)		
				T–O[b]	Si–O[c]	Al–O[c]
Trioctahedral						
42 – clinochlore II*b*-2	1.378	8.5	9.9	1.668	1.612	1.742
37 – clinochlore II*b*-4	1.010	7.2	8.8	1.659	1.611	1.741
36 – clinochlore II*b*-4	0.980	7.2	8.6	1.653	1.612	1.742
82 – clinochlore II*b*-4	0.944	6.9	8.3	1.652	1.613	1.743
82 – clinochlore II*b*-2	0.944	6.8	8.3	1.653	1.612	1.742
15 – clinochlore II*b*-4	0.840	6.5	7.3	1.651	1.615	1.745
Dioctahedral						
Cookeite – I*aa*	0.958	14	16.6	1.657 (×3) 1.685	1.598	1.728
2 – donbassite I*a*-2	0.860	13.5	15.9	1.675 1.617	1.600	1.730

[a]Sample reference in the paper.
[b]From structural refinement.
[c]Calculated using the following equation derived from Equation 3: (Si–O) = ($b_{tet.}$ – $\sqrt{2}^{IV}$AlΔ)/($4\sqrt{2}$), with $b_{tet.}$ obtained from Equation 4 along with α_{ref}, and with Δ = 0.13 being the difference between Si–O and Al–O bond lengths.

For TO phyllosilicates (excluding ^{IV}Al- and $^{IV}Fe^{3+}$-serpentines and modulated phyllosilicates), TOT neutral structures, micas (excluding those with small interlayer cations (Na and Ca) and with interlayer depletion (micaceous samples)) and chlorites, the O sheet dimension, and thus *R*, mainly drives *b*. The various slopes observed (Fig. 23a) for the various families are then related to the relative importance of the adjustments of T and O sheets in the misfit accommodation. This agrees well with Bailey (1984b), who stated that 'the T sheets appear sufficiently flexible to conform to the lateral dimensions dictated by smaller O sheets, and T and O lateral dimensions are similar enough that articulation of T with O sheets can be accomplished readily by tetrahedral rotation and additional thinning or thickening of O sheets'. The thinning or thickening of phyllosilicate O sheets is compared here to the thickness of their hydroxide counterparts (i.e. hydroxides with the same *R* as the considered phyllosilicates).

It is worth noting that O sheet thickening occurs (% O enlargement < 0 in Fig. 23c) when the O sheet remains smaller than the T sheet ($b/b_{tet.}$ < 1 in Fig. 23b).

For tetrasilicic micas and the muscovite–phlogopite mica series, $b < b_{tet.}$, whatever the value of *R* (Fig. 23b), whereas the octahedral flattening varies continuously, with the thicknesses of O sheets being similar to those of their hydroxide counterparts for $R \approx 0.62$ and 0.65 Å, respectively (Fig. 23c). The slopes of the tetrasilicic mica (Si_4)° and trisilicic mica (M–Ph)° regression lines are similar. For the same *R*, *b* values and flattening of the O sheet are greater for trisilicic micas than for tetrasilicic micas (Fig. 23c), agreeing well with the O sheet thickness measured using structural refinement (Table 11). Only one refined data point for talc was available for comparison with neutral TOT

https://doi.org/10.1180/clm.2023.20 Published online by Cambridge University Press

Table 10. Regression parameters proposed for the various mineral families investigated.

Regression type	$b = AR + B$	$b/b_{tet.} = CR + D$	% O enlargement[a] $= ER + F$
Hydroxides	4.51*R* + 6.22		
MO(OH) oxyhydroxides	4.6673*R* + 6.0546		
LDHs	4.2043*R* + 6.3758		
TO phyllosilicates			
Kaolinite–lizardite (*K–L*)	1.5092*R* + 8.1371	0.1649*R* + 0.889	−33.489*R* + 21.497
Greenalite–caryopilite (*G–C*)	6.8545*R* + 4.3037	0.7489*R* + 0.47	
Al-serpentines (*G–C*)'		0.7489*R* + 0.47	
Fe^{3+}-serpentines (*Fe^{3+}–Serp*)'		0.7489*R* + 0.43	
Neutral TOT phyllosilicates			
Pyrophyllite–talc (*P–T*)	1.1162*R* + 8.3691	0.122*R* + 0.9144	−38.126*R* + 24.21
Micas[b]			
Muscovite–phlogopite (*M–Ph*)	1.1479*R* + 8.3794	0.1229*R* + 0.8975	−37.514*R* + 24.23
Phlogopite–annite (*Ph–A*)	2.3942*R* + 7.4821	0.2564*R* + 0.8014	−20.056*R* + 11.66
Tetrasilicic micas	0.8694*R* + 8.4637	0.0944*R* + 0.925	−39.421*R* + 24.328
Phengite–micaceous samples		0.2373*R* + 0.8376[c]	−46.185*R* + 28.869[d]
Chlorites	2.2995*R* + 7.6655	0.1991*R* + 0.8504	−24.452R + 16.031

[a]Compared to hydroxides.
[b]See Table 7 for details on sub-relationships.
[c]Refers to phengites.
[d]Refers to micaceous samples.

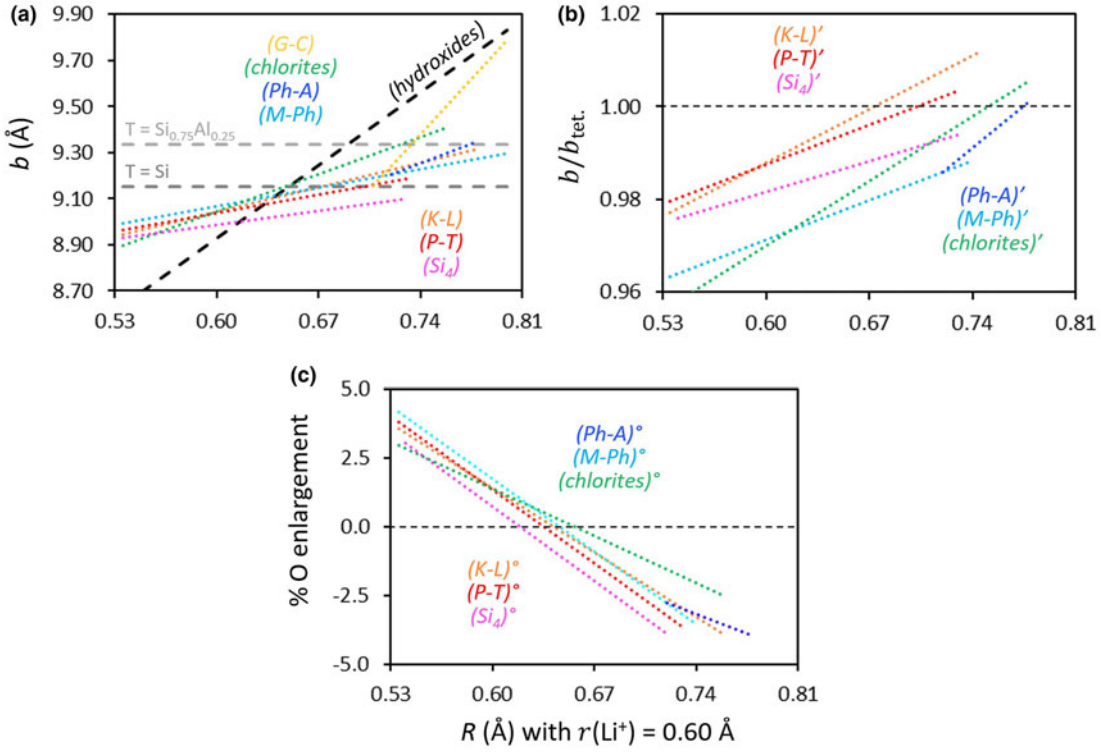

Figure 23. (a) *b vs R* calculated with $r(Li^+) = 0.60$ Å for the various studied phyllosilicates structures: horizontal dashed grey lines = calculated theoretical 'free' T sheet (dark grey: unsubstituted; light grey: $Si^{IV}_{0.75}Al_{0.25}$); black dashed line = experimentally determined regression for hydroxides (see text for details); coloured dotted lines = regression lines determined in this study, such as kaolinite–lizardite (*K–L*), pyrophyllite–talc (*P–T*), muscovite–phlogopite (*M–Ph*), phlogopite–annite (*Ph–A*), tetrasilicic micas (*Si_4*), (*chlorites*) and TO-modulated phyllosilicates (*G–C*). (b) $b/b_{tet.}$ *vs R* for the same phyllosilicates as in (a). (c) Percentage of octahedral enlargement compared to hydroxides (see text for details) *vs R* for the same phyllosilicates as in (a). The intersections between the 0% O enlargement line (black dashed line) and the coloured dotted lines correspond to *R* for which the thickness of the O sheets is the same for phyllosilicates and hydroxides. Above this 0% O enlargement line, the O sheets of phyllosilicates are thinner than the hydroxides for the same *R*, whereas below this line they are thicker.

structures without interlayer cations, as the (*P–T*)° line also has a similar slope to the tetrasilicic (*Si_4*)° and trisilicic (*M–Ph*)° mica lines.

For talc, the octahedral flattening is comparatively more pronounced than for tetrasilicic micas and comparatively less pronounced than for trisilicic micas (Fig. 23c), agreeing well with the O sheet thicknesses (Table 11). However, the calculated values of the tetrahedral rotation angle α are lower for tetrasilicic micas compared to trisilicic ones, but they are far greater than the measured ones (Table 11). For tetrasilicic micas, the tetrahedral

https://doi.org/10.1180/clm.2023.20 Published online by Cambridge University Press

Table 11. Structural details for some phyllosilicates for comparison. Sample reference from Table 6 for micas and Table 4 for talc. *R* calculated using $r(Li^+) = 0.60$ Å. Tetrahedral rotation angle α_{ref}: measured using structural refinement; α_{calc}: calculated ($\alpha = \arccos(b/b_{tet.})$; Equation 4; see text for details). % O enlargement compared to hydroxides; O sheet thickness measured by structure refinement and α_{ref}: from Brigatti & Guggenheim (2002) for micas and from Drits *et al.* (2012) for talc.

	Sample	*R* (Å)	*b* (Å)	α_{ref} (°)	α_{calc} (°)	% O enlargement	O sheet thickness (Å)
Si_3Al K-mica	5 – muscovite	0.581	9.074	7.7	12.1	2.7	2.107
Si_3Al Cs-mica	49 – nanpingite	0.577	9.076	5.7	12.8	2.9	2.079
Si_4 K-mica	96 – polylithionite	0.578	8.968	3.0	11.5	1.6	2.095
Si_3Al K-mica	85 – ferrian phlogopite	0.677	9.210	7.3	10.5	–0.7	2.112
Si_3Al K-mica	137 – ferrian phlogopite	0.685	9.212	7.4	10.4	–1.0	2.113
Si_3Al K-mica	146 – lithian siderophyllite	0.677	9.195	4.1	10.2	–0.8	2.109
Si_4 K-mica	105 – tainiolite	0.680	9.065	1.1	7.9	–2.4	2.192
Si_4 K-mica	3 – celadonite	0.682	9.050	1.3	9.0	–2.6	2.249
Si_3Al K-mica	98 – fluoro-phlogopite	0.720	9.238	7.6	10.1	–2.9	2.138
Si_4 K-mica	104 – tetra-silicic–F phlogopite	0.720	9.086	1.4	6.9	–4.0	2.186
Talc		0.720	9.173	3.6	0	–3.1	2.168

rotations probably have to be limited to ensure sufficiently large holes for K, and the contribution of the O sheet has to be more pronounced to allow congruency between the O and T sheet dimensions.

For lizardites and talcs, $b > b_{tet.}$ for $R > \sim 0.67$ and ~ 0.70 Å, respectively (Fig. 23a), but for the tetrasilicic and muscovite–phlogopite micas, the octahedral flattening varies continuously whatever the value of *R*.

For chlorites and phlogopite–annite, the O sheet becomes greater in the lateral dimension than T sheet for high *R*, and tetrahedral substitution rates are greater and thickening of O sheets occurs more strongly than for the other phyllosilicates (Fig. 23c).

These results agree well with previous works (e.g. Toraya, 1981; Lin & Guggenheim, 1983; Weiss *et al.*, 1985, 1992), and especially with Hazen & Wones (1972), who suggested that octahedral flattening is controlled by the octahedral cation radius.

The aforementioned structurally based interpretation probably underlies the approximately similar regression lines observed for the (*K–L*), (*P–T*), (*Si*$_4$) and (*M–Ph*) sample series (Fig. 23a), suggested that tetrahedral rotations and O sheet flattening are the primary crystallographic distortions allowing the T and O sheet accommodation. The role of the presence of a T sheet on *b* can also be evidenced by analysing the evolution of the *b vs R* regression line of trioctahedral micas and chlorites. The greater *b* values obtained for these minerals for great *R* values compared to other phyllosilicates (Fig. 23a & Table 10) could be due to the presence of trioctahedral O sheets coupled to large lateral T sheet dimensions. The above two features probably strengthen the decrease in tetrahedral rotation (Fig. 23b) and limit O sheet flattening (Fig. 23c) in trioctahedral micas and chlorites compared to the other phyllosilicates.

The (*G–C*) line exhibits a greater slope than the correlation obtained for chlorites or even for the hydroxides (Fig. 23a). This probably indicates a strong influence of the O sheets (which are similar to hydroxides sheets; Fig. 6b) over the T sheets for the (*G–C*) sample series and may explain the origins of the observed corrugated structures as a way to accommodate the dimensional misfit in these minerals. Such a mechanism is less likely to occur for TOT structures due to the constraints applied by the two sandwiching T sheets. The (*G–C*) line intersects the correlation line for chlorites when the dimensional misfit between T and O sheets is minimal (Fig. 23a). Note that even if the slope of the (*G–C*) line is greater than that observed for the hydroxides, the two lines never intersect (Fig. 23a), probably providing evidence of a structural limit to misfit accommodation.

The similarity of *b* values between chlorites and serpentines for the same octahedral composition may explain their intimate relationships in geological processes (e.g. Ryan & Hillier, 2002; Zhang *et al.*, 2021).

For ^{IV}Al- and Fe^{3+}-serpentines, excellent regressions were obtained for $b/b_{tet.}$ *vs R* (Fig. 6a), and the results obtained using Equation 10 were improved by integrating the tetrahedral sheet composition using Equation 11:

$$b/b_{tet.} = C\,R + D \quad (11)$$

with $b_{tet.}$ calculated according to Equation 3 and *C* and *D* being experimentally obtained regression parameters (Table 10).

As expected, micas with small interlayer cations (Na and Ca) or those that are not silicic appear ouside of the trends, and specific processes that ensure congruency between sheets cannot be assessed using this simplistic approach.

The schematized, structurally based interpretation of the control of *b* by *R* in hydroxides and various phyllosilicates represents the principal processes but is not unique. As evidenced for the synthetic mica series, the presence of sub-relationships related to limited solid solutions is also responsible for variations in the regression lines. Moreover, this study shows that for smectites and micas, as expected, the layer charge, especially that arising from tetrahedral substitution, probably also impacts the observed *b* values.

Conclusion

According to the abundant literature, the octahedral chemical composition of phyllosilicates is related to *b*. Using the mean ionic radius of octahedral cations, *R* allows us to generalize the various correlations that can be found in the literature between *b* and the octahedral chemistry of phyllosilicates and hydroxides, which are often restricted to limited types of sample series in terms of chemical composition or dioctahedral *vs* trioctahedral character. Integrating the tetrahedral sheet composition using $b_{tet.}$ for phyllosilicates that possess tetrahedral substitutions improves the relation between *b* and *R*.

A nanomechanistic interpretation based on misfit accommodation by coupling more or less pronounced tetrahedral rotation and O sheet flattening explains the results well globally, and this

https://doi.org/10.1180/clm.2023.20 Published online by Cambridge University Press

potentially impacts the processes of formation and transformation of phyllosilicates.

Refining the proposed model to account for structural peculiarities could represent a logical next step to this work.

Acknowledgements. We thank the anonymous reviewers for their careful and constructive reviews, which improved the quality of the paper significantly. We also thank Milan Rieder, who kindly provided us with a valuable table of mica data he obtained half a century ago, and Alain Meunier for his valuable comments on a preliminary version.

Financial support. We thank the European Joint Program EURAD (WP 'Future' – grant ID 847593), the French government programme 'Investissements d'Avenir' (EUR INTREE, reference ANR-18-EURE-0010) and the European Union (ERDF) and 'Région Nouvelle Aquitaine' for providing financial support for this study.

Conflicts of interest. The authors declare none.

References

Allmann R. (1968) The crystal structure of pyroaurite. *Acta Crystallographica*, **B24**, 972–977.

Anderson C.S. & Bailey S.W. (1981) A new cation ordering pattern in amesite-2H_2. *American Mineralogist*, **66**, 185–195.

Andreani M., Grauby O., Barronnet A. & Munoz M. (2008) Occurrence, composition and growth of polyhedral serpentine. *European Journal of Mineralogy*, **20**, 159–171.

Andrieux P. & Petit S. (2010) Hydrothermal synthesis of dioctahedral smectites: the Al-Fe^{3+} chemical series. Part I: influence of experimental conditions. *Applied Clay Science*, **48**, 5–17.

Arima M., Fleet M. E. & Barnett R. L. (1985) Titanian berthierine: a Ti-rich serpentine-group mineral from the Picton ultramafic dyke, Ontario. *The Canadian Mineralogist*, **23**, 213–220.

Badaut D., Decarreau A. & Besson G. (1992) Ferripyrophyllite and related Fe^{3+} rich 2:1 clays in recent deposits of Atlantis II deep Read Sea. *Clay Minerals*, **27**, 227–244.

Bailey S.W. (1966) The status of clay minerals structures. Pp. 1–23 in: *Proceedings of the Fourteenth National Conference on Clays and Clay Minerals* (S.W. Bailey, editor). Oxford, UK: Pergamon Press.

Bailey S.W. (1981) Structures of layer silicates. Pp. 1–124 in: *Crystal Structures of Clay Minerals and their X-Ray Identification* (G.W. Brindley & G. Brown, editors). Mineralogical Society, London, UK.

Bailey S.W. (1984a) Classification and structures of the micas. Pp. 1–12 in: *Micas (Reviews in Mineralogy, Volume 13)* (S.W. Bailey, editor). Mineralogical Society of America, Washington, DC, USA.

Bailey S.W. (1984b) Crystal chemistry of the true micas. Pp. 13–60 in: *Micas (Reviews in Mineralogy, Volume 13)* (S.W. Bailey, editor). Mineralogical Society of America, Washington, DC, USA.

Bailey S.W. (1988) Odinite, a new dioctahedral–trioctahedral 1:1 Fe^{3+}-rich clay mineral. *Clay Minerals*, **23**, 237–247.

Bailey S.W. (1991a) Chlorites: structures and crystal-chemistry. Pp. 347–453 in: *Hydrous Phyllosilicates (Reviews in Mineralogy, Volume 19)* (S.W. Bailey, editor). Mineralogical Society of America, Washington, DC, USA.

Bailey S.W. (1991b) Introduction. Pp. 1–8 in: *Hydrous Phyllosilicates (Reviews in Mineralogy, Volume 19)* (S.W. Bailey, editor). Mineralogical Society of America, Washington, DC, USA.

Bailey S.W. (1991c) Structures and compositions of other trioctahedral 1:1 phyllosilicates. Pp. 169–188 in: *Hydrous Phyllosilicates (Reviews in Mineralogy, Volume 19)* (S.W. Bailey, editor). Mineralogical Society of America, Washington, DC, USA.

Baron F., Petit S., Tertre E. & Decarreau A. (2016a) Influence of aqueous Si and Fe(III) speciation on tetrahedral Fe(III) substitution in nontronites: a clay synthesis approach. *Clays and Clay Minerals*, **64**, 189–203.

Baron F., Pushparaj S.S.C., Fontaine C., Sivaiah M.V., Decarreau A. & Petit S. (2016b) Microwave-assisted hydrothermal synthesis of Ni-Mg layered silicate clays. *Current Microwave Chemistry*, **3**, 85–89.

Baron F., Petit S., Pentrack M., Decarreau A. & Stucki J. (2017) Revisiting the nontronite Mössbauer spectra. *American Mineralogist*, **102**, 1501–1515.

Baronnet A., Mellini M. & Devouard B. (1994) Sectors in polygonal serpentine. A model based on dislocations. *Physics and Chemistry of Minerals*, **21**, 330–343.

Bates T.F. (1959) Morphology and crystal chemistry of 1:1 layer lattice silicates. *American Mineralogist*, **44**, 78–114.

Bayliss P. (1981) Unit cell data of serpentine group minerals. *Mineralogical Magazine*, **44**, 153–156.

Bayliss P., Berry L.G., Mrose M.E. & Smith D.K. (1980) *Mineral Powder Diffraction File*. JCPDS, Swarthmore, PA, USA.

Bellotto M., Rebours B., Clause O., Lynch J., Bazin D. & Elkaïm E. (1996) A reexamination of hydrotalcite crystal chemistry. *Journal of Physical Chemistry*, **100**, 8527–8534.

Bentabol M. & Ruiz Cruz M.D. (2013) Chemistry, morphology and structural characteristics of synthetic Al–Ni and Al–Co-lizardites. *Applied Clay Science*, **77**, 68–78.

Bentabol M., Ruiz Cruz M.D. & Huertas F.J. (2009) Isomorphous substitution *vs* defect density in hydrothermally synthesized (200 °C) Fe^{3+}, Ga^{3+} and Cr^{3+} -substituted kaolinites. *Applied Clay Science*, **45**, 36–43.

Bentabol M., Ruiz Cruz M.D. & Sobrados I. (2010) Chemistry, morphology and structural characteristics of synthetic Al-lizardite. *Clay Minerals*, **45**, 131–143.

Billault V., Beaufort D., Patrier P. & Petit S. (2002) Crystal-chemistry of Fe-sudoites from Mac Arthur River U-deposits (Saskatchewan, Canada). *Clays and Clay Minerals*, **50**, 70–81.

Birch W.D., Pring A., Reller A. & Schmalle H.W. (1993) Bernalite, $Fe(OH)_3$, a new mineral from Broken Hill, New South Wales: description and structure. *American Mineralogist*, **78**, 827–834.

Bish D.L. (1981) Distortions in the lizardite structure: a distance least squares study. *EOS*, **62**, 417.

Bish D.L. & Von Dreele R.B. (1989) Rietveld refinement of non-hydrogen atomic positions in kaolinite. *Clays and Clay Minerals*, **37**, 289–296.

Braithwaite R.S.W., Dunn P.J., Pritchard R.G. & Paar W.H. (1994) Uowaite, a reinvestigation. *Mineralogical Magazine*, **58**, 79–85.

Brigatti M.F. (1983) Relationships between composition and structure in Fe-rich smectites. *Clay Minerals*, **18**, 177–186.

Brigatti M.F. & Guggenheim S. (2002) Mica crystal chemistry and the influence of pressure, temperature, and solid solution on atomistic models. Pp. 1–97 in: *Micas: Crystal Chemistry and Metamorphic Petrology (Reviews in Mineralogy and Geochemistry, Volume 46)* (A. Mottana, F.P. Sassi, J.B. Thompson Jr. & S. Guggenheim, editors). Mineralogical Society of America, Chantilly, Virginia.

Brigatti M.F., Lugli C., Poppi M., Foord E.E. & Kile D.E. (2000) Crystal chemical variations in Li- and Fe-rich micas from Pikes Peak batholith (central Colorado). *American Mineralogist*, **85**, 1275–1286.

Brigatti M.F., Kile D.E. & Poppi M. (2001) Crystal structure and crystal chemistry of lithium-bearing muscovite-2M_1. *Canadian Mineralogist*, **39**, 1171–1180.

Brigatti M.F., Mottana A., Malferrari D. & Cibin G. (2007) Crystal structure and chemical composition of Li-, Fe-, and Mn-rich micas. *American Mineralogist*, **92**, 1395–1400.

Brigatti M.F., Malferrari D, Laurora A. & Elmi C. (2011) Structure and mineralogy of layer silicates: recent perspectives and new trends. *EMU Notes in Mineralogy*, **11**, 1–71.

Brigatti M.F., Galán E. & Theng B.K.G. (2013) Structure and mineralogy of clay minerals. Pp. 21–81 in: *Developments in Clay Science – Volume 5A. Handbook of Clay Science*, 2nd edition (F. Bergaya & G. Lagaly, editors). Elsevier, Amsterdam, The Netherlands.

Brindley G.W. (1982) Chemical compositions of berthierines. *Clays and Clay Minerals*, **30**, 153–155.

Brindley G.W. & Kao C.C. (1984) Structural and IR relations among brucite-like divalent metal hydroxides. *Physics and Chemistry of Minerals*, **10**, 187–191.

Brindley G.W. & Kikkawa S. (1979) A crystal-chemical study of Mg,Al and Ni, Al hydroxyl-perchlorates and hydroxyl-carbonates. *American Mineralogist*, **64**, 836–841.

Brindley G.W. & Wan H.M. (1975) Compositions, structures and thermal behavior of nickel containing minerals in the lizardite–nepouite series. *American Mineralogist*, **60**, 863–871.

https://doi.org/10.1180/clm.2023.20 Published online by Cambridge University Press

Brindley G.W. & Youell R.F. (1953) Ferrous chamosite and ferric chamosite. *Mineralogical Magazine*, **30**, 57–70.

Brindley G.W., Dunham K.C., Eyles V.A. & Taylor J.H. (1951) The crystal structure of chamosite minerals. *Mineralogical Magazine*, **29**, 502–525.

Brindley G.W., Bish D.L. & Wan H-M. (1977) The nature of kerolite, its relation to talc and stevensite. *Mineralogical Magazine*, **41**, 443–452.

Brindley, G.W., Bish D.L. & Wan H.-M. (1979) Compositions, structures, and properties of nickel-containing minerals in the kerolite–pimelite series. *American Mineralogist*, **64**, 615–625.

Brown I.D. & Shannon R.D. (1973) Empirical bond-strength-bond-length curves for oxides. *Acta Crystallographica*, **A29**, 266–282.

Buckley H.A., Bevan J.C., Brown K.M. & Johnson L.R. (1978) Glauconites and celadonites: two separate mineral species. *Mineralogical Magazine*, **42**, 373–382.

Capitani G. & Mellini M. (2004) The modulated crystal structure of antigorite: the $m = 17$ polysome. *American Mineralogist*, **80**, 147–155.

Capitani G., Compagnoni R., Cossio R., Botta S. & Mellini M. (2021) The intracrystalline microstructure of Monte Fico lizardite, by optics, μ-Raman spectroscopy and TEM. *European Journal of Mineralogy*, **33**, 425–432.

Caruso L.J. & Chernosky J.V. (1979) The stability of lizardite. *The Canadian Mineralogist*, **17**, 757–769.

Chemtob S.M., Nickerson R.D., Morris R.V., Agresti D.G. & Catalano J.G. (2015) Synthesis and structural characterization of ferrous trioctahedral smectite: implications for clay mineral genesis and detectability on Mars. *Journal of Geophysical Research Planets*, **120**, 1119–1140.

Chernosky J.V. Jr (1975) Aggregate refractive indices and unit cell parameters of synthetic serpentine in the system $MgO–Al_2O_3–SiO_2–H_2O$. *American Mineralogist*, **60**, 200–208.

Choi S.J., Oh J.M. & Choy J.H. (2008) Human-related application and nanotoxicology of inorganic particles: complementary aspects. *Journal of Materials Chemistry* 18, 615–620.

Chukhrov F.V., Zvyagin B.B., Drits V.A., Gorshkov A., Ermilova L.P., Goilo E.A. & Rudnitskaia E.S. (1979a) The ferric analogue to pyrophyllite and related phases. Pp. 55–64 in: *Developments in Sedimentology*, vol. **27** (M.M. Morland & V.C. Farmer, editors). Amsterdam, The Netherlands: Elsevier.

Chukhrov F.V., Zvyagin B.B., Drits V.A., Gorshkov A., Ermilova L.P., Goilo E.A. & Rudnitskaia E.S. (1979b) Über ferripyrophyllit. *Chemie der Erde*, **38**, 324–330.

Coey J.M.D., Chukhrov F.V. & Zvyagin B.B. (1984) Cation distribution, Mössbauer spectra and magnetic properties of ferripyrophyllite. *Clays and Clay Minerals*, **32**, 198–204.

Cooper M.A. & Hawthorne F.C. (1996) The crystal structure of shigaite, $[AlMn_2^{2+}(OH)_6]_3(SO_4)_2Na(H_2O)_6\{H_2O\}_6$, a hydrotalcite-group mineral. *The Canadian Mineralogist*, **34**, 91–97.

Corona J.C., Jenkins D.M. & Dyar D. (2015) The experimental incorporation of Fe into talc: a study using X-ray diffraction, Fourier transform infrared spectroscopy and Mössbauer spectroscopy. *Contributions to Mineralogy and Petrology*, **170**, 1–15.

Costantino U., Marmottini F., Nocchetti M. & Vivani R. (1998) New synthetic routes to hydrotalcite-like compounds. Characterisation and properties of the obtained materials. *European Journal of Inorganic Chemistry*, **10**, 1439–1446.

Costantino U., Nocchetti M., Sisani M. & Vivani R. (2009) Recent progress in the synthesis and application of organically modified hydrotalcites. *Zeitschrift für Kristallographie*, **224**, 273–281.

d'Espinose de la Caillerie J.B., Kermarec M. & Clause O. (1995) Impregnation of gamma-alumina with Ni(II) or Co(II) ions at neutral pH: hydrotalcite-type coprecipitate formation and characterization. *Journal of the American Chemical Society*, **117**, 11471–11481.

Dalmon J.A. & Martin G.-A. (1968) Sur la préparation et la structure de silicates basiques de cobalt et de magnésium de type talc et antigorite. *Comptes Rendus de l'Académie des Sciences, Paris*, **267**, 610–614.

Decarreau A. (1980) Cristallogenèse expérimentale des smectites magnésiennes : hectorite, stévensite. *Buletin de Mineralogie*, **103**, 579–590.

Decarreau A. (1983) *Etude expérimentale de la cristallogenèse des smectites. Mesures des coefficients de partage smectites trioctaèdriques-solution aqueuse pour les métaux M^{2+} de la première série de transition*. Sciences Géologiques, Mémoire n° 74. Université Louis Pasteur, Strasbourg, France, 185 pp.

Decarreau A. & Petit S. (2014) Fe^{3+}/Al^{3+} partitioning between tetrahedral and octahedral sites in dioctahedral smectites. *Clay Minerals*, **49**, 657–665.

Deer W.A., Howie R.A. & Zussman J. (2009) Pyrophyllite paragenesis. Pp. 69–73 in: *Rock Forming Minerals vol 3C: Layered Silicates Excluding Micas and Clay Minerals)* (W.A Deer., R.A. Howie & J. Zussman, editors). Geological Society of London, London, UK.

Dekov V.M., Kamenov G.D., Stummeyer J., Thiry M., Savelli C., Shanks W.C. *et al.* (2007) Hydrothermal nontronite formation at Eolo Seamount (Aeolian volcanic arc, Tyrrhenian Sea). *Chemical Geology*, **245**, 103–119.

de la Calle C. & Suquet H. (1991) Vermiculite. Pp. 455–496 in: *Hydrous Phyllosilicates (Reviews in Mineralogy, Volume 19)* (S.W. Bailey, editor). Mineralogical Society of America, Washington, DC, USA.

De Waal S.A. (1970) Nickel minerals from Barberton, South Africa: III. Willemseite, a nickel-rich talc. *American Mineralogist*, **55**, 31–42.

Donnay G., Morimoto N., Takeda H. & Donnay J.H.D. (1964) Trioctahedral one-layer micas: I. Crystal structure of a synthetic iron mica. *Acta Crystallographica*, **17**, 1369–1373.

Drits V.A., McCarty D.K. & Zviagina B.B. (2006) Crystal-chemical factors responsible for the distribution of octahedral cations over *trans-* and *cis*-sites in dioctahedral 2:1 layer silicates. *Clays and Clay Minerals*, **54**, 131–152.

Drits V.A., Guggenheim S., Zviagina B.B. & Kogure T. (2012) Structures of the 2:1 layers of pyrophyllite and talc. *Clays and Clay Minerals*, **60**, 574–587.

Eberl D., Jones B.F. & Khoury H.N. (1982) Mixed-layer kerolite/stevensite from the Amargosa Desert, Nevada. *Clays and Clay Minerals*, **39**, 321–326.

Ennadi A., Legrouri A., De Roy A. & Besse J. P. (2000) X-Ray diffraction pattern simulation for thermally treated [Zn–Al–Cl] layered double hydroxide. *Journal of Solid Solid State Chemistry*, **152**, 568–572.

Evans B.W. (1976) Stability of chrysotile and antigorite in the serpentinite multisystem. *Schweizer Mineralogische und Petrographische Mitteilungen*, **56**, 79–93.

Evans B.W. (2004) The serpentinite multisystem revisited: chrysotile is metastable. *International Geology Review*, **46**, 479–506.

Evans B.W. & Guggenheim, S. (1991) Talc, pyrophyllite, and related minerals. Pp. 225–294 in: *Hydrous Phyllosilicates (Reviews in Mineralogy, Volume 19)* (S.W. Bailey, editor). Mineralogical Society of America, Washington, DC, USA.

Falini G., Foresti E., Gazzano M., Gualtieri A.F., Leoni M., Lesci I.G. & Roveri N. (2004) Tubular-shaped stoichiometric chrysotile nanocrystals. *Chemistry – A European Journal*, **10**, 3043–3049.

Faust G.T., Hataway J.C. & Millot G. (1959) A restudy of stevensite and allied minerals. *American Mineralogist*, **44**, 342–370.

Ferrage E. (2016) Investigation of the interlayer organization of water and ions in smectite from the combined use of diffraction experiments and molecular simulations: a review of methodology, applications and perspectives. *Clays and Clay Minerals*, **64**, 346–371.

Ferrage E., Lanson B., Sakharov B., Geoffroy N., Jacquot E. & Drits V. (2007) Investigation of dioctahedral smectite hydration properties by modeling of X-ray diffraction profiles: influence of layer charge and charge location. *American Mineralogist*, **92**, 1731–1743.

Fiore S., Huertas F.J., Huertas F. & Linares J. (1995) Morphology of kaolinite crystals synthesized under hydrothermal conditions. *Clays and Clay Minerals*, **43**, 353–360.

Foord E.E., Starkey H.C., Taggart J.E. & Shawe D.R. (1987) Reassessment of the volkonskoite–chromium smectite nomenclature problem. *Clays and Clay Minerals*, **35**, 139–149.

Forano C., Costantino U., Prévôt V. & Taviot Gueho C. (2013) Layered double hydroxides (LDH). Pp. 745–782 in: *Developments in Clay Science – Volume 5A. Handbook of Clay Science*, 2nd edition (F. Bergaya & G. Lagaly, editors). Elsevier, Amsterdam, The Netherlands.

Forbes W.C. (1969) Unit-cell parameter and optical properties of talc on the join $Mg_3Si_4O_{10}(OH)_2–Fe_3Si_4O_{10}(OH)_2$. *American Mineralogist*, **54**, 1399–1408.

Frondel C. & Ito J. (1966) Hendricksite: a new species of mica. *American Mineralogist*, **51**, 1107–1123.

Frondel C. & lto J. (1975) Zinc-rich chlorites from Franklin, New Jersey with a note on chlorite nomenclature. *Neues Jahrbuch fiir Mineralogie Abhandlungen*, **123**, 111–115.

https://doi.org/10.1180/clm.2023.20 Published online by Cambridge University Press

Gaudin A., Petit S., Rose J., Martin F., Decarreau A., Noack Y. & Borschneck D. (2004) The accurate crystal chemistry of ferric smectites from the lateritic nickel ore of Murrin Murrin (Western Australia). II: spectroscopic (IR and EXAFS) approaches. *Clay Minerals*, **39**, 453–467.

Geiger C.A., Henry D.L., Bailey S.W. & Maj J.J. (1983) Crystal structure of cronstedtite $2H_2$. *Clays and Clay Minerals*, **31**, 97–108.

Gerth J. (1990) Unit-cell dimension of pure and trace metal associated goethites. *Geochimica Cosmochimica Acta*, **54**, 363–371.

Giese R.F. (1991) Kaolin minerals: structure and stabilities. Pp. 29–66 in: *Hydrous Phyllosilicates (Reviews in Mineralogy, Volume 19)* (S.W. Bailey, editor). Mineralogical Society of America, Washington, DC, USA.

Gillery F.H. (1959) The X-Ray study of synthetic Mg-Al serpentines and chlorites. *American Mineralogist*, **44**, 143–152.

Grauby O., Petit S., Decarreau A. & Baronnet A. (1994) The nontronite–saponite series: an experimental approach. *European Journal of Mineralogy*, **6**, 99–112.

Grégoire B., Ruby C. & Carteret C. (2012) Structural cohesion of MII–MIII layered double hydroxides crystals: electrostatic forces and cationic polarizing power. *Crystal Growth & Design*, **12**, 4324–4333.

Grüner J.W. (1944) The composition and structure of minesotaite, a common iron silicate in iron formations. *American Mineralogist*, **29**, 363–372.

Guggenheim S. (1984) The brittle micas. Pp. 61–104 in: *Micas (Reviews in Mineralogy, Volume 13)* (S.W. Bailey, editor). Mineralogical Society of America, Washington, DC, USA.

Guggenheim S. & Bailey S.W. (1982) The superlattice of minnesotaite. *Canadian Mineralogist*, **20**, 579–584.

Guggenheim S. & Bailey S.W. (1989) An occurrence of a modulated serpentine related to the greenalite–caryopilite series. *American Mineralogist*, **74**, 637–641.

Guggenheim S. & Eggleton R.A. (1986) Structural modulations in iron-rich and magnesium-rich minnesotaite. *The Canadian Mineralogist*, **24**, 479–497.

Guggenheim S. & Eggleton R. A (1987) Modulated 2:1layer silicates: review, systematics and predictions. *American Mineralogist*, **72**, 724-738.

Guggenheim S. & Eggleton R.A. (1988) Crystal chemistry, classification, and identification of modulated layer silicates. Pp. 675–725 in: *Hydrous Phyllosilicates (Reviews in Mineralogy, Volume 19)* (S.W. Bailey, editor). Mineralogical Society of America, Washington, DC, USA.

Guggenheim S.V. & Eggleton R.A. (1998) Modulated crystal structures of greenalite and caryopilite: a system with long-range, in-plane structural disorder in the tetrahedral sheet. *The Canadian Mineralogist*, **36**, 163–179.

Guggenheim S.V. & Zhan W. (1998) Effect of temperature on the structures of lizardite-1*T* and lizardite $2H_1$. *The Canadian Mineralogist*, **36**, 1587–1594.

Guidotti C.V., Mazzoli C., Sassi F. & Blencoe J. (1992). Compositional controls on the cell dimensions of 2M1 muscovite and paragonite. *European Journal of Mineralogy*, **4**, 283–297.

Hazen R.M. & Wones D.R. (1972) The effect of cation substitutions on the physical properties of trioctahedral micas. *American Mineralogist*, **57**, 103–129.

Heuser M., Andrieux P., Petit S. & Stanjek H. (2013) Iron-bearing smectites: a revised relationship between structural Fe, *b* cell edge lengths and refractive indices. *Clay Minerals*, **48**, 97–103.

Hewitt D.A. & Wones D.R. (1975) Physical properties of some synthetic Fe–Mg–Al trioctahedral biotites. *American Mineralogist*, **60**, 854–862.

Higashi S., Miki K. & Komarneni S. (2002) Hydrothermal synthesis of Zn-smectites. *Clays and Clay Minerals*, **50**, 299–305.

Hill R.J. (1979) Crystal structure refinement and electron density distribution in diaspore. *Physics and Chemistry of Minerals*, **5**, 179–200.

Huminicki D.M.C. & Hawthorne F.C. (2003) The crystal structure of nikischerite, $NaFe_6^{2+}Al_3(SO4)_2(OH)_{18}(H_2O)_{12}$, a mineral of the shigaite group. *The Canadian Mineralogist*, **41**, 79–82.

Hybler J. (2016) Crystal structure of cronstedtite-$6T_2$, a non-MDO polytype. *European Journal of Mineralogy*, **28**, 777–788.

Hybler J. & Sejkora J. (2017) Polytypism of cronstedtite from Chyňava, Czech Republic. *Journal of Geosciences*, **62**, 137–146.

Hybler J., Petříček V., Ďurovič S. & Smrčok Ľ. (2000) Refinement of the crystal structure of cronstedtite-1*T*. *Clays and Clay Minerals*, **48**, 331–338.

Hybler J., Sejkora J. & Venclík V. (2016) Polytypism of cronstedtite from Pohled, Czech Republic. *European Journal of Mineralogy*, **28**, 765–775.

Hybler J., Števko M., & Sejkora J. (2017) Polytypism of cronstedtite from Nižná Slaná, Slovakia. *European Journal of Mineralogy*, **29**, 91–99.

Hybler J., Dolniček Z., Sejkora J. & Števko M. (2020) Polytypism of cronstedtite from Nagybörzsöny, Hungary. *Clays and Clay Minerals*, **68**, 632–645.

Hybler J., Dolniček Z., Sejkora J. & Števko M. (2021) Polytypism of cronstedtite from Ouedi Beht, El Hammam, Morocco. *Clays and Clay Minerals*, **69**, 702–734.

Iriarte I., Petit S., Huertas J., Fiore S., Grauby O., Decarreau A. & Linares J. (2005) Synthesis of kaolinite with a high level of Fe^{3+} for Al substitution. *Clays and Clay Minerals*, **53**, 1–10.

Jahanbagloo I.C. & Zoltai T. (1968) The crystal structure of a hexagonal Al-serpentine. *American Mineralogist*, **53**, 14–24.

Jain A., Ong S.P., Hautier G., Chen W., Richards W.D., Dacek S. *et al.* (2013) The Materials Project: a materials genome approach to accelerating materials innovation. *APL Materials*, **1**, 011002.

Jasmund K. & Sylla H.M. (1971) Synthesis of Mg and Ni antigorite. *Contributions to Mineralogy and Petrology*, **34**, 84–86.

Jasmund K., Sylla H.M. & Freund F. (1976) Solid solution in synthetic serpentines phases. Pp. 267–274 in: *Proceedings of the International Clay Conference* (S.W. Bailey, editor). Calgary, AL, Canada: Applied Publishing Ltd.

Joussein E., Petit S., Chruchman J., Theng B., Righi D. & Delvaux B. (2005) Halloysite clay minerals – a review. *Clay Minerals*, **40**, 383–426.

Kato T. (1963) New data on the so-called bementite. *Journal of the Mineralogical Society of Japan*, **6**, 93–103.

Khoury H.N., Mackenzie R.C., Russel J.D. & Tait J.M. (1984) An iron free volkonkoite. *Clay Minerals*, **19**, 43–57.

Kloprogge J.T. (2017) Application of vibrational spectroscopy in clay minerals synthesis. Pp. 222–287 in: *Infrared and Raman Spectroscopies of Clay Minerals (Developments in Clay Science, Vol. 8)* (W.P. Gates, J.T. Kloprogge, J. Madejová & F. Bergaya, editors). Elsevier, Amsterdam, The Netherlands.

Knurr R.A. & Bailey S.W. (1986) Refinement of Mn-substituted muscovite and phlogopite. *Clays and Clay Minerals*, **34**, 7–16.

Kodama H., De Kimpe C.R. & Dejou J. (1988) Ferrian saponite in a gabbro saprolite at Mont Mégantic, Quebec. *Clays and Clay Minerals*, **36**, 102–110.

Kohler T. & Armbruster T. (1997) Hydrogen bonding and Jahn–Teller distortion in groutite α-MnOOH and manganite γ-MnOOH, and their relations to the manganese dioxides ramsdellite and pyrolusite. *Journal of Solid State Chemistry*, **133**, 486–500.

Köster H.M., Ehrlicher U., Gilg H.A., Jordan R., Murad E. & Onnich K. (1999) Mineralogical and chemical characteristics of five nontronites and Fe-rich smectites. *Clay Minerals*, **34**, 579–599.

Lee S.S., Guggenheim S., Dyar M.D. & Guidotti C.V. (2007) Chemical composition, statistical analysis of the unit cell, and electrostatic modeling of the structure of Al-saturated chlorite from metamorphosed rocks. *American Mineralogist*, **92**, 954–965.

Lin J.-C. & Guggenheim S. (1983) The crystal structure of a Li,Be-rich brittle mica: a dioctahedral-trioctahedral intermediate. *American Mineralogist*, **68**, 130–142.

Lombardo G.M., Pappalardo G.C., Punzo F., Costantino F., Costantino U. & Sisani M. (2005) A novel integrated X-ray powder diffraction (XRPD) and molecular dynamics (MD) approach for modelling mixed-metal (Zn, Al) layered double hydroxides (LDHs). *European Journal of Inorganic Chemistry*, **24**, 5026–5034.

MacEwan D.M.C. (1961) Montmorillonite minerals. Pp. 143–207 in: *The X-Ray Identification and Crystal Structures of Clay Minerals*, 2nd edition (G. Brown, editor). Mineralogical Society, London, UK.

Maksimovic Z. (1966) Kerolite–pimelite series from Goles Mountain, Yugoslavia. Pp. 97–105 in: *Proceedings of the International Clay Conference* (L. Heller, editor). Jerusalem, Israel: Israel Program for Scientific Translations.

Maksimovic Z. & Bish D. (1978) Brindleyite, a nickel-rich aluminous serpentine mineral analogous to berthierine. *American Minereralogist*, **63**, 484–489.

Manohara G.V. & Vishnu Kamath P. (2010) Synthesis and structure refinement of layered double hydroxides of Co, Mg and Ni with Ga. *Bulletin of Materials Science*, **33**, 325–331.

Manohara G.V., Prasanna S.V. & Vishnu Kamath P. (2011) Structure and composition of the layered double hydroxides of Mg and Fe: implications

https://doi.org/10.1180/clm.2023.20 Published online by Cambridge University Press

for anion-exchange reactions. *European Journal of Inorganic Chemistry*, **16**, 2624–2630.
Martin F., Petit S., Decarreau A., Grauby O., Hazemann J.L. & Noack Y. (1992) Experimental study of (Si–Ge) tetrahedral solid solution in Ni–Co–Mg talcs. *Thin Solid Films*, **222**, 189–195.
Martin de Vidales J.L., Pozo M., Alia J.M., Garcia-Navaro F. & Rull F. (1991) Kerolite–stevensite mixed-layers from the Madrid basin, central Spain. *Clay Minerals*, **26**, 329–342.
Martin F., Ildefonse P., Hazemann J.L., Mathe P., Noack Y., Grauby O. *et al.* (1997) Gallium crystal chemistry in synthetic goethites. *Journal de Physique III*, **C2**, 821–822.
Martin F., Petit S., Decarreau A., Ildefonse P., Grauby O., Beziat D. *et al.* (1998) Ga/Al substitutions in synthetic kaolinites and smectites. *Clay Minerals*, **33**, 231–241.
Mathieson A.M. & Walker G.F. (1954) Crystal structure of magnesium-vermiculite. *American Mineralogist*, **39**, 231–255.
McCauley J.W. & Newnham R.E. (1971) Origin and prediction of ditrigonal distortions in micas. *American Mineralogist*, **56**, 1626–1638.
Mellini M. (1982) The crystal structure of lizardite 1*T*: hydrogen bonds and polytypism. *American Mineralogist*, **67**, 587–598.
Mellini M. (2013) Structure and microstructure of serpentine minerals. *EMU Notes in Mineralogy*, **14**, 153–179.
Mellini M. & Viti C. (1994) Crystal structures of lizardites-1*T* from Elba, Italy. *American Mineralogist*, **79**, 1194–1198.
Mellini M. & Zanazzi P.F. (1987) Crystal structures of lizardites-1*T* and lizardites-2H_1 from Coli, Italy. *American Mineralogist*, **72**, 943–948.
Mellini M., Cressey G., Wicks F.J. & Cressey B.A. (2010) The crystal structure of Mg end-member lizardite-1T forming polyhedral spheres from the Lizard, Cornwall. *Mineralogical Magazine*, **74**, 277–284.
Mercier P.H.J., Rancourt D.G., Robert Jean-Louis, Berman R.G. & Redhammer G.J. (2005) Fundamental difference between synthetic powder and natural or synthetic single-crystal 1*M* micas: geometric homo-octahedral *vs* geometric meso-octahedral sheets. *American Mineralogist*, **90**, 399–410.
Merlino S. & Orlandi P. (2001) Carraraite and zaccagnaite, two new minerals from the Carrara marble quarries: their chemical compositions, physical properties, and structural features. *American Mineralogist*, **86**, 1293–1301.
Mills S.J., Whitfield P.S., Wilson S., Woodhouse J.N., Dipple G.M., Raudsepp M., Francis C.A. (2011) The crystal structure of stichtite, re-examination of barbertonite, and the nature of polytypism in MgCr hydrotalcites. *American Mineralogist*, **96**, 179–187.
Nadeau P.H., Farmer V.C., Mc Hardy W.J. & Bain D.C. (1985) Compositional variations of the Unterrupsroth beidellite. *American Mineralogist*, **70**, 1004–1010.
Nestroinaya O.V., Ryltsova I.G., Lebedeva O.E., Uralbekov B.M. & Ponomarenko O.I. (2017) Synthesis and thermal transformation of multi-component layered double MgCo/AlFe hydroxides with hydrotalcite structure. *Russian Journal of General Chemistry*, **87**, 163–167.
Olsen E.J. (1961) Six-layer ortho-hexagonal serpentine from the Labrador trough. *American Mineralogist*, **46**, 434–438.
Parise J.B., Leinenweber K., Weidner D.J., Tan K. & von Dreele R.B. (1994) Pressure-induced H bonding: neutron diffraction study of brucite, Mg$(OD)_2$, to 9.3 GPa. *American Mineralogist*, **79**, 193–196.
Pastor-Rodriguez J. & Taylor H.F.W. (1971) Crystal structure of coalingite. *Mineralogical Magazine*, **38**, 286–294.
Pauling L. (1930) The structures of the chlorites. *Proceedings of the National Academy of Sciences of the United States of America*, **16**, 578–582.
Peacor D.R., Essene E.J., Simmons W.B. Jr & Bigelow W. (1974) Kellyite a new Mn–Al member of the serpentine group from Bald Knob, North Carolina, and new data on grovesite. *American Mineralogist*, **59**, 1153–1156.
Perdikatsis B. & Burzlaff H. (1981) Struktuverfeinerung am Talk $Mg_3[(OH)_2Si_4O_{10}]$. *Zeitschrift für Kristallographie*, **156**, 177–186.
Peterson R.C., Hill R.J. & Gibbs G.V. (1979) A molecular-orbital study of distortions in the layer structures brucite, gibbsite and serpentine. *The Canadian Mineralogist*, **17**, 703–713.
Petit S. (1990) Etude cristallochimique de kaolinites ferrifères et cuprifères de synthèse (150–250°C). PhD thesis, Université de Poitiers, Poitiers, France.
Petit S. & Decarreau A. (1990) Hydrothermal (200°C) synthesis and crystal chemistry of iron-rich kaolinites. *Clay Minerals*, **25**, 181–196.
Petit S., Decarreau A., Eymery J.P. & Thomassin J.H. (1988) Synthèse de kaolinites ferriques à 200°C. Comparaison avec des kaolinites d'altération supergène : teneur en fer, morphologie, cristallinité. *Comptes Rendus de l'Académie des Sciences*, **307**, 1961–1966.
Petit S., Prot T., Decarreau A., Mosser C. & Toledo-Groke C. (1992) Crystallochemical study of a population of particles in smectites from a lateritic weathering profile. *Clays and Clay Minerals*, **40**, 436–445.
Petit S., Caillaud J., Righi D., Madejová F., Elsass F. & Köster H.M. (2002) Characterization and crystal chemistry of Fe-rich montmorillonite from Ölberg, Germany. *Clay Minerals*, **37**, 283–297.
Petit S., Righi D. & Decarreau A. (2008) Transformation of synthetic Zn-stevensite into Zn-talc induced by the Hofmann–Klemen effect. *Clays and Clay Minerals*, **56**, 645–654.
Petit S., Decarreau A., Gates W., Andrieux P. & Grauby O. (2015) Hydrothermal synthesis of dioctahedral smectites: the Al–Fe^{3+} chemical series. Part II: crystal-chemistry. *Applied Clay Science*, **104**, 96–105.
Petit S., Baron F., Grauby O. & Decarreau A. (2016) Revisiting the cation mas-valence sum approach to assigning infrared OH-bands in dioctrahedral smectites in the light of new data from synthetic Ga-Fe^{3+} smectites. *Vibrational Spectroscopy*, **87**, 137–142.
Petit S., Baron F. & Decarreau A. (2017) Synthesis of nontronite and other iron-rich smectites: a critical review. *Clay Minerals*, **52**, 469–483.
Post J.L., Cupp B.L. & Madsen F.T. (1997) Beidellite and associated clays from the De Lamar mine and Florida Mountain area, Idaho. *Clays and Clay Minerals*, **45**, 240–250.
Pozo M. & Casas J. (1999) Origin of kerolite and associated Mg clays in palustrine-lacustrine environments. The Esquivas deposit (Neogene Madrid basin, Spain). *Clay Minerals*, **34**, 395–418.
Radha A.V., Vishnu Kamath P. & Shivakumara C. (2007) Order and disorder among the layered double hydroxides: combined Rietveld and DIFFaX approach. *Acta Crystallographica Section B: Structural Science*, **63**, 243–250.
Radha S., Prasanna S.V. & Vishnu Kamath P. (2011) Polytype selection by intercalated anions: design and synthesis of the 3R_2 polytype of the layered double hydroxide of Zn and Al. *Crystal Growth Design*, **11**, 2287–2293.
Radoslovich E.W. (1962) The cell dimensions and symmetry of layer lattice silicates. II. Regression relations. *American Mineralogist*, **47**, 617–636.
Radoslovich E.W. (1963) The cell dimensions and symmetry of layer lattice silicates. VI. Serpentine and kaolin morphology. *American Mineralogist*, **48**, 368–378.
Radoslovich E.W. & Norrish K. (1962) The cell dimensions and symmetry of layer lattice silicates. I. Some structural considerations. *American Mineralogist*, **47**, 599–616.
Redhammer G.J. & Roth G. (2002) Single-crystal structure refinements and crystal chemistry of synthetic trioctahedral micas $KM_3(Al^{3+},Si^{4+})_4O_{10}(OH)^2$, where $M = Ni^{2+}$, Mg^{2+}, Co^{2+}, Fe^{2+}, or Al^{3+}. *American Mineralogist*, **87**, 1464–1476.
Rieder M. (1970) Chemical composition and physical properties of lithium-iron micas from the Krusné hory Mts. (Erzgebirge) part A: chemical composition. *Contributions to Mineralogy and Petrology*, **27**, 131–158.
Rieder M., Pichova A., Fassova M., Fediukova E. & Cerny P. (1971) Chemical composition and physical properties of lithium-iron micas from the Krusné hory Mts. (Erzgebirge), Czechoslovakia and Germany. Part B: cell parameters and optical data. *Mineralogical Magazine*, **38**, 190–196.
Rieder M., Cavazzini G., D'yakonov Y.S., Frank-Kamenetskii V.A., Gottardi G., Guggenheim S. *et al.* (1998) Nomenclature of the micas. *The Canadian Mineralogist*, **36**, 905–912.
Rius J. & Allmann R. (1984) The superstructure of the double layer mineral wermlandite, $[Mg_7(Al_{0.57}Fe_{0.43})_2(OH)_{18}][(Ca_{0.6}Mg_{0.4})(SO_4)_2,12H_2O]$. *Zeitschrift für Kristallographie*, **168**, 133–144.
Robert J.L. (1976) Phlogopite solid solutions in the system K_2O–MgO–Al_2O_3–SiO_2–H_2O. *Chemical Geology*, **17**, 195–212.
Robinson G.W. & Chamberlain S.C. (1984) Famous mineral localities: the Sterling Mine Antwerp, New York. *The Mineralogical Record*, **July–August**, 199–216.
Roussel H., Briois V., Elkaim E., de Roy A. & Besse J. P. (2000) Cationic order and structure of [Zn−Cr−Cl] and [Cu−Cr−Cl] layered double hydroxides: a XRD and EXAFS study. *Journal of Physical Chemistry B*, **104**, 5915–5923.

https://doi.org/10.1180/clm.2023.20 Published online by Cambridge University Press

Rule A.C. & Bailey S.W. (1987) Refinement of the crystal structure of a monoclinic ferroan clinochlore. *Clay and Clay Minerals*, **35**, 129–138.

Russell J.D. & Clark D.R. (1978) The effect of Fe-for-Si substitution on the *b*-dimension of nontronite. *Clay Minerals*, **13**, 133–137.

Ryan P.C. & Hillier S. (2002) Berthierine/chamosite, corrensite, and discrete chlorite from evolved verdine and evaporite-associated facies in the Jurassic Sundance Formation, Wyoming. *American Mineralogist*, **87**, 1607–1615.

Saalfeld H. & Wedde M. (1974) Refinement of the crystal structure of gibbsite, $Al(OH)_3$. *Zeitschrift für Krystallographie*, **139**, 129–135.

Sankaranarayanan, S., Sharma, A. & Srinivasan, K. (2015) CoCuAl layered double hydroxides – efficient solid catalysts for the preparation of industrially important fatty epoxides. *Catalysis Science & Technology*, **5**, 1187–1197.

Schmidt M.W., Dugnani M. & Artioli G. (2001) Synthesis and characterization of white micas in the join muscovite–aluminoceladonite. *American Mineralogist*, **86**, 555–565.

Schulze D.G. (1984) The influence of aluminum on iron oxides. VIII. Unit-cell dimensions of Al-substituted goethites and estimation of Al from them. *Clays and Clay Minerals*, **38**, 36–44.

Schwertmann U., Gasser U. & Sticher H. (1989) Chromium for iron substitution in synthetic goethites. *Geochimica Cosmochimica Acta*, **53**, 1293–1297.

Shannon R.D. (1976) Revised effective ionic radii and systematic studies of interatomic distances in halides and chalcogenides. *Acta Crystallographica*, **A32**, 751–767.

Shannon R.D., Gumerman P.S. & Chenavas J. (1975) Effect of octahedral distortion on mean Mn^{3+}–O distances. *American Mineralogist*, **60**, 714–716.

Shirozu M & Bailey S.W. (1966) Crystal structure of a two-layer Mg-vermiculite. *American Mineralogist*, **51**, 1124–1143.

Smyth J.R., Dyar M.D., May H.M., Bricker O.P. & Acler J.G. (1997) Crystal structure refinement and Mössbauer spectroscopy of an ordered, triclinic clinochlore. *Clays and Clay Minerals*, **45**, 544–550.

Środoń J. (2013) Identification and quantitative analysis of clay minerals. Pp. 25–49 in: *Developments in Clay Science – Volume 5B. Handbook of Clay Science*, 2nd edition (F. Bergaya & G. Lagaly editors). Elsevier, Amsterdam, The Netherlands.

Steadman R. & Youell R.F. (1958) Mineralogy and crystal structure of greenalite. *Nature*, **181**, 45.

Steinfink H. (1958) The crystal structure of chlorite. I. A monoclinic polymorph. *Acta Crystallographica*, **11**, 191–195.

Stiers W. & Schwertmann U. (1985) Evidence of manganese substitution in synthetic goethite. *Geochimica Cosmochimica Acta*, **49**, 1909–1911.

Suquet H., De La Calle C. & Pezerat H. (1975) Swelling and structural organization of saponite. *Clays and Clay Minerals*, **23**, 1–9.

Suquet H., Ijyama J.T., Kodama H. & Pezerat H. (1977) Synthesis and swelling properties of saponites with increasing layer charge. *Clays and Clay Minerals*, **25**, 231–242.

Suquet H., Malard C., Copin E. & Pézerat H. (1981) Variation du paramètre *b* et de la distance basale (001) dans une série de de saponites à charge croissante. *Clay Minerals*, **16**, 53–67.

Taner M.F. & Laurent R. (1984) Iron-rich amesite from Lake Asbestos mine, Black Lake, Quebec. *The Canadian Mineralogist*, **22**, 437–442.

Tomisaka T. & Kato T. (1963) A study of the polymorphism of serpentine minerals. *Journal of the Mineralogical Society of Japan*, **6**, 209–229.

Toraya H. (1981) Distortions of octahedra and octahedral sheets in 1*M* micas and the relation to their stability. *Zeitschrift für Kristallographie*, **157**, 173–190.

Tsipursky S.I. & Drits V.A. (1984) The distribution of octahedral cations in the 2:1 layers of dioctahedral smectites studied by oblique-texture electron diffraction. *Clay Minerals*, **19**, 177–193.

von Engelhardt W. (1942) Die strukturen von thuryngit, bavalit, und chamosit und ihre stellung in der chloritgruppe. *Zeitschrift für Kristallographie, Kristallgeometrie, Kristallphysik, Kristallchemie*, **104**, 152–159.

Wahle M.W., Bujnowski T.J., Guggenheim S. & Kogure T. (2010) Guidottite, the Mn-analogue of cronstedtite: a new serpentine-group mineral from South Africa. *Clays and Clay Minerals*, **58**, 364–376.

Weiss Z., Rieder M., Chmielová M. & Krajíček J. (1985) Geometry of the octahedral coordination in micas: a review of refined structures. *American Mineralogist*, **70**, 747–757.

Weiss Z., Rieder M. & Chmielová M. (1992) Deformation of coordination polyhedra and their sheets in phyllosilicates. *European Journal of Mineralogy*, **4**, 665–682.

Whitney G. & Northrop H.R. (1986) Vanadium chlorite from a sandstone-hosted vanadium-uranium deposit, Henry Basin, Utah. *Clays and Clay Minerals*, **34**, 488–495.

Wicks F.J. & Hawthorne F.C. (1986) Distance least-squares modelling of lizardite lT structure. P. 144 in: *Program Abstracts II Joint Annual Meeting of the Geological Association of Canada and Mineralogical Association of Canada*. Ottawa, ON, Canada: Open Library.

Wicks F.J. & O'Hanley D.S. (1991) Serpentine minerals: structures and petrology. Pp. 91–167 in: *Hydrous Phyllosilicates (Reviews in Mineralogy, Volume 19)* (S.W. Bailey, editor). Mineralogical Society of America, Washington, DC, USA.

Wicks F.J. & Whittaker J.W. (1975) A reappraisal of the structures of the serpentine minerals. *The Canadian Mineralogist*, **13**, 227–243.

Wiewiora A. (1990) Crystallochemical classifications of phyllosilicates based on the unified system of projection of chemical composition: III. The serpentine-kaolin group. *Clay Minerals*, **25**, 93–98.

Wiewiora A. & Weiss Z. (1990) Crystallochemical classifications of phyllosilicates based on the unified system of projection of chemical composition: II. The chlorite group. *Clay Minerals*, **25**, 83–92.

Wiewiora A. & Wilamowski A. (1996) The relation between composition and *b* for chlorites. *Geologica Carpathica Clays*, **5**, 79–87.

Wiewiora A., Raussel-Colomb J.A. & Garcia-Gonzales T. (1991) The crystal structure of amesite from Mount Sobotka: a nonstandard polytype. *American Mineralogist*, **76**, 647–652.

Wilkins R.W.T. & Ito J. (1967) Infrared spectra of some synthetic talcs. *American Mineralogist*, **52**, 1649–1661.

Wise W.S. & Eugster H.P. (1964) Celadonite: synthesis, thermal stability and occurrence. *American Mineralogist*, **49**, 1031–1083.

Wones D.R. & Eugster H.P. (1965) Stability of biotite: experiment, theory and application. *American Mineralogist*, **50**, 1228–1272.

Yoder H.S. & Eugster H.P. (1955) Synthetic and natural muscovite. *Geochimica Cosmochimica Acta*, **8**, 225–280.

Yoshimura T., Shirozu H. & Hirowabori F. (1963) Bementite and pyromanganite from the Ichinomata mine, Kunamoto prefecture. *Journal of the Mineralogical Society of Japan*, **3**, 457–467.

Zazzi A, Hirsch T.K., Leonova E., Kaikkonen A., Grins J., Annersten H. & Eden M. (2006) Structural investigations of natural and synthetic chlorite minerals by X-ray diffraction, Mössbauer spectroscopy and solid-state nuclear magnetic resonance. *Clays and Clay Minerals*, **54**, 252–265.

Zhang H., Gilbert B. & Banfield J.F. (2021) Atomic perspective on the serpentine–chlorite solid-state transformation. *Chemistry of Materials*, **33**, 6338–6345.

Zheng H. & Bailey S.W. (1989) Structure of intergrown triclinic and monoclinic IIb chlorites from Kenya. *Clay and Clay Minerals*, **37**, 308–316.

Zheng H. & Bailey S.W. (1997a) Refinement of an amesite-$2H_1$ polytype from Postmasburg, South Africa. *Clay and Clay Minerals*, **45**, 301–310.

Zheng H. & Bailey S.W. (1997b) Refinement of the cookeite '*r*' structure. *American Mineralogist*, **82**, 1007–1013.

Zviagina B.B. & Drits V.A. (2019) Structural factors affecting the crystal-chemical variability in Al-rich K-dioctahedral $2M_1$ micas. *Clay Minerals*, **54**, 1–11.

https://doi.org/10.1180/clm.2023.20 Published online by Cambridge University Press